Department of Civil and Structural Engineering

Proceedings of the 24th Nordic Seminar on Computational Mechanics

Edited by Jouni Freund and Reijo Kouhia

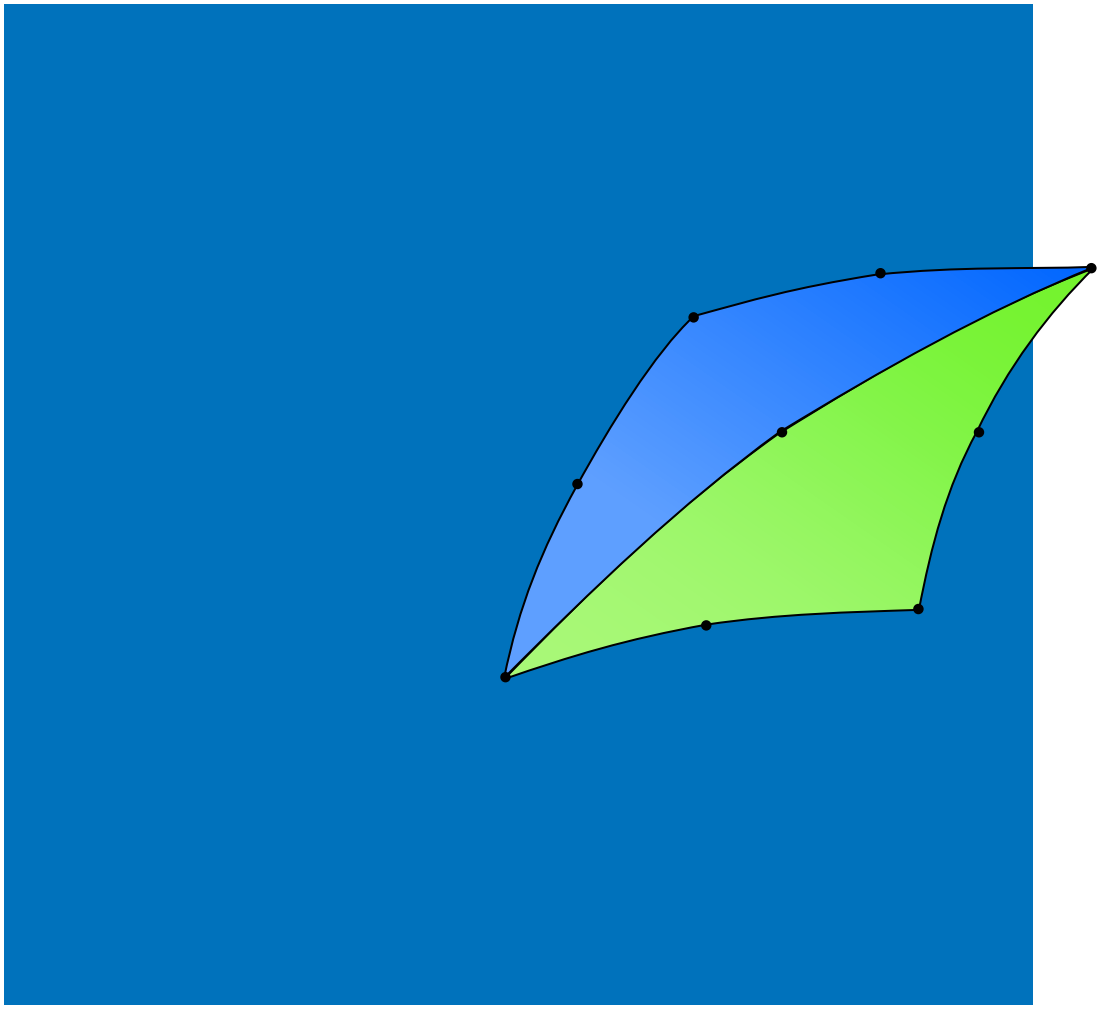

Aalto University

SCIENCE + TECHNOLOGY

CONFERENCE PROCEEDINGS

Aalto University publication series
SCIENCE + **TECHNOLOGY** 23/2011

Proceedings of the 24th Nordic Seminar on Computational Mechanics

Edited by Jouni Freund and Reijo Kouhia

Aalto University
School of Engineering
Department of Civil and Structural Engineering

Aalto University publication series
SCIENCE + **TECHNOLOGY** 23/2011

ISBN 978-952-60-4346-3 (pdf)
ISBN 978-952-60-4347-0 (printed)
ISSN-L 1799-4896
ISSN 1799-490X (pdf)
ISSN 1799-4896 (printed)

Unigrafia Oy
Helsinki 2011

Finland

This proceedings is dedicated to Professor Martti Mikkola
on the occasion of his 75th birthday

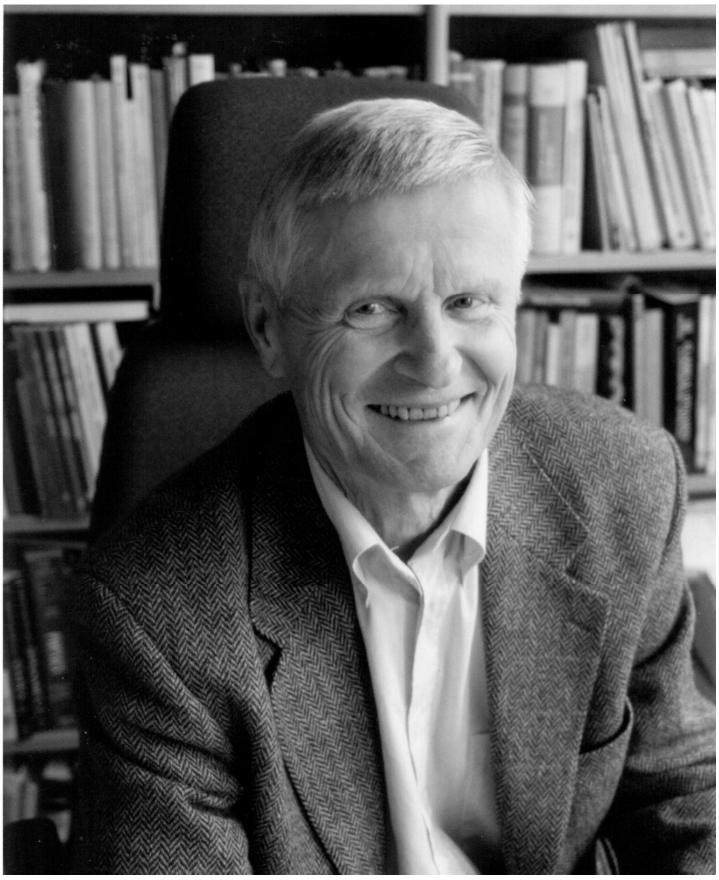

Preface

This book contains the extended abstracts of lectures presented at the 24th Nordic Seminar on Computational Mechanics (NSCM-24), held at the Marina Congress Center, Helsinki, Finland, 3-4 November 2011, and hosted by Aalto University School of Engineering.

The Nordic Association of Computational Mechanics (NoACM) was founded in October 1988. Its objective is to stimulate and promote research and applications within the area of computational mechanics. The main activity of NoACM is the annual two day seminar which provides a forum for personal contacts and for the exchange of ideas. Young researches, including doctorate and graduate students, are particularly welcome. Thus, making a friendly and creative atmosphere for the participants is considered important.

This year's seminar contains ten invited plenary lectures, three invited keynote lectures and 60 contributed presentations which sums up to 73 presentations altogether. The seminar will honour professor Martti Mikkola's 75th anniversary. In this proceedings, the invited plenary lectures are placed first followed by the presentations in the other sessions. Some of the presentations are published as a full length peer reviewed journal paper in *Rakenteiden Mekaniikka (Journal of Structural Mechanics)*. For these presentations, only the summaries are included in this proceedings.

Sincere thanks go to the thematic session organisers, all of the authors and participants for making the NSCM-24 a stimulating conference. Finally, we thank all the sponsors: ETI Products, Federation of Finnish Learned Societies, FEMdata, Finnforest, Finnish Association of Civil Engineers RIL, FMC Group – (Finnmap Consulting, KPM-Engineering, Aaro Kohonen), Konecranes, Magnus Ehrnrooth Foundation, Magnus Malmberg Consulting Engineers, Numerola, Pontek Consulting Engineers, Process Flow, Ruukki Construction, SITO, STX Finland, TVO, VTT Technical Research Centre of Finland, whose support was indispensable for the organisation of this seminar.

Otaniemi, October 2011

Jouni Freund and Reijo Kouhia

Table of contents

Constitutive modeling:

Numerical techniques:

Multiscale modeling in solid mechanics: thematic session organised by F. Larsson

Optimisation:

Stability:

Multibody mechanics 1: thematic session organised by J. Mäkinen, M. Matikainen

Keynote lecture:

Dynamics:

Solids and fluids:

Multibody mechanics 2: thematic session organised by J. Mäkinen, M. Matikainen

Keynote lecture:

Applications:

Micro- and nano-mechanics:

Rakenteiden Mekaniikka (Journal of Structural Mechanics)
Vol. 44, No 3, 2011, pp. 156-171

Thermodynamic interpretation of finite volume algorithms

Arkadi Berezovski

Summary. The thermodynamic consistency is a desired feature of numerical algorithms for physical problems. Such a consistency can be achieved if the computational cells are considered as discrete thermodynamic systems. It is shown that faithful, accurate, and conservative finite-volume algorithms are compatible with thermodynamics through the identification of numerical fluxes and excess quantities.

Key words: conservation laws, finite-volume methods, thermodynamics

Centre for Nonlinear Studies
Institute of Cybernetics at Tallinn University of Technology
Akadeemia tee 21
Tallinn, 12618, Estonia
Arkadi.Berezovski@cs.ioc.ee

Proceedings of the 24th Nordic Seminar on Computational Mechanics
J. Freund and R. Kouhia (Eds.)

A new concept for a very large twin hull cruise ship

Pål G. Bergan[1], and Justin Chanwook Jang[2]

[(1)]Ocean Systems Engineering, KAIST and Structural Engineering, NTNU, 7034 Trondheim, Norway, Pal.Bergan@ntnu.no
[(2)]Ocean Systems Engineering, KAIST, Daejeon 305-701, Republic of Korea, blueocean@kaist.ac.kr

Summary. A proposed cruise ship concept consists of a wide, catamaran type ship with two sleek, wave-piercing hulls. The overall length is 366 m and the total width is 70 m. There are two separate superstructures facilitating more than two thousand passenger cabins, all with exterior balconies. The twin hull design implies good stability and seaworthiness; however, the deck connecting the two hulls will be exposed to extreme environmental forces. To this end a ship-wide, cellular deck structure is devised for strength and stiffness. The ship also features many new solutions for the structure as well as protected space for life and service boats, and a possibility for use of a spectacular, large kite as well as wind foils for supplementary propulsion.

Key words: computational mechanics, cruise ship, twin hull, innovation

Introduction

The cruise market is showing strong and continuous growth and cruise operators are in search of new concepts and bigger ships that can offer more spectacular experience for the passenger. The actual value and performance of a cruise ship is determined by its design, onboard facilities and entertainment, as well as technical performance in terms of seaworthiness, environmental performance, and safety.

In spite of recent years with economical difficulties in many countries the cruise market seems to be in positive development. The annual growth of passenger journeys is currently at 7.7 percent with an estimated total number of number of 14.3 million passengers in 2010; this last figure is expected to grow to 21.6 million in 2014 [1]. Currently the Asian market makes out only 4.2 percent of the world cruise market; it is believed that this market has potential for growing much faster than other markets and that this may only be achieved by introducing a new type of mega cruise ship.

There are some notable characteristics of the cruise market development. First of all, the size of cruise ships are typically classified in different groups spanning from small ships 2-10000 GT, via 10-60000 GT, 60-100000 GT, and the very large ship beyond 100000GT. In the future we may also include ultra-large cruise ships beyond 250000 GT. The number of ships in the “very large” group is clearly the one that will be growing fastest in years to come, possibly with a rate of more than 10.0 percent per year. It also seems clear that the actual size of ships within the large ship category is also

increasing with many ships larger than 150000 GT. For instance, since 2009 several ships in the "Oasis Class" with more than 225000 GT have been built in Finnland.

A new cruise ship concept

The current study concerns a very large catamaran suited as a platform for a cruise ship, see figure 1. It is seen that there are two very long and sleek hulls that are connected with a strong deck at a good distance above the water line. Each hull structure carries its own, large superstructure; these are connected at high level at the fore bridge area of the ship. Some characteristic geometric measures are:

Length OA:	366m
Length Deck:	300m
Breadth Deck:	18m+22m+18m = 58m
Breadth WL:	25m+20m+25m = 70m
Draught at waterline:	9m
Freeboard Deck:	7m
Freeboard:	16m
Depth to Upper Deck:	22m +10m = 32m (+45m wind foils)
Displacement:	86828 m^3
Gross Tonnage:	260000 ton

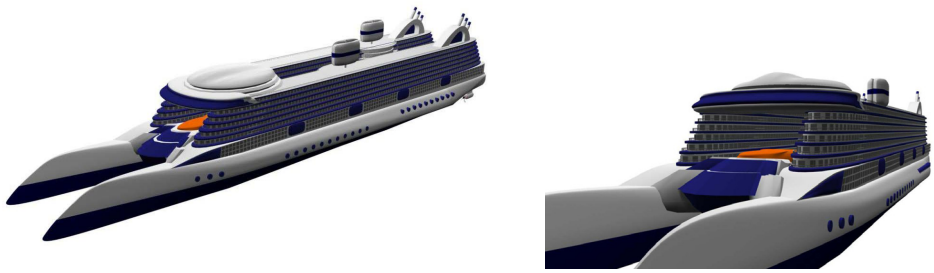

Figure 1. Views of the proposed cruise catamaran

The two hulls with the interconnecting deck structure may be built with conventional high strength steel. The chosen shape of the two hulls and the connecting deck structure is illustrated in figure 2. The bows have an extended lower end and will as such be "wave piercing". The reason for this choice is that we would like to reduce pitching accelerations during coarse head seas. The wave piercing behaviour implies that there will be much more wave overflow and green seas on the fore part of the hulls; however, this area is only a very small part of the overall deck area that will not be accessible for passengers.

A target for the connecting deck design has been to provide a structural connection between the two hulls that is strong and stiff enough to withstand the extreme forces that the ship will be subjected to during severe sea conditions. At the same time the large volume of the deck structure provides very valuable internal space that ideally should be available for use without obstructions from extensive

structural members and barriers. As will be described later in this paper, such a performance is achieved by using a highly efficient cellular structural design.

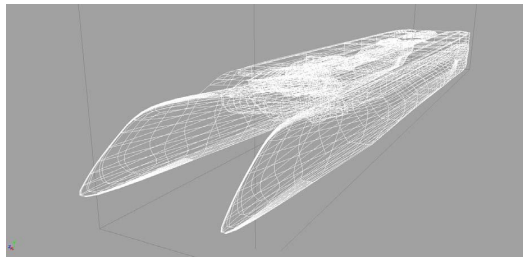

Figure 2. Surface lines showing shape of hulls and deck

Safety and environmental performance

The fact that the mega-size catamaran represents something new means that hazard identification, safety case assessments, and incorporation of the best active and passive safety measures become all the more important. The new safety philosophy within SOLAS 2010 Chapter "Safe Return to Port for Passenger Ships" has extensive implications for the planning of the catamaran cruise ship. A crucial parameter is damage stability. It turns out that twin hulls can easily be compartmented with bulk heads and even double exterior skins below the water line zone.

Similarly, fire zoning, fire barriers and curtains, and fire fighting measures can be implemented just as well or even better than in the case of mono-hulls. Unlike current cruise ships the mid-ship open deck goes along the entire length of the ship and provides a large exterior zone where passengers may gather in situations of danger rather than having to escape along the exterior sides of the ship onto traitorous water.

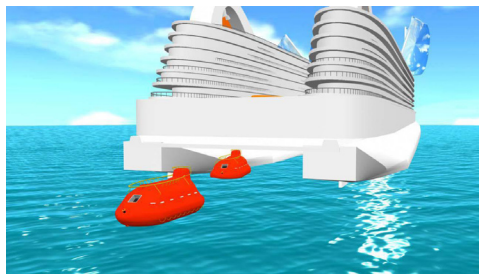

Figure 3. Lifeboats launched from interior wet deck

Life boats may be located on the exterior along the entire length of the superstructures. However, in the "spirit of innovation" another, more radical solution is here suggested. The water between the two hulls is clearly calmer and better protected than is the case for the sea along the exterior sides. An idea is thus to provide docking space for life boats above the wet deck inside the main deck structure that combines twin hulls, see figure 3. Having 6000 people onboard requires life boat capacity for

more than 5000 people. This can only be done with very large life boats such as the 370 person life boats used for Oasis of the Seas [2].

Cruise passenger are increasingly aware of the importance of environmental impact and environmental performance. A spectacular feature that may contribute towards a positive image of the ship is the capability of launching a large kite from two retractable launching masts at the bows of the ship, see figure 4. The fact that there will be two masts enhances the operational efficiency of such a kite. The sail itself can easily be packed away when not in use.

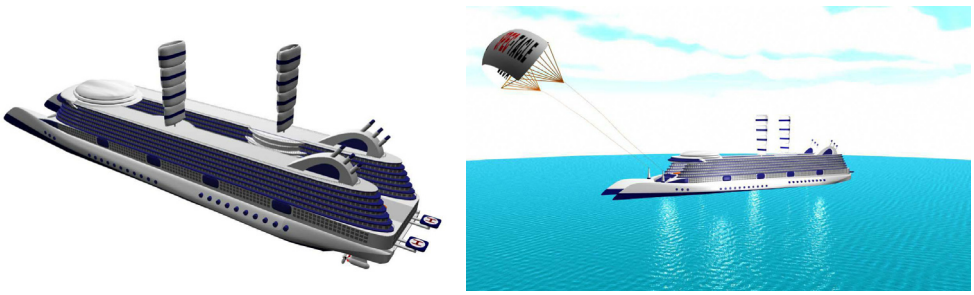

Figure 4. Kite propulsion and telescopic air foils

The figure also two telescopic and adjustable air foils, one on each superstructure. These air foils can be deployed and oriented in accordance with best use of wind conditions and provide "free" and environmentally friendly propulsion. When not in use the air foils are compacted on the upper decks, see figure 4, whereas they can quickly be telescopically extended when needed. The fact that the catamaran is very wide and stable makes such a feature possible, whereas a conventional mono-hull cruise ship would have difficulties with heeling and stability during operation of such large wind foils.

Hydrodynamics and structural performance

No doubt hydrodynamics and sea-keeping for this mega-catamaran may provide a greater challenge than is the case for conventional ships. So far only preliminary assessments have been carried out in this respect; further studies and optimisation will have to be carried out in the future. A general observation is that the two very sleek hulls will have relatively little wave resistance whereas their skin or surface friction will be relatively larger than for corresponding mono-hull ships. It is still too early to say whether some positive wave cancellation effects may be achieved between the two hulls; this is also left for further studies.

Some preliminary resistance calculations based on Holtrop and Mennen method [3] indicates that the total resistance of the catamaran will be somewhat larger than for a "theoretical", corresponding mono-hull ship where the current twin hulls are merged into a single body. However, this increased resistance is not very large. Typically the power requirement for the catamaran is estimated to be the same as for a corresponding mono-hull with 2 to 3 knots higher speed. Considering that the catamaran easily lends itself to kite power as well as air foil power the comparison may in the end turn out to be in the favour of the catamaran.

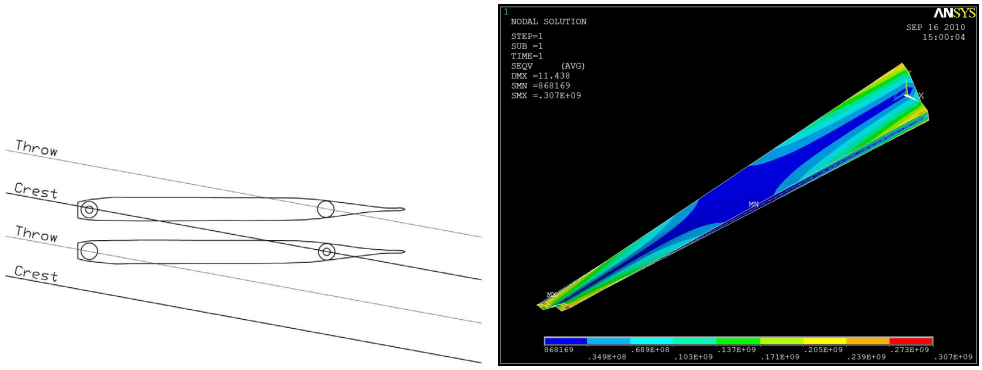

Figure 5. Incoming waves at 80 degrees and deck stresses

A large catamaran can be designed with the same safety and strength levels as for a conventional ship. A catamaran ia exposed to some unusual wave forces; this particularly concerns skew incoming waves from the side that will expose the twin hulls to an extremely severe warping (twisting) load condition, see figure 5.

Realizing this particular challenge the deck that binds the two hulls has to be designed in an innovative way. This is done by using a cellular, double deck where the cells are continuously connected with each other and oriented in the transverse direction of the ship. It can be shown that this kind of cell structure is extremely stiff and strong. This structure is also very well suited for load conditions which impose large transverse bending moments on the connecting deck.

Calculations with the finite element program ANSYS has revealed that it will not be difficult to all safety requirements for this deck. Figure 5 shows stress results obtained for the most severe warping load condition for this deck. The design of other parts of the ship is rather straight forward; and force and stress can easily be determined in a conventional way by finite element analysis and checked for compliance in relation to rule requirements.

References

1. Wahlstrom, R., '2011 Cruise Line Market Share and Revenue Projections', *Cruise Market Watch Announce*, 2010.
2. Guy, J., 'Schat-Harding Provides 370-Person Mega Lifboats to World's Largest Cruise Ship', *Schat Harding*, 2009.
3. Holtrop, J., Mennen, G.G.J., 'An Approximate Power Prediction Method', *International Shipbuilding Progress*, 1988

Acknowledgements

The research was supported by the World Class University program of the National Research Foundation of Korea funded by the Ministry of Education, Science and Technology (R31-2008-000-10045-0).

Proceedings of the 24th Nordic Seminar on Computational Mechanics
J. Freund and R. Kouhia (Eds.)

Motion of a solid with large deformations

Elena Bonetti[1], Pierluigi Colli[1], Michel Frémond[2]

(1) Laboratorio Lagrange, Dipartimento di Matematica``F.Casorati", Università di Pavia Italy, elena.bonetti@unipv.it, pierluigi.colli@unipv.it
(2) Laboratorio Lagrange, Dipartimento di Ingegneria Civile, Università di Roma "Tor Vergata", Italy, michel.fremond@lagrange.it

Summary. We investigate the motion of a solid with large deformations assuming the rotation matrix and the impenetrability reaction depend on their neighbourhood. We prove that there exists a motion which satisfies the equations of mechanics.

Key words: motion. large deformation, rotation matrix, impenetrability reaction

Proceedings of the 24th Nordic Seminar on Computational Mechanics
J. Freund and R. Kouhia (Eds.)

Large eddy simulation studies on convective atmospheric boundary layer

Antti Hellsten and Sergej Zilitinkevich

Finnish Meteorological Institute, P.O.Box 503, FI-00101 HELSINKI,
antti.hellsten@fmi.fi sergej.zilitinkevich@fmi.fi

Summary. This article describes current Large-Eddy Simulation (LES) -based research activities at Finnish Meteorological Institute focusing on convective atmospheric boundary layer. The convective atmospheric boundary layer is first introduced and its main characteristics are briefly discussed. The related research problems are then presented, and the LES method we use for these studies is briefly introduced.

Key words: convection, turbulence, atmospheric boundary layer, large-eddy simulation, LES

Introduction

Atmospheric boundary layer (ABL) is defined as the layer next to the ground surface in which ground directly influences the atmosphere. The most influential effects from the ground surface are vertical fluxes of momentum, heat and moisture. Also fluxes of various admixtures, both natural and anthropogenic, are important ABL processes. The depth of ABL can vary from few tens of meters in certain high-latitude winter conditions to several kilometres in summer-time fair-weather conditions, especially on low latitudes. The former is an example of strong stable stratification and the latter of unstable stratification leading to development of convective boundary layer (CBL) which is the topic of this paper.

Unstable stratification takes place when ground surface is heated and becomes warmer than air above it. In other words, when the surface heat flux is positive (upwards). This leads to instability and formation of convective plumes or up-drafts and corresponding down-drafts. Such structures are very efficient mixing agents, and as a result a mixed layer develops above the unstable surface layer. In the mixed layer, local stability is near neutral on the average because the potential temperature is approximately height-constant there. Also the mean wind is practically constant in the mixed layer. CBL grows in time against stable stratification in the free atmosphere as the up-drafts hammer the stably stratified air aloft (capping inversion). Between the mixed layer and the free atmosphere, there is an entrainment zone where the heat flux is negative. This means that CBL is heated not only from the ground but also through its top boundary on the altitude z_i. Figure 1 illustrates the structure of the CBL and shows examples of horizontally averaged profiles of heat-flux, temperature and wind components for a

horizontally homogeneous dry barotropic CBL with geostrophic wind of 18 m/s and constant surface heat-flux of 128 W/m^2.

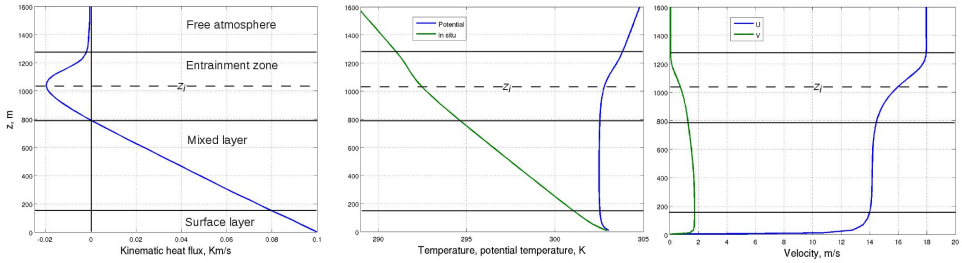

Figure 1. Structure of convective boundary layer with mean geostrophic wind of 18 m/s and surface heat flux of 128 W/m^2. Spatially averaged profiles of kinematic heat flux, potential and in-situ temperatures and wind components.

Buoyant up-drafts and down-drafts are coherent structures with remarkably long lifetimes compared to the less-organized turbulent motion also present everywhere in the CBL. These structures can take the form of convective cells typical in weak-wind conditions or nearly wind-wise oriented rolls typical in stronger wind, see Fig 2. Convective structures are embedded in locally generated ordinary turbulence with very wide range of scales. Therefore they cannot be easily separated from the ordinary turbulence. The convective structures very efficiently transport heat upwards and momentum downwards even though the local mean gradients of velocity and potential temperature in the mixed layer are essentially zero as shown in Figure 1. This means that the classical gradient transport hypothesis and eddy-viscosity concept do not form a feasible basis for parametrizing (modelling) convective mixing.

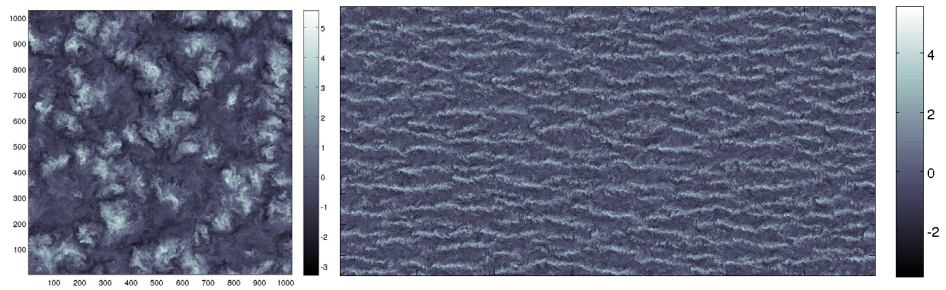

Figure 2. Example of cell convection (left) and roll convection (right). Vertical velocity on a horizontal cut plane in the mixed layer is shown by gray scale. Note that the images have different scales; the left image covers approximately 10 km□10 km and the right one covers about 35 km□70 km.

We live in the ABL and the weather conditions we feel in our everyday life depend very much on the ABL processes. However, most of such processes have so small length scales that

they cannot be captured by the numerical weather-prediction models because of their limited resolution. Therefore these processes must be parameterized in such models. As another example, global warming depends very essentially on the processes which control the thermal balance of ABL, hence we must deepen our understanding of the ABL dynamics and thermodynamics in both stable and convective cases, both cases are important.

CBL has been studied relatively much during several decades already. Even LES-based research started very early, already in the beginning of 1970's when Deardorff carried out his pioneering LES studies of CBL [1-3]. Thus many basic processes are quite well understood, but many open questions still remain. A few such research questions that we are focusing on at Finnish Meteorological Institute (FMI) are introduced in the next section. Some results are shown in the oral presentation, although the space does not permit to present them in this paper.

Some CBL-related research questions currently studied at FMI

Scaling and similarity analysis

Scaling of the pure convection situation with no mean wind has been known since Deardorff's work [2]. Similarly, the scaling of the surface layer, the Monin-Obukhov similarity theory [4], has been well established since the 1950's. However, there is no systematic scaling and similarity analysis proposed for a wide range of stability regimes from pure convection to near neutral CBL. Making use of dimensional analysis and our LES results with wide range of stability conditions as well as other parameters make it possible to look for appropriate scaling and similarity states. This is currently being done for barotropic CBLs and will later be extended to practically more relevant baroclinic situations.

Contribution of coherent structures to fluxes and variances

As mentioned above, the eddy-viscosity approach is not suitable for parametrizing convection in CBL owing to its non-local nature. On the other hand, smaller-scale ordinary turbulence also present in CBL can well be parametrized using the eddy-viscosity approach. So called mass-flux approach, see e.g. [5], has been applied to parametrize the contributions of the convective coherent structures on the total fluxes. However, in order to do so, these two types of motion must be somehow separated from each other in LES data to provide data for calibrating such parametrizations. How to separate coherent structures from ordinary turbulence is not a well posed problem as the energy spectrum is continuous, I.e. there is no spectral gap between these two types of motion. However, we have tried different kinds of partitionings and they quite systematically show that the coherent structures build up most of the fluxes and variances. However, proper separation criteria applicable throughout the CBL is still to be found.

Spectral energy transfer

The classical picture of turbulence, emanating from the long research history of homogeneous turbulence, involves the concept of forward energy cascade. That is, energy is fed into the largest turbulent structures and it gradually cascades towards smaller and smaller eddies until it is dissipated into heat mostly by the small-scale motion with very sharp gradients. However, there are reasons to assume that in CBL also inverse cascade may happen from middle-sized structures to the largest coherent ones. Buoyant energy insertion on the ground surface happens in filament-like relatively narrow up-drafts which increase in breadth with increasing altitude. This may be an indication of inverse energy cascade. However, the existence of such inverse cascade has neither been proven nor quantified, yet. We are currently studying this problem from our LES-results. If it can be shown that the inverse energy cascade exists in CBL, the current theories of CBL turbulence should possibly be revised.

Computational methods

We use an LES model called PALM for our CBL studies. PALM is efficiently parallelized and designed for ABL problems (Raasch & Schröter 2001; Letzel et al. 2008). PALM has been developed at Leibniz Universität Hannover and adopted as a research tool at FMI in 2009. PALM is a finite difference method for incompressible filtered Navier-Stokes equations with Boussinesq approach to buoyancy. Advection can be discretized using a second-order central scheme [8] or a fifth-order upstream scheme [9]. Solution of the incompressible Navier-Stokes system is based on the projection method [10]. Pressure can be solved in the Fourier space in cases of horizontally homogeneous boundary layer (periodic boundary conditions) or using a multi-grid method for inhomogeneous cases. We are employing the former option for our studies discussed in this paper. An explicit third-order accurate Runge-Kutta scheme is used for time integration. PALM models the sub-grid scale turbulence by a one-equation model [11].

Owing to the efficient parallelization of PALM based on the Message Passing Interface(MPI), we are routinely computing problems with of the order of 500 million grid nodes using 500-600 processing elements on the Cray XT-5 supercomputer environment at FMI. As part of a grid-independence study, we have successfully carried out an LES with over two billion nodes using 1296 parallel processes.

References

[1] J.W. Deardorff, Preliminary results from numerical integration of the unstable boundary layer, *J. Atmos. Sci.*, 27:1209-1211, 1970.

[2] J.W. Deardorff, Convective velocity and temperature scales for the unstable planetary boundary layer and for Raleigh convection, *J. Atmos. Sci.*, 27:1211-1213, 1970.

[3] J.W. Deardorff, Numerical investigation of neutral and unstable boundary layers, *J. Atmos. Sci.*, 29:91-115, 1972.

[4] A.S. Monin and A.M. Obukhov, Osnovnye zakonomernosti turbulentnogo peremeshivanija v prizemnom sloe atmosfery (Basic laws of turbulent mixing in the atmosphere near the ground), *Trudy geofiz. inst. AN SSSR*, 24:301-304, 1954.

[5] S. Cheinet, A multiple mass-flux parameterization for the surface-generated convection. Part I: dry plumes, *J. Atmos. Sci.*, 60(18):2313-2327, 2003.

[6] S. Raasch and M. Schröter, A large-eddy simulation model performing on massively parallel Computers. *Meteorologische Zeitschrift* 10(5): 363-372, 2001.

[7] M. Letzel, M. Krane and S. Raasch, High resolution urban large-eddy simulation studies from street canyon to neighbourhood scale. *Atmospheric environment* 42(38): 8770–8784, 2008.

[8] S.A. Piaseck and G. P. Williams, Conservation properties of convection difference schemes. *J. Comput. Phys.*, 198: 580-616, 1970.

[9] L.J. Wicker and W. C. Skamarock, Time-splitting methods for elastic models using forward time schemes. *Mon. Wea. Rev.*, 130: 2088-2097, 2002.

[10] A.J. Chorin, Numerical solution of the Navier-Stokes equations. *Mathematics of Computation* 22, 745-762, 1968.

[11] J.W. Deardorff, Stratocumulus-capped mixed layers derived from a three-dimensional model. *Boundary-Layer Meteorology* 18: 495-527, 1980.

Proceedings of the 24th Nordic Seminar on Computational Mechanics
J. Freund and R. Kouhia (Eds.)

Modeling and analysis of rotating solids and structures

Steen Krenk

Department of Mechanical Engineering, Technical University of Denmark; sk@mek.dtu.dk

Summary. It is demonstrated that the inertial terms in the dynamic equations of motion in a moving frame take a simple universal form in terms of the classic mass matrix, when the traditional Lagrangian approach with local velocities as time derivatives of position is replaced by a Hamiltonian approach, in which absolute velocities and local positions are interpolated by identical shape functions. The resulting equations take on a simple systematic form that lends itself naturally to conservative time integration and permits a simple algorithmic damping scheme in terms of local motion.

Key words: Time integration, conservative integration, structural dynamics.

Introduction

Rotating structures are acted on by inertial forces generated by the rotation. If the local displacement of the structure at a generic point is represented by shape functions and local velocities are obtained by time differentiation of the interpolated displacements, the inertial effects from rotation leads to mass matrices containing the angular velocity and acceleration of the rotating frame of reference. While the inertial forces can be obtained via rearranging individual parts of the original mass matrix – see e.g. [1] – the appearance of separate representations of the inertial effects in the discretized system equations is computationally inconvenient and complicates the development of conservative time integration algorithms for rotating structures. This problem can be resolved by adopting a Hamiltonian view of mechanics, in which displacements and velocities (momentum) appear as independent variables, and therefore are interpolated separately from their nodal values. Hereby all inertial effects are represented by the classic mass matrix, and the effects of rotational convection are represented by global operations via vector products with the angular velocity of the rotating frame of reference.

The nodal displacements and velocities constitute a state-space representation of the local motion. When the local displacements are combined with the absolute velocities the corresponding hybrid state-space equations of motion take a particularly simple form without the angular acceleration and with the angular velocity only in linear form. A conservative integration algorithm for the hybrid state-space variables is obtained by using the mean value of the angular velocity over the current integration interval. For changing angular velocity the conservative integration format is different from the classic collocation format exemplified by the Newmark scheme. A damping based on local motion can be introduced by a simple modification of the coefficients of the state-space integration format.

Lagrange-Hamilton basics

Let a structure be described by a set of generalized coordinates $\boldsymbol{q} = [q_1, q_2, \cdots]^T$ with time derivative $\dot{\boldsymbol{q}} = [\dot{q}_1, \dot{q}_2, \cdots]^T$. The Lagrangian functional is then defined by

$$\mathcal{L} = \int_{t_1}^{t_2} L(\boldsymbol{q}, \dot{\boldsymbol{q}}, t)\, dt \tag{1}$$

in terms of the Lagrangian density

$$L(\boldsymbol{q},\dot{\boldsymbol{q}},t) \;=\; T(\boldsymbol{q},\dot{\boldsymbol{q}},t) \;-\; V(\boldsymbol{q},t), \tag{2}$$

where $T(\boldsymbol{q},\dot{\boldsymbol{q}},t)$ is the kinetic energy, while $V(\boldsymbol{q},t)$ is a potential. The equations of motion follow from the variational condition $\delta\mathcal{L} = 0$, whereby

$$\frac{d}{dt}\Big(\frac{\partial L}{\partial \dot{\boldsymbol{q}}}\Big) \;-\; \frac{\partial L}{\partial \boldsymbol{q}} \;=\; \boldsymbol{0}. \tag{3}$$

In the Lagrangian formulation the variables are the generalized displacements $\boldsymbol{q}$, and the equations of motion are second order differential equations in these variables.

The Hamiltonian formulation starts by introducing the term in the parenthesis of (3) as the independent momentum,

$$\boldsymbol{p} \;=\; \frac{\partial L}{\partial \dot{\boldsymbol{q}}^T}. \tag{4}$$

The Hamiltonian $H(\boldsymbol{q},\boldsymbol{p},t)$ is then defined from the Lagrangian $L(\boldsymbol{q},\dot{\boldsymbol{q}},t)$ by the Legendre transform

$$H(\boldsymbol{q},\boldsymbol{p},t) \;=\; \dot{\boldsymbol{q}}^T\boldsymbol{p} \;-\; L(\boldsymbol{q},\dot{\boldsymbol{q}},t), \tag{5}$$

where the displacements $\boldsymbol{q}$ and the momentum $\boldsymbol{p}$ are treated as independent variables. The equations of motion then follow from stationarity in the classic form

$$\frac{d\boldsymbol{p}}{dt} \;=\; -\frac{\partial H}{\partial \boldsymbol{q}^T}, \qquad \frac{d\boldsymbol{q}}{dt} \;=\; \frac{\partial H}{\partial \boldsymbol{p}^T}. \tag{6}$$

The important observation in the present context is that by introducing the additional conjugate variable $\boldsymbol{p}$, the original set of second order differential equations are transformed into a set of first order equations in $\boldsymbol{q}$ and $\boldsymbol{p}$. The symmetric form of the Hamiltonian equations suggest representation of these independent variables by identical interpolation schemes.

Rotating structures

A rotating structure is illustrated in Fig. 1. The position of the nodes are described by the coordinates $\boldsymbol{x}_n$ in a frame of reference rotating with angular velocity $\boldsymbol{\Omega}$. A generic point with internal coordinate $\boldsymbol{\xi}$ is the given in the local frame in terms of the coordinates of the nodes as

$$\boldsymbol{x}_\xi \;=\; \underbrace{\boldsymbol{N}(\boldsymbol{\xi})}_{3\times N}\boldsymbol{x}_n. \tag{7}$$

The issue here is the representation of the corresponding velocity.

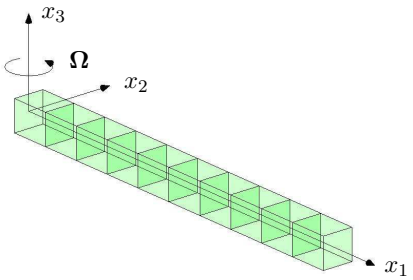

Figure 1. Solid body in frame $\{x_1, x_2, x_3\}$ rotating with angular velocity $\boldsymbol{\Omega}$.

Classic representation

The classic approach is Lagrangian in the sense that the local components of the global velocity $\boldsymbol{v}_\xi$ is obtained at the generic point $\boldsymbol{x}_\xi$ as an absolute time derivative, combining the local velocity and a convective velocity from the rotation of the frame of reference,

$$\boldsymbol{v}_\xi \;=\; D_t \boldsymbol{x}_\xi \;=\; (\partial_t + \tilde{\boldsymbol{\Omega}})\boldsymbol{x}_\xi, \tag{8}$$

where the notation $\tilde{\boldsymbol{\Omega}} = \boldsymbol{\Omega}\times$ is used for the skew symmetric matrix representing the vector product. The kinetic energy is given in terms of the absolute velocity as

$$T \;=\; \int_V \tfrac{1}{2}\rho\, \boldsymbol{v}_\xi^T \boldsymbol{v}_\xi \, dV_\xi. \tag{9}$$

The absolute velocity depends on the local nodal velocity $\dot{\boldsymbol{x}}_n$ and the local position $\boldsymbol{x}_n$ and substitution from (8) gives the discretized form

$$T \;=\; \tfrac{1}{2}[\dot{\boldsymbol{x}}_n^T, \boldsymbol{x}_n^T] \begin{bmatrix} \boldsymbol{M}_{00} & \boldsymbol{M}_{01} \\ \boldsymbol{M}_{10} & \boldsymbol{M}_{11} \end{bmatrix} \begin{bmatrix} \dot{\boldsymbol{x}}_n \\ \boldsymbol{x}_n \end{bmatrix}, \tag{10}$$

where the block matrices $\boldsymbol{M}_{jk}$ are defined by

$$\boldsymbol{M}_{jk} \;=\; \int_V \rho\, \boldsymbol{N}(\boldsymbol{\xi})^T (\tilde{\boldsymbol{\Omega}}^T)^j \tilde{\boldsymbol{\Omega}}^k \boldsymbol{N}(\boldsymbol{\xi})\, dV_\xi. \tag{11}$$

It is seen that the angular velocity $\boldsymbol{\Omega}$ is imbedded inside the volume integral. For elements that are not based on identical interpolation of all three displacement components – essentially all non-isoparametric elements – moving the angular velocity vector outside the integral requires some measure of restructuring of the mass matrix. In cases with time-dependent angular velocity this formulation therefore involves reassembly of the inertial matrices containing $\boldsymbol{\Omega}$ as well as terms representing the time derivatives of these matrices.

Hamiltonian representation

In the Hamiltonian formulation the generalized displacement vector $\boldsymbol{x}$ is supplemented by the corresponding momentum vector, defined via (4). The present paper is concerned with formulations in which the mass matrix is constant. This class includes isoparametric elements and elements that can be constructed using a definition of generalized strains as a quadratic function of the generalized displacements. The latter group includes energy-consistent moderate-strain formulations of e.g. beams, plates and shallow shells. When the mass matrix is constant the momentum vector can be replaced by the nodal velocity vector. The absolute velocity at a generic point $\boldsymbol{\xi}$ then follows from the interpolation format (7) as

$$\boldsymbol{v}_\xi \;=\; \boldsymbol{N}(\boldsymbol{\xi})\boldsymbol{v}_n \;=\; \boldsymbol{N}(\boldsymbol{\xi}) D_t \boldsymbol{x}_n. \tag{12}$$

In this format the velocity interpolates the nodal values obtained via the convected differential operator $D_t = \lceil \partial_t + \tilde{\boldsymbol{\Omega}} \rfloor = \partial_t + \tilde{\boldsymbol{\Omega}}_D$, now extended to global form by defining the block diagonal matrix $\tilde{\boldsymbol{\Omega}}_D = \lceil \tilde{\boldsymbol{\Omega}}, \cdots, \tilde{\boldsymbol{\Omega}} \rfloor$. This format gives the kinetic energy in terms of the mass matrix as

$$T \;=\; \tfrac{1}{2}[\dot{\boldsymbol{x}}_n^T, \boldsymbol{x}_n^T] \begin{bmatrix} \boldsymbol{M} & \boldsymbol{M}\tilde{\boldsymbol{\Omega}}_D \\ \tilde{\boldsymbol{\Omega}}_D^T \boldsymbol{M} & \tilde{\boldsymbol{\Omega}}_D^T \boldsymbol{M} \tilde{\boldsymbol{\Omega}}_D \end{bmatrix} \begin{bmatrix} \dot{\boldsymbol{x}}_n \\ \boldsymbol{x}_n \end{bmatrix}, \tag{13}$$

and thus the inertial loads from convection are obtained from global operations on the assembled mass matrix $\boldsymbol{M}$.

Equations of motion

The equations of motion can be expressed in several different forms. While the particular form may be less important when discussing the exact continuous case, the choice of format is a central issue in the development of discrete time integration algorithms. In the following only the discretized form is used, represented in terms of the nodal values, and the subscript n is therefore omitted.

Lagrangian form with classic interpolation

The equations of motion in the second-order Lagrange format (3) follow directly from differentiation of the discretized kinetic energy (10) and a potential $V(\boldsymbol{x})$ giving external forces $\boldsymbol{f}$ and internal forces $\boldsymbol{g}(\boldsymbol{x})$. The result is the classic equation

$$\boldsymbol{M}_{00}\ddot{\boldsymbol{x}} + (\boldsymbol{M}_{01} - \boldsymbol{M}_{10})\dot{\boldsymbol{x}} - \boldsymbol{M}_{11}\boldsymbol{x} + \dot{\boldsymbol{M}}_{01}\boldsymbol{x} + \boldsymbol{g}(\boldsymbol{x}) = \boldsymbol{f}. \tag{14}$$

In the case of isoparametric elements the angular velocity may be applied to the assembled mass matrix, and the equation takes the somewhat more intuitive form

$$\boldsymbol{M}\ddot{\boldsymbol{x}} + (\boldsymbol{M}\tilde{\boldsymbol{\Omega}}_D + \tilde{\boldsymbol{\Omega}}_D\boldsymbol{M})\dot{\boldsymbol{x}} + \tilde{\boldsymbol{\Omega}}_D\boldsymbol{M}\tilde{\boldsymbol{\Omega}}_D\boldsymbol{x} + \boldsymbol{M}\dot{\tilde{\boldsymbol{\Omega}}}_D + \boldsymbol{g}(\boldsymbol{x}) = \boldsymbol{f}. \tag{15}$$

The second term is the gyroscopic or Coriolis force, the third is the centrifugal force, and the fourth term is the effect of angular acceleration. Even this special form, where the angular velocity has been extracted to the global format, does not lend itself immediately to energy conserving time integration because angular acceleration appears directly in the equation and the angular velocity appears in quadratic as well as in linear form. This dynamic equation is typically integrated by classic collocation schemes of collocation type, se e.g. [2].

Hybrid state-space format

The hybrid state-space format appears naturally, when observing that for the present problem $\boldsymbol{p} = \boldsymbol{M}\boldsymbol{v}$, and thus a natural variable combination is the local displacement $\boldsymbol{x}$ and the global velocity $\boldsymbol{v}$. The hybrid state-space equations of motion then take the form, [3],

$$\begin{bmatrix} \boldsymbol{0} & \boldsymbol{M} \\ -\boldsymbol{M} & \boldsymbol{0} \end{bmatrix} \begin{bmatrix} \dot{\boldsymbol{u}} \\ \dot{\boldsymbol{v}} \end{bmatrix} + \begin{bmatrix} \boldsymbol{g}(\boldsymbol{u}) + \tilde{\boldsymbol{\Omega}}_D\boldsymbol{M}\boldsymbol{v} \\ \boldsymbol{M}\tilde{\boldsymbol{\Omega}}_D^T\boldsymbol{u} + \boldsymbol{M}\,\boldsymbol{v} \end{bmatrix} = \begin{bmatrix} \boldsymbol{f} \\ -\boldsymbol{M}\tilde{\boldsymbol{\Omega}}_D^T\boldsymbol{x}_0 \end{bmatrix}. \tag{16}$$

where the displacements have been introduced as the difference between the current and the initial position, $\boldsymbol{u} = \boldsymbol{x} - \boldsymbol{x}_0$. These equations appear as a simple generalization of the classic state-space equations, e.g. [4], augmented by two linear terms in the angular velocity $\boldsymbol{\Omega}$. The hybrid state-space equations lend themselves directly to energy conserving time integration and permit a simple monotonic algorithmic damping scheme. This format is easily extended to models in which rotations are represented in quadratic form in terms of the generalized displacements, [5].

Conservative time integration

Conservative time integration algorithms are typically obtained from a time integral of the state-space equations of motion – in the present case (16). For structures with constant mass matrix the fist term changes directly into a similar term with the time increments of the state-space variables, $\Delta\boldsymbol{u}$ and $\Delta\boldsymbol{v}$. The issues to be resolved lie in the second term, which now represents a 'mean value' over the time integration interval Δt. It has been demonstrated in [3] that conservation properties are attained when the angular velocity $\boldsymbol{\Omega}$ is represented by its algebraic mean value of the initial and final values of the integration interval $\bar{\boldsymbol{\Omega}}$. In most problems

involving rotating bodies or structures the stiffening effect from stresses due to the centrifugal load play an essential role in balancing the direct centrifugal load term $\tilde{\boldsymbol{\Omega}}_D^T \boldsymbol{M} \tilde{\boldsymbol{\Omega}}_D$ to a greater or lesser extent, and geometric stiffness is therefore an important aspect of the problem. For elements with a quadratic strain measure, as in the present case, the effect of the kinematic non-linearity can be accounted for by the following simple result for the representative mean value of the internal forces, [4],

$$\boldsymbol{g}(\boldsymbol{u})_* \;=\; \overline{\boldsymbol{g}(\boldsymbol{u})} \;-\; \tfrac{1}{4}\Delta \boldsymbol{K}^g \Delta \boldsymbol{u}, \tag{17}$$

where $\Delta \boldsymbol{K}^g$ is the increment of the geometric stiffness matrix over the time interval Δt. In spite of the fact that this term formally is a 'higher order term' it is important for consistency and accuracy in problems depending on geometric stiffness.

When these two results are incorporated, the integrated form of the state-space equations of motion take the form

$$\begin{bmatrix} \frac{1}{4}\Delta t \Delta \mathbf{K}^g & \boldsymbol{M} \\ -\boldsymbol{M} & \boldsymbol{0} \end{bmatrix} \begin{bmatrix} \Delta \boldsymbol{u} \\ \Delta \boldsymbol{v} \end{bmatrix} + \Delta t \begin{bmatrix} \overline{\boldsymbol{g}(\boldsymbol{u})} + \bar{\tilde{\boldsymbol{\Omega}}}_D \boldsymbol{M} \bar{\boldsymbol{v}} \\ \boldsymbol{M} \bar{\tilde{\boldsymbol{\Omega}}}_D^T \bar{\boldsymbol{u}} \;+\; \boldsymbol{M}\, \bar{\boldsymbol{v}} \end{bmatrix} \;=\; \Delta t \begin{bmatrix} \boldsymbol{f}_* \\ -\boldsymbol{M} \bar{\tilde{\boldsymbol{\Omega}}}_D^T \boldsymbol{x}_0 \end{bmatrix}. \tag{18}$$

A local form of the energy balance can be obtained by expressing the absolute velocity $\boldsymbol{v}$ in terms of the local velocity $\dot{\boldsymbol{u}}$ from (8). Multiplication of the hybrid state-space equations (18) by $[\Delta \boldsymbol{u}^T, \Delta \boldsymbol{v}^T]$ leads to the following energy increment equation, [5],

$$\Big[\tfrac{1}{2}\dot{\boldsymbol{u}}^T \boldsymbol{M} \dot{\boldsymbol{u}} - \tfrac{1}{2}\boldsymbol{x}^T (\tilde{\boldsymbol{\Omega}}_D^T \boldsymbol{M} \tilde{\boldsymbol{\Omega}}_D)\boldsymbol{x} + G(\boldsymbol{u})\Big]_n^{n+1} \;+\; \overline{\boldsymbol{v}^T \boldsymbol{M} (\Delta \tilde{\boldsymbol{\Omega}}_D \boldsymbol{x})} \;=\; \Delta \boldsymbol{u}^T \boldsymbol{f}_*, \tag{19}$$

where $G(\boldsymbol{u}) = \Delta \boldsymbol{u}^T \boldsymbol{g}(\boldsymbol{u})$ is the increment of the internal energy, and $\Delta \boldsymbol{u}^T \boldsymbol{f}_*$ defines the work of the external force. The mean value term gives a direct representation of the contribution from angular acceleration within the time increment.

Local algorithmic damping

It is often desirable to introduce dissipation – partly to represent actual damping in the structure, and partly to dissipate high-frequency response components that are above the Nyquist frequency limit for reproduction of a continuous signal by its time-discretized counterpart. A convenient way of identifying a suitable format for algorithmic damping is to identify a desirable form of its dissipative contribution D to the energy balance equation. It has been demonstrated that for a stationary structure a suitable dissipation function is a quadratic form in the increments of the state-space variables, $D = \frac{1}{2}(\Delta \dot{\boldsymbol{u}}^T \boldsymbol{M} \Delta \dot{\boldsymbol{u}} + \Delta \boldsymbol{u}^T \boldsymbol{K} \Delta \boldsymbol{u})$, where $\boldsymbol{K}$ is a representative value of the stiffness matrix, [4]. In the present context it is desirable to formulate the dissipation in terms of local velocity $\dot{\boldsymbol{u}}$ in order for a purely convective rotation to be undamped. Furthermore, as seen from the energy balance equation, the local stiffness is reduced by $\tilde{\boldsymbol{\Omega}}_D^T \boldsymbol{M} \tilde{\boldsymbol{\Omega}}_D$. Thus, a suitable form of the dissipation potential in the present case is, [5],

$$D = \tfrac{1}{2}\alpha \Big\{ \Delta \dot{\boldsymbol{u}}^T \boldsymbol{M} \Delta \dot{\boldsymbol{u}} + \Delta \boldsymbol{u}^T (\boldsymbol{K} - \bar{\tilde{\boldsymbol{\Omega}}}_D^T \boldsymbol{M} \bar{\tilde{\boldsymbol{\Omega}}}_D) \Delta \boldsymbol{u} \Big\}. \tag{20}$$

The algorithm is formulated in terms of the absolute velocity $\boldsymbol{v}$. The local velocity $\dot{\boldsymbol{u}}$ is therefore eliminated in favor of the absolute velocity via the relation (8), whereby the dissipation potential takes the simple matrix form

$$D = \tfrac{1}{2}\alpha \left[\Delta \boldsymbol{u}^T, \Delta \boldsymbol{v}^T\right] \begin{bmatrix} \boldsymbol{K} & \bar{\tilde{\boldsymbol{\Omega}}}_D \boldsymbol{M} \\ \boldsymbol{M} \bar{\tilde{\boldsymbol{\Omega}}}_D^T & \boldsymbol{M} \end{bmatrix} \begin{bmatrix} \Delta \boldsymbol{u} \\ \Delta \boldsymbol{v} \end{bmatrix} \tag{21}$$

When introducing $-D$ on the right side of the total energy balance equation, it is seen that the matrix including the factor $\frac{1}{2}\alpha$ should be included in the first matrix of the conservative

equations of motion (18). Hereby the discretized hybrid state-space equations take the final form

$$\begin{bmatrix} \frac{1}{4}\Delta t\Delta \boldsymbol{K}^g + \frac{1}{2}\alpha\Delta t\boldsymbol{K} & (\boldsymbol{I} + \frac{1}{2}\alpha\Delta t\bar{\bar{\boldsymbol{\Omega}}}_D)\boldsymbol{M} \\ \boldsymbol{M}(-\boldsymbol{I} + \frac{1}{2}\alpha\Delta t\bar{\bar{\boldsymbol{\Omega}}}_D^T) & \frac{1}{2}\alpha\Delta t\boldsymbol{M} \end{bmatrix} \begin{bmatrix} \Delta \boldsymbol{u} \\ \Delta \boldsymbol{v} \end{bmatrix} + \Delta t \begin{bmatrix} \overline{\boldsymbol{g}(\boldsymbol{u})} + \bar{\bar{\boldsymbol{\Omega}}}_D \boldsymbol{M}\bar{\boldsymbol{v}} \\ \boldsymbol{M}\bar{\bar{\boldsymbol{\Omega}}}_D^T \bar{\boldsymbol{u}} + \boldsymbol{M}\bar{\boldsymbol{v}} \end{bmatrix} = \Delta t \begin{bmatrix} \boldsymbol{f}_* \\ -\boldsymbol{M}\bar{\bar{\boldsymbol{\Omega}}}_D^T \boldsymbol{x}_0 \end{bmatrix}. \tag{22}$$

It is noted that the the damping terms proportional to parameter α contribute in the form of symmetric terms in the first matrix. The combination of terms in the upper left corner of this matrix also indicates that the contribution $\frac{1}{4}\Delta\mathbf{K}^g$ has the form of a damping term. As the increment of the geometric stiffness may change sign, omission of this term by a simplified integration of the non-linear internal forces would lad to oscillations as illustrated in [4].

The non-dimensional damping parameter α appearing in the equations of motion can be related asymptotically to the modal damping ratio ζ_k in the low-frequency regime, [6],

$$\zeta_k \sim \tfrac{1}{2}\alpha\,(\omega_k\Delta t) \tag{23}$$

Thus, for the lower modes algorithmic damping in terms of the scalar damping parameter α leads to damping proportional to the modal frequency ω_k.

Numerical solution

The numerical solution of the hybrid state-space equations (22) proceeds in a simple step-by-step manner. First the equations are reformulated by using he second equation to express the current velocity $\boldsymbol{v}_n$ in terms of the current displacement $\boldsymbol{u}_n$. This expression is used to eliminate the current velocity $\boldsymbol{v}_n$ from the first equation, which then takes the form of a modified non-linear quasi-static static problem, for which standard solution procedures are available. When $\boldsymbol{u}_n$ has been determined, the current velocity $\boldsymbol{v}_n$ is determined from the relation used to eliminate this variable in the first step. Convergence is usually good due to the presence of the inertial terms that typically exercise a stabilizing effect for small time steps. Details and examples may be found in [4], [3] and [5].

References

[1] A.A. Shabana. *Dynamics of Multibody Systems*. Cambridge University Press, Cambridge, UK, 2005.

[2] M. Géradin and D. Rixen. *Mechanical Vibrations, Theory and Applications to Structural Dynamics*, 2nd ed. Wiley, Chichester, UK, 1997.

[3] S. Krenk and M.B. Nielsen. Hybrid state-space time integration in a rotating frame of reference. *International Journal for Numerical Methods in Engineering*, **87**:1301-1324, 2011.

[4] S. Krenk. *Non-linear Modeling and Analysis of Solids and Structures*. Cambridge University Press, Cambridge, UK, 2009.

[5] S. Krenk and M.B. Nielsen. Hybrid state-space time integration of rotating beams, 2011. (submitted for publication)

[6] S. Krenk. Extended state-space time integration with high-frequency energy dissipation. *Inernational Journal for Numerical Methods in Engineering*, **73**:1767–1787, 2008.

Proceedings of the 24th Nordic Seminar on Computational Mechanics
J. Freund and R. Kouhia (Eds.)

Adaptive reduction of finite element models in computational solid mechanics

Mats Larson, Håkan Jakobsson

Department of Mathematics and Mathematical Statistics
Umeå University, SE-901 87 Umeå, Sweden
mats.larson@math.umu.se, hakan.jakobsson@math.umu.se

Summary. In this plenary lecture some results on the adaptive construction of reduced finite element models are presented. In particular we focus on the Craig-Bampton component mode synthesis method and develop a posteriori error estimates and adaptive algorithms for a basic model problem, the elliptic eigenvalue problem and the frequency response problem.

Key words: model reduction, reduced order modeling, a posteriori error estimation, adaptivity, component mode synthesis, Craig-Bampton method

Introduction

The finite element method has a long tradition of use in solid mechanics and is commonly the method of choice for solving problems in elasticity. Sometimes however, finite element models may prove to be too computationally expensive to use in practical applications. In particular this may be the case when solving certain time dependent problems, large scale eigenvalue problems, or in frequency response analysis of complex structures. In such instances it may instead be preferable to construct a reduced finite element model with much fewer degrees of freedom off line, and use this less expensive model in the on line simulation. This process is commonly referred to as model reduction, reduced order modeling, or model order reduction.

In model reduction the objective is to find a low dimensional subspace of the finite element function space that still captures the solution to a sufficient degree of accuracy. To accomplish this, model reduction commonly relies on the incorporation of certain a priori knowledge in the model. For instance, if one is interested in the behavior of an elastic body in some specific frequency range, a low dimensional subspace that captures this behavior may be defined by using a basis of elastic eigenmodes vibrating in that same frequency range. Likewise, if it is known that forces act on a body in a certain region, basis functions designed to capture these forces may be included in the basis. As a result of the incorporation of knowledge in the model, its generality is decreased. This poses a limitation in instances where for example load patterns are very general, or changing over time, or if the dominating frequency range is very broad. In such instances it may be favorable to be able to evaluate a coarse model first, register where for example loads occur, and then update the reduced model to incorporate the a posteriori knowledge obtained, i.e. construct the reduced model adaptively. In this plenary lecture we discuss how this can be accomplished for reduced models in general, and in particular the Craig-Bampton component mode synthesis method (CB-CMS). We develop adaptive algorithms based on duality based a posteriori error estimates for CB-CMS applied to a basic model problem [3], the elliptic eigenvalue problem [4], and the frequency response problem [5]. See also [6].

The elliptic eigenvalue problem

Continuous model

Let Ω be a domain in space with boundary $\partial\Omega$ occupied by a homogeneous isotropic elastic material. Assume that the boundary consists of two disjoint parts Γ_N and Γ_D, where the body is traction free on Γ_N, and no displacements occur on Γ_D.

If the strains or deformations within Ω are small (infinitesimal), the resonance frequencies of the body are obtained by solving an eigenvalue problem for the unknown eigenpairs $(\lambda, \boldsymbol{u})$

$$-\rho\lambda\boldsymbol{u} - \nabla\cdot\boldsymbol{\sigma}(\boldsymbol{u}) = \boldsymbol{0}, \quad \boldsymbol{x}\in\Omega, \tag{1a}$$

$$\boldsymbol{u} = \boldsymbol{0}, \quad \boldsymbol{x}\in\Gamma_D, \tag{1b}$$

$$\boldsymbol{n}\cdot\boldsymbol{\sigma}(\boldsymbol{u}) = \boldsymbol{0}, \quad \boldsymbol{x}\in\Gamma_N, \tag{1c}$$

where $\boldsymbol{u} = \boldsymbol{u}(\boldsymbol{x}, t)$ are the vector displacements, $\boldsymbol{\sigma}(\cdot)$ is the stress tensor, and $\rho = \rho(\boldsymbol{x})$ denotes density. Further, stress is described in terms of the Cauchy strain tensor $\boldsymbol{\varepsilon}(\boldsymbol{u}) = 1/2(\nabla\boldsymbol{u}+\nabla\boldsymbol{u}^T)$ through Hooke's law, which may be written $\boldsymbol{\sigma}(\boldsymbol{u}) = 2\mu\boldsymbol{\varepsilon}(\boldsymbol{u}) + \kappa(\nabla\cdot\boldsymbol{u})\boldsymbol{I}$, for isotropic materials. Here μ and κ are the Lamé material parameters, and $\boldsymbol{I}$ is the identity tensor.

Finite element model

Let the domain Ω be partitioned into simplices, and let V^h be the space of continuous piecewise polynomials on the mesh. The finite element method for the eigenvalue problem reads: find $(\lambda^h, \boldsymbol{U}) \in \mathbb{R}\times V^h$, such that

$$a(\boldsymbol{U}, \boldsymbol{v}) = \lambda^h(\boldsymbol{U}, \boldsymbol{v}), \quad \forall\boldsymbol{v}\in V^h, \tag{2}$$

where $a(\cdot,\cdot)$ is the bounded, coercive, bilinear form

$$a(\boldsymbol{w}, \boldsymbol{y}) = (\boldsymbol{\sigma}(\boldsymbol{w}), \boldsymbol{\epsilon}(\boldsymbol{y})), \quad \forall\boldsymbol{w}, \boldsymbol{y}\in V^h. \tag{3}$$

Reduced model

Let $V^{h,m}\subset V^h$ be a low dimensional subspace. We then seek $(\lambda^m, \boldsymbol{U}^m)\in\mathbb{R}\times V^{h,m}$, such that

$$a(\boldsymbol{U}^m, \boldsymbol{v}) = \lambda^m(\boldsymbol{U}^m, \boldsymbol{v}), \quad \forall\boldsymbol{v}\in V^{h,m}. \tag{4}$$

The challenge is to construct the subspace $V^{h,m}\subset V^h$ in such a way that it is low dimensional while still maintaining good approximation properties for the problem at hand. There are of course many ways to construct the reduced space. Below we briefly describe the Craig-Bampton method.

Craig-Bampton component mode synthesis

Below follows a brief description of the Craig-Bampton component mode synthesis method [2] in a variational setting [1].

Consider a domain Ω for simplicity partitioned into two subdomains Ω_1 and Ω_2 interfacing at Γ. A decomposition of V^h associated with the partition may be constructed by defining subspaces $V_i^h\subset V^h$ associated with Ω_i, by $V_i^h = \{\boldsymbol{v}\in V^h : \boldsymbol{v}|_{\Omega\setminus\Omega_i} = 0\}$, $i = 1, 2$, and a subspace V_0^h associated with Γ, by $V_0^h = \{\mathcal{E}\boldsymbol{\nu}\in V^h : \boldsymbol{\nu}\in V^h|_\Gamma\}$, where $V^h|_\Gamma$ denotes the restriction of V^h to Γ and $\mathcal{E}\boldsymbol{\nu}\in V^h$ denotes the harmonic extension of a function $\boldsymbol{\nu}\in V^h|_\Gamma$ to Ω. That is, $\mathcal{E}\boldsymbol{\nu}$ is defined by the problem: find $\mathcal{E}\boldsymbol{\nu}\in V^h$, such that

$$a(\mathcal{E}\boldsymbol{\nu}, \boldsymbol{v}) = 0, \quad \forall\boldsymbol{v}\in V_i^h, \quad i = 1, 2, \tag{5}$$

$$\mathcal{E}\boldsymbol{\nu}|_\Gamma = \boldsymbol{\nu}. \tag{6}$$

With the V_i^h, $i = 0, 1, 2$, defined as above, it follows that an a-orthogonal decomposition of V^h is given by

$$V^h = \bigoplus_{i=0}^{2} V_i^h. \tag{7}$$

For each subspace V_i^h, $i = 0, 1, 2$, an eigenvalue problem is defined: find $(\lambda_i, \boldsymbol{z}_i) \in \mathbb{R} \times V_i^h$, such that

$$a(\boldsymbol{z}_i, \boldsymbol{v}) = \lambda_i(\boldsymbol{z}_i, \boldsymbol{v}), \quad \forall \boldsymbol{v} \in V_i^h, \tag{8}$$

A basis for each V_i^h, is then given by $V_i^h = \text{span}\{\boldsymbol{z}_i\}_{i=1}^{n_i}$, where n_i is the dimension of V_i^h. By truncating the bases, reduced subspaces V_i^{h,m_i}, $i = 0, 1, 2$, are obtained. That is, let V_i^{h,m_i} be defined by $V_i^{h,m_i} = \text{span}\{\boldsymbol{z}_i\}_{i=1}^{m_i}$, where $m_i < n_i$. A reduced space $V^{h,\boldsymbol{m}}$, where $\boldsymbol{m} = (m_i)_{i=0}^2$ is then defined by

$$V^{h,\boldsymbol{m}} = \bigoplus_{i=0}^{2} V_i^{h,m_i}. \tag{9}$$

A posteriori error estimation and adaptivity

Error estimates

Let $\boldsymbol{R}_i^h(\boldsymbol{W}, \gamma) \in V_i^h$ denote the discrete subspace residual defined for $(\gamma, \boldsymbol{W}) \in \mathbb{R} \times V^h$ by

$$(\boldsymbol{R}_i^h(\gamma, \boldsymbol{W}), \boldsymbol{v}) = a(\boldsymbol{W}, \boldsymbol{v}) - \gamma(\boldsymbol{W}, \boldsymbol{v}), \quad \forall \boldsymbol{v} \in V_i^h. \tag{10}$$

Then the estimate

$$\lambda^{\boldsymbol{m}} - \lambda^h = \leq c\lambda^h \sqrt{2I_2}, \tag{11}$$

holds for the reduction error in the eigenvalue $\lambda^{\boldsymbol{m}}$, and

$$|\!|\!| \boldsymbol{E} |\!|\!| \leq c\Big(\sqrt{I_1} + S(\lambda^h)\sqrt{2I_2}\Big), \tag{12}$$

holds for the reduction error in an eigenmode $\boldsymbol{U}^{\boldsymbol{m}}$, where $I_1 = I_1(\lambda^{\boldsymbol{m}}, \boldsymbol{U}^{\boldsymbol{m}})$ and $I_2 = I_2(\lambda^{\boldsymbol{m}}, \boldsymbol{U}^{\boldsymbol{m}})$ respectively, are defined by

$$I_1(\lambda^{\boldsymbol{m}}, \boldsymbol{U}^{\boldsymbol{m}}) = \sum_{i=0}^{n} \frac{1}{\Lambda_{i,m_i+1}} \|\boldsymbol{R}_i^h(\lambda^{\boldsymbol{m}}, \boldsymbol{U}^{\boldsymbol{m}})\|^2, \tag{13}$$

$$I_2(\lambda^{\boldsymbol{m}}, \boldsymbol{U}^{\boldsymbol{m}}) = \sum_{i=0}^{n} \frac{1}{\Lambda_{i,m_i+1}^2} \|\boldsymbol{R}_i^h(\lambda^{\boldsymbol{m}}, \boldsymbol{U}^{\boldsymbol{m}})\|^2, \tag{14}$$

and $S(\lambda^h)$ is a stability factor defined by

$$S(\lambda^h) = \max_{\lambda_j^h \neq \lambda^h} \frac{\lambda^h \sqrt{\lambda_j^h}}{|\lambda^h - \lambda_j^h|}. \tag{15}$$

Adaptive algorithm

An adaptive algorithm based on the above estimate with the objective of accurately computing an eigenvalue or eigenmode may take the form:

1. Start with a guess of the subspace dimensions $\boldsymbol{m}$.
2. Solve the problem (4) for the displacements $\boldsymbol{U}^{\boldsymbol{m}}$.
3. Compute the error indicators $\eta_i = \|\boldsymbol{R}_i^h(\lambda^{\boldsymbol{m}}, \boldsymbol{U}^{\boldsymbol{m}})\|^2/\Lambda_{i,m_i+1}$ and use them together with a refinement rule to decide suitable levels of refinement in each subspace.
4. Repeat steps 2–4 until satisfactory results have been obtained.

Numerical results

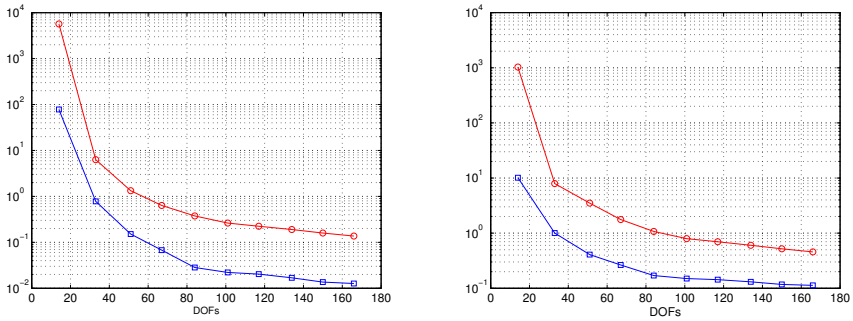

(a) Eigenvalue error (b) Eigenmode error

Figure 1. Semilog plots of the eigenvalue error $E = \lambda_{10}^{\boldsymbol{m}} - \lambda_{10}^h$ and the energy norm of eigenmode error $\boldsymbol{E} = (I - \mathcal{P}_{\lambda^h})\boldsymbol{U}_{10}^{\boldsymbol{m}}$ together with the corresponding estimates vs. the number of DoF, as the adaptive algorithm proceeds. Legend: error, square; estimate, circle.

References

[1] F. Bourquin, *Component mode synthesis and eigenvalues of second order operators: Discretization and algorithm*, Math. Model. Numer. Anal. (1992), no. 26, 385–423.

[2] R. R. Craig and M. C. C. Bampton, *Coupling of substructures for dynamic analysis*, AIAA J (1968), no. 6, 1313–1321.

[3] H. Jakobsson, F. Bengzon, and M. G. Larson, *Adaptive Component Mode Synthesis in Linear Elasticity*, Int. J. Numer. Meth. Engng **86** (2011), 829–844.

[4] H. Jakobsson and M. G. Larson, *A posteriori error analysis of component mode synthesis for the elliptic eigenvalue problem*, Computer Methods in Applied Mechanics and Engineering **200** (2011), no. 41 –44, 2840 – 2847.

[5] ———, *A Posteriori Error Analysis of Component Mode Synthesis for the Frequency Response Problem*, submitted, 2011.

[6] Håkan Jakobsson, *Adaptive reduction of finite element models in computational solid mechanics*, Ph.D. thesis, Umeå University, Department of Mathematics and Mathematical Statistics, 2011.

Proceedings of the 24th Nordic Seminar on Computational Mechanics
J. Freund and R. Kouhia (Eds.)

Standard gradient models and gradient plasticity

Quoc-Son Nguyen

Laboratoire de Mecanique des Solides Ecole Polytechnique, 91128 Palaiseau, France

Summary. The standard gradient models have been intensively studied in the literature, cf. Fremond (1985) or Gurtin (1991) for various applications in plasticity, damage mechanics and multi-phase analysis. The governing equations for a solid have been introduced essentially from an extended version of the virtual equation. It is shown here that these equations can also be derived from the formalism of energy and dissipation potentials and appear as a generalized Biot equation for the solid. For a time-independent process such as incremental plasticity or brittle damage, our attention is focussed on the derivation of the governing equations of the global response and of the rate response, on the associated variational principles and on some general results such as the question of uniqueness for a solid submitted to a quasi-static loading. A consistent mathematical description of the theory of Gradient Plasticity is given.

Key words: gradient plasticity, extended virtual equation, dissipation potential

Introduction

The introduction of the gradients of the state variables such as the strain, the internal parameter and even the temperature in Solid Mechanics has been much discussed in the literature since the pioneering works of Mindlin and Toupin in second-gradient elasticity. Especially, in the two last decades, standard gradient theories has been considered in many papers, cf. for example [12], [14] , [26], [17], [30], [9], for the modeling of phase change and of solids with microstructures. In particular, in Fr´emond or Gurtin's approach, the governing equations have been originally derived from an additional virtual work equation. These models have been applied in various applications such as gradient plasticity and gradient damage.

The objective of this paper is to revisit the proposed approach. Using the formalism of the generalized standard materials [28], a dissipation analysis is considered in order to derive the general expression of the governing equations for the internal parameters in terms of the energy and dissipation potentials. Gradient and higher-gradient models can be discussed in the same spirit. In particular, the governing equations for the standard gradient models can be written as a generalized Biot equation for the solid. For a time-independent behaviour such as incremental plasticity or brittle fracture or brittle damage, our attention is focussed on the derivation of some theoretical results, which are well known in classical plasticity, such as the governing equations of the global response and the determination of the rate response and the associated variational principles. A consistent mathematical description of the theory of Gradient Plasticity is proposed

References

[1]. E.C. Aifantis. On the microstructural origin of certain inelastic models. *J. Eng. Mat. Tech*., 106:326–330, 1984.

[2] M.A. Biot. *Mechanics of incremental deformation*. Wiley, New York, 1965.

[3] B. Bourdin, Francfort G.A., and Marigo J.J. Numerical experiments in revisited brittle fracture. *J. Mech. Phys. Solids*, 48:797–826, 2000.

[4] R. de Borst and H.B. Muhlhaus. Gradient-dependent plasticity: formulation and algorithmic aspects. *Int. J. Num. Meth. Engrg*, 35:521–539, 1992.

[5] G. Duvaut and J.L. Lions. *Les inéquations en mécanique et en physique*. Dunod,Paris, 1972.

[6] N.A. Fleck and J.W. Hutchinson. Strain gradient plasticity. *Adv. Appl. Mech*., 33:295–361, 1997.

[7] N.A. Fleck and J.W. Hutchinson. A reformulation of strain gradient plasticity. *J. Mech- Phys. Solids*, 49:2245–2271, 2001.

[8] N.A. Fleck and J.R. Willis. A mathematical basis for strain-gradient plasticity theory, part ii. *J. Mech- Phys. Solids*, 57:1045–1057, 2009.

[9] S. Forest, J.M. Cardona, and R. Sievert. Thermoelasticity of second-grade media. In Maugin, Drouot, and Sidoroff, editors, *Continuum Thermodynamics*. Kluwer, Dordrecht, 2000.

[10] G. Francfort and J.J. Marigo. Revisiting brittle fracture as an energy minimization problem. *J. Mech. Phys. Solids*, 46:1319–1342, 1998.

[11] G. Francfort and A. Mielke. Existence results for a class of rate-independent material models with nonconvex elastic energies. *J. R. A. Math. Mech*., 595:55–91, 2006.

[12] M. Frémond. Contact unilatéral avec adhérence. une théorie du premier gradient. In G. Del Piero and F. Maceri, editors, *Unilateral problems in structural analysis*, pages 117–137. CISM Course 304, Springer-Verlag, Wien, 1985.

[13] M. Frémond. Shape memory alloy: a thermo-mechanical macroscopic theory.In *Shape memory alloys*, pages 3–68. CISM Course 351, Springer-Verlag, Wien, 1996.

[14] M. Frémond and B. Nedjar. Damage, gradient of damage and principle of virtual power. *Int. J. Solids and Structures*, 33:1083–1103, 1996.

[15] P. Germain. *Cours de mécanique des milieux continus*. Masson, Paris, 1973.

[16] A. Giacomini and A. Musesti. Two-scale homogenization for a model in strain gradient plasticity. *ESAIM: Control, Optimisation and Calculus of Variations*, doi:10.1051/cocv/2010036, 2011.

[17] M. E. Gurtin. Generalized Ginzburg-Landau and Cahn-Hilliard equations based on a microforce balance. *Physica D*, 92:178–192, 1996.

[18] M. E. Gurtin and L. Anand. A theory of strain-gradient plasticity for isotropic, plastically irrotational materials. *J. Mech- Phys. Solids*, 53:1624–1649, 2005.

[19] B. Halphen and Q.S. Nguyen. Sur les matériaux standard généralisés. *J. Mecanique,* 14:1–37, 1975.

[20] H. Henry and H. Levine. Dynamic instabilities of fracture under biaxial strain using a phase-field model. *Phys. Rev. Let*., 93:105504, 2004.

[21] R. Hill. A general theory of uniqueness and stability in elastic/plastic solids. *J.Mech. Phys. Solids*, 6:236–249, 1958.
[22] E. Lorentz and S. Andrieux. A variational formulation for nonlocal damage models. *Int. J. Plasticity*, 15:119–138, 2003.
[23] E. Lorentz and A. Benallal. Gradient constitutives relations: numerical aspect and application to gradient damage. *Comp. Meth. Appl. Mech. Engng.*, 194:5191–5220, 2005.
[24] A. Mainik and A. Mielke. Global existence for rate-independent gradient plasticity at finite strain, 2009.
[25] J. Mandel. *Cours de mécanique des milieux continus*. Gauthier-Villars, Paris, 1966.
[26] G.A. Maugin and W. Muschik. Thermodynamics with internal variables, part 1: General concepts. *J. Non-equilibrium Thermodynamics*, 19:217–249, 1994.
[27] J.J. Moreau. Sur les lois de frottement, de plasticité et de viscosité. *C. R. Acad. Sciences*, 271:608–611, 1970.
[28] Q. S. Nguyen and S. Andrieux. The non-local generalized standard approach: a consistent gradient theory. *C. R. Mecanique*, 333:139–145, 2005.
[29] Q.S. Nguyen. *Stability and Nonlinear Solid Mechanics*. Wiley, Chichester, 2000.
[30] C. Polizzotto. Unified thermodynamic framework of nonlocal/gradient continuum theories. *Eur. J. Mech. A/Solids*, 22:651–668, 2003.
[31] T. Svedberg and K. Runesson. A thermodynamically consistent theory of gradientregularized plasticity coupled to damage. *Int. J. of Plasticity*, 13:669–696, 1997.

Proceedings of the 24th Nordic Seminar on Computational Mechanics
J. Freund and R. Kouhia (Eds.)

Variationally consistent computational homogenization – Selected issues and applications

K. Runesson and F. Larsson

Dept. of Applied Mechanics, SE-41296 Göteborg, Sweden, keru@chalmers.se

Summary. This contribution describes some recent developments in computational homogenization and the resulting FE^2-strategy, both from a conceptual viewpoint and with respect to selected applications.

Key words: homogenization, variationally consistent, discretization-based, model-based, scale-bridging

Introduction

One of the fastest growing research fields in the international solid mechanics community is multiscale material modeling, ranging from the quantum to the continuum level, [2]. From an engineering viewpoint, the challenge is to model the physics on the "appropriate" (sub)scale while extracting the output on the macroscale with sufficient accuracy. Hereby, a classical concept is (analytical or mathematical) homogenization. For linear and static response this operation can be done once and for all, socalled upscaling; however, for nonlinear and non-standard problems the homogenization is not (entirely) trivial.

Concept of variationally consistent homogenization

In this contribution we review some recent developments, primarily within our research group, related to scale transition involving computational homogenization on a Representative Volume Element (RVE). A key concept is "variationally consistent homogenization" (VCH), which is closely related to the well-established paradigm of Variational Multiscale Modeling, [1]. The VCH-concepts leads naturally to "discretization-based" homogenization, whereby the order of homogenization is determined by the polynomial order of the macro-scale element approximation (and is not determined a priori as a model assumption), [3], [4]. However, the link to the classical "model-based" homogenization (of any given order) is also discussed. We illustrate the developments in tutorial fashion for a simple model problem, before giving the more abstract general setting that holds for a large class of problems in space/time. In any case, when only a single subscale is involved, the resulting computational strategy is known as FE^2. Examples of (still) outstanding issues are: choice of efficient prolongation (boundary) conditions on the RVE, bounds on the effective properties from "virtual testing" statistics, "equation switching" from subscale to the macroscale, etc. Applications to materials within our research group range from graphene (atomistic subscale) to porous granular media (particle/matrix composite with pore fluid seepage).

Within the paradigm of VCH we also discuss a strategy for bridging the two extremes of complete scale separation (based on RVE-computations) and single-scale resolution. Such bridging is accomplished adaptively in a virtually "seamless" fashion, and it is based on the aim to control discretization as well as model errors.

Application problems

We present computational results from some "standard" and "non-standard" homogenization problems. As a standard problem, we consider deformation of a polycrystalline metal (such as Duplex Stainless Steel). As examples of non-standard problems we consider the liquid-phase sintering of a P/M-component, seepage in a porous medium (which represents equation switching from the meso- to the macroscale) and atomistic modeling of graphene. In the latter case the Quasi-Continuum method is employed, whereby model adaptivity is a key feature. Finally, we consider the problem of a sharp crack in a particle composite within the realm of a scale-bridging strategy.

References

[1] T. J. R. Hughes, G.R. Feijóo. L. Mazzei and J-B. Quincey: The varaiational multiscale method - a paradigm for computational mechanics. *Comput. Methods in Applied Mechanics and Engineering*, 166:3-24, 1998.

[2] M. G. D. Geers, V. G. Kouznetsova, and W. A. M. Brekelmans: Multi-scale computational homogenization: Trends and challenges. *J. Computational and Applied Mathematics*, 234:2175-2182, 2010.

[3] F. Larsson and K. Runesson: Adaptive bridging of scales in continuum modeling based on error control. *Int. J. Multiscale Computational Engineering*, 6:371-392, 2008.

[4] F. Larsson and K. Runesson: On two-scale adaptive FE-analysis of micro-heterogeneous media with seamless scale-bridging. *Comput. Methods in Applied Mechanics and Engineering*, 2010 in press.

Proceedings of the 24th Nordic Seminar on Computational Mechanics
J. Freund and R. Kouhia (Eds.)

Rail- and roadway dynamics – uncoupled and coupled analysis

Nils-Erik Wiberg

Department of Applied Mechanics, Chalmers University of Technology, Gothenburg, Sweden,
e-mail: nils-erik.wiberg@chalmers.se

Summary. To understand the physical phenomena and to be able to propose countermeasures/ improvements, simulation tools to perform computations of the entire dynamical system including subground, track structure and the train have been developed. In particular, effort has been devoted to the wave propagation problem related to high-speed trains running at soft ground materials. As the speed of the train approaches and exceeds the natural (Rayleigh) wave propagation velocity of the ground material, shock waves similar to a sonic boom originate from the onrushing train. The computational models and the solution algorithms developed are equally applicable to roadway vehicle-structure-underground systems.

Key words: railway, roadway, dynamics, coupled, fem, porous media

Dynamics for the railway system

The primary objective of the project has been to extend the capabilities for computational modeling, prediction and simulation of the elastic response of the train, track structure and soil in the railway system. The problem area contains several computational challenges and requires efficient techniques to handle time integration of large-scale problems, infinite domains, non-linear material responses etc. [1]. In many applications the soil is water saturated and the combined action of elastic deformation and flow has to be accounted for. Thus uncoupled as well as coupled analysis have been performed. Four main features have been studied:

1. The integration of three-dimensional rigid body dynamics with finite elements for analysis of vehicle – track – subground interaction problems.
2. In order to reduce unphysical reflections from FE-boundaries in the solution two approaches have been developed. A scaled boundary finite element method and a Method with an iteracting fictitious layer of visco-elastic elements simulating the unbounded surrounding domain.
3. Adaptive analysis of moving trains over long distances (up to 400m) by moving FE-mesh calculations.

4. Coupled solid-fluid analysis of wave propagation in water saturated soils under high-speed trains.

The outcome is an advanced application for vehicle – track – subground interaction problems in 3D over long distances [2]. The car, bogies and wheels are treated as rigid bodies connected by springs and dampers by use of constraint equations. The wheels of the vehicle are connected to the rail by moving constraint equations. The constraint equations give an indefinite system of equations.

Solver based on multi-grid, error estimation and adaptive refinement

Efficient solvers based on a combination of multi-grid, error estimation and adaptive refinement for linear as well as nonlinear cases have been developed to reduce execution times and memory requirements. The solution time, using multi-grid PCG-preconditioning, is substantially reduced compared to conventional implicit solvers based on factorization. Moreover, the indefinite system of the Lagrange multiplier approach to handle constraint equations requires additional preconditioning to guarantee convergence and reduce the number of iterations [3].

It is possible to alter geometry, ground material characteristics, use semi-active suspension features as well as study various types of imperfections in the track structure over the course of a moving vehicle simulation. Numerical simulations where the train is represented as a collection of moving loads as well as a multi-body system with complete train-track interaction are demonstrated.

Coupled solid-fluid dynamic analysis of road and railway structures

The computational models and the solution algorithms developed are equally applicable to roadway vehicle-structure-underground systems. The paper also includes studies combining elastic deformations and water flow in the ground [4]. A FE-formulation for the dynamic behavior of water saturated porous media is presented. The transient response of a 2D-model of a railway to moving traffic loading as well as a wet asphalt pavement loaded by wheel impact pressure are studied. Figure 1 shows some results below.

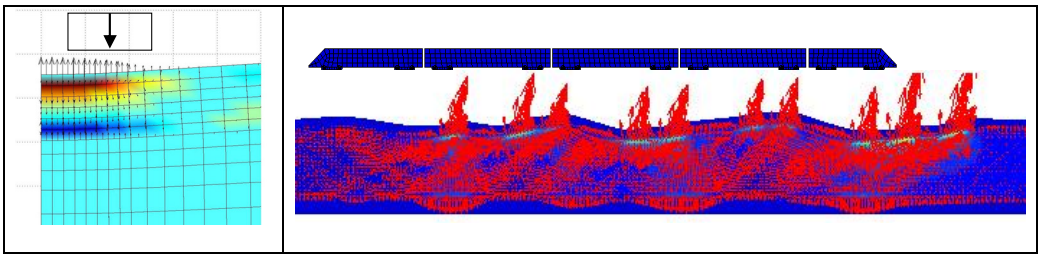

Figure 1. Simulations of coupled dynamic deformation and water flow (magnified deformations, color-scale water-pressure, arrows water-flow): Left: Wet asphalt pavement loaded by wheel impact pressure. Right: Train running on water-saturated soil.

It is also demonstrated that the simulations of soft asphalt in the summer season differ a lot whether dynamical effects are considered or not, while stiff asphalt during winter is hardly not affected at all. In the traffic load example, large magnification of displacements occurs for certain vehicle speeds both for porous and solid media theories.

Acknowledgements

The content of the paper is based on research done in cooperation with my former PhD-students Torbjörn Ekevid, Per Kettil, Håkan Lane and Bernd Lenhof. They are greatly acknowledged.

References

[1] T. Ekevid and N.-E. Wiberg, Wave propagation related to high-speed trains - a scaled boundary FE-approach for unbounded domains, *Computer Methods in Applied Mechanics and Engineering*, 191(36):3947-3964, 2002.
[2] H. Lane, P. Kettil and N.-E. Wiberg, Moving finite elements and dynamic vehicle interaction, *European Journal of Mechanics – A/Solids*, 27(4):515-531, 2008.
[3] P. Kettil, T. Ekevid and N.-E. Wiberg, Towards fully mesh adaptive FE-simulations in 3D using multigrid solver, *Computers & Structures*, 81(8-11):735-746, 2003.
[4] P. Kettil, B. Lenhof, K. Runesson and N.-E. Wiberg, Coupled simulation of wave propagation and water flow in soil induced by high speed trains, *Int. J. for Numerical and Analytical Methods in Geomechanics*, 32 (11):1311-1319, 2008.

Proceedings of the 24th Nordic Seminar on Computational Mechanics
J. Freund and R. Kouhia (Eds.)

Atomistic simulation of metal–polymer adhesion

J. Y. Wu, S. Nagao, J. Y. He, and Z. L. Zhang

NTNU Nanomechanical Lab, Norwegian University of Science and Technology (NTNU), N7491 Trondheim, Norway, email: Zhiliang.zhang@ntnu.no

Summary. Metal coated micron-sized polymer particles find wide applications in anisotropic conductive adhesives. Adhesion between the metal coating and polymer core is crucial for the mechanical integrity and electrical performance of the adhesives. In this study molecular dynamics simulation has been conducted to investigate the tensile and shear strength of a metal−polymer interface.

Key words: metal-polymer interface, adhesion, molecular dynamics simulations.

Introduction

The micron-size monodisperse polymer particles have received great industrial and scientific attentions over the past two decades due to a wide variety of applications such as toners, instrument calibration standards, column packing materials for chromatography, biomedical and biochemical analyses[1-3]. A new area which utilizes metal-coated conductive polymer particles for anisotropic conductive adhesives applications in liquid crystal display and microsystems[4] has recently emerged. The metalized polymer particles have the potential to shrink the package size, reduce manufacturing cost, and be lead-free. However, a critical issue of the metal-coated polymer particles concerns the adhesion between metal and polymer, which strongly affects the resulting mechanical and thermal properties. The adhesion strength, in turn, depends mostly on the interface chemistry and interface atomic-scale morphology. The strength and reliability of metal-polymer joints are mainly the result of the play of forces of intermolecular interaction between metal and polymer. The interaction between these condensed bodies at distances on the nano-size refers to a very complicated set of inter-connected phenomena that is far from being understood. Therefore, the present work uses atomistic simulation to study the tensile and shear strength of a Nickel−s-PMMA interface at the molecular level.

Methods and Models

Usually, the PMMA monomers are connected to form different stereo-regular tacticity. In this study, only s-PMMA type chains are built by monomers connected stepwise with

proper energy. Ten polymer chains (the number of C/H/O atoms per chain is 1000/1602/400) are randomly placed into an amorphous cuboid cell with cell parameter: a=b=57.656Å, c=100Å, based on self-avoiding walking method. In order to create surface joint with metal, only two periodic boundary conditions (along the x and y directions) are imposed in the amorphous cell system. Six nickel atom layers with $(\bar{1}\bar{1}\bar{1})$ surface contacted amorphous polymer are placed in both ends in the direction z. To model the s-PMMA−Nickel interface, the consistent valence force field (CVFF)[5] is employed in all our simulations using the open source MD code LAMMPS[6].The system is initially energy-minimized using the conjugate gradients method and then relaxed by a set of MD simulations: NVT for 100 ps at 300 K→ NPT for 100 ps at 300K → NVT for 200 ps from 300 K to 1000K, nickel atoms are fixed in z direction→ NVT for 200 ps from 1000K to 300K→ NPT for 5ns at 300K. The interface model of s-PMMA−Nickel at equilibrium state is shown in Fig.1, in which only backbone atoms and metal atoms are shown for the sake of clarity. After the equilibrium, a tensile test is conducted by given a constant velocity of nickel plates (1m/s and -1m/s) in the z direction. Similarly, a constant velocity of nickel plates (1m/s and -1m/s) is given in x direction for the shear test.

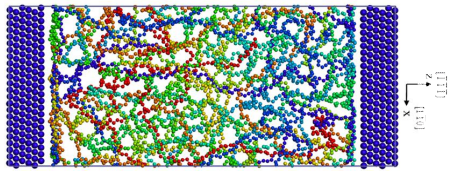

Fig. 1 The interface atomic model of s-PMMA−Nickel at equilibrium state, only backbone atoms and metal atoms are shown for clarity. Different chains are colored to chain number.

Results and Discussion

Equilibrium properties of s-PMMA−Nickel interface

The polymer chain structures at the two interfacial regions have been analyzed by dividing space across the film into parts separated by planes parallel to the solid surface, of width equal to around 1 Å. Fig. 2 displays the average mass density and average force distributions across the $(\bar{1}\bar{1}\bar{1})$ surface for the interface system. Near the nickel surface, the density profile exhibits a peak from the highly attractive metal surface, and the global mass density of polymer between two metal plates is around 1.1g/cm^3. The densified polymer on the metal surface can be attributed to the highly attractive force as presenting double two peaks of force near both end surfaces in Fig. 2. The highest peaks around 10 Å and 95 Å demonstrate high repulsive force owing to too small average distance between surface polymer and metal atoms. The two opposite lower peaks around 12 Å and 93 Å represent high attractive force between polymer and metal for these two parts. Fig. 3 shows local mass density gradient for interface system at the equilibrium state. It is observed that high density gradient locates at the metal surface as expected. In the middle region the density gradient is relative small that explains an equilibrium state of system has reached.

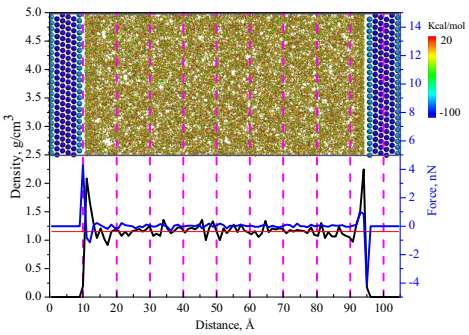

Fig. 2 Density and force profile of polymer at equilibrium state

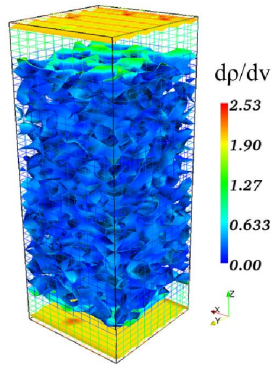

Fig. 3 Local density gradient at equilibrium state

Tensile strength of s-PMMA−Nickel interface

Starting from the equilibrated s-PMMA−Nickel system, MD simulations were performed to simulate the tensile strength of interface. Fig. 4a displays the pulling force on nickel plate as a function of strain. It is observed that the pulling force increases linearly as strain increase to 5% strain for both metal plates, which means the elastic stretch occurs in polymer. Then softening and hardening occurs similar to the bulk polymer. Fig 4b displays one snapshot of interface failure at 30% strain. Near the surface, cavities can be seen in the ellipses shown in the figure that represent the interface failure.

Shear strength of s-PMMA−Nickel interface

Fig. 5 shows the pulling force on nickel plate as a function of displacement of plate together with one snapshot of the interface in the shear test at 50 Å displacements of nickel plate. Similar to the tensile test, the pulling force increases linearly as displacement of plate increase to 5 Å for both metal plate. A small pop-in occurs and then the pulling force continues to increase with a reduced rate until a sudden drop, which indicates the failure of s-PMMA−Nickel interface.

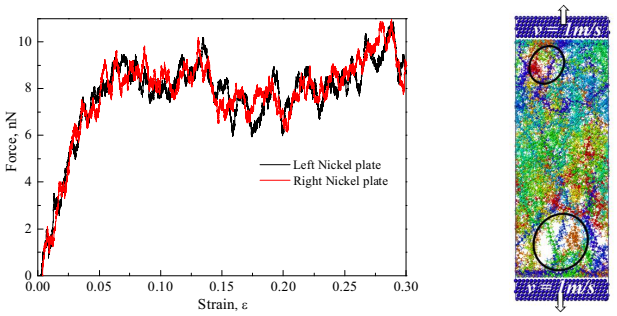

Fig.4 a. the pulling force on nickel plate as a function of strain. b. Snapshot of interface failure

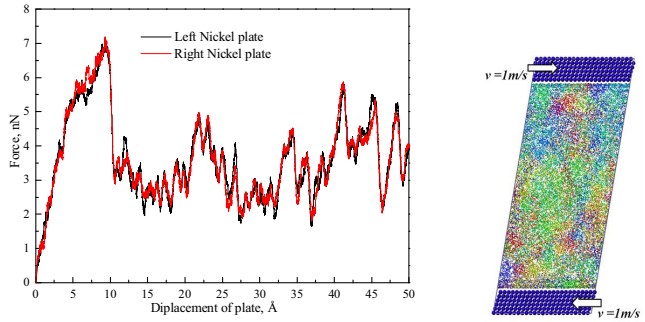

Fig.5 a. the pulling force on nickel plate as a function of displacement of plate. b. Snapshots of shear test of interface at 50 Å displacements of nickel plate

Summary

Atomistic simulations have been performed to investigate the tensile and shear strength of a metal–polymer interface. A densified polymer layer on metal surface has been observed due to high interaction between metal and polymer. Cavities can be observed near the interface at large strains during tensile test. Interface failure easily occurs at only 5 Å displacements of nickel plates during shear test.

Reference

[1] Lok, K. P.; Ober, C. K., Particle size control in dispersion polymerization of polystyrene, Canadian Journal of Chemistry. 63(1): 209–216 (1985).
[2] M. Okuo, Polymer Particles (Advances in Polymer Science) (Hardcover), Springer, 1 edition (May 23, 2005).
[3] Sugimoto, T., Monodispersed Particles (Studies in Surface Science and Catalysis) (Hardcover), Elsevier Science, 1 edition (February 8, 2001)
[4] http://www.conpart.no/
[5] Dauber-Osguthorpe, P.; Roberts, V. A.; Osguthorpe, D. J.; Wolff, J.; Genest, M.; Hagler, A. T., Structure and energetics of ligand binding to proteins: *E. coli* dihydrofolate reductase-trimethoprim, a drug-receptor system, Proteins: Structure, Function and Genetics, 4, 31-47 (1988).
[6] Plimpton, S. J., Fast Parallel Algorithms for Short-Range Molecular Dynamics, Journal of Computational Physics, 117(1):1-19(1995); http://lammps.sandia.gov

Rakenteiden Mekaniikka (Journal of Structural Mechanics)
Vol. 44, No 3, 2011, pp. 260-278

Isogeometric analysis of finite deformation nearly incompressible solids

Kjell Magne Mathisen, Knut Morten Okstad, Trond Kvamsdal and Siv Bente Raknes

Summary. This paper addresses the use of isogeometric analysis to solve finite deformation solid mechanics problems, in which volumetric locking may be encountered. The current work is based on the foundation developed in the project *ICADA* for linear analysis, that herein is augmented with additional capabilities such that nonlinear analysis of finite deformation problems in solid mechanics involving material and geometrical nonlinearities may be performed. In particular, we investigate two mixed forms based on a three-field Hu-Washizu variational formulation, in which displacements, mean stress and volume change are independently approximated. The performance of the mixed forms is assessed by studying two numerical examples involving large-deformation nearly incompressible elasticity and elastoplasticity. The results obtained with NURBS are shown to compare favorable with classical Lagrange finite elements.

Key words: isogeometric analysis, near incompressibility, volumetric locking, mixed formulation, finite deformation, hyperelasticity, plasticity

Kjell Magne Mathisen, Siv Bente Raknes
Department of Structural Engineering
Norwegian University of Science and Technology, NO-7491 Trondheim, Norway
kjell.mathisen@ntnu.no, siv.bente.raknes@ntnu.no

Knut Morten Okstad, Trond Kvamsdal
Department of Applied Mathematics
SINTEF ICT, NO-7465 Trondheim, Norway
knut.morten.okstad@sintef.no, trond.kvamsdal@sintef.no

Proceedings of the 24th Nordic Seminar on Computational Mechanics
J. Freund and R. Kouhia (Eds.)

Analysis-suitable modeling for isogeometric shell analysis

Susanne Støle-Hentschel[1]and Geir Skeie[2]

(1)DNV, Veritasveien 1, N-1367 Høvik, Susanne.Stole.Hentschel@dnv.om
(2)DNV, Veritasveien 1, N-1367 Høvik, Geir.Skeie@dnv.om

Summary. The paper presents strategies for producing *Computer Aided Design* (CAD) models that are suitable for *Isogeometric Analysis* (IGA) . By extending traditional CAD tools slightly, complex analysis-suitable shell models can be produced. It is shown how trimmed objects can be converted to untrimmed objects. By comparing analysis results of various modeling techniques including T-splines, the influence of the modeling concept is analyzed.

Key words: isogeometric analysis, analysis-suitable modeling, shells, T-splines, bottom-up modeling

Introduction

In 2005 Hughes and collaborators [3], introduced the concept of IGA to improve the transition between CAD models and Finite Element Analysis. In order to make use of IGA in the industry, it is necessary to establish guidelines for producing *Analysis Suitable Models*. The paper highlights the influence of the chosen modeling strategy on the analysis. We present bottom-top modeling enhanced by building blocks and show how trimmed objects may be dealt with. Since general CAD tools do not contain real solid models, a natural approach in simulation is to address surface models. In the current study the surface models are analyzed with continuum based shell formulations.

The first section outlines the main problems in modeling for IGA and introduces techniques to work around the problems in an efficient way. The second section is devoted to the applied shell theory and its implementation. The results of the analysis are presented in the third section.

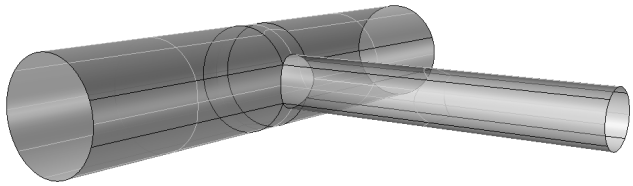

Figure 1. A watertight but inexact representation of an intersection of cylinders with different radii.

Strategies for finding analysis suitable models

Problems with traditional CAD

Traditional CAD tools are built for generating design visually, i. e. the underlying representation is of minor concern. The concept may have been generally applicable for traditional Finite

Element Analysis, where meshes of the models were used for analysis. However, when performing the analysis on the CAD model itself, the way the object is built defines if it is suitable for analysis. One of the major concerns in modeling for IGA is how to deal with boolean operations. Some attempts have been made to deal with trimmed surfaces in analysis, Kim et al. [5]. Nevertheless, in most work in IGA trimming is avoided.

Watertight or exact?

In certain cases one has to compromise between a watertight and an exact geometry. In the model of Figure 1, at least one of the cylinders has to be deformed locally to ensure the overall C^0 continuity. Analogous to traditional Finite Elements, the exactness of the intersection may be improved by increasing the number of control points. When building an exact but not watertight model, the analysis may be performed by setting additional constraints. The latter approach was not studied in this work.

Bottom-up strategy

A common approach in the CAD world is to start with the outer boundaries of the object and to add details later in the process. For IGA analysis suitable models however, a bottom-up strategy may be more convenient. In that way it is easier to ensure that all neighboring patches match on their common edges. Incorporating building blocks for advanced features may help to increase the efficiency of this process. In addition to providing analysis-suitable models, building blocks may be designed with optimal parameterization for analysis. Figure 2(a) shows a IGA analysis suitable midship section composed of over 3000 patches. One of the applied building blocks used during modeling is shown in Figure 2(b). The four patches were automatically constructed from parameters for the patch width and height and the radius and height of the hole. Another efficient strategy is to construct patches from the neighbor's edges and additional curves of the corresponding topology. The bottom-up strategy enables us to build analysis-suitable models where built-in blocks may help to avoid trimmed surfaces.

Untrimming trimmed objects

The bottom-up strategy shows one example of how traditionally trimmed objects may be constructed in an analysis-suitable way. However for complicated configurations, general construction tools are difficult to implement directly. In these cases the built-in boolean operations may be used intermediately to generate non-trimmed objects. The cylinder intersection in Figure 1 was constructed by cutting the intersection curve and the end curves of the object. The single patches were generated by lofting and swifting the matching end curves.

T-splines

When modeling with T-splines, many problems of traditional CAD systems are automatically dealt with. In general, objects are represented by a single patch so that inter-patch continuity is not an issue. In addition to that, T-junctions make it possible to delete single knot spans from T-spline geometries. Figure 2(c) shows a T-splines alternative for connecting cylinder of different radii. A portion of the basic cylinder was removed after refining around the connecting cylinder. Finally, the connecting cylinder was merged to the hole. The smooth transition in the intersection region is a typical characteristic of T-splines. To ensure a tight transition region, the generated hole has to surround the circular shape of the entering cylinder closely. T-splines enables local refinement that may be an advantage in both modeling and analysis.

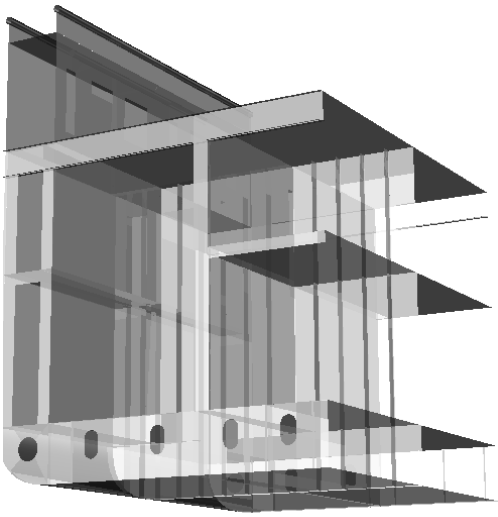

(a) Frame part of a ship section.

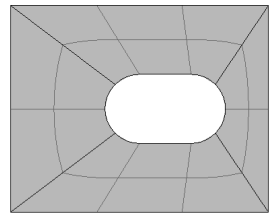

(b) Untrimmed plate with hole.

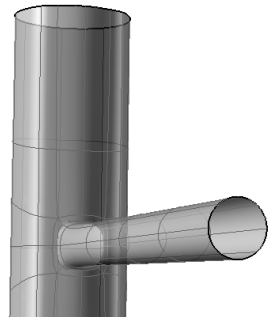

(c) T-spline cylinder intersection.

Figure 2. Examples of analysis suitable models.

Shell theory

A number of shell models are available in the literature. The classical and enhanced shell theories are based on surface models. The Kirchhoff-Love three-parameter shell model and the five-parameter Mindlin-Reissner shell model[1] are in wide use and have also been pursued within IGA. The former poses a challenge in a classical Finite Element setting due to the C^1 requirements on the displacement field. IGA enables higher order continuity and the Kirchhoff-Love model has re-emerged in analysis, especially in nonlinear problems and in rotation free form, Kindle et al. [4], Benson et al. [2]. The use of Mindlin-Reissner models has also been reported, Benson et al. [1] and Skeie et al. [6]. In the current work we use the formulation in Skeie et al. [6] which resembles the higher order shell elements found in commercial packages.

Results

Figure 3(a) shows two approaches for modeling a cylinder intersection of 90 degrees. The first model is an analysis suitable representation of a simple boolean operation, as described for Figure 1. The second model was generated with a pipe command from the T-spline plug-in for Rhino. The anlysis was performed by fixing the underlying cylinder and subjecting the entering cylinder to an upward force. The T-spline model was converted to a NURBS model. The results in the Figures 3(b) and 3(c) show a significant lower stresses for the smoother transition.

[1]also denoted shear deformable shell model

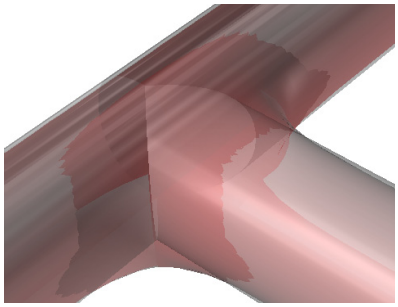

(a) Overlap of T-spline and NURBS model of a cylinder intersection.

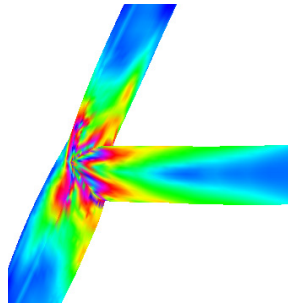

(b) Deformation and von Mises stress distribution around a sharp transition.

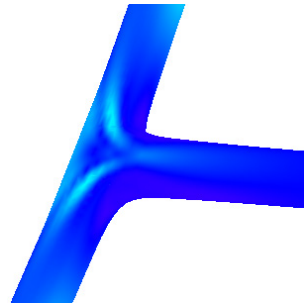

(c) Deformation and von Mises stress distribution around a smooth transition.

Figure 3.

References

[1] D. J. Benson, Y. Bazilevs, M.C. Hsu, and T.J.R. Hughes. Isogeometric shell analysis: The Reissner-Mindlin shell. *Computer Methods in Applied Mechanics and Engineering*, 199(5-8):276 – 289, 2010.

[2] D.J. Benson, Y. Bazilevs, M.-C. Hsu, and T.J. Hughes. A large deformation, rotation-free, isogeometric shell. *Computer Methods in Applied Mechanics and Engineering*, 200(13-16):1367 – 1378, 2011.

[3] T.J.R. Hughes, J. A. Cottrel, and Y. Bazilevs. Isogeometric analysis: CAD, finite elements, NURBS, exact geometry and mesh refinement. *Computer Methods in Applied Mechanics and Engineering*, 194:4135—4195, 2005.

[4] J. Kiendl, K.-U. Bletzinger, J. Linhard, and R. Wüchner. Isogeometric shell analysis with Kirchhoff-Love elements. *Computer Methods in Applied Mechanics and Engineering*, In Press, Corrected Proof:–, 2009.

[5] H. J. Kim., Y.D. Seo, and S.-K. Youn. Isogeometric analysis for trimmed CAD surfaces. *Comput. Methods Appl. Mech. Engrg.*, 198:2982–2995, 2009.

[6] Geir Skeie, Susanne Støle-Hentschel, and Torgeir Rusten. Linear isogeometric shell analysis in marine applications. In A. Eriksson and G. Tibert, editors, *23rd Nordic Seminar on Computational Mechanics, NSCM-23*, 2010.

Proceedings of the 24th Nordic Seminar on Computational Mechanics
J. Freund and R. Kouhia (Eds.)

Isogeometric Kirchhoff-Love plate elements

Knut Morten Okstad[1], Trond Kvamsdal[1], Kjell Magne Mathisen[2], and Siv Bente Raknes[2]

[(1)]SINTEF ICT, Department of Applied Mathematics, Alfred Getz vei 1, NO-7465 Trondheim, {Trond.Kvamsdal, Knut.Morten.Okstad}@sintef.no
[(2)]Norwegian University of Science and Technology, Department of Structural Engineering, Richard Birkelands vei 1a, NO-7491 Trondheim, {Kjell.Mathisen, Siv.Bente.Raknes}@ntnu.no

Summary. We present herein a family of isogeometric plate elements suitable for solving Kirchhoff-Love thin plate problems. The fourth order Kirchhoff-Love thin plate theory is characterized by requiring C^1 continuous transversal displacements w. This is a challenge for traditional finite elements (FE) methods and has typical been circumvented by introducing rotational degrees of freedom, that adds complexity to the FE-formulation. However, the isogeometric FE approach is well suited to handle problems of higher regularity as the B-spline or NURBS typically facilitate C^{p-1} regularity. Thus, isogeometric elements with $p \geq 2$ may solve Kirchhoff-Love thin plate problems with only transversal displacements.

Key words: thin plates, C^1 finite elements, isogeometry

Introduction

The maritime and offshore structures are often characterized by being thin-walled, i.e. that the thickness of structural elements like plates and shell are small compared to the in plane size of the element. A plate is a plane structural element whereas shell is non-planar, i.e. plates may be consider a special (or simplified) type of shells. In the ICADA project we aim for developing isogeometric finite elements suitable for analysing maritime and offshore thin walled structures. Our goals include both small (infinitesimal) and finite deformation finite element models for both plates and shells, and we find it natural to start out by developing isogeometric plate elements for small (infinitesimal) deformations.

For small (infinitesimal) deformations of plates we may use linear plate theories where we have decoupled the in-plane and out-of plane (transversal) deformation modes. Kirchhoff-Love theory is the common approach to solve thin plate problems involving pure transversal deformations. It may be consider as the natural 2D extension of the Euler-Bernoulli 1D beam theory. It may also be looked upon as a reduced order model, i. e. a 2D theory for representing a 3D elastic continua with one dimension (the thickness direction) much smaller than the two others. Given a hexahedral solid denoted Ω and let $l = \min\{\mathrm{l_x}, \mathrm{l_y}\}$ be the characteristic length parameter for the in-plane size of the plate, whereas $t = l_z$ be the thickness in the normal to the plane direction. We assume here that the thickness t is constant. Then, the Kirchhoff-Love thin plate theory is assumed to be valid for $t/l \leq 1/10$.

The mathematical formulation

The Kirchhoff-Love hypothesis implies that the 3D displacement field has the form:

$$u_\alpha(x_1, x_2, x_3) = u_\alpha(x_1, x_2, 0) - x_3 \frac{\partial w(x_1, x_2, 0)}{\partial x_\alpha} \; ; \quad \alpha = 1, 2 \tag{1}$$

$$u_3(x_1, x_2, x_3) = w(x_1, x_2, 0) \tag{2}$$

Herein, we will only address transversal loaded thin plates with small deformations and therefore we only need to determine the transversal displacement of the mid-surface $w := w(x_1, x_2, 0)$.

The governing equation (PDE) for a homogeneous isotropic Kirchhoff-Love thin plate of constant stiffness D, is the following biharmonic partial differential differential equation (PDE):

$$
\begin{aligned}
D\nabla^4 w &= q \quad \text{in } \Omega && (3)\\
w &= \bar{w} \quad \text{on } \partial\Omega_{D_w} && (4)\\
\frac{\partial w}{\partial n} &= \bar{\theta} \quad \text{on } \partial\Omega_{D_\theta} && (5)\\
M(w) &= \bar{M} \quad \text{on } \partial\Omega_{N_M} && (6)\\
Q(w) &= \bar{Q} \quad \text{on } \partial\Omega_{N_Q} && (7)
\end{aligned}
$$

The biharmonic operator $\nabla^4 = \nabla^2\nabla^2$ is given by

$$
\nabla^4 \equiv \frac{\partial^4}{\partial x^4} + 2\frac{\partial^4}{\partial x^2 \partial y^2} + \frac{\partial^4}{\partial y^4} \tag{8}
$$

and is of order $2m$ where $m = 2$. In general for PDEs we do have m different Dirichlet boundary conditions (BCs) and m different Neumann BCs. The Dirichlet BCs are applied to $w, \frac{\partial w}{\partial n}, ..., \frac{\partial^{m-1} w}{\partial n^{m-1}}$. Thus for thin plates up to first order normal derivatives (n is the outer normal for the plate boundary), see Equations (4) and (5). The Neumann BC are respectively for normal moment in Equation (6) and for shear force in Equation (7).

The corresponding finite element formulation is as follows: Find $w_h \in \mathcal{W}_h \subset \mathcal{W}$ such that

$$
a(w_h, v_h) = l(v_h) \quad \forall v_h \in \mathcal{V}_h \subset \mathcal{V} \tag{9}
$$

where the bilinear form $a(\cdot,\cdot)$ and the linear form $l(\cdot)$ is given by:

$$
\begin{aligned}
a(w_h, v_h) &= (D\nabla^2 w_h, \nabla^2 v_h)_\Omega && (10)\\
l(v_h) &= (q, v_h)_\Omega + (\bar{M}, v_h)_{\partial\Omega_M} + (\bar{Q}, v_h)_{\partial\Omega_Q} && (11)
\end{aligned}
$$

The inner product is defined as follows:

$$
(u, v)_\Gamma = \int_\Gamma u \cdot v \, \mathrm{d}\Gamma \tag{12}
$$

Proper function spaces for respectively the trial displacements w and the test displacements v are as follows:

$$
\begin{aligned}
\mathcal{W} &= \left\{ w \in H^2(\Omega) \mid w = \bar{w} \text{ on } \partial\Omega_w \text{ and } \frac{\partial w}{\partial n} = \bar{\theta} \text{ on } \partial\Omega_\theta \right\} && (13)\\
\mathcal{V} &= \left\{ v \in H^2(\Omega) \mid v = 0 \text{ on } \partial\Omega_w \text{ and } \frac{\partial v}{\partial n} = 0 \text{ on } \partial\Omega_\theta \right\} && (14)
\end{aligned}
$$

In isogeometric FE methods we introduce splines as basis functions. The most common spline bases are tensorial either defined by B-splines or NURBS. Herein we will use B-splines as well as locally refined B-splines denoted LR B-splines. Tensorial 2D B-splines of polynomial order p in x-direction and q in y-direction and regularity C^r in x-direction and C^s in y-direction may be written as follows:

$$
\mathcal{S}^{r,s}_{p,q}(\xi, \eta) = \sum_{i=1}^{m}\sum_{j=1}^{n} \phi^r_{i,p}\, \eta^s_{j,q} \tag{15}
$$

When we do local refinement (LR B-splines) we loose the tensorial character of the splines space. Hence, we introduce the following notation for our splines space herein: $\mathcal{S}^r_p$. Thus, we assume

the same polynomial order and regularity in both coordinate directions. Proper function spaces for respectively the FE trial displacements w_h and the FE test displacements v_h to achieve compatible FE spaces are as follows:

$$\mathcal{W}_h(\Omega) = \left\{ w_h \in \mathcal{W}(\Omega) \mid w_h(F^{-1}(x_1, x_2)) \in \mathcal{S}_p^r(\xi, \eta) \right\} \tag{16}$$

$$\mathcal{V}_h(\Omega) = \left\{ v_h \in \mathcal{V}(\Omega) \mid v_h(F^{-1}(x_1, x_2)) \in \mathcal{S}_p^r(\xi, \eta) \right\} \tag{17}$$

where the coordinate mapping F is assumed to be an onto and invertible mapping between the parameter domain $\square$ and the true domain Ω i.e. for any $(x_1, x_2) \in \Omega$ there exist $(\xi^*, \eta^*) \in \square$ such that $(x_1, x_2) = F(\xi^*, \eta^*)$.

Numerical examples

To test the spline-based Kirchhoff–Love plate element, we consider an example with known analytical solution. Figure 1 shows a simply supported rectangular plate subjected to a partial pressure load on a rectangular region of dimension $c \times d$ centered at $x = \xi, y = \eta$.

The analytic thin-plate solution to this problem may be obtained by expanding the load into a Fourier-sine series. The resulting expressions for the transverse displacement and associated bending moments may then be written as [1]:

$$\begin{Bmatrix} w \\ M_{xx} \\ M_{yy} \\ M_{xy} \end{Bmatrix} = \sum_{m=1}^{\infty} \sum_{n=1}^{\infty} \frac{p_{zmn}}{(\alpha_m^2 + \beta_n^2)^2} \begin{Bmatrix} \frac{1}{D} \sin \alpha_m x \sin \beta_n y \\ (\alpha_m^2 + \nu \beta_n^2) \sin \alpha_m x \sin \beta_n y \\ (\beta_n^2 + \nu \alpha_m^2) \sin \alpha_m x \sin \beta_n y \\ (\nu - 1) \alpha_m \beta_n \cos \alpha_m x \cos \beta_n y \end{Bmatrix} \tag{18}$$

where $\alpha_m = \frac{m\pi}{a}$, $\beta_n = \frac{n\pi}{b}$, and

$$p_{zmn} = \frac{16 p_z}{mn\pi^2} \sin \alpha_m \xi \sin \beta_n \eta \sin \alpha_m \frac{c}{2} \sin \beta_n \frac{d}{2} \tag{19}$$

These expressions may then be used to assess the accuracy of the FE solution both pointwise and globally through an energy norm. If Figure 2 we plot the convergence of the energy norm error $\|e\| = \sqrt{a(w - w_h, w - w_h)}$ for the case $c = d = 0.4$ for four different simulations. The adaptive simulations are based on LR B-spline discretizations, whereas for the uniform refinement simulations we use tensorial B-splines. The distribution of the computed bending moments on the finest adaptive cubic mesh is shown in Figure 3.

References

[1] S. P. Timoshenko and S. Woinowsky-Krieger. *Theory of Plates and Shells*. McGraw–Hill, New York, NY, USA, 1970.

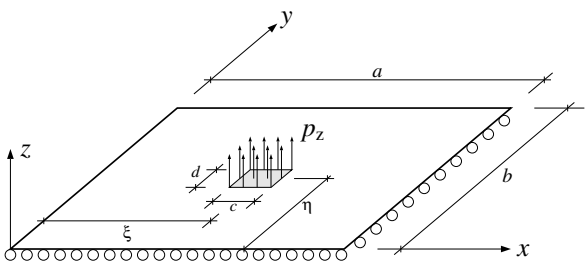

Geometry: $a = b = 10$
$\xi = \eta = 5$
$t = 0.1$ (plate thickness)

Material: $E = 2.1 \times 10^{11}$
$\nu = 0.3$
$D = \frac{Et^3}{12(1-\nu)}$

Figure 1. Simply supported rectangular plate with partial pressure load.

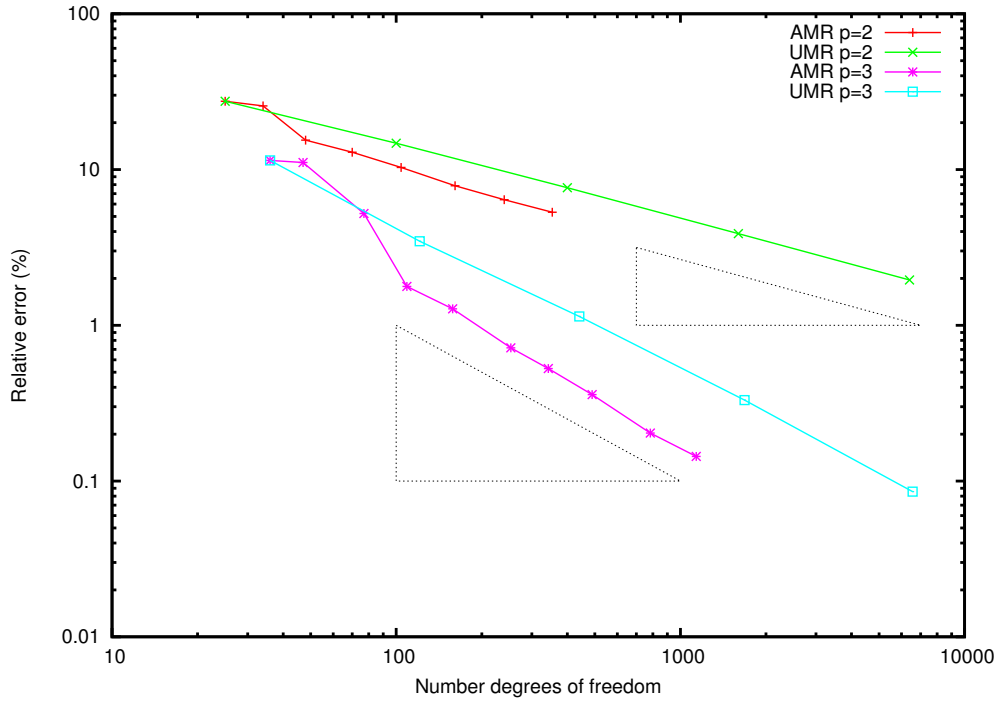

Figure 2. Simply supported rectangular plate with partial pressure load: Convergence of the global relative error for the case $c = d = 0.4$ for two adaptive simulations (AMR) and two uniform refinement simulations (UMR), using quadratic ($p = 2$) and cubic ($p = 3$) spline elements.

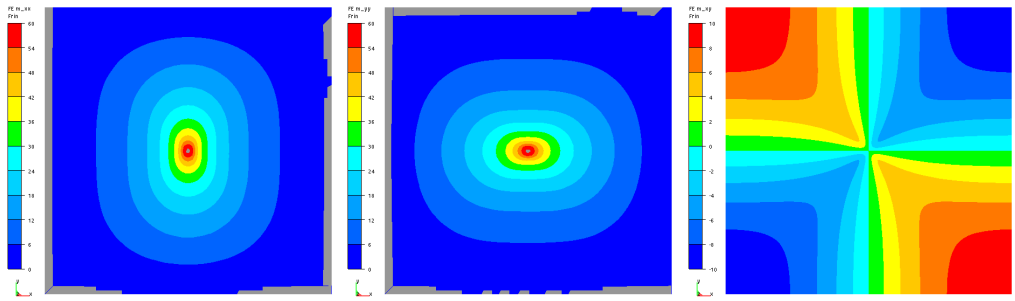

Figure 3. Simply supported rectangular plate with partial pressure load: Bending moment distributions for the case $c = d = 0.4$ on the finest adaptive cubic mesh.

Proceedings of the 24th Nordic Seminar on Computational Mechanics
J. Freund and R. Kouhia (Eds.)

Adaptive mesh refinements using LR B-splines for elliptic problems

Trond Kvamsdal and Kjetil Andre Johannessen

Norwegian University of Science and Technology, Department of Mathematical Sciences, Alfred Getz vei 1, NO-7491 Trondheim, Trond.Kvamsdal@math.ntnu.no and kjetijo@math.ntnu.no

Summary. In this paper, we investigate adaptive refinement using the newly invented locally refined B-splines (LR B-splines). The main idea is illustrated through idealized examples and its performance are tested on classical benchmark elliptic problems.

Key words: isogeometric analysis, LR B-splines, adaptive refinement

Introduction

The new paradigm of Isogeometric analysis, which was introduced by Professor Thomas J. R. Hughes and coworkers, demonstrates that much is to be gained with respect to efficiency, quality and accuracy in analysis by replacing traditional Finite Elements by volumetric NURBS elements. However, NURBS are not flexible enough to be a common basis for future CAD and FEA due to the lack of local refinement. The proposed LR B-splines by Dokken et. al [1] have the potential to form a better framework for future interoperable CAD and FEA systems.

Dokken et. al [1] describes how to manipulate the basis functions when inserting knot lines. However, there are a number of options regarding choosing which knot lines to use for refinement purposes. The inserted knot lines must at least entirely split an existing basis function, which puts a minimum length requirement on it, but there is no maximum requirement. As it turns out, we have several options available when doing the refinement. Not only of the length and position of the knot lines, but also their multiplicity as splines open for duplicate knots.

Adaptive finite element method

Many problems in science and engineering may be addressed by solving a variational problem. The existence and uniqueness of the solution is guaranteed by the Lax-Milgram theorem; Given a Hilbert space V, a continuous, coercive bilinear form $a(\cdot,\cdot)$ and a continuous linear functional $l \in V^*$ where V^* is the dual space to V, there exists a unique $u \in V$ such that

$$a(u,v) = l(v) \quad \forall v \in V. \tag{1}$$

The Galerkin Finite Element (FE) approximation to this variational problem may then be given as follow: Given $V_h \subset V$ and $l \in V^*$, find $u_h \in V_h$ such that

$$a(u_h,v) = l(v) \quad \forall v \in V_h. \tag{2}$$

For cases when the bilinear form $a(\cdot,\cdot)$ is selfadjoint the FE-solution u_h is the optimal solution to the analytical solution u measured in the "a-norm" (i.e. "energy-norm" symbolized with $_E$):

$$||u-u_h||_E = \sqrt{a(u-u_h,u-u_h)}. \tag{3}$$

Assume that we addressing self adjoint elliptic problems of second order (e.g. Poisson or linear elasticity), then if the analytical solution is sufficiently smooth, i.e. $\mathbf{u} \in H^{p+1}$, and the FE mesh $\mathcal{M}_h$ is regular and quasi-uniform, the error in the approximate FE-solution on a family of refined meshes $\{\mathcal{M}_h\}$, is bounded by (see Kvamsdal and Okstad [2])

$$||u - u_h||_E = Ch^p ||u||_{H^{p+1}} \tag{4}$$

where C is some problem-dependent constant, h is the characteristic size of the finite elements, p is the degree of the largest complete polynomial in the FE basis functions and $||\mathbf{u}||_{H^{p+1}}$ denotes the Sobolev norm of order $p+1$.

For problems where the solution is not sufficiently smooth, $u \notin H^{p+1}$, e.g. problems with singular points within the solution domain or on its boundary, we have the error bound

$$||u - u_h||_E = Ch^\beta ||u||_{H^{\beta+1}} \tag{5}$$

where the value of the non-negative real parameter β depends on how the family of meshes $\{\mathcal{M}_h\}$ are created.[1] Assume that λ is a real number characterizing the strength of the singularity. For a sequence of uniformly, or nearly uniformly, refined meshes we then have

$$\beta = \min\{p, \lambda\} \tag{6}$$

Thus, when $\lambda < p$ the rate of convergence is limited by the strength of the singularity and not the polynomial order. However, for a proper sequence of adaptively refined meshes with nearly equidistributed error throughout the mesh, we may achieve

$$\beta = p \tag{7}$$

Hence, by proper adaptive mesh refinement (AMR) we may utilize the full power of higher order methods and that is highly relevant for Isogeometric FE-methods. The importance of the LR B-splines is therefore to use them as an enabling technology for achieving optimal convergence order, i.e. accurate and efficient FE-models. In general the analytical solution is not available so we have to rely on *a posteriori* error estimates. However, herein we focus on the use of LR B-Splines for local refinement, and we have thus chosen to do the numerical test on a nontrivial benchmark problem with known analytical solution, i.e. we use the analytical "energy-error" as input to the refinement algorithm.

The refinement algorithm is based on refining a prescribed portion of the elements, i.e. $\alpha \cdot n_{el}$ having the greatest elemental contribution, ρ_e, to the global relative error, ρ

$$\rho_e = \frac{||u - u_h||_{E(\Omega_e)}}{||u||_{E(\Omega)}} \quad \text{and} \quad \rho = \frac{||u - u_h||_{E(\Omega)}}{||u||_{E(\Omega)}} = \sqrt{\sum_e^{n_{el}} \rho_e^2} \tag{8}$$

In classical FEM, the traditional way of refining a quadrilateral element is by subdivision, i.e. inserting a cross to obtain four new elements. If the aspect ratio (width to length ratio) is undesirable large, one may extend the algorithm to inserts only a single line, splitting the element into two new elements. This way of adaptive refinement give raise to so-called "hanging nodes" for which there are several techniques to reestablish the appropriate C^0- continuity. Herein, we subdivide marked elements into four new elements by inserting a cross (ignoring large aspect ratio elements for now) through the element center. As discussed above, the length of the crossing lines will have to be of a certain length in order to actually split a basis function properly. The actual length is depending on the topology of the mesh, and may split some neighboring elements into two new elements. In order to do a proper splitting we have as a pre-processing step established a list telling us which basis functions have support on each element. This information is needed when assembling the stiffness matrix. By using this list we may extract the required length of the new knot lines without doing any costly topology search.

[1] As β is not necessarily an integer, $||u||_{H^{\beta+1}}$ is a *a Sloboditskii* norm.

Numerical example - The L-shape problem

The problem consist of solving the stationary heat equation, or Laplace equation $\nabla^2 u = 0$ on a L-shaped domain $\Omega = [-1,1]^2 \setminus [0,1]^2$ with appropriate boundary conditions, i.e.

$$\nabla^2 u = 0 \text{ in } \Omega, \quad u = 0 \text{ on } \Gamma_D \text{ and } \frac{\partial u}{\partial \mathbf{n}} = g \text{ on } \Gamma_N \tag{9}$$

with $g(x,y)$ given by the exact solution at the Neumann boundary and $\mathbf{n}$ being the outward unit normal to the boundary. It can be shown that

$$u(r,\theta) = r^{2/3} \sin\left(\frac{2\theta + \pi}{3}\right) \tag{10}$$

is the analytical solution to the given boundary value problem. The homogeneous Dirichlet boundary is given at $y = 0, x \in [0,1]$ and $x = 0, y \in [0,1]$, while all other edges are given with Neumann conditions (see figure 1). Note that the exact solution of this problem have a stress singularity at the origin. The strength of the singularity $\lambda = \frac{2}{3}$, hence for uniform refinement we may only assume a convergence rate $\beta = \frac{2}{3}$. Thus, our aim is to see whether local refinement using LR B-splines may increase the convergence rate.

An example on a LR B-spline mesh after adaptive refinements is shown in figure 2. As is seen, the LR B-splines allow us to refine locally around the origin where the singularity appears.

In figure 3 we display the convergence rate for the global relative energy error vs number of degrees of freedom (ndof) in a log-log plot. We display the results obtained with four different mesh refinement sequences using cubic (LR) B-splines: a) uniform refinement, b) m1-refinement, c) m2-refinement and d) m3-refinement. Here we use the notation m1- m2- and m3-refinement to indicate adaptive refinement using LR B-splines with different multiplicity of the knot-lines. Here m1-refinement means single knot line refinement with C^2-continuity, m2-refinement means double knot line refinement with C^1-continuity and m3-refinement corresponds to triple knot line refinement with C^0 continuity. Increased multiplicity makes the LR B-spline refinement more local, i.e. less propagation of the refinement to elements surrounding elements marked for subdivision. On the other hand increased multiplicity causes an increased growth of the degrees of freedom in the finite element system.

We see that the convergence for uniform mesh refinement is limited by the strength of the singularity, i.e. a convergence rate is equal to $-\beta/2 = -1/3$.[2] However, adaptive refinement using LR B-splines all gives optimal convergence rate $-\beta/2 = -3/2$. Furthermore, that single knot-line refinement (m1-refinement) is the most accurate per degrees of freedom (dof). Thus, the results seems to indicate that *regularity* is more important than *locality*.

Acknowledgement

The authors acknowledge the financial support from the Norwegian Research Council and the industrial partners of the ICADA-project; Ceetron, Det Norske Veritas and Statoil. They also acknowledge the support from the other co-workers in the ICADA-project.

References

[1] T. Dokken, T. Lyche and K.F. Pettersen. LR B-Splines. *In preparation.*

[2] T. Kvamsdal and K.M. Okstad. Error estimation based on superconvergent patch recovery using statically admissible stress fields. *International Journal for Numerical Methods in Engineering*, 42:443-472,1998.

[2] For 2D problem we do have that ndof $\propto h^{-1/2}$.

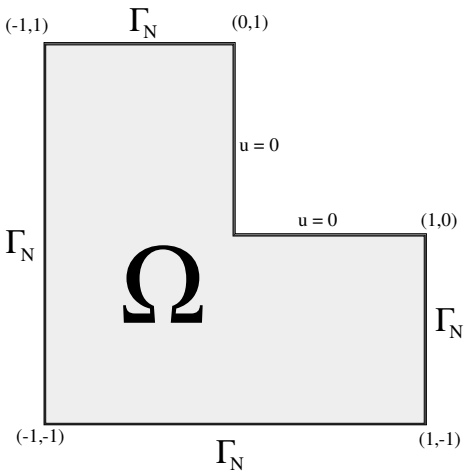

Figure 1: The L-shape problem

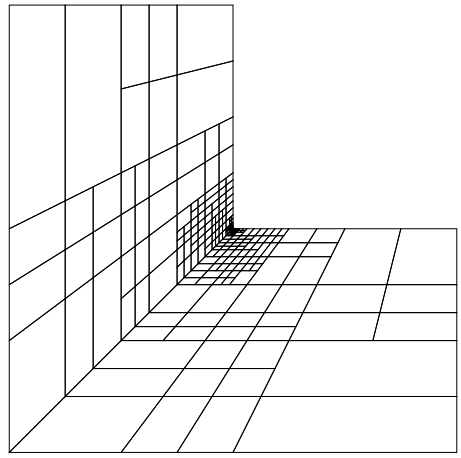

Figure 2: The 15th iteration (m1)

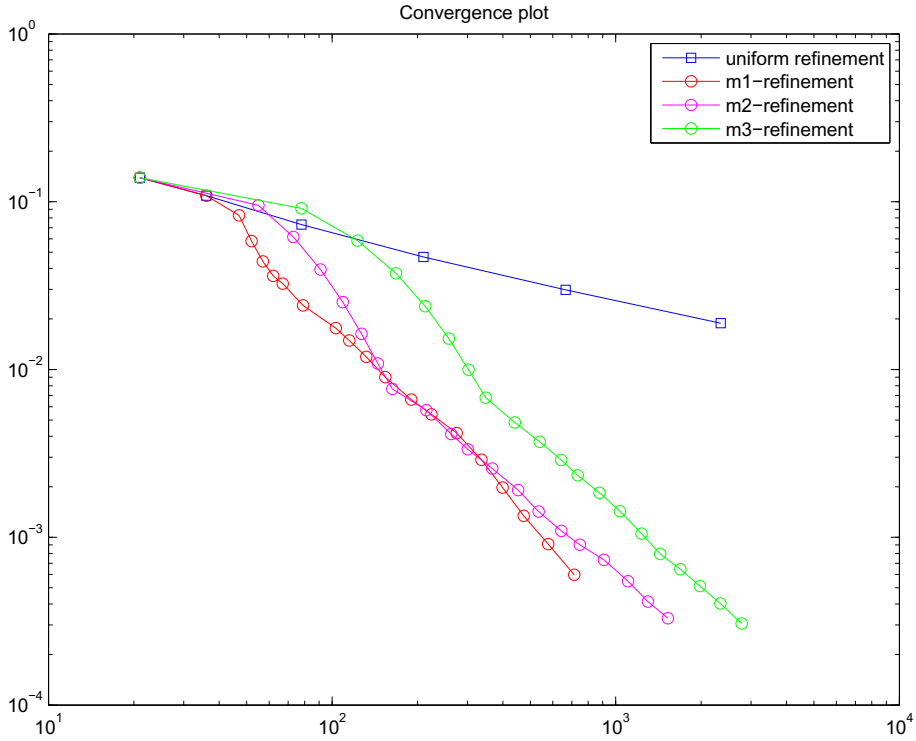

Figure 3: Convergence rates of the L-shape problem using different refinement techniques

Proceedings of the 24th Nordic Seminar on Computational Mechanics
J. Freund and R. Kouhia (Eds.)

On the spurious oscillations in B-spline finite element method

Radek Kolman, Jiří Plešek, Miloslav Okrouhlík and Dušan Gabriel

Institute of Thermomechanics, Academy of Sciences of the Czech Republic
Dolejškova 5, 182 00 Prague, Czech Republic, E-mail: kolman@it.cas.cz.

Summary. The spatial discretization of elastic continuum by the finite element method (FEM) introduces dispersion errors to numerical solutions of stress wave propagation problems. Moreover, oscillations near the sharp wavefront in FE solution appear. This phenomena is called Gibb's effect. Isogeometric analysis, where continuous piecewise higher order polynomials are used as shape functions, improves the dispersion errors and frequency spectrum in comparison with Lagrangian finite elements. B-spline basis functions can be used for one-dimensional cases. In this initial work, the B-spline based finite element method is tested in numerical modelling in one-dimensional elastic wave propagation. The special attention is paid to the study of spurious oscillations in wavefront propagation problems with stress discontinuities.

Key words: elastic wave propagation, B-spline based finite element method, spurious oscillations

Introduction

A lot of methods for the numerical solution of wave propagation problems in elastic solids have been developed, for example finite difference method, front tracking algorithms, space-time treatment methods, oscillations filtering by postprocessing, finite element spatial discretization with the finite difference in time (semidiscretization), discontinuity Galerkin's method and variational construction method and more others. In this paper, only the semidiscretization method is tested in one-dimensional elastic wave propagation. For the spatial discretization, the continuous Galerkin's approximation method is employed [3].

A modern approach in the finite element analysis is the isogeometric analysis (IGA) [1], where shape functions are based on varied types of splines. For example, B-spline (basis spline), NURBS, T-spline and others are used for spatial discretization. This approach has an advantage that the geometry and approximation of the field of unknown quantities is prescribed by the same technique. Another benefit is that the approximation is smooth. It was shown for the isogeometric approach, that the optical modes did not exist against higher order Lagrangian finite elements. Further, dispersion and frequency errors for isogeometric analysis were reported to decrease with increasing order of spline [1]. The B-spline based FEM with the small dispersion errors [1] and the variation diminishing property [9] could eliminate the spurious oscillations, which are the product of the Gibb's effect and the dispersion behaviour of FEM.

B-spline based finite element method

In Computer-Aided Design (CAD), a B-spline curve is given by the linear combination of B-spline basis functions $N_{i,p}$ [9]

$$\mathbf{C}(\xi) = \sum_{i=1}^{n} N_{i,p}(\xi)\,\mathbf{B}_i, \tag{1}$$

where $\mathbf{B}_i, i = 1, 2, \ldots, n$ are corresponding coordinates of control points. B-spline basis functions $N_{i,p}(\xi)$ are prescribed by the Cox-de Boor recursion formula [9]. For a given knot vector Ξ, $N_{i,p}(\xi)$ are defined recursively starting with piecewise constants ($p = 0$)

$$N_{i,0}(\xi) = \begin{cases} 1 & \text{if} \quad \xi_i \leq \xi \leq \xi_{i+1}, \\ 0 & \text{otherwise.} \end{cases} \tag{2}$$

For $p = 1, 2, 3, ...$, they are defined by

$$N_{i,p}(\xi) = \frac{\xi - \xi_i}{\xi_{i+p} - \xi_i} N_{i,p-1}(\xi) + \frac{\xi_{i+p+1} - \xi}{\xi_{i+p+1} - \xi_{i+1}} N_{i+1,p-1}(\xi). \tag{3}$$

A knot vector in one dimensional case is a non-decreasing set of coordinates in the parameter space, written $\Xi = \{\xi_1, \xi_2, ..., \xi_m\}$, where $\xi_i \in R$ is the i-th knot, i is the knot index, $i = 1, 2, \ldots, m$, where $m = n + p + 1$, p is the polynomial order, and n is the number of basis functions. The main properties of B-spline basis functions are introduced in [9].

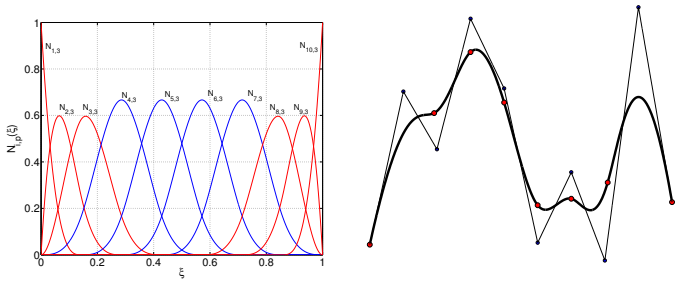

Figure 1. Cubic B-spline basis functions (on the left) and an open cubic B-spline curve interpolating end points (on the right) for ten control points and uniform knot vector.

The knot vector for an open B-spline curve interpolating end points should be in the form $\Xi = \{a, \ldots, a, \xi_{p+2}, \ldots, \xi_n, b, \ldots, b\}$, where values are usually set as $a = 0$ and $b = 1$. The multiplicity of the first and last knot value is $p + 1$. If the values ξ_{p+1} up to ξ_{n+1} are chosen uniformly, the knot vector Ξ is called uniform, otherwise non-uniform [9]. An example of cubic B-spline basis functions and an open cubic B-spline curve interpolating end points with its control polygon is displayed in figure 1.

In the B-spline based FEM [1], the approximation of the displacement field u^h is given by

$$u^h(\xi) = \sum_{i=1}^{n} N_{i,p}(\xi)\, u_i^{\mathrm{B}}, \tag{4}$$

where u_i^{B} is the component of the vector of control variables – displacements corresponding to the control points. Remark, the linear B-spline FEM is identical with the standard linear FEM. In the following text, the continuous Galerkin's approximation method [3] for the numerical solution of partial differential equations is employed. Spatial discretization of elastodynamics problems by the finite element method leads to [3]

$$\mathbf{M}\ddot{\mathbf{u}} + \mathbf{K}\mathbf{u} = \mathbf{R}. \tag{5}$$

Here, $\mathbf{M}$ is the mass matrix, $\mathbf{K}$ the stiffness matrix, $\mathbf{R}$ is the time-dependent load vector, $\mathbf{u}$ and $\ddot{\mathbf{u}}$ contain control point variables–displacements and accelerations. Mass matrix, stiffness matrix and load vector are defined by the same relationships as the standard FEM [3].

A lot of discrete time direct integration methods for the system (5) were developed [3]. In this work, the Newmark method [7] and the central difference method [2] are employed. If the theory of linear elastodynamics is considered, then the mass matrix $\mathbf{M}$ and the stiffness matrix $\mathbf{K}$ are constant. These matrices are evaluated by the Gauss-Legendre quadrature formula [3].

Problem description

In this contribution, the crucial test is a problem of axial elastic waves propagation in a free-fixed "thin" bar under the force loading prescribed by the Heaviside step function, see figure 2. The shock loading generates the sharp stress and velocity wavefront in the shape of discontinuity. The parameters of the task are set: the bar length $L = 1\,m$, the cross-section $A = 1\,m^2$, Young's modulus $E = 1\,Pa$, the mass density $\rho = 1\,kg/m^3$ and the amplitude of impact pressure $\sigma_0 = 1\,Pa$. The analytical solution of this impact problem could be found in reference [6], where the displacement field $u(x,t)$ without a wave reflection in the time range $t \in [0, L/c_0]$ is

$$u(x,t) = v_0\,(t - x/c_0)\,H(t - x/c_0), \tag{6}$$

where the impact velocity is given by $v_0 = \sigma_0/\sqrt{E\rho}$ and $H(t)$ is the Heaviside time step function [5]. Wave speed in an elastic bar is prescribed by the relationship $c_0 = \sqrt{E/\rho}$.

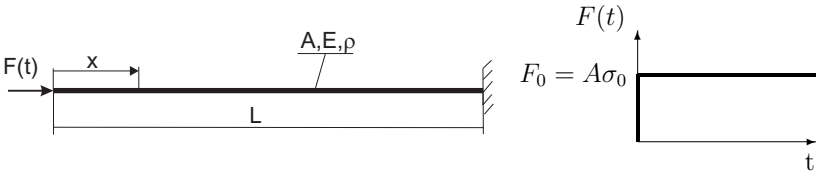

Figure 2. Scheme of an elastic free-fixed bar under a shock loading.

Finite element response

The response of the elastic bar is computed numerically by the Newmark method (NM) [7] with the consistent mass matrix [3] and the central difference method (CDM) [2] with the lumped mass matrix by the "row sum" method [3]. Time step for NM is chosen as $\Delta t^{NM} = 1/8\,T_{min}$, where T_{min} is the minimal vibration period of the whole system (5). It is valid $T_{min} = 2\pi/\omega_{max}$, where ω_{max} is the maximum eigenfrequency of the whole system (5). The period elongation error for NM with this time step is smaller than 5% [3]. Time step for CDM is set with respect to the stability condition [8] and good dispersion behaviour. Practically, time step is chosen as $\Delta t^{CDM} = 0.99999\Delta t_{crit}$, where the critical value is given by $\Delta t_{crit} = 2/\omega_{max}$ [8].

The bar is discretized by linear ($p = 1$) and cubic ($p = 3$) B-splines with $n = 100$ control points. The knot vector is used the uniform ones and the parameterization is set linear by the Greville abscissa [4]. The courses of dimensionless stress σ/σ_0 along the bar computed by NM and CDM are depicted on figures 3 and 4 at time $t = 0.5L/c_0$. The theoretical wavefront takes place in half of the bar and the stress value in the overlaying area has the magnitude $\sigma = -\sigma_0$.

Conclusions

In the numerical test, the oscillations near sharp wavefronts for the B-spline based FEM are smaller than for the classical FEM due to the variation diminishing property and better dispersion. Further, the oscillations for IGA is reported to decrease with increasing order of splines, but there are not absolutely eliminated. The post-shock oscillations are typical for CDM and the front-shock oscillations arise for the Newmark method. The best results have been obtained for CDM with near the critical time step and linear finite elements. In future, a choice of the time step for the direct integration methods and mass lumping will be in the centre of attention.

Acknowledgment

This work was supported by the grant projects GA ČR 101/09/1630, P101/10/P376, 101/07/1471 and P101/11/0288 under AV0Z20760514.

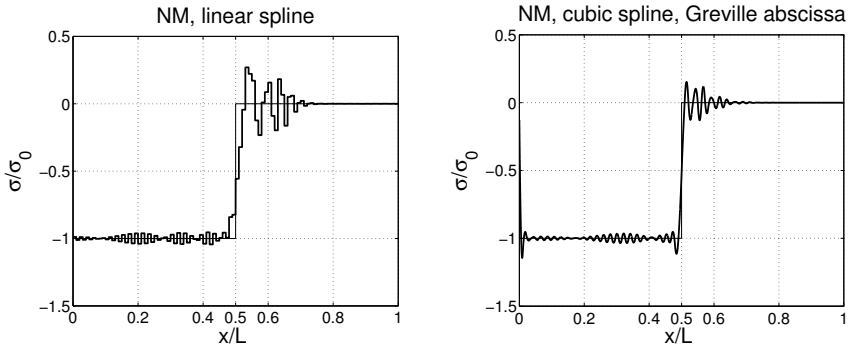

Figure 3. Stress in an elastic bar under the shock loading at time $t = 0.5L/c_0$ computed by the Newmark method for linear (on the left) and cubic (on the right) B-splines.

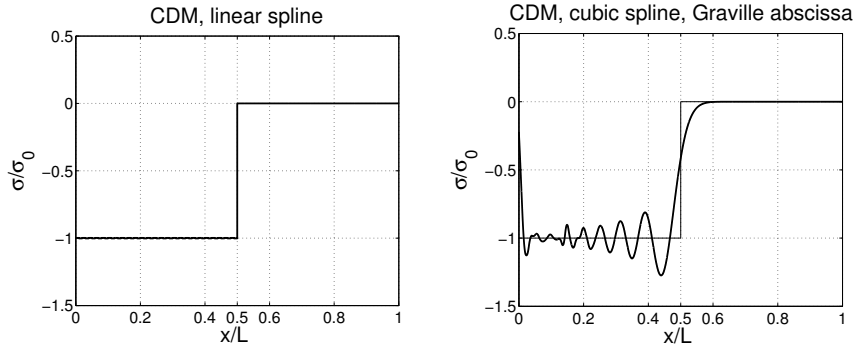

Figure 4. Stress in an elastic bar under the shock loading at time $t = 0.5L/c_0$ computed by the central difference method for linear (on the left) and cubic (on the right) B-splines.

References

[1] J.A. Cottrell, T.J.R. Hughes and Y. Bazilevs. *Isogeometric Analysis: Toward Integration of CAD and FEA*. John Wiley & Sons, New York, 2009.

[2] M.A. Dokainish and K. Subbaraj. A survey of direct time-integration methods in computational structural dynamics - I. Explicit methods. *Comp.& Struct.*, 32(6):1371–1386 1989

[3] T.J.R. Hughes. *The Finite Element Method: Linear and Dynamic Finite Element Analysis*. New York: Prentice-Hall, Englewood Cliffs, 1983.

[4] T.N.E. Greville. On the normalization of the B-splines and the location of the nodes for the case of unequally spaced knots. O. Shiska eds. *Inequalities*, Academic Press, New York, 1967.

[5] R.P. Kanwal. *Generalized Functions: Theory and Technique*. Birkhäuser, Boston, 1998.

[6] H. Kolsky. *Stress Wave in Solids*. New York: Dover Publications, 1963.

[7] N.M. Newmark. A method of computation for structural dynamic. *Journal of the Engineering Mechanics Division*, 85:67–94, 1959.

[8] K.C. Park. Practical aspect of numerical time integration. *Comp.& Struct.*, 7:343–353, 1977.

[9] L. Piegl and W. Tiller. *The NURBS Book*. Springer-Verlag, 1997.

Proceedings of the 24th Nordic Seminar on Computational Mechanics
J. Freund and R. Kouhia (Eds.)

A classical lamination model of bi-stable woven composite tape-springs

Yoann Prigent, Pau Mallol, and Gunnar Tibert

KTH, Royal Institute of Technology, Department of Mechanics
SE-100 44 Stockholm, Sweden, tibert@kth.se

Summary. This extended abstract presents the work done so far on modeling woven composite materials, specifically two carbon fiber reinforced plastics materials: twill and plain weave. The material model has been initially verified against data available in a database.

Key words: bi-stability, tape spring, woven carbon fiber composite, strain energy.

Introduction

For decades tape-springs has been used as deployable structures in space due to its compact stowed volume and good structural characteristics when deployed. Metallic tape springs are only stable in the deployed state so a robust containing solution needs to be used to keep them coiled. Moreover, during deployment an active control scheme must be used to prevent blooming [1]. These aspects pose issues on the overall mass budget, reliability and complexity for such mechanisms. However, bi-stable tape springs made of, for instance, woven carbon fiber reinforced plastics (CFRP), show two well-defined stable configurations: the completely stowed and completely uncoiled configurations. Bi-stability in such deployable structures allows a dramatic reduction in mass as well as in control complexity thus, increasing the reliability of the system.

CFRP modeling

The main modeling difficulties come from the orthotropy of the material and its characteristic woven structure (Fig. 1), embedded in a cured resin matrix. In a plain weave (Fig. 2) odd bundles pass over one and under one perpendicular bundle, and even bundles reverse this order. In the twill type (Fig. 3) odd bundles pass over two perpendicular bundles and under one, while even bundles reverse this order.

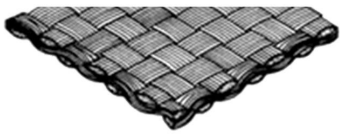

Figure 1: Plain weave woven scheme.

Figure 2: Plain weave CFRP.

Figure 3: Twill CFRP.

Bi-stability

In this context, the term bi-stability is used when a structure shows two well-defined stable configurations: coiled and straight (deployed) ones. These two configurations represent local minima of the stored strain energy and, to transit from one to another, external *activation energy* must be provided. Such *activation energy* is in our case a bending moment applied on the edges of the straight configuration in order to flatten it (Fig. 4). Once a certain point (point A in Fig. 4) is reached, the tape-spring section becomes flat and tends to coil in a virtual cylinder with axis perpendicular to the straight configuration axis, storing the generated strain energy. If then we start removing the bending moment applied, the strain energy is slowly released and two phenomena may occur: either the tape spring snaps back to the straight configuration (point B in Fig. 4) or it remains rolled-up storing strain energy (Fig. 5).

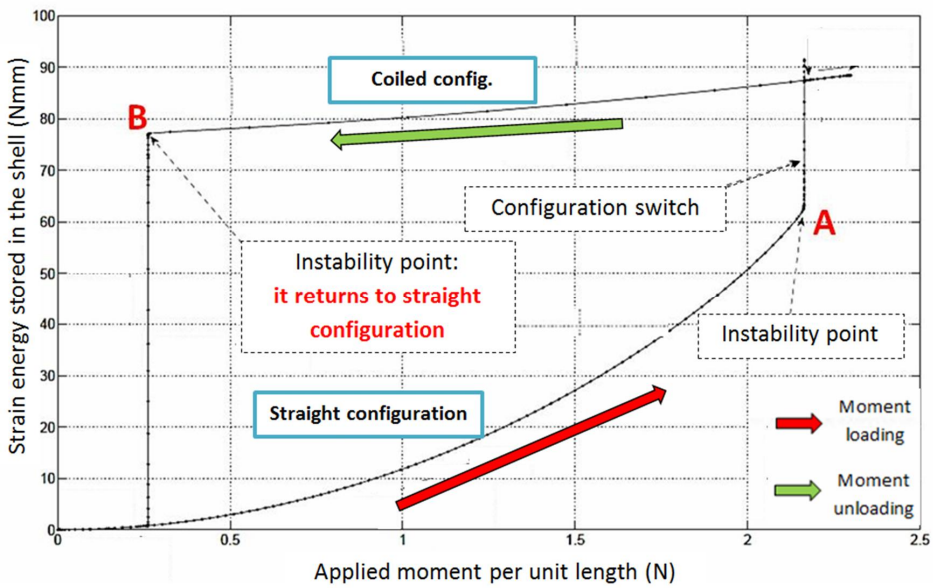

Figure 4: Strain energy curves for a non-bi-stable tape-spring.

Models

The material model developed here is based on Naik's model [2], which simplifies the unit cell of the material of Fig. 1 into a four layer cell made of two resin layers on the outer layers and the interlacing carbon fiber bundles as separated unidirectional (UD) plies as in Fig. 6. Naik's model predicts well the in-plane behavior of the material but not the out-of-plane behavior and the bending stiffness is a crucial parameter here since it is the origin of the strain energy generated. Thus, the strain energy is directly related to the bi-stability characteristics of the boom. Consequently, Naik's model was modified by dividing the basic cell into a series of plies, until a model that permits to vary the thickness and position of each layer (Fig. 7) to tune the bending characteristics without affecting the in-plane properties of the material.

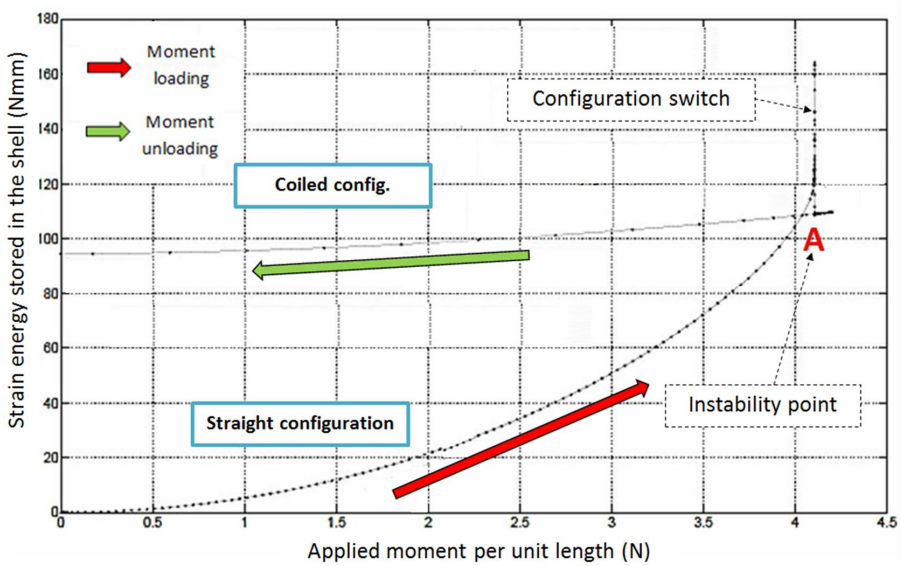

Figure 5: Strain energy curves for a bi-stable tape-spring.

After tuning the material model parameters against data from a database, it is implemented in the coiling simulation developed in the software Abaqus. With the proper boundary conditions on the booms, the tips are flattened over the spool, Fig. 8(a), making coincident the edge nodes with a set of nodes in the spool. Rotation is then applied to the spool, pulling the boom and coiling it, Fig. 8(b), which generates strain energy that is stored on the coiled configuration. When only the transition zone (a few centimeters) is left, the coiling stops, Fig. 8(c). Note that it is vital to keep this transition zone since it is the mechanism that drives the deployment towards the second stable configuration.

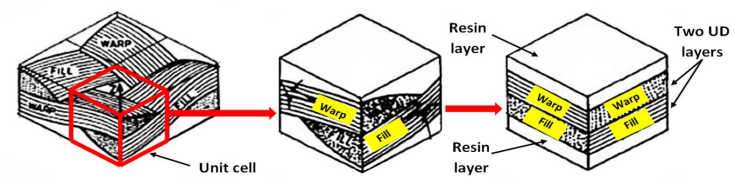

Figure 6: Unit cell simplification in Naik's model (from [2]).

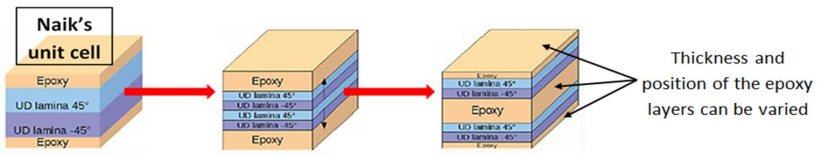

Figure 7: Naik's cell model modification to obtain the proposed model.

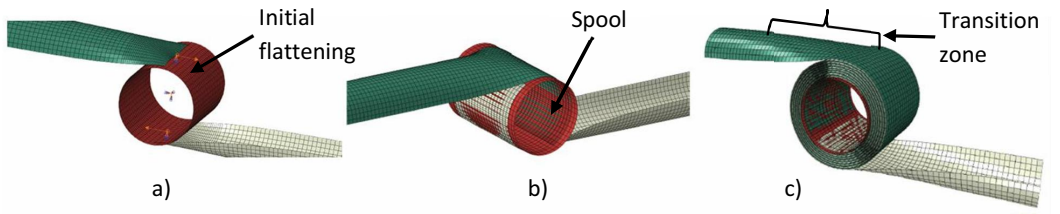

Figure 8: Coiling simulation steps.

Results

A case example is shown in Table 1. It corresponds to a plain weave specimen with fiber volume content (V_f) of 0.85, gap ratio (g/a) of 0.21 and fiber direction at 45° bias, which is a well-approximated example of the plain weave CFRP we have for the project and to be used in our simulations. V_f is a common parameter that comes along other properties and defines the volume of fibers with respect to the resin; g/a is a parameter created here in order to take into account the gaps observed in the plain weave case; the bias is measured with respect to the longitudinal direction of the boom and must be 45° here to ensure a symmetrical mechanical properties longitudinally (0°) and transversely (90°) to the tape-spring.

Table 1: Plain weave with $V_f = 0.85$, g/a = 0.21 and at 45° bias.

Property	Model prediction	Error with respect to database values
Tensile modulus (GPa)	11.75	–1.48
Shear modulus (GPa)	27.0	+2.98
Poisson's ratio (-)	0.794	–0.92

Discussion and conclusions

Bi-stability strongly relies on the out-of-plane properties (bending) thus a model that is accurate in bending is crucial. Previous modeling techniques were not successful (or computationally too expensive [3]). To address this aspect a modified Naik's model was developed. The modifications made on Naik's model has provided a significantly improvement on the results agreement with real material properties. However, several aspects need to be improved and others further investigated to include them in our analyses, i.e. observed creep, low temperature sensitivity and friction during deployment.

References

[1] T. Murphey et al. *Deployable booms and antennas using bi-stable tape-springs*. 24th Annual AIAA/USU Conference on Small Satellites, 2010, paper SSC10-X-6.

[2] N.K. Naik and V.K. Ganesh. *An analytical method for plain weave fabric composites*. Composites, vol. 26, 1995.

[3] Y. Prigent. *A finite element model of bi-stable woven composite tape-springs*. MSc thesis, KTH, 2011.

Proceedings of the 24th Nordic Seminar on Computational Mechanics
J. Freund and R. Kouhia (Eds.)

Experiments on Nomex® honeycomb compliance

A. Karakoç[1] and J. Freund

(1)Researcher, Aalto University FI-00076 Aalto Finland, alp.karakoc@aalto.fi

Summary. This article presents an experimental method to measure the compliances of cellular structures composed of hexagonal cells. The experiments are based on uni-axial tension tests for Nomex® honeycomb cores. Specimens with various material orientations relative to loading direction are tested. Consequently, the relationship between stress and strain tensors is constructed.

Key words: Cellular, experiment, Nomex®, honeycomb, stress, strain

Introduction

An experimental method is presented to measure the in-plane compliance matrices of Nomex® honeycomb cores without a priori assumptions such as orthotropy, etc. In order to obtain compliance, uni-axial tension tests are carried out for different material orientations. Marker tracking technique is used to determine positions of the marker points on the material. These data are processed to get strain of the measuring domain while the stress is estimated through external loading and core geometry. Analysis is confined to a measuring domain under near constant stress and strain.

Methodology

Stress-strain relation in laboratory *XY*-coordinate system is given by

$$\{\mathbf{e}\} = [\mathbf{C}]\{\mathbf{s}\} = [\mathbf{T}]^{\mathrm{T}}[\underline{\mathbf{C}}][\mathbf{T}]\{\mathbf{s}\}. \tag{1}$$

In expression (1), $\{\mathbf{e}\}$ and $\{\mathbf{s}\}$ are the column vector representations of strain and stress tensors with assumption of symmetry ($e_{ij} = e_{ji}$ and $s_{ij} = s_{ji}$ for $i, j \in \{X, Y\}$), while $[\mathbf{C}]$ is the square matrix representation for the compliance tensor $\mathbf{C}$ in *XY*-coordinate system [1]. In order to obtain compliance matrix $[\underline{\mathbf{C}}]$ in material *WL*-coordinate system, orthogonal transformation $[\mathbf{T}]$ of the second form in (1) is used [2], which is followed by least square fitting to experimental data on $\{\mathbf{e}\}$ and $\{\mathbf{s}\}$. The purpose is to solve $[\underline{\mathbf{C}}]$ using various material orientations relative to the loading direction.

Experiments

Material type, displacement of hydraulic actuator and specimen orientation angle relative to uni-axial load are considered as the independent variables. Material type is described in terms of the cell wall thickness t, height h, length l and corner angle θ, cell wall elastic modulus E_s, and core thickness $\mathcal{T}$. The dependent variables of experiments are the load vector $\vec{F}$ and position data of the markers in the measurement domain, which are used in the stress and strain calculations.

Three different cell sizes c_1=5 mm, c_2=6 mm and c_3=13 mm, and two different core thicknesses $\mathcal{T}_1$ = 7 mm and $\mathcal{T}_2$ = 12 mm are used in order to evaluate the effects of dimensional parameters on the effective in-plane mechanical properties. Samples are formed based on these two parameters, while the specimens of each sample are prepared using four different orientations φ_1=0˚, φ_2=90˚, $\varphi_{3,4}$=±45˚ relative to uni-axial loading as seen in figure 1. In defining specimen dimensions and testing, ASTM C363 test method for sandwich constructions and cores is taken into account [3].

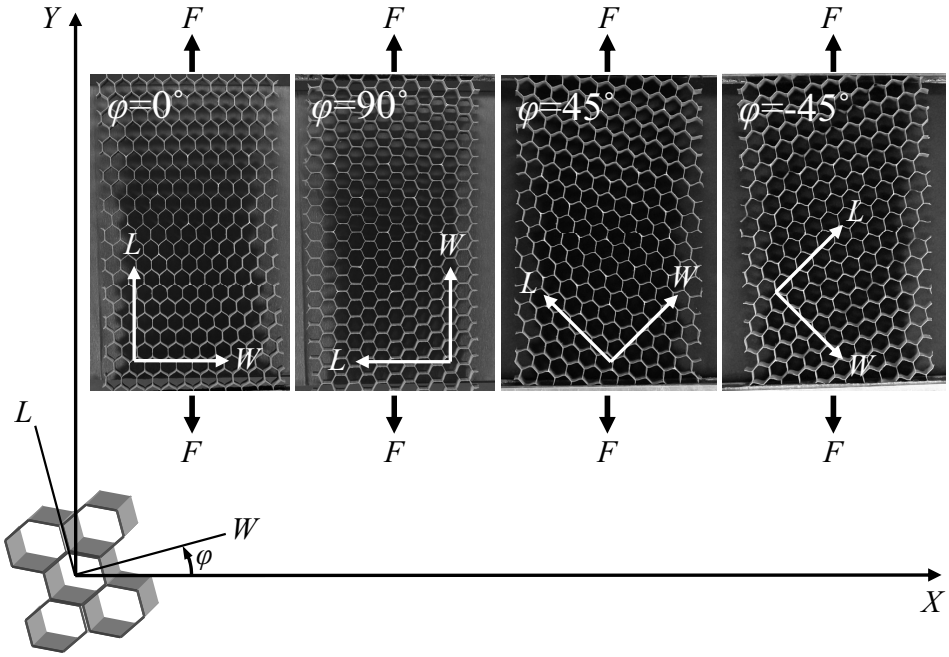

Figure 1. Specimens with different material orientations relative to loading direction.

Experiments are carried out in a steel frame of 920 × 920 mm^2 with wall thickness of 60 mm. The large frame gives flexibility to test large sheets and provides suitable loading condition on the measurement region. Bottom section of the specimen is fixed using fixture plates connected to a stationary joint; whereas, top section is adjusted to move upwards and downwards along an axis. The actuating system consists of a hydraulic servo cylinder with a pressure up to 16 MPa. Test duration changes between 3 to 6 minutes with a constant loading rate.

Analysis

Marker tracking and displacement analysis

Marker center coordinates (X_i, Y_i) inside the measurement domain are calculated with marker tracking technique. For this purpose, an in-house code has been developed and verified with rigid body motion tests.

The marker displacements associated with frame *f* are obtained as

$$\begin{Bmatrix} u_i \\ v_i \end{Bmatrix} = \begin{Bmatrix} X_i^{f+1} - X_i^f \\ Y_i^{f+1} - Y_i^f \end{Bmatrix}. \tag{2}$$

in which, u and v are the displacements along X- and Y-axes, respectively. Then, continuous displacement field $\vec{u}_f$ is obtained as a linear function by means of least square analysis of the marker displacements. As a result of partial differentiation of $\vec{u}_f$, deformation gradient $[\mathbf{F}] = [\mathbf{R}][\mathbf{U}]$ is calculated.

Strain and stress measures

In order to eliminate the effect of rotation in strain calculations, the Green-Lagrange strain measure **E** is used in terms of right stretch tensor **U**. According to [4],

$$[\mathbf{E}] = \frac{1}{2}([\mathbf{U}]^2 - [\mathbf{I}]) \tag{3}$$

in which **I** is the identity tensor and $[\mathbf{U}] = [\boldsymbol{\epsilon}] + [\mathbf{I}]$. In case of small strain assumption, expression (3) becomes

$$[\mathbf{E}] = \frac{1}{2}([\mathbf{I}] + 2[\boldsymbol{\epsilon}] + [\boldsymbol{\epsilon}]^2 - [\mathbf{I}]) \approx [\boldsymbol{\epsilon}]. \tag{4}$$

For the constitutive modelling, the stress measure should be selected invariant to rotations and symmetric because of the strain measure characteristics in expressions (3) and (4). The first property is satisfied with first Piola-Kirchhoff stress tensor **P**, while the latter is satisfied with second Piola-Kirchhoff stress tensor **S**. First Piola-Kirchhoff stress tensor **P** is expressed in terms of infinitesimal load vector $d\vec{F}$, unit area dA and unit surface normals $\vec{N}^1$, $\vec{N}^2$ in the initial configuration. Hence,

$$\begin{Bmatrix} dF_X^i \\ dF_Y^i \end{Bmatrix} = \begin{bmatrix} P_{XX} & P_{YX} \\ P_{XY} & P_{YY} \end{bmatrix} \begin{Bmatrix} N_X^i \\ N_Y^i \end{Bmatrix} dA, \; i \in \{1, 2\}. \tag{5}$$

Then **S**, which is symmetric and energy conjugate to **E**, is calculated as

$$[\mathbf{S}] = [\mathbf{F}]^{-1}[\mathbf{P}]. \tag{6}$$

Results

Since the main purpose is to calculate the compliance matrices as tabulated in table 1, the study is limited to small displacements of cell walls under bending deformation.

Table 1. Effective in-plane mechanical properties for tested Nomex® honeycomb cores. Prefix S- stands for sample, while the following figures are for cell size c and core thickness $\mathcal{T}$.

Sample	l [mm]	t [mm]	θ [°]	E_W [kPa]	E_L [kPa]	G_{WL} [kPa]	ν_{WL}	ν_{LW}
S-5-7	2.5	0.05	32	121.0	158.5	92.6	1.12	1.47
S-5-12	2.5	0.05	34	105.8	159.8	98.3	0.97	1.47
S-6-7	3.2	0.06	26	171.9	118.0	64.3	1.31	0.89
S-6-12	3.2	0.06	28	150.0	105.7	71.4	1.29	0.91
S-13-7	6.6	0.13	32	122.9	154.2	91.9	1.26	1.58
S-13-12	6.8	0.13	32	96.5	128.2	84.6	0.91	1.21

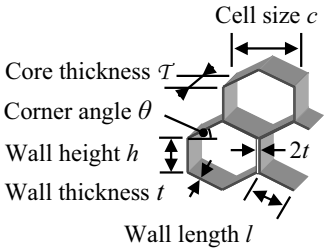

Concluding remarks

In this study, uni-axial tension tests are conducted with Nomex® honeycomb cores with various material orientations relative to loading direction. Results of these experiments are given in terms of the stress and strain measures and processed with transformation and least squares functions to obtain the full compliance matrices.

Acknowledgments

The authors gratefully acknowledge the financial support of Multidisciplinary Institute of Digitalisation and Energy through Energy Efficient Wood Processing and Machining Project (E-wood) and the Ministry of Education of Finland through the National Graduate School in Engineering Mechanics.

References

[1] T. Belytschko, W.K. Liu, B. Moran, *Nonlinear Finite elements for Continua and Structures*, Wiley-Sons, 2000.

[2] R.M. Jones, *Mechanics of Composite Materials*, McGraw-Hill Book Company, 1975.

[3] MIL-STD-401B, *Military standard sandwich constructions and core materials, general test methods*, Department of Defense, 1967.

[4] Z.P. Bazant, Easy-to-compute tensors with symmetric inverse approximating Hencky finite strain and its rate, *Journal of Engineering Materials*, 120: 131-136, 1998.

Proceedings of the 24th Nordic Seminar on Computational Mechanics
J. Freund and R. Kouhia (Eds.)

Hypo– and hyperinelasticity applied to modeling of compacted graphite iron machining simulations

Goran Ljustina, Martin Fagerström, and Ragnar Larsson

Division of Material and Computational Mechanics
Department of Applied Mechanics
Chalmers University of Technology, SE-412 96 Göteborg, Sweden

Summary. In the present paper we are concerned with constitutive modeling and validation of the thermomechanically coupled Compacted Graphite Iron (CGI) machining problem. Particular emphasis is placed on the significance of the choice of different hypoelastic-inelastic formulations in terms of four different objective stress rate formulations. We also relate to a thermodynamically consistent hyperelastic–inelastic formulation based on multiplicative decomposition of the deformation gradient. The consequently induced tangent material behavior is then derived in the spatial setting in terms of the Oldroyd stress rate, and it is compared to the hypo–formulations. The Johnson–Cook (JC) model is taken as the main prototype for the modeling of isotropic hardening, strain rate and temperature dependencies. The different models are compared in simple shear, uniaxial tensile–compressive tests, and finally in a representative CGI–machining simulation, and the resulting mechanical isothermal behavior obtained from the different ways of establishing the objective stress rate are surprisingly similar.

Key words: Johnson-Cook plasticity, hypoelastic-inelastic, hyperelastic-inelastic,, objective stress rates

Constitutive modeling of pearlite phase in CGI microstructure

The Johnson–Cook model

We shall consider various constitutive formats applied to the JC–model representing isotropic material hardening, rate dependence, and temperature dependent material properties. In this development, we first note that the standard form of this model is quite often established in the Green–Naghdi stress rate $\hat{\boldsymbol{\tau}}$ assuming isotropy in the rate behavior for the elastic response. We thus simply postulate the objective stress rate in terms of the elastic material operator $\boldsymbol{E}^e$ as

$$\hat{\boldsymbol{\tau}} = \boldsymbol{E}^e : \left(\bar{\boldsymbol{l}} - \boldsymbol{l}^{th}\right) \text{ with } \boldsymbol{l}_p = \lambda \boldsymbol{f} \ , \ \boldsymbol{f} = \frac{3}{2}\frac{\boldsymbol{\tau}_{dev}}{\tau_e} \ , \ \boldsymbol{l}^{\text{th}} = \alpha\dot{\theta}\boldsymbol{1} \tag{1}$$

The JC–model is quite often specified in terms of a "rate dependent yield function", However, in order to fit the model into the presently proposed constitutive formats, the model is considered recast into the Perzyna viscoplasticity format where the overstress function is specified in terms of a quasistatic yield function Φ as

$$\begin{cases} \lambda = \dot{\epsilon}_0 \exp\left[\frac{<\Phi>}{C(1-\theta^m)(A+Bk^n)}\right] & \rightsquigarrow \ \lambda > 0 \text{ if } \frac{\lambda}{\dot{\epsilon}_0} \geq 1 \\ \Phi \leq 0, \ \lambda \geq 0, \ \lambda\Phi = 0 & \rightsquigarrow \ \lambda > 0 \text{ if } \frac{\lambda}{\dot{\epsilon}_0} < 1 \end{cases} \tag{2}$$

where the yield function is defined by $\Phi = \tau_e - (A + Bk^n)(1 - \theta^m)$. As to the material parameters involved, we note that A, B and C are material parameters representing initial yield, hardening and rate sensitivity, respectively. In addition, the exponent n represents the hardening, whereas the exponent m represents the temperature dependence.

Relation between hyperelastic–inelastic and hypo–formulations

In this subsection we scrutinize formulations based on the objective spatial Zaremba-Jaumann, Green-Naghdi, Oldroyd and Mandel stress rates as compared to a corresponding thermodynamically consistent one.

The hypoelastic–inelastic framework

The considered objective spatial Zaremba-Jaumann, Green-Naghdi, Oldroyd and Mandel stress rates are obtained based on induced, differently back–rotated material stresses – either the stress tensor $\boldsymbol{T}$, the second Piola Kirchhoff stress tensor $\boldsymbol{S}$ or the Mandel stress tensor $\boldsymbol{M}$ associated with the Kirchhoff stress $\boldsymbol{\tau}$ are considered. These stresses and their associated objective rates are defined as

$$\begin{aligned} \boldsymbol{T} &= \boldsymbol{R}^t \cdot \boldsymbol{\tau} \cdot \boldsymbol{R} \Rightarrow \dot{\boldsymbol{T}} = \boldsymbol{R}^t \cdot \hat{\boldsymbol{\tau}} \cdot \boldsymbol{R} \\ \boldsymbol{S} &= \boldsymbol{F}^{-1} \cdot \boldsymbol{\tau} \cdot \boldsymbol{F}^{-t} \Rightarrow \dot{\boldsymbol{S}} = \boldsymbol{F}^{-1} \cdot \overset{\square}{\boldsymbol{\tau}} \cdot \boldsymbol{F}^{-t} \\ \boldsymbol{M} &= \boldsymbol{F}^{t} \cdot \boldsymbol{\tau} \cdot \boldsymbol{F}^{-t} \Rightarrow \dot{\boldsymbol{M}} = \boldsymbol{F}^{t} \cdot \overset{\triangledown}{\boldsymbol{\tau}} \cdot \boldsymbol{F}^{-t} \end{aligned} \tag{3}$$

where $\hat{\boldsymbol{\tau}}$ and $\overset{\square}{\boldsymbol{\tau}}$ are the symmetric Green-Naghdi and Oldroyd stress rates, respectively. As to the Mandel stress rate $\overset{\triangledown}{\boldsymbol{\tau}}$ it is generally non–symmetric but may be shown to be symmetric provided that e.g. elastic and plastic isotropy in the rate response is at hand. As a consequence of (3), we find that these stress rates are obtained as

$$\begin{aligned} \hat{\boldsymbol{\tau}} &= \dot{\boldsymbol{\tau}} - \boldsymbol{\omega} \cdot \boldsymbol{\tau} + \boldsymbol{\tau} \cdot \boldsymbol{\omega} \\ \overset{\square}{\boldsymbol{\tau}} &= \dot{\boldsymbol{\tau}} - \boldsymbol{l} \cdot \boldsymbol{\tau} - \boldsymbol{\tau} \cdot \boldsymbol{l}^t \\ \overset{\triangledown}{\boldsymbol{\tau}} &= \dot{\boldsymbol{\tau}} + \boldsymbol{l}^t \cdot \boldsymbol{\tau} - \boldsymbol{\tau} \cdot \boldsymbol{l}^t \end{aligned} \tag{4}$$

where $\boldsymbol{F}$ is the deformation gradient tensor and $\boldsymbol{R}$ is the rotational part of the continuum deformation gradient, i.e. $\boldsymbol{F} = \boldsymbol{R} \cdot \boldsymbol{U}$, where $\boldsymbol{U}$ is the symmetric right stretch tensor, which in turn is related to the prominent right Cauchy-Green deformation tensor as $\boldsymbol{C} = \boldsymbol{F}^t \cdot \boldsymbol{F} = \boldsymbol{U} \cdot \boldsymbol{U}$.

The hyperelastic–inelastic framework

It is of significant interest to relate the proposed constitutive relations based on a hypoelastic-inelastic response to a generalized dissipative material based on the hyperelastic-inelastic formulation, whose basic concepts originally were proposed in Ref. [1]. As opposed to the hypo-inelastic formulations, the basic idea is to assume the presence of a stored energy function $\psi\left[\bar{\boldsymbol{C}}\right]$, as a function of the elastic (reversible) part of the deformation; It is thereby assumed that the deformation gradient can be considered decomposed multiplicatively into a reversible component $\bar{\boldsymbol{F}}$ and an irreversible component $\boldsymbol{F}_p$ defined as $\boldsymbol{F} = \bar{\boldsymbol{F}} \cdot \boldsymbol{F}_p$, which induce the additive decomposition, in much the same fashion as in Eq. (1), of the spatial velocity gradient $\boldsymbol{l} = \dot{\boldsymbol{F}} \cdot \boldsymbol{F}^{-1}$ as

$$\boldsymbol{l} = \bar{\boldsymbol{l}} + \boldsymbol{l}_p \tag{5}$$

Within the hyperelastic-inelastic framework, the structure of the constitutive relations are based on the second law of thermodynamics specified in the dissipation inequality $\mathcal{D} \geq 0$. More specifically, a thermodynamically consistent model should satisfy the inequality

$$\mathcal{D} = \frac{1}{2}\boldsymbol{S} : \dot{\boldsymbol{C}} - \dot{\psi}\left[\bar{\boldsymbol{C}}, k\right] = \boldsymbol{\tau} : \boldsymbol{l}_p + \kappa \dot{k} \geq 0 \text{ with } \bar{\boldsymbol{S}} = 2\frac{\partial \psi}{\partial \bar{\boldsymbol{C}}} \text{ , } \boldsymbol{\tau} = \bar{\boldsymbol{F}} \cdot \bar{\boldsymbol{S}} \cdot \bar{\boldsymbol{F}}^t \text{ and } \kappa = -\frac{\partial \psi}{\partial k} \tag{6}$$

where $\bar{\boldsymbol{S}}$ is the second Piola–Kirchhoff stress tensor defined on an intermediate configuration, as induced by the multiplicative decomposition. We thus carefully note that the difference between

hypo– and hyperelastic-inelastic formulations is that hyperelastic-inelastic models possess a total stress-strain relation, whereas rate formulated models within the "hypo–framework" generally lack this property.

In order to characterize the consequent tangential response, we introduce the the symmetric *elastic* Oldroyd rate as $\overset{\square}{\bar{\boldsymbol{\tau}}} = \bar{\boldsymbol{F}} \cdot \dot{\bar{\boldsymbol{S}}} \cdot \bar{\boldsymbol{F}}^t$ leading to

$$\overset{\square}{\bar{\boldsymbol{\tau}}} = \dot{\boldsymbol{\tau}} - \bar{\boldsymbol{l}} \cdot \boldsymbol{\tau} - \boldsymbol{\tau} \cdot \bar{\boldsymbol{l}}^t = \boldsymbol{E}_2^e : \bar{\boldsymbol{l}} \text{ with } \boldsymbol{E}_2^e = \left(\bar{\boldsymbol{F}} \bar{\otimes} \bar{\boldsymbol{F}}\right) : \boldsymbol{L}_2^e : \left(\bar{\boldsymbol{F}}^t \bar{\otimes} \bar{\boldsymbol{F}}^t\right) \text{ and } \boldsymbol{L}_2^e = 4 \frac{\partial^2 \psi}{\partial \bar{\boldsymbol{C}} \otimes \partial \bar{\boldsymbol{C}}} \quad (7)$$

where $\boldsymbol{E}_2^e$ is the elastic second Eulerian material tangent operator. It may be noted that within the present framework, cf. Eq. (1), we define $\boldsymbol{l}_p = \lambda \boldsymbol{f}$ whereby $\boldsymbol{f}$ and $\boldsymbol{\tau}$ commute and

$$\overset{\square}{\bar{\boldsymbol{\tau}}} = \boldsymbol{E}_2^e : \bar{\boldsymbol{l}} - 2\lambda \boldsymbol{f} \cdot \boldsymbol{\tau} = \boldsymbol{E}_2^e : \boldsymbol{l} - \left(\boldsymbol{E}_2^e : \boldsymbol{f} + 2\boldsymbol{f} \cdot \boldsymbol{\tau}\right) \lambda \quad (8)$$

Please note that the present framework implies a thermodynamically consistent formulation in the sense that the postulated Oldroyd rate behavior is in line with a dissipative material based on a hyperelasto-viscoplastic formulation along with a multiplicative split of the deformation gradient.

A consistent Johnson-Cook model

In order to compare with the hypoelastic-inelastic formulation, we may propose a simple Neo-Hookean hyperelastic-inelastic extension of the JC–model developed in Subsection , where the explicit expression for the free energy is taken as $\psi = \psi^{iso} + \psi^{vol} + \psi^{mic}$ with, in particular, the special formulation with respect to the thermal behavior, cf. Ref. [2], taken as

$$\psi^{iso} = \frac{1}{2} G \left(\hat{I}_1 - 3\right) \ , \ \psi^{vol} = \frac{1}{2} K \left(\left(\bar{J} - 1\right)^2 - 6\bar{J}\left(\bar{J} - 1\right)\alpha\theta\right) \ , \ \psi^{mic} = \frac{B}{n+1} k^{n+1} \left(1 - \theta^m\right) \quad (9)$$

In (9), $\hat{I}_1$ is the first invariant of the elastic isochoric right Cauchy-Green deformation tensor, i.e. $\hat{I}_1 = \bar{J}^{-\frac{2}{3}} \mathbf{1} : \bar{\boldsymbol{C}}$, and $\bar{J} = J$ represents the volumetric part of the deformation. Hence, in view of (6) the total stress response may be formulated in terms of the Kirchhoff stress as

$$\boldsymbol{\tau} = G \bar{J}^{-\frac{2}{3}} \left(\bar{\boldsymbol{b}} - \frac{\bar{I}_1}{3} \mathbf{1}\right) + K \bar{J} \left(\bar{J}\left(1 - 6\alpha\theta\right) - 1 + 3\alpha\theta\right) \mathbf{1} \quad (10)$$

For the considered hyper–elastic model the reduced dissipation is simply obtained from (6) as

$$\mathcal{D} = \left(\Phi + A\left(1 - \theta^m\right)\right) \lambda \geq 0 \quad (11)$$

We remark that the dissipation $\mathcal{D}$ in (11) is generally different from what traditionally is used for hypo–formulations to describe the dissipated energy converted to heat, i.e. ηw_p, where $w_p = \boldsymbol{\tau} : \boldsymbol{l}_p$ is the plastic work rate and η is an inelastic heat fraction parameter determining the amount of the plastic work rate that is transformed into heat. In (11) this effect is accounted for by the inclusion of the hardening (or amount of "cold work") in $\mathcal{D}$.

Isothermal shear– test of the JC–model with respect to objective stress rates

Let us next consider the constitutive response at a simple shear tests (at room temperature) pertinent to the JC–model along with a calibrated set of material parameters. In the analysis, the constitutive framework is varied based on the hypo-inelastic framework, involving the objective stress rate formulations, and the hyper-inelastic framework (where two models are considered). We expect a slight difference in response depending on which stress rate the rate behavior $\boldsymbol{E}^e : \bar{\boldsymbol{l}}$

(where $\boldsymbol{E}^e$ is the elastic constant stiffness modulus tensor) is postulated with respect to. We thus consider the response of the stress rates formulated as

$$\begin{aligned}
\hat{\boldsymbol{\tau}} &= \boldsymbol{E}^e : \bar{\boldsymbol{l}} && \text{SGN} \\
\overset{\triangledown}{\boldsymbol{\tau}} &= \boldsymbol{E}^e : \bar{\boldsymbol{l}} && \text{SMR} \\
\overset{\square}{\boldsymbol{\tau}} &= \boldsymbol{E}^e : \bar{\boldsymbol{l}} && \text{SOR} \\
\overset{\square}{\boldsymbol{\tau}} &= \underbrace{\boldsymbol{E}^e : \bar{\boldsymbol{l}}}_{\boldsymbol{E}^e_2 : \bar{\boldsymbol{l}}} - 2\lambda \boldsymbol{f} \cdot \boldsymbol{\tau} && \text{SORa}
\end{aligned} \tag{12}$$

As to the Oldroyd stress rate (4b) two alternative choices are considered: The first one is the standard *SOR*–model, where linear elastic response in the Oldroyd stress rate is specified, cf. (4b), whereas for the second *SORa*–model, cf. Eq. (8), the Oldroyd stress rate is consistent with the hyperelastic–inelastic modeling framework.

The results for the simple shear test are shown in Fig. 1, where it is observed that all stress rate formulations yield more or less the same shear stress response. However, a comparison between the other stress components during the shear deformation reveals a spurious normal σ_{11}–stress component for the Oldroyd *SOR* model as depicted in Figure 1. This error in the normal stress component generally leads to an incorrect estimation of stress triaxiality in the material, which in turn is of vital importance for diagnosing ductile fracture in the machining simulations.

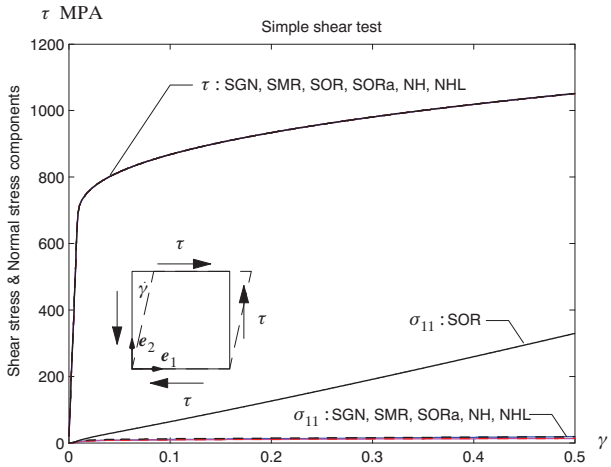

Figure 1. Shear test with respect to different objective stress rates for calibrated material parameters. We have $\dot{\gamma} = 2500$ at room temperature.

References

[1] B. Halphen and Q. S. Nguyen, Sur les materiaux standard generalises, *J. Mecanique*, 14, 39–63, 1975.

[2] M. Fagerström and R. Larsson, A thermo-mechanical cohesive zone formulation for ductile fracture, *Journal of the Mechanics and Physics of Solids*, 56, 3037–3058,2008.

Proceedings of the 24th Nordic Seminar on Computational Mechanics
J. Freund and R. Kouhia (Eds.)

Dispersion analysis of a continuum damage model

Juha Hartikainen[1], Kari Kolari[2], and Reijo Kouhia[1]

(1)Aalto University, Department of Civil and Structural Engineering
PO Box 12100, FI-00076 Aalto, juha.hartikainen@aalto.fi, reijo.kouhia@aalto.fi
(2)VTT Technical Research Center of Finland, PO Box 1000, FI-02044 VTT, kari.kolari@vtt.fi

Summary. A disperison analysis of a scalar continuum damage model is carried out in a uniaxial case.

Key words: continuum damage mechanics, dispersion analysis, phase velocity, group velocity

Introduction

In continuum damage mechanics degradation of elastic properties is described by using a state variable which measures local damage relative to a certain direction. If the orientations of cracks and cavities are assumed to be distributed uniformly in all direction, only a single scalar variable, D is sufficient to describe the damaging process [1, 2]. The stress σ is obtained from

$$\sigma = (1 - D)E\epsilon, \tag{1}$$

where E is the Young's modulus and ϵ is the strain. For convenience the integrity parameter $\beta = 1-D$ is used in the sequel. The evolution of integrity is governed by the Kachanov-Rabotnov type model

$$\dot{\beta} = -\frac{\beta^k}{t_\mathrm{d}} \left(\frac{Y}{Y_\mathrm{r}} \right)^r, \tag{2}$$

where t_d, k and r are material parameters, Y is the thermodynamic force conjugate to the integrity rate $\dot{\beta}$, and has the expression

$$Y = \frac{1}{2}E\epsilon^2 = \frac{1}{2E}\left(\frac{\sigma}{\beta}\right)^2. \tag{3}$$

The reference value Y_r can be chosen freely, here it is defined as $Y_\mathrm{r} = \sigma_\mathrm{r}^2/2E$, where σ_r is an arbitrary reference stress. Usually the value $k = -1$ is chosen in equation (2) [1, 2]. However, in a recent paper [3] it is shown that such a choice will lead to unphysically high wavespeeds for long waves.

Equation of motion

The equation of motion for a uniform bar is

$$\rho\frac{\partial^2 u}{\partial t^2} - \frac{\partial \sigma}{\partial x} = 0, \tag{4}$$

where ρ is the mass density of the material. For the dispersion analysis, the equations (4) and (1)-(2) are written in a non-dimensional form by defining the following non-dimensional

quantities:

$$\tau = t/t_{\mathrm{e}}, \quad t_{\mathrm{e}} = L/c_{\mathrm{e}}, \quad \text{where} \quad c_{\mathrm{e}} = \sqrt{E/\rho}, \tag{5}$$

$$\xi = x/L, \quad \bar{u} = u/L, \quad s = \sigma/\sigma_{\mathrm{r}}, \quad \epsilon_{\mathrm{r}} = \sigma_{\mathrm{r}}/E, \tag{6}$$

where L is a typical characteristic length of the bar, and c_{e} is the speed of an elastic wave. In addition, it is convenient to define the relative strain e and the non-dimensional time parameter τ_{d} as

$$e = \epsilon/\epsilon_{\mathrm{r}}, \qquad \tau_{\mathrm{d}} = t_{\mathrm{d}}/t_{\mathrm{e}}. \tag{7}$$

Using the non-dimensional quantities, the equation of motion (4) takes the form

$$\frac{\partial^2 \bar{u}}{\partial \tau^2} - \epsilon_{\mathrm{r}} \frac{\partial s}{\partial \xi} = 0. \tag{8}$$

The constitutive equations (1)-(2) take the form

$$s = \beta e, \tag{9}$$

$$\frac{\mathrm{d}\beta}{\mathrm{d}\tau} = -{\tau_{\mathrm{d}}}^{-1} \beta^k \left(\frac{Y}{Y_{\mathrm{r}}}\right)^r = -{\tau_{\mathrm{d}}}^{-1} \beta^{k-2r} s^{2r} \equiv g(\beta, s). \tag{10}$$

Dispersion analysis

A continuum is said to be dispersive if waves with different wave length or frequency propagate with different velocities. The ability to transform the shape of waves seems a necessary condition for continua to capture localisation phenomena. In a classical strain-softening solid, the waves are not dispersive, which means that the continuum is not able to transform propagating waves into stationary localisation waves [4]. In the dispersion analysis, a single linear harmonic wave is considered and the displacement field u for an infinitely long 1-D continuum has the form

$$u(x,t) = A \exp\left[i(kx - \omega t)\right], \tag{11}$$

in which k is the wave number, ω is the angular frequency and A is a coefficient. The non-dimensional form of the wave is

$$\bar{u}(\xi,\tau) = \bar{A} \exp[i(\bar{k}\xi - \bar{\omega}\tau)], \quad \text{where} \quad \bar{k} = kL, \quad \text{and} \quad \bar{\omega} = \omega t_{\mathrm{e}}. \tag{12}$$

Linearising the equation of motion (8) at state β_*, s_*, and taking the time derivative w.r.t. the non-dimensional time, results in equation

$$\frac{\partial^3 \bar{u}}{\partial \tau^3} - \epsilon_{\mathrm{r}} \frac{\partial \dot{s}}{\partial \xi} = \frac{\partial^3 \bar{u}}{\partial \tau^3} - \epsilon_{\mathrm{r}} \left(\beta_* \frac{\partial^2 e}{\partial \xi \partial \tau} + e_* \frac{\partial^2 \beta}{\partial \xi \partial \tau}\right) = 0. \tag{13}$$

Divergence of the integrity rate is

$$\frac{\partial^2 \beta}{\partial \tau \partial \xi} = \frac{\partial g}{\partial \beta}|_* \frac{\partial \beta}{\partial \xi} + \frac{\partial g}{\partial s}|_* \frac{\partial s}{\partial \xi} = g_1 \frac{\partial \beta}{\partial \xi} + g_2 {\epsilon_{\mathrm{r}}}^{-1} \frac{\partial^2 \bar{u}}{\partial \tau^2}, \tag{14}$$

where the following abbreviations are used

$$g_1 = \frac{\partial g}{\partial \beta}|_* = -\frac{k-2r}{\tau_{\mathrm{d}}} \beta_*^{k-2r-1} s_*^{2r} \quad \text{and} \quad g_2 = \frac{\partial g}{\partial s}|_* = -\frac{2r}{\tau_{\mathrm{d}}} \beta_*^{k-2r} s_*^{2r-1}. \tag{15}$$

Using the equation of motion (8) $\partial\beta/\partial\xi$ can be eliminated and results in

$$\frac{\partial^3 \bar{u}}{\partial \tau^3} - h_0 \frac{\partial^3 \bar{u}}{\partial \xi^2 \partial \tau} - h_1 \frac{\partial^2 \bar{u}}{\partial \tau^2} + h_2 \frac{\partial^2 \bar{u}}{\partial \xi^2} = 0, \tag{16}$$

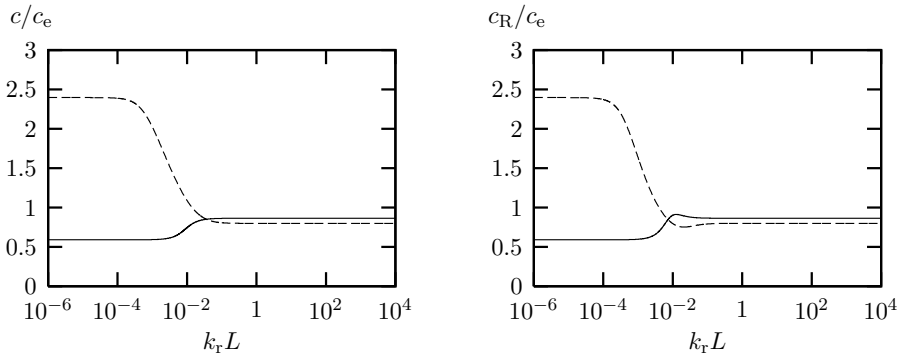

Figure 1. Elastic damaging bar: phase (l.h.s.) and group velocity (r.h.s.) as a function of wavenumber at the strain value $e = 1.2$. Solid line corresponds to the case $k = 1$ and the dashed line $k = -1$, respectively.

where

$$h_0 = \beta_*, \tag{17}$$

$$h_1 = g_1 + s_*\beta_*^{-1}g_2 = -\frac{k}{\tau_d}\beta_*^{k-2r-1}s_*^{2r}, \tag{18}$$

$$h_2 = \beta_* g_1 = -\frac{k-2r}{\tau_d}\beta_*^{k-2r}s_*^{2r}. \tag{19}$$

Substituting the expression for harmonic wave (11) into (16), yields an equation which only can be satisfied if the wavenumber is complex, i.e. $\bar{k} = \bar{k}_r + \bar{\alpha}i$, which means that the harmonic wave is attenuated exponentially when traversing through the bar as

$$\bar{u}(\xi,\tau) = \bar{A}\exp(-\bar{\alpha}\xi)\exp[i(\bar{k}_r\xi - \bar{\omega}\tau)]. \tag{20}$$

This will result in the dispersion relation

$$i\left[\bar{\omega}^3 - h_0\bar{\omega}(\bar{k}_r^2 - \bar{\alpha}^2) - 2h_2\bar{k}_r\bar{\alpha}\right] + 2h_0\bar{\omega}\bar{k}_r\bar{\alpha} + h_1\bar{\omega}^2 - h_2(\bar{k}_r^2 - \bar{\alpha}^2) = 0. \tag{21}$$

Since both the real and imaginary part of this expression has to vanish, it will result in two equations from which the wavenumber $\bar{k}_r$ and the damping coefficient $\bar{\alpha}$ can be solved. After manipulations, resulting equations are

$$\bar{k}_r{}^4 - a_1\bar{k}_r^2 - a_0^2\bar{\omega}^2 = 0, \quad \bar{\alpha} = a_0\bar{\omega}/\bar{k}_r, \tag{22}$$

where

$$a_0 = \frac{(h_2 - h_0h_1)\bar{\omega}^2}{2(h_0^2\bar{\omega}^2 + h_2^2)}, \qquad h_2 - h_0h_1 = \frac{2r}{\tau_d}\beta_*^{k-2r}s_*^{2r}, \tag{23}$$

$$a_1 = h_0^{-1}(\bar{\omega}^2 - 2h_2a_0). \tag{24}$$

Clearly the term a_0 is positive, but the sign of the term a_1 depends on the state. Thus, the solution of (22) can be written as

$$\bar{k}_r^2 = \tfrac{1}{2}|a_1|\left(\sqrt{1 + 4(a_0/a_1)^2} + \mathrm{sign}(a_1)\right), \quad a_1 \neq 0. \tag{25}$$

The group and phase velocities c_R and c, respectively, are defined as

$$c_R = \frac{d\omega}{dk_r} = c_e\frac{d\bar{\omega}}{d\bar{k}_r} \quad \text{and} \quad c = \frac{\omega}{k_r} = c_e\frac{\bar{\omega}}{\bar{k}_r}, \tag{26}$$

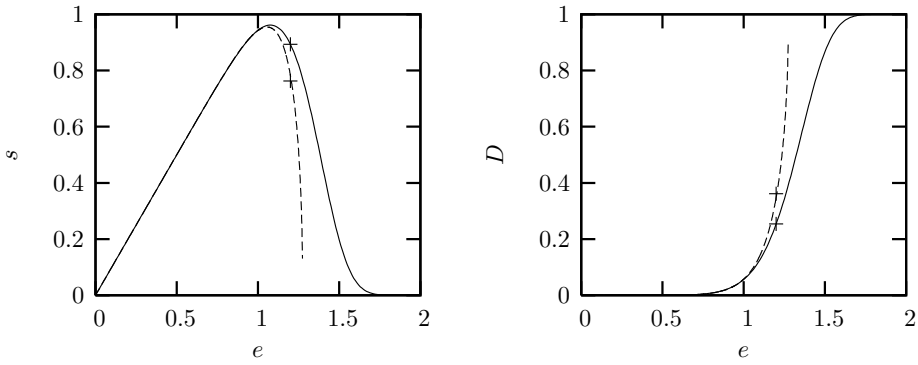

Figure 2. Elastic damaging bar: stress-strain (l.h.s.) and damage-strain (r.h.s.) curves. Solid line corresponds to the case $k = 1$ and the dashed line $k = -1$, respectively.

and they are shown as a function of the wavenumber in fig. 1 for a constant strain rate loading case at a post-peak state. In the figure, the following values are used: $E = 40$ GPa, $\sigma_{\mathrm{r}} = 20$ MPa, $t_{\mathrm{d}} = 1$ s, $r = 4$, and the loading rate is 10^{-3} s^{-1}. The stress-strain curves and the damage evolution are plotted in fig. 2.

Notice that the group velocity is now larger than the phase velocity for the case $k = 1$, a situation which is referred to as anomalous dispersion ([5], p. 218). For $k = -1$ the elastic damaging bar exhibits normal dispersion, i.e. $c_{\mathrm{R}} < c$. It is clearly seen that for the case $k = -1$ the phase velocity exceeds the elastic wavespeed for long waves, but for the case $k = 1$ the phase velocity is below the speeed of an elastic wave for all wavelengths.

Concluding remarks

A dispersion analysis of a Kachanov-Rabotnov type damage evolution equation is given. It is observed that the most used form of the evolution equation ($k = -1$) will result in unphysically high wavespeeds for long waves. An alternative form of the damage evolution equation is given which also has a desirable feature of limited damage growth ($k \geq 1$). In a further study the complete strain-rate dependent ductile-to-brittle constitutive model [6, 7] will be analysed.

References

[1] J. Lemaitre, J.-L. Chaboche. *Mechanics of solid materials*, Cambridge University Press, 1990.

[2] J. Lemaitre. *A course on damage mechanics*, Springer-Verlag, Berlin, 1992.

[3] H. Askes, J. Hartikainen, K. Kolari, R. Kouhia. Dispersion analysis of a strain-rate dependent ductile-to-brittle transition model. *Proceedings of the 10th Finnish Mechanics Days*, 3-4.12.2009, Jyväskylä, Finland R. Mäkinen, P. Neittaanmäki, T. Tuovinen and K. Valpe (eds.), pp. 478–489.

[4] L.J. Sluys. *Wawe propagation, localisation and dispersion in softening solids*, PhD thesis, Department of Civil Engineering, Delft University of Technology, 1992.

[5] J.D. Achenbach. *Wave propagation in elastic solids*. North-Holland series in applied mathematics and mechanics, Vol 16, 1973.

[6] S. Fortino, J. Hartikainen, K. Kolari, R. Kouhia and T. Manninen. A constitutive model for strain-rate dependent ductile-to-brittle transition. *The IX Finnish Mechanics Days*, 13-14.6.2006, Lappeenranta, Finland R. von Hertzen and T. Halme (eds.), pp. 652–662.

[7] J. Hartikainen, K. Kolari and R. Kouhia. A constitutive model for strain-rate dependent ductile-to-brittle transition. *Proceedings of the 23rd Nordic Seminar on Computational Mechanics*, KTH Stockholm, Sweden, A. Eriksson and G. Tibert (eds.), pp. 38–41.

Proceedings of the 24th Nordic Seminar on Computational Mechanics
J. Freund and R. Kouhia (Eds.)

Computational modeling of case II diffusion in polymeric materials

Swantje Bargmann[1], Andrew McBride[2] and Paul Steinmann[2]

(1)Institute of Mechanics, University of Dortmund, Germany
swantje.bargmann@tu-dortmund.de
(2)Chair of Applied Mechanics, University of Erlangen-Nuremberg, Germany
andrew.mcbride@ltm.uni-erlangen.de, paul.steinmann@ltm.uni-erlangen.de

Summary. Case II type diffusion can occur when a low molecular weight solvent is exposed to the surface of a polymeric solid. The diffusion of the solvent within the polymer causes the polymer to swell significantly. Furthermore, the polymer undergoes a glass-to-rubber type transition. The rate at which the solvent diffuses within the polymer is dependent upon the relaxation state of the polymer. This contribution discusses the computational modeling of the case II phenomenon. The geometrically nonlinear case is considered. The general framework is introduced by considering the problem of coupled deformation, heat conduction and species diffusion.

Key words: continuum mechanics, case II, diffusion, coupled problems, multiphysics

Case II diffusion in polymers

The problem of interest is the diffusion of a solvent within a polymeric solid. Classical diffusion (also termed Fickian diffusion) is characterized by a process wherein the solid material undergoes negligible rearrangement due to the presence of the diffusing solvent, or indeed where the molecular rearrangements within the polymer happen so fast as to be instantaneous from the perspective of the diffusing species. Fick's first law, with its assumption that the diffusive flux is proportional to the gradient of the concentration, proves adequate to describe a broad range of diffusion processes.

The diffusion of a low-molecular weight solvent within a glassy polymeric solid can exhibit significant deviations from classical Fickian diffusion. When a solvent penetrates the polymer near the glass transition temperature, three main phenomena occur: (1) The transport of the solvent follows a non-classical law until a characteristic time t_c. After t_c the usual Fickian behavior takes over and Fick's law is valid. (2) A sharp moving front divides the polymer into two regions. Ahead of the front the polymer is still glassy due to a low solvent concentration. Behind the front, under the action of the solvent, the glassy state is undone and plasticization occurs. (3) Macroscopic elastic stresses between plasticized and glassy regions develop and eventually decay as the sample reaches equilibrium. In particular, the inner rigid glassy regions constrain the swelling of the outer plasticized portion. Case II diffusion is classified as a traveling wave (or S-shape) form of the probability density (concentration) profiles with a straight line form of the isotherm sorption curve for early times of the process. It differs significantly from classical Fickian diffusion and is usually studied in experiments of sorption and permeation of low molecular weight species in thin polymeric membranes. This non-classical type of diffusion was coined case II diffusion by Alfrey, Gurnee and Lloyd (1966) who were the first to document it.

The classical equations governing Fickian diffusion are parabolic and ignore the influence of external stresses on the diffusion process. These two shortcomings are essential to address in order to accurately predict the coupled diffusion–deformation processes that occur in case II diffusion. Typical industrial applications can be found in e.g. pharmaceutical, biological, environmental or automotive fields. Such possible applications include the removal of solvent from polymer solutions during dry spinning, microlithography, diffusional release of pollutants and additives from polymers into the environment, controlled release of agricultural chemicals, film casting and coating, development of photoresists, neurotransmitters transport, or controlled-release drug delivery devices, for example.

The objective of this contribution is to provide an overview of non-Fickian case II type diffusion and its computational modeling. The mathematical model rigorously accounts for the complex, non-linear coupled interactions between the polymeric solid and the diffusing solvent. Moreover, it is derived from thermodynamic principles and presented within the framework of non-linear continuum mechanics. The multiphysics problem considers deformation, diffusion and heat conduction. This leads to a highly nonlinear and coupled system of equations which requires a robust solution algorithm. The numerical implementation of the model is done within the context of the finite element method.

References

[1] T. Alfrey, E. F. Gurnee, W. G. Lloyd, *Diffusion in glassy polymers.* Journal of Polymer Science Part C, 12, 249–261, 1966

[2] S. Bargmann, A.T. McBride, P. Steinmann, *Models of solvent penetration in glassy polymers with an emphasis on case II diffusion. A comparative review.* Applied Mechanics Reviews, accepted for publication, DOI: 10.1115/1.4003955, 2011

[3] A. Fick, *On liquid diffusion.* Philosophical Magazine, 10, 30–39, 1855

[4] A.T. McBride, S. Bargmann, P. Steinmann *Geometrically nonlinear continuum thermomechanics coupled to diffusion: a framework for case II diffusion.* Advances in Extended and Multifield Theories for Continua, Springer, accepted for publication, 2011

[5] A.T. McBride, A. Javili, P. Steinmann, S. Bargmann *Geometrically nonlinear continuum thermomechanics with surface energies coupled to diffusion.* Journal of the Mechanics and Physics of Solids, doi:10.1016/j.jmps.2011.06.002, accepted for publication, 2011

[6] P. Steinmann, A.T. McBride, S. Bargmann, A. Javili *A deformational and configurational framework for geometrically nonlinear continuum thermomechanics coupled to diffusion.* International Journal of Non-Linear Mechanics, accepted for publication, doi:10.1016/j.ijnonlinmec.2011.05.009, 2011

Proceedings of the 24th Nordic Seminar on Computational Mechanics
J. Freund and R. Kouhia (Eds.)

A DAE approach for solving the elasto-plastic boundary value problem

Mathias Wallin and Eric Borgqvist

Solid Mechanics, Lund University, Box 118, 221 00 Lund, Sweden
Mathias.Wallin@solid.lth.se, Eric.Borgqvist@solid.lth.se

Summary. In this study an alternative integration scheme for elasto-plasticity based on a Diagonal Implicit Runge-Kutta (DIRK) scheme originally proposed by Ellsiepen (1999) is investigated. In contrast to clasical approaches, the DIRK scheme is applied to the balance of momentum as well as the constitutive evolution equations. The presented numerical algorithm is applied to an elasto-plastic bounadry value problem and the examples reveal that a significant increase in accuracy can be obtained at virtually no cost using the DIRK scheme.

Key words: elasto-plasticity, numerical integration

Introduction

The elasto-plastic boundary value problem is governed by balance of momentum and constitutive evolution equations that control the material response locally. Since explicit algorithms are restricted to relativly short loading duration, implict algorithms are frequently employed. The size of the time steps taken in the implicit algorithms are typically based on a heuristic rule which is not related to the accuracy of the elasto-plastic boundary value problem.

The canonical numerical method for performing the integration of the constitutive laws was proposed by Wilkins (1964) and is based on a backward Euler approximation of the evolution equations in combination with enforcement of the yield condition at the end of the integration interval. The Wilkin's method or the radial-return method are considered as being independent of the balance of momentum. However, in Fritzen (1997) the elasto-plastic boundary value problem was identified as being a set of differential algebraic equations (DAE). In Ellsiepen and Hartmann (2001) it was shown that the low-order embedded Diagonally Implicit Runge-Kutta (DIRK) schemes (e.g. Ellsiepen (1999)) together with the multi-level Newton-Raphson algorithm is particular suitable for solving elasto-plastic boundary value problems. This class of methods preserve the sparsity present in the canonical implicit solution procedure and it has also proven to have superior accuracy over the classical implicit solution procedure. Moreover, since the method is embedded it provides an error estimation of the local error which enables an efficient step-length control. The method has previously been successfully applied to: visco-plasticity small strains (Ellsiepen and Hartmann (2001)); finite strain viscoelasticity (Hartmann (2002)); metal powder plasticity (Hartmann and Bier (2008)) and incompressible materials (Hartmann *et al.* (2008)).

In the present work the numerical sensitivity of the classical damage evolution law proposed by Lemaitre (1985) will be compared to the damage evolution law proposed by Bonora (1997). In contrast to the Lemaitre model, the Bonora model involves a threshold for the damage evolution. This threshold poses a problem for both integration schemes and it is of particular interest to investigate the performance of the DIRK scheme for this model. To evaluate the performance of the numerical schemes and models use will be made of structural iso-error plots where the accuracy of the entire boundary value problem is evaluated. This contrasts many previous studies where iso-error plots have been used to illustrate the accuracy of the constitutive equations only.

Problem formulation

The balance of linear momentum is governed by the (static) principle of virtual work in the reference configuration, Ω_0, i.e.

$$\boldsymbol{R} = \int_{\partial\Omega_{0t}} \delta\boldsymbol{w} \cdot \boldsymbol{T} dS + \int_{\Omega_0} \delta\boldsymbol{w} \cdot \boldsymbol{b} dV = \int_{\Omega_0} \delta\boldsymbol{E} : \boldsymbol{S} dV \quad \forall \delta\boldsymbol{w} \tag{1}$$

where $\boldsymbol{T}$ and $\boldsymbol{b}$ are the traction and body force vector. The second Piola-Kirchhoff stress and the virtual strain are denoted $\boldsymbol{S}$ and $\delta\boldsymbol{E}$. For a general class of elasto-plastic constitutive models the irreversible evolution equation can be formulated as

$$\dot{\boldsymbol{z}} = \lambda \boldsymbol{N}. \tag{2}$$

where, λ, is the magnitude of the plastic increment. The internal state variables, $\boldsymbol{z}$ can for instance represent plastic strains, backstress and damage variables. The generalized plastic flow direction is a function of the internal variable $\boldsymbol{z}$ and current displacement field, i.e. $\boldsymbol{N} = \boldsymbol{N}(\boldsymbol{z}, \boldsymbol{u})$. For rate-independent plasticity the yield condition, $f = 0$, will serve as an algebraic constraint equation that sets the magnitude of λ.

Solution procedures

A spatial discreteization using the Finite-Element method of the system (1) and (2) results in

$$\begin{aligned} \boldsymbol{R} &= \boldsymbol{R}(\boldsymbol{a}, \boldsymbol{z}^\alpha, t) = \boldsymbol{0} \\ \dot{\boldsymbol{z}}^\alpha &= \dot{\lambda}^\alpha \boldsymbol{N}^\alpha(\boldsymbol{z}^\alpha, \boldsymbol{a}) \\ f(\boldsymbol{z}^\alpha, \boldsymbol{a}) &= 0 \end{aligned} \tag{3}$$

where the superscript $\alpha = 1..N_{gp}$ where N_{gp} represents the number of gausspoints. Moreover, in the following discussion, we will collect the state-variables and displacement field, $\boldsymbol{u}$ in a state vector, i.e. $\boldsymbol{y} = \{\boldsymbol{z}^\alpha,\ \boldsymbol{a}\}$ where $\boldsymbol{a}$ represents the nodal displacements.

In the present approach a DIRK scheme will be applied to the boundary value problem (3). The solution to an intial value problem in a DIRK scheme is obtained as

$$\boldsymbol{y}(t_{n+1}) \approx \boldsymbol{y}_{n+1} = \boldsymbol{y}_n + \Delta t_n \sum_{i=1}^{s} b_i \boldsymbol{f}(t + c_i \Delta t_n, \boldsymbol{y}(t_n + c_i \Delta t_n)) \tag{4}$$

where b_i are weight factors and c_i coefficients that determine the location of the quadrature points, stages. The number of stages is denoted s are defined by $T_{ni} = t_n + c_i \Delta t$. To evaluate

(4) the stage values $\boldsymbol{y}(t_n + c_i\Delta t_n)$ are required. The stage values are approximated in a manner similar to (4), i.e.

$$\boldsymbol{y}(t_n + c_i\Delta t_n) \approx \boldsymbol{Y}_{ni} = \boldsymbol{y}(t_n) + \Delta t_n \sum_{j=1}^{s} a_{ij}\dot{\boldsymbol{Y}}_{nj} \tag{5}$$

where a new set of weighting factors a_{ij} were introduced. The stage derivatives, $\dot{\boldsymbol{Y}}_{nj}$, present in (5) are defined as

$$\dot{\boldsymbol{Y}}_{nj} = \boldsymbol{f}(T_{nj}, \boldsymbol{Y}_{nj}) \tag{6}$$

Note that the quadrature points T_{nj} in (6) coincides with the quadrature points in (4). Insertion of (6) into (5) results in a non-linear system in the stage variables $\boldsymbol{Y}_{ni}$, i.e. $\boldsymbol{r}(\boldsymbol{Y}_{n1}, \boldsymbol{Y}_{n2}, ..., \boldsymbol{Y}_{ns}) = \boldsymbol{0}$. This system can be solved for the stage variables $\boldsymbol{Y}_{n1}$, $\boldsymbol{Y}_{n2}$, ...,$\boldsymbol{Y}_{ns}$ and once the stage variables are calculated the updated state $\boldsymbol{y}_{n+1}$ can be calculated using (4). The DIRK scheme employed in the present study is given by the Butcher tableau 1. Besides being an efficient higher order integration scheme the DIRK scheme also provides an error control which can be used to determine a suitable time step. Assume that $\hat{\boldsymbol{y}}_{n+1}$ is the solution at t_{n+1} from a RK-method of order q and that $\boldsymbol{y}_{n+1}$ is the solution from a RK-method of order $q+1$. Subtracting $\boldsymbol{y}_{n+1}$ from $\hat{\boldsymbol{y}}_{n+1}$ provides an estimate for the local integration error, i.e.

Table 1. Butcher tableau for the two stage DIRK-method proposed by Ellsiepen (1999).

γ	γ	
1	$1-\gamma$	γ
	$1-\gamma$	γ
	$1-\hat{\gamma}$	$\hat{\gamma}$

$\gamma = 1 - \frac{1}{2}\sqrt{2}$

$\hat{\gamma} = 2 - \frac{5}{4}\sqrt{2}$

$$\boldsymbol{\kappa} = \hat{\boldsymbol{y}}_{n+1} - \boldsymbol{y}_{n+1} \tag{7}$$

The error estimation $\boldsymbol{\kappa}$ can be determined at virtually no extra cost using an embedded Runge Kutta method since $\hat{\boldsymbol{y}}_{n+1}$ is calculated using the same stages as for the lower order method $\boldsymbol{y}_{n+1}$. For Ellsiepen's method the b_i coefficients for the embedded method given in the last row of the tableau Tab 1. The error estimation for an embedded scheme is given by

$$\boldsymbol{\kappa} = \Delta t_n \sum_{i=1}^{s} (\hat{b}_i - b_i)\dot{\boldsymbol{Y}}_{ni}. \tag{8}$$

Numerical examples

To investigate the numerical sensitivity of the constitutive model in conjunction with the presented numerical integration scheme the boundary value problem depicted in Fig. 1a will be considered. Referring to Fig. 1b and Fig. 1c it can be concluded that the RK-based integration schemes shows significant higher accuracy than the IE based integration scheme; the error is approximately one magnitude lower than the IE based scheme. It is also emphasized that the computational cost is almost identical for the simulations shown in Fig. 1a and Fig. 1b.

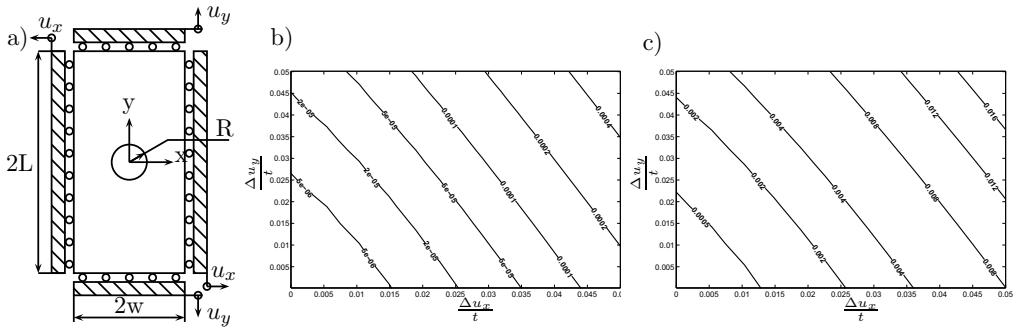

Figure 1. a) Illustration of the boundary value problem used in the numerical simulation. b) Iso-error (in isotropic damage) plot using the Runge Kutta b) Iso-error plot (in isotropic damage) using the Implicit Euler method.

References

Bonora, N. (1997). A non-linear CDM model for ductile failure. *Engineering Fracture Mechanics*, **58**, 11–28.

Ellsiepen, P. (1999). *Zeit- und ortsadaptive Verfahren angewandt auf Mehrphasenprobleme poröser Medien*. Ph.D. thesis, University of Stuttgart, Stuttgart, Germany.

Fritzen, P. (1997). *Numerische Behandlung nichtlinearer Probleme der Elastizitäts- und Plastizitätstheorie*. Ph.D. thesis, Universty of Darmstadt, Darmstadt, Germany.

Lemaitre, J. (1985). A continuous damage mechanics model for ductile failure. *Journal of Engng. Mat. and Tech.*, **107**, 83–89.

Wilkins, M. L. (1964). Calculation of elasto-plastic flow. In *Methods of Computational Physics 3* ,eds., B. Alder et. al. Academic Press, New York.

Hartmann, S. (2002). Computation in finite-strain viscoelasticity: Finite elements based on the interpretation as differential-algebraic equations. *Comput. Methods Appl. Mech. Engrg*, **191**, 1439–1470.

Hartmann, S. and Bier, W. (2008). High-order time integration applied to metal powder plasticity. *International Journal of Plasticity*, **24**, 17–54.

Hartmann, S., Quint, K. J., and Arnold, M. (2008). On plastic incompressibility within time-adaptive finite elements combined with projection techniques. *Comput. Methods Appl. Mech. Engng.*, **198**, 178–193.

Ellsiepen, P. and Hartmann, S. (2001). Remarks on the interpretation of current non-linear finite element analyses as differential equations. *International Journal for Numerical Methods in Engineering*, **51**, 679–707.

Proceedings of the 24th Nordic Seminar on Computational Mechanics
J. Freund and R. Kouhia (Eds.)

System modeling for delamination detection using support vector machines and neural networks

Ljubov Feklistova and Helle Hein

Institute of Computer Science, University of Tartu
Liivi 2, 50409 Tartu, Estonia, ljubov.feklistova@ut.ee, helle.hein@ut.ee

Summary. Delamination detection in the supporting structures is an important issue in contemporary engineering in terms of reliability and consistency of the structure. Many modern sensors are based on piezoelectric effect or acoustic emission which may cause by-effects. The aim of the present paper is to develop a complex approach for delamination detection in homogeneous and composite beams using Euler-Bernoulli theory of bending, support vector machines (SVM) and artificial neural networks (ANN). The significance of the proposed add-in system lies in its ability to make fast accurate calculation. The applicability of the method has been tested by numerical experiments in the Matlab environment.

Key words: free vibrations, Euler-Bernoulli beam theory, delamination, support vector machines, neural networks.

Introduction

Structural health monitoring (SHM) is one of the actual topics in contemporary engineering such as aviation, material science, geodesy, metallurgy, etc. SHM detects damage or structural faults at an early stage (manufacturing phase) before they reach a crucial level or cause significant economical losses. Nowadays, monitoring is carried out using actuators or damage detection sensors. Modern sensitive systems are based on piezoelectric effect, acoustic emission, etc. [1, 2, 3]. Pressure, force and strain can be measured quite precisely. However, the techniques are not risk-free: voltage unbalance degrades motor efficiency, causes rotor losses, increases temperature [4]; emerging electrical field or resonance cause occasionally structural damage to the surface [3, 5].

According to Baccarini, Silva, et al. [4] and P. Konar, P. Chattopadhyay [6], machine vibration is the best indicator of the structure's overall technical condition, and it can be used as one of the first indicators of emerging defects. The authors asserted that each mechanical fault, including delamination, generates vibrations in its own specific frequency domain [6].

This paper focuses on the calculations of delamination in homogeneous and composite beams using the vibration-based damage detection methods and real-time measured structural response signals viz a mode shape and a modal frequency. In order to improve conventional methods for delamination detection, the presented complex method is combined of the support vector machines and neural networks. The paper is divided into five sections. Section two describes dynamic responses of vibrating beams. Section three provides an overview of support vector machines and selection of the most informative patterns from a data set. Section four introduces the complex technique for delamination calculation. Various numerical examples are presented in section five.

Dynamic response of vibrating beams with delaminations

A vibrating system with n delaminations can be considered as a combination of $3n + 1$ beam sections, connected at the delamination boundaries. Each section can be treated as a classical Euler-Bernoulli beam model with a constrained mode, rigid connector and bending-extension coupling [7]. The governing equation for the intact beam sections is

$$D_i \frac{d^4 w_i}{dx^4} + \rho_i A_i \frac{d^2 w_i}{dt^2} = 0, \tag{1}$$

where i=1,...,3n+1; $w_i(x,t)$ is the vertical displacement of the i-th beam section; D_i is the bending stiffness; ρ_i is the density of material; A_i is the cross-sectional area; x is the axial coordinate and t is the time [8].

Integration of support vector machine

A vibrating system with a delamination is a non-linear system. Therefore, it is difficult to establish a firm relationship between the frequencies and size/location of the delamination. In this paper, the SVM is used to model the non-linear dynamics of a vibrating beam with a delamination.

The SVM is a relatively new and powerful tool for pattern classification and regression based on statistical learning theory [4]. It is capable of mapping non-linear functions quite efficiently [9]. The main idea of SVM can be described as follows. The SVM attempts to put separating hyperplane with maximum margin between the data points in the feature space so that generalization is performed with the least error and the data is divided into two classes: "positive" $(+1)$ and "negative" (-1) [9]. The latter concept can be extended to multi-class problems, too. The nearest points that are used to define the margin are called support vectors and they define the classifier. The hyperplane itself is oriented in such a way that the distance between the hyperplane and the support vectors in each class is maximal.

Consider a sample training set (x_i, y_i), where $x_i \in \mathbb{R}^n$ is the training data, $y_i \in \{-1, 1\}$ is the class of labels for $x_i, ..., x_N$ (N is the total number of samples). The hyperplane $f(x) = 0$ that separates the data into two classes is a solution to the convex quadratic optimization problem:

$$\begin{aligned} &\textit{Minimize } \frac{1}{2}||w||^2 \\ &\textit{Subject to } y_i(w^T x_i + b) > 1, i = 1, ..., N, \end{aligned} \tag{2}$$

where w is the orientation vector and b is the location parameter, respectively. Once the algorithm is trained, it can be tested with new data points. For any new set of data, SVM uses w and b to predict the class it should belong to.

If data to be classified is non-linearly separable, it is mapped onto a high-dimensional feature space, where the linear classification is possible. A more detail description of SVM can be found in [10].

Modeling system

In the present research paper on the delamination detection in vibrating systems, the focus is placed on useful data selection by SVM before the patterns are fed into ANNs. Therethrough, the risks of ANN overtraining are reduced and ANN are trained by the most informative patterns.

The complex approach includes the following steps. The modal frequencies of a vibrating beam are computed in the Matlab environment. The obtained data is used for training SVMs. Using quadratic or Gaussian radial basis functions, SVM divides the data into two groups: the patterns that belong to the central part of the vibrating system and to its ends. According to the group, two ANNs with different architectures are created and trained by the appropriate

Table 1. Delamination prediction (height and distance) in a homogeneous clamped-clamped beam.

Exact location of delamination		Predictions without SVM			Predictions with SVM		
Height	Distance	Height	Distance	R^2	Height	Distance	R^2
0.2000	0.0500	0.1983	0.0501	0.9999	0.1988	0.0502	1.0000
0.5000	0.0500	0.4030	0.0504	0.8278	0.4969	0.0505	0.9998
0.3200	0.1100	0.3264	0.1102	0.9051	0.3183	0.1024	0.9957
0.4400	0.1400	0.4420	0.1417	0.9997	0.4419	0.1401	0.9998
0.1700	0.2300	0.1696	0.2291	0.9975	0.1703	0.2303	0.9996
0.4700	0.2600	0.4702	0.2613	0.9972	0.4692	0.2602	0.9999
0.2000	0.3200	0.1986	0.3200	0.9999	0.1990	0.3196	1.0000
0.2600	0.3500	0.2710	0.3501	0.9892	0.2607	0.3497	1.0000
0.5000	0.4100	0.5027	0.4088	0.9998	0.4955	0.4092	0.9996
0.3800	0.5000	0.3651	0.5054	0.9457	0.3846	0.4988	0.9920

patterns using different learning algorithms (Levenberg-Marquardt, Bayesian). Once the system is trained, it is ready for testing. When a frequency signal is received from the sensor, it is first processed by SVM and then loaded into the appropriate ANN in order to detect the location and/or size of the delamination.

Numerical simulations

First, the suggested approach for delamination detection was applied to the homogeneous beam with clamped-clamped ends and a delamination of 0.2 unit length. The SVM was trained by quadratic kernel function and divided a set of training data of 246 patterns into two groups: 196 patterns for the central part and 50 patterns specific to the ends. Each training pattern contained six frequencies. Two ANNs were trained by the corresponding set and predicted the location of the delamination: the height and the distance from the left end to the delamination. Table 1 shows the results of predictions with and without using the SVM. A coefficient of multiple determination R^2 shows the closeness of fit. Ideally, R^2 is equal to 1. In the table, it is seen that the complex approach is noticeably more accurate at the calculation of the delamination at the ends of the beam than the alternative method.

Secondly, the proposed method was examined on a composite beam: $T300/934$ graphite/epoxy beam with a $[0^0/90^0]_{2s}$ stacking sequence. The dimensions of the 8-ply beam are $127\times12.7\times1.016$ mm^3. The material properties for the lamina are $E_{11} = 134$ GPa; $E_{22} = 10.3$ GPa; $G_{12} = 5$ GPa; $\nu_{12} = 0.33$ and $\rho = 1.48 \times 103$ kg/m^3. The SVM and ANNs computed the length of the delamination in the mid-plane. Table 2 shows the results of the predictions by the complex approach and by the alternative method without SVM. The suggested technique is more accurate. This is explained by the selection of the training patterns by SVM.

Concluding remarks

The main objective of this work was to develop a complex method for delamination detection in vibrating systems using SVMs and ANNs. The frequency based training patterns were obtained computationally in the Matlab environment since delamination influences significantly the frequency domain of vibrating systems. The signals were classified by SVM into two classes: if the delamination occurred near the edges of the system or in the central part. Next, the patterns were fed into ANNs in order to compute the location/size of the delamination. The proposed approach came up with very good results using only one SVM classification procedure and two

Table 2. Delamination length prediction in a composite clamped-clamped beam.

Exact length of delamination	Predictions without SVM		Predictions with SVM	
Length	Length	R^2	Length	R^2
0.0066	0.0056	0.9999	0.0066	1.0000
0.0090	0.0081	0.9999	0.0090	1.0000
0.0410	0.0403	0.9999	0.0410	1.0000
0.0610	0.0612	1.0000	0.0610	1.0000
0.0802	0.0806	0.9999	0.0802	1.0000
0.1378	0.1373	0.9973	0.1379	0.9999
0.1642	0.1643	1.0000	0.1643	1.0000
0.2122	0.2104	0.9995	0.2120	1.0000
0.2546	0.2529	0.9998	0.2542	1.0000
0.3217	0.3216	1.0000	0.3220	1.0000

ANNs, and therefore it might be attractive for online monitoring.

Acknowledgement

Financial support from the Estonian Science Foundation under Grant ETF 8830 is gratefully acknowledged.

References

[1] I. Payo and J. Hale. Sensitivity analysis of piezoelectric paint sensors made up of PZT ceramic powder and water-based acrylic polymer. *Sensors and Actuators A: Physical*, 18(1):77–89,2011.

[2] R. Lya, M. Rguitia, S. D'Astorga, A. Hajjajic, C. Courtoisa, A. Lerichea. Modeling and characterization of piezoelectric cantilever bending sensor for energy harvesting. *Sensors and Actuators A: Physical*, 168(1):95–100,2011.

[3] R. Teti, K. Jemielniak, G. O'Donnell, D. Dornfeld. Advanced monitoring of machining operations. *CIRP Annals - Manufacturing Technology*, 59(2):717–739,2010.

[4] L. Baccarini, V. Silva, B. Menezes, W. Caminhas. SVM practical industrial application for mechanical faults diagnostic. *Expert Systems with Applications*, 38(6):6980–6984,2011.

[5] N. Fiscoa, H. Adeli. Smart structures: Part II - Hybrid control systems and control strategies. *Scientia Iranica*, 18(3):285–295,2011.

[6] P. Konar and P. Chattopadhyay. Bearing fault detection of induction motor using wavelet and Support Vector Machines (SVMs). *Applied Soft Computing*, 11(6):4203–4211,2011.

[7] P.M. Mujumdar, S. Suryanarayan. Flexural vibrations of beams with delaminations. textitJournal of Sound and Vibration, 125:441–461,1988.

[8] H. Hein, L. Feklistova. Computationally efficient delamination detection in composite beams using Haar wavelets. *Mechanical Systems and Signal Processing*, 25(6),2257–2270,2011.

[9] K. Salahshoor, M. Kordestani, M. Khoshro. Fault detection and diagnosis of an industrial steam turbine using fusion of SVM (support vector machine) and ANFIS (adaptive neuro-fuzzy inference system) classifiers. *Energy*, 35(12):5472–5482,2010.

[10] Vapnik, V. N. *The nature of statistical learning theory*. Springer, Berlin, 1995.

Proceedings of the 24th Nordic Seminar on Computational Mechanics
J. Freund and R. Kouhia (Eds.)

Artificial neural networks for nonlinear dynamic response simulation in mechanical systems

Niels H. Christiansen[1,2], Jan Høgsberg[1], and Ole Winther[3]

(1)Department of Mechanical Engineering, Technical University of Denmark, Kgs. Lyngby, Denmark, e-mail: Niels.Christiansen@dnv.com
(2)DNV Denmark, Hellerup, Denmark
(3)Department of Informatics and Mathematical Modeling, Technical University of Denmark, Kgs. Lyngby, Denmark

Summary. It is shown how artificial neural networks can be trained to predict dynamic response of a simple nonlinear structure. Data generated using a nonlinear finite element model of a simplified wind turbine is used to train a one layer artificial neural network. When trained properly the network is able to perform accurate response prediction much faster than the corresponding finite element model. Initial result indicate a reduction in cpu time by two orders of magnitude.

Key words: Nonlinear structural dynamics, Artificial neural networks.

Introduction

Time domain simulation of nonlinear systems using finite element method (FEM) analysis can be computationally very expensive - especially in fatigue calculations where long response histories are needed in order to obtain reliable time series statistics. The use of artificial neural networks (ANN) combined with classical methods have shown promising results in reducing this computational cost [1]. This paper presents a hybrid method for simulation of dynamic response of a simple nonlinear structure. It is shown how an ANN can be trained to predict dynamic response of a simplified model of a wind turbine. FEM models of nonlinear structures often require fine element mesh discretization, small time step size and iterative procedures in order to obtain equilibrium between internal and external forces. For large complex models this can be very time consuming. The ANN's ability to perform nonlinear mapping between a given input and a system output makes it capable of response prediction without equilibrium iterations. Hence, a properly trained ANN can save a lot of computational effort in response prediction.

Artificial neural network

The architecture of a typical one layer artificial neural network is shown in Figure 1. The ANN consists of an input layer, a hidden layer and an output layer. Each connection between two neurons in two neighboring layers has a weight. Training of an ANN is optimization of these weights for a given data training set.

Following [2] the ANN set up and training procedure can be written as follows. The ANN output is calculated by

$$\mathbf{y} = \mathbf{W}_o^\top \mathbf{z}, \qquad \mathbf{z} = \tanh\left(\mathbf{W}_i^\top \mathbf{x}\right), \qquad x_0 \equiv z_0 \equiv 1, \tag{1}$$

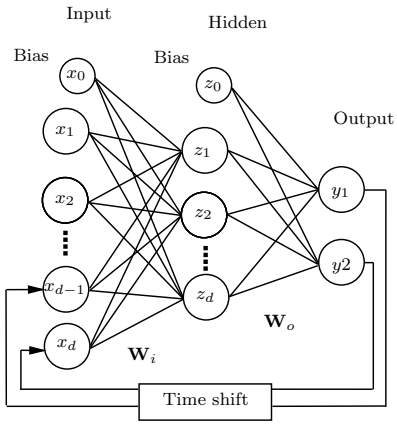

Figure 1. Sketch of artificial neural network.

where $\mathbf{x}$ is input vector, $\mathbf{y}$ is output vector and $\mathbf{W}_i$ and $\mathbf{W}_o$ are neuron connection weights between input and hidden layer and hidden and output layer, respectively. The tangent hyperbolic is used as activation function between input and hidden layer.

The error function which is minimized during training can be written as

$$E\left(\mathbf{W}\right) = \frac{1}{2}\sum_{n=1}^{N}\sum_{k=1}^{c}\{y(\mathbf{x}^n;\mathbf{W})_k - t_k^n\}^2 + \frac{1}{2}\alpha\mathbf{W}^2, \tag{2}$$

where y is the ANN output, t is the target value and α is the weight decay that controls the value of the weights and prevents the ANN from overfiting to noise in the training data. Optimal weights are found with an iterative procedure stepping in weight space towards minimal error. The weight update is done by gradient decent going the opposite direction of the cost functions gradient as in (3).

$$\mathbf{W}_{new} = \mathbf{W}_{old} + \Delta\mathbf{W}, \qquad \Delta\mathbf{W} = -\eta\frac{\partial E\left(\mathbf{W}\right)}{\partial\mathbf{W}}, \tag{3}$$

where η is the learning step size parameter. This parameter can either be constant or updated during the training of the ANN. For this application the dynamic learning step size parameter is adjusted for each iteration so that it is increased if the training error is decreased compared to previous iteration step and reduced if the training error increases.

Structural model

To illustrate the hybrid method a simplified model of a wind turbine is set up, see Figure 2. The height of the wind turbine is 100 m. The diameter of the turbine steel tower is 4 m with a wall thickness of 0.1 m. At the top of the tower a $100 \cdot 10^3$ kg mass is placed to represent the nacelle and turbine blades. The lowest eigenfrequency of the structure is 0.3 Hz. The load $\mathbf{f}(t)$ applied to the structure corresponds to the horizontal load on a 100 m diameter rotor in a 15 m/s wind. The mean wind load is 284 kN with a standard deviation of 44 kN.

The FEM model of the structure uses co-rotational beam element formulation as described in [3]. This formulation separates beam motion into two parts: a rigid body motion associated with a local frame of reference, and a deformation of the beam within this frame. The local deformation of the beam element implies geometrical stiffness contributions which depend on the deformation. Thus, we have a nonlinear model which can handle large deformations, when the governing equation is given as

$$\mathbf{M}\ddot{\mathbf{r}} + \mathbf{C}\dot{\mathbf{r}} + \mathbf{K}(\mathbf{r})\mathbf{r} = \mathbf{f}(t). \tag{4}$$

The lumped masses and beam stiffness contributions are assembled in a mass matrix $\mathbf{M}$ and a stiffness matrix $\mathbf{K}$, respectively. The beam is Rayleigh damped through damping matrix $\mathbf{C}$ introducing 3 % damping to the lowest vibration mode of the wind turbine. The force vector $\mathbf{f}$ consists of external force components at each degree of freedom (DOF) for each time step and the vector $\mathbf{r}$ contains the degrees of freedom (DOF) of the structure. Note that the components in the stiffness matrix $\mathbf{K}$ dependent on the deflection $\mathbf{r}$ of the structure. In the FEM model the turbine tower is divided into 10 elements.

The response of the structure is calculated by Newmark's method of direct integration. The Newton-Raphson method is used to achieve force equilibrium in each time step and the update of the stiffness matrix follows the proce dures described in [3]. The time step size is 0.1 s and equilibrium is assumed when force and displacement residuals are below 1 %.

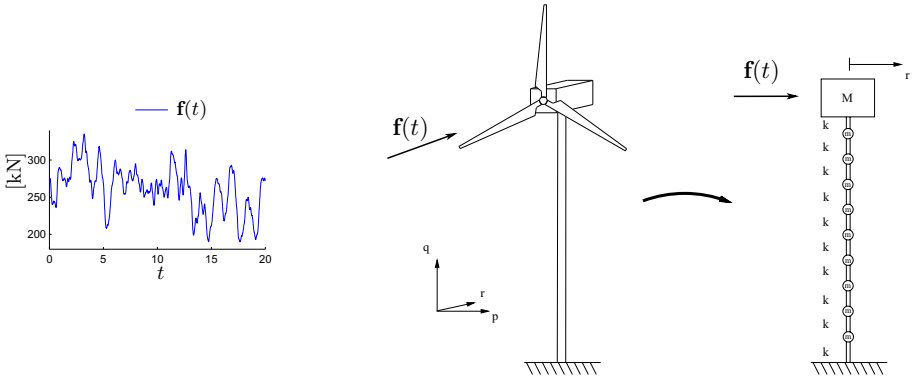

Figure 2. a) Harmonic wind load, b) Sketch of wind turbine, c) Simple turbine FEM model.

Based on the response history data generated by the FEM model an ANN is trained to predict the future dynamic response of the wind turbine.

Simulation

The ANN is designed and trained to predict the horizontal deflection of the wind turbine at the location of the mass M, see Figure 2. Note that the ANN output only gives the horizontal response of top and hence, as oppose to the FEM model, not the response of all model DOFs. The load together with the state space variables $(r, \dot{r})$ of previous time steps are used as ANN input

$$\mathbf{x}_t = [f(t) \dots f(t-d) \quad r(t-1) \quad \dot{r}(t-1) \dots r(t-d) \quad \dot{r}(t-d)]^T, \tag{5}$$

where d is number of previous time steps included in the input i.e. the model memory. ANN output is the current deflection and velocity

$$\mathbf{y}_t = [r(t) \quad \dot{r}(t)]^T \tag{6}$$

Since the ANN in this case simulate a theoretical model of a physical system and therefore replicate an exact solution to the system equations of motion there is no noise in the target output data. Therefore the weight decay in (2) is set to zero ($\alpha = 0$) in this example.

The wind turbine response history generated by the FEM model (4) is divided into a training and a test set as shown on Figure 3. Out of the 100 s response history the first 80 s is used

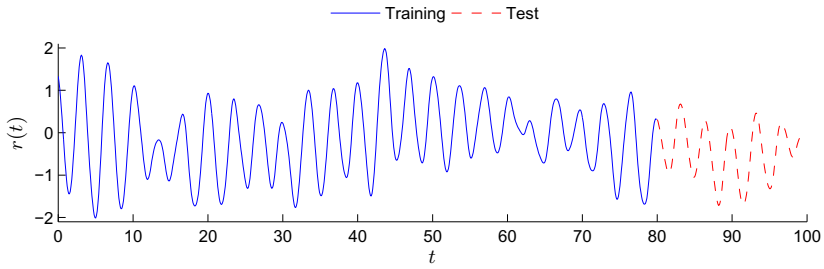

Figure 3. Training and test data.

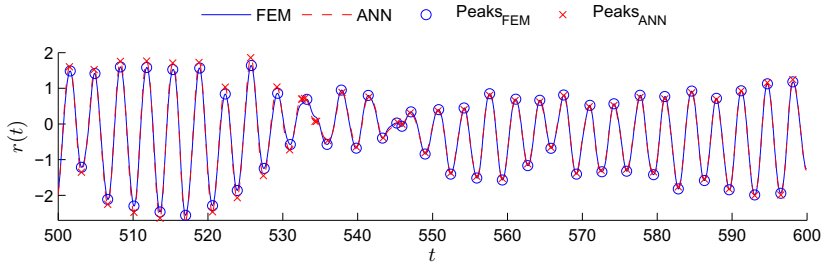

Figure 4. Exact FEM solution together with ANN simulation.

for training the ANN and the last 20 s is used for testing. With a time step size of 0.1 s and a dominating vibration frequency of 0.3 Hz, this gives a training set of 800 points covering about 24 vibration cycles. Parameter investigations not included in this paper show that an accurate, compact and robust ANN is obtained with 50 units in the hidden layer and 10 previous time steps. After training the ANN is able to predict the wind turbine response to a similar wind load history as the one used to generate the training data. The results of simulations using FEM model and ANN is shown in Figure 4. It is seen that the ANN captures the dynamics of the system very well and predicts the deflection quite accurately.

Concluding remarks

In the example presented in this paper the reduction in cpu time spend on a simulation of 10 min. wind is about a factor of 100 when using the ANN compared to the FEM - that is when the ANN is set up and trained. This factor is obviously dependent on the structure, the loading, model configuration etc. However, the examples indicates that the method holds a great potential. Furthermore, the reduction in calculation cost may be increased even further if it is possible to skip a few post possessing steps so that, instead of just predicting structural response, the ANN can be trained to predict material stresses or structural damage directly based on force input.

References

[1] R. Guarize, N.A.F. Matos, L.V.S. Sagrilo, and E.C.P. Lima. Neural networks in dynamic response analysis of slender marine structures. *Applied Ocean Research*, (29):191–198, January 2008.

[2] Christopher M. Bishop. *Pattern Recognition and Machine Learning*. Springer, October 2006.

[3] Steen Krenk. *Non-linear Modeling and Analysis of Solids and Structures*. Cambridge University Press, August 2009.

Proceedings of the 24th Nordic Seminar on Computational Mechanics
J. Freund and R. Kouhia (Eds.)

Investigation of a finite element formulation of Lighthill's acoustic analogy

Johan Nilsson[1], Robert-Zoltan Szasz[2], Per-Anders Wernberg[1], Per-Erik Austrell[1]

(1)Division of Structural Mechanics, Lund University, Box 118, 221 00 Lund, Sweden,
Johan.Nilsson@construction.lth.se
(2)Division of Fluid Mechanics, Lund University

Summary. A finite element formulation of Lighthill's acoustic analogy used to compute aeroacoustic noise is studied in the present paper. It is a hybrid method where as a first step the acoustical sources are computed from an incompressible CFD simulation using OpenFOAM. These sources are then used in the CALFEM finite element toolbox which solves Lighthill's equation. The method has been tested on the case of flow past a generic side view mirror mounted on a flat plate and the results has been compared to measurements found in the literature.

Key words: aeroacoustics, finite element method, CFD, hybrid methods, computational aeroacoustics, Lighthill's acoustic analogy

Introduction

One of the main difficulties in the area of Computational Aeroacoustics (CAA) is the large disparity in energy and length scales between the fluid mechanics and acoustics. Resolving the acoustics directly within a CFD simulation solving Navier-Stokes equations usually puts too high demands on resolution and numerical schemes to be practically possible. Therefore it is common to work with hybrid methods that treat the fluid mechanics and acoustics separately. This enables the use of different domains, mesh resolution, discretisation and even solution methods.

Theory

Most hybrid methods in CAA, including the one in the present work, are based on, or derived from, the following inhomogeneous acoustic wave equation originally derived by Lighthill [1]

$$\frac{1}{c_0^2}\frac{\partial^2 p'}{\partial t^2} - \frac{\partial^2 p'}{\partial x_i^2} = \frac{\partial^2 T_{ij}}{\partial x_i \partial x_j} \tag{1}$$

$$T_{ij} = \rho u_i u_j + \delta_{ij}(p' - c_0^2 \rho') - \tau_{ij}. \tag{2}$$

where p' are the pressure fluctuations, ρ' are the density fluctuations, u_i are the velocity components, c_0 is the speed of sound, τ_{ij} are the viscous stresses and δ_{ij} is the Kronecker delta. If the right hand side is independent of the left hand side, this equation can be seen as an inhomogeneous wave equation in an isotropic medium at rest. This means that all the sound propagation is separated from the sound generation or in other words, the acoustic field can not affect the flow field. In general the flow and the acoustics cannot be separated, but there are many cases when this assumption applies.

It is most common to solve (1) or another analogy formulation derived from (1), such as the one by Ffwocs-Williams and Hawkings [2] which takes into account solid and moving surfaces, by using Green functions and integrals. These are particularly advantageos for large open acoustic domains, such as airframe noise. In the present work a finite element formulation of (1) is studied. This was first suggested by Oberai et al. [3] and has also been studied by Escobar [4] among others. This approach is more suitable for confined aeroacoustic problems where multiple reflections or if coupled structure-acoustical effects are important as both of these effects are taken into account by the FEM solver. In contrast, these effects are difficult to include in integral formulations.

FEM formulation

By doing the usual steps in a FEM derivation, multiplying with a test function v integrating over the whole acoustic domain Ω and applying Green-Gauss theorem the weak form of (1) is obtained.

$$\frac{1}{c_0^2}\int_\Omega v\frac{\partial^2 p'}{\partial t^2}dV + \int_\Omega \frac{\partial v}{\partial x_i}\frac{\partial p'}{\partial x_i}dV = \int_{\partial\Omega} v\frac{\partial p'}{\partial n_i}dS + \int_\Omega v\frac{\partial^2 T_{ij}}{\partial x_i \partial x_j}dV \tag{3}$$

After applying the finite element approximation this becomes

$$\mathbf{M}\ddot{\mathbf{p}} + \mathbf{K}\mathbf{p} = \mathbf{f}_s + \mathbf{f}_q \tag{4}$$

$$\mathbf{M} = \frac{1}{c_0^2}\int_\Omega \mathbf{N}^T\mathbf{N}dV,\ \mathbf{K} = \int_\Omega (\nabla\mathbf{N})^T\nabla\mathbf{N}dV,\ \mathbf{f}_s = \int_{\partial\Omega}\mathbf{N}^T\frac{\partial p'}{\partial n_i}dS,\ \mathbf{f}_q = \int_\Omega \mathbf{N}^T\frac{\partial^2 T_{ij}}{\partial x_i\partial x_j}dV \tag{5}$$

where $\mathbf{N}$ are the element shape functions and $\mathbf{p}$ are the nodal values of p'.

However, the implemented method solves the problem in the frequency domain:

$$(-\omega^2\mathbf{M} + \mathbf{K})\hat{\mathbf{p}} = \hat{\mathbf{f}}_s + \hat{\mathbf{f}}_q \tag{6}$$

This enables the use of a simple absorbing boundary conditions. The relation between displacement and pressure can be written as

$$\frac{\partial p'}{\partial n} = -\frac{i\rho_0\omega}{Z}p' \tag{7}$$

where Z is the impedance. This applied to the boundary term in (6) giving.

$$\mathbf{f}_Z = -i\omega\rho_0\int_{\partial\Omega_Z}\mathbf{N}^T\frac{1}{Z}p'dS = -i\omega\rho_0\int_{\partial\Omega_Z}\mathbf{N}^T\frac{1}{Z}\mathbf{N}dS\hat{\mathbf{p}} \tag{8}$$

Finally the set of equations solved by the acoustical solver are

$$(-\omega^2\mathbf{M} + i\omega\mathbf{C} + \mathbf{K})\hat{\mathbf{p}} = \hat{\mathbf{f}}_s + \hat{\mathbf{f}}_q, \quad \mathbf{C} = \rho_0\int_{\partial\Omega_Z}\mathbf{N}^T\frac{1}{Z}\mathbf{N}dS \tag{9}$$

Implementation

An overview of the implemented method is shown in figure 1. First the CFD solver, in this case OpenFOAM, is run to compute the acoustical sources. These sources are interpolated to the acoustic mesh, which is much coarser than the CFD mesh. They are also converted to the frequency domain using FFT. Finally the acoustical solver CALFEM is run using the interpolated and converted sources as input.

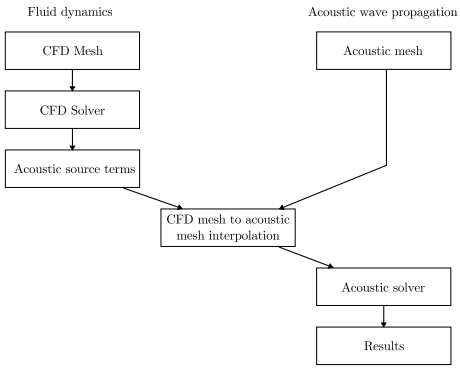

Figure 1. Overview of the implemented method.

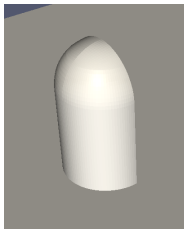

Figure 2. Mirror geometry.

Interpolation

It is important that the interpolation is carefully done as this can affect the result dramatically otherwise. To obtain a good result the interpolation has to conserve the acoustic energy. What is done is that first the acoustical source density is integrated over the cell in the CFD mesh to create an acoustical source focused at the centre of the cell. Then it is determined in which element in the acoustic mesh the CFD cell centre is located in. After that the local generalised coordinates are computed from the global coordinates. This is done by a Newton-Rhapson loop since it is a non-linear problem. Finally the standard FE shape functions are used to interpolate the contribution of the CFD cell to the nodes in the acoustical element.

Test case

To test the method the aerodynamically induced noise around a generic side view mirror was simulated. The mirror is a half cylinder with a quarter sphere on the top, see figure 2. The freestream velocity in the data used was $U = 39$ m/s. Measurements were performed by Daimler-Chrysler covered in [5], [6] and [7] and some of the data kindly provided by Dr. Franz R. Klimetzek at Daimler. Since the Mach number is low and there is no (significant) acoustic coupling with the flow the CFD simulation is incompressible. Turbulence was modeled using large eddy simulation (LES) with the Smagorinsky model. Since the flow can be seen as incompressible and there are no significant differences in temperature, the source term in (2) is approximated as

$$T_{ij} \approx \rho u_i u_j \tag{10}$$

The computed sound pressure levels at a microphone located at a position in the far field is shown in figure 3. The line marked non-conservative uses an interpolation tool included in OpenFOAM which does not conserve the acoustic energy. By using consverative interpolation as described in the previous section the result is significantly improved and a slope somewhat similar to the measurements can be seen. However the noise levels are far over predicted. The cause of this is not yet known. A grid sensitivity study on the acoustic mesh showed that a fairly coarse mesh can be used. There was hardly any difference at all between an acoustic mesh with about 35 000 elements and 280 000 elements. By comparison the CFD-mesh used had around 3 million cells. The acoustic grid insensitivity and the importance of conservative interpolation is similar to the study by Escobar [4], but in his test cases the result is not significantly over predicted. Different ways to discretise the source term (10) was also investigated. This included different schemes from OpenFOAM and applying an FE-based method described in [4]. The FE-based method increased the over prediction compared to the ordinary central differencing OpenFOAM scheme, see figure 4.

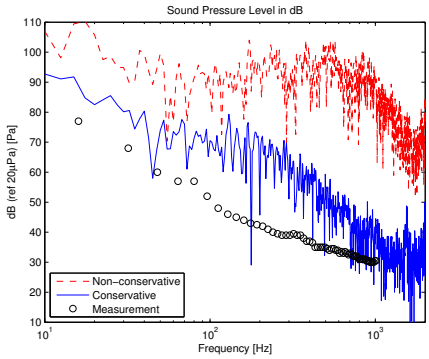

Figure 3. SPL at a microphone positioned in the far-field. Comparison between non-conservative and conservative interpolation.

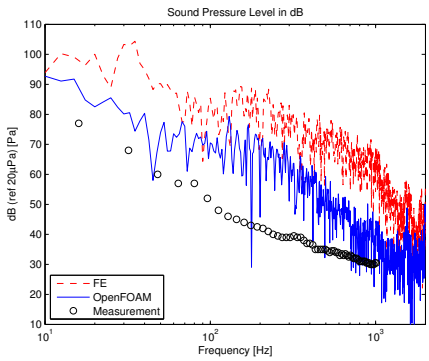

Figure 4. SPL at a microphone positioned in the far-field. Comparison between FE and OpenFOAM discretisation.

Acknowledgements

This work was supported by SAAB and the Swedish Agency for Innovation Systems (VINNOVA). The CFD simulations were performed on resources provided by the Swedish National Infrastructure for Computing (SNIC) at Lunarc, Lund University. We would also like to express our gratitude to Dr. Franz R. Klimetzek at Daimler, who let us use their experimental data.

References

[1] M. J. Lighthill. On Sound Generated Aerodynamically. I. General Theory. *Proceedings of the Royal Society London*, 211: 564-587, 1952.

[2] J. E. Ffowcs-Williams and D. L. Hawkings. Sound Generation by Turbulence and Surfaces in Arbitrary Motion. *Philosophical Transactions of the Royal Society of London.* 1969, 321-342.

[3] A. A. Oberai, F. Roknaldin, T. J. R. Hughes. Computational procedures for determining structural-acoustic response due to hydrodynamic sources. *Computational Methods in Applied Mechanics and engineering* 190: 345-361, 2000

[4] M. Escobar. Finite Element Simulation of Flow-Induced Noise using Lighthill's Acoustic Analogy. *PhD Thesis. Der Technischen Fakultät der Universität Erlangen-Nürnberg*, 2007.

[5] R. Höld, A. Brenneis, A. Eberle, V. Schwarz, R. Siegert. Numerical Simulation of Aeroacoustic Sound Generated by Generic Bodies Placed on a Plate: Part I - Prediction of Aeroacoustic Sources. *Fifth AIAA/CEAS Aeroacoustics Conference, Seattle, WA, May 10-12.* Paper No. AIAA-99-1896, 1999

[6] R. Siegert, V. Schwarz, J. Rechenberger. Numerical Simulation of Aeroacoustic Sound Generated by Generic Bodies Placed on a Plate: Part II - Prediction of Radiated Sound Pressure. *Fifth AIAA/CEAS Aeroacoustics Conference, Seattle, WA, May 10-12.* Paper No. AIAA-99-1895, 1999

[7] T. Rung, D. Estricht, J. Yan, F. Thiele. Sound Radiation of the Vortex Flow Past a Generic Side Mirror. *Eigth AIAA/CEAS Aeroacoustics Conference, Breckenridge, CO, Jun 17-19.* Paper No. AIAA-2002-2549, 2002

Proceedings of the 24th Nordic Seminar on Computational Mechanics
J. Freund and R. Kouhia (Eds.)

Reducing the integration error of cohesive elements

B.L.V. Bak[1] and E. Lund[2]

(1)Siemens Wind Power A/S, Denmark, brian.bak@siemens.com
(2)Department of Mechanical and Manufacturing Engineering Aalborg University, Denmark, el@m-tech.aau.dk

Summary. This paper focuses on analyzing the significance of the method used for the numerical integration of the internal forces of linear cohesive elements. The currently used 4 point Newton-Cotes integration introduces a large error and is one of the limiting factors for utilizing a smaller number of elements in the cohesive zone. It is shown that for other integration methods larger elements can be utillized with less iterations and yield more accurate results.

Key words: numerical integration, cohesive zone modeling, composite structures

Introduction

This work is conducted by Siemens Wind Power A/S in collaboration with Aalborg University. Siemens Wind Power A/S is one of the leading manufacturers of wind turbines. The blades of the wind turbine are made as a laminated glass-epoxy-balsa sandwich structure. The main failure mechanism of such a structure is delamination damage from a single load or cyclic loading. Thus, it is important to be able to predict the onset of damage delamination and its development. The work presented here is conducted within the framework of cohesive zone modeling that was first introduced in [1, 4] and is an indirect way of applying classical fracture mechanics where the critical energy release rate is represented by the work of tractions applied on the crack faces. There are several research contributions within the field of implementing the cohesive zone model into the finite element method. The element investigated in this paper is the bilinear, 8-noded, zero thickness interface element for 3D models with a capability of simulating mixed mode delamination using a bilinear traction-separation law [2, 3, 5].

Currently, the implementations of the cohesive zone model are not suitable for simulating delamination damage in large structures in the magnitude of meters when the cohesive zone is in the magnitude of a few millimeters, because of the high resolution of elements needed with a high computational effort as a consequence. Furthermore, the perspectives of using the cohesive elements with a stress-cycle criterion for modeling fatigue driven delamination calls for a better prediction of the in-situ stresses in the cohesive zone, which traditionally is solved using smaller elements.

So far the work on increasing the solution speed of delamination simulations by utilization of larger elements has focused on relaxing the penalty stiffness of the cohesive law and/or the onset displacements [6]. Both methods are a way to enlarge the cohesive zone and thereby having a higher resolution of elements in the zone without decreasing the element size. However, the downside of relaxing the onset displacement has a direct influence on the ability to predict the onset of delamination damage. This is not important when simulating simple precracked structures like the double cantilevered beam (DCB) test specimen, but in the case of analyzing real structures like wind turbine blades without precracks the correct simulation of onset becomes

a very important part of the delamination damage simulation. The penalty stiffness influences the overall structural response as it introduces a, within the cohesive framework, non-physical compliance to the interface. Furthermore, the chosen bilinear relation between onset displacement, penalty stiffness and critical energy release rate constrains the possibilities for relaxing the penalty stiffness and the onset displacement.

In 2D models of DCB specimens an oscillating response curve is observed. This has led to the idea that the internal forces and stiffness of the element are varying in an unattended way because of an erroneous prediction of the internal forces in the numerical integration of the element. The errors introduced by different integration methods based on the Newton-Cotes integration rule are evaluated and simulation of a DCB-specimen is conducted to investigate integration routines in order to get accurate simulation results at the least possible computational effort.

Analysis of the integration error

The cohesive element, see [2, 3, 5] for details, is programmed in Maple 13 and evaluated in the entire domain for different opening modes in order to investigate the equations being integrated and how well they obey the restrictions for exact integration using the Newton-Cotes integration rule. The equation for the displacement interpolation is bilinear in the natural coordinates η and ξ. The equation for the opening displacements, $\mathbf{\Delta}$ of the element are polynomial fractions with products of ξ^n and η^n where n = 0,1,2 in both nominator and denominator. The equation for the secant stiffness, $(1-d)K$ (K is the penalty stiffness) and damage parameter, d are polynomial fractions with products of ξ^n and η^n where n = 0,1,2,3,4 in both nominator and denominator. The equation for the stresses, τ are polynomial fractions with products of ξ^n and η^n where n = 0,1,...,6 in both nominator and denominator. Furthermore, the absolute value function is present in both the nominator and denominator of the equations for the secant stiffness and stresses. The equations for Δ, d, $(1-d)K$ and τ are plotted in natural coordinates in Figure 1 for two different opening configurations. Material properties used for the element are for UD glass-epoxy laminate. The nodal displacement are chosen to illustrate the characteristic shape of the normal stresses and the secant stiffness.

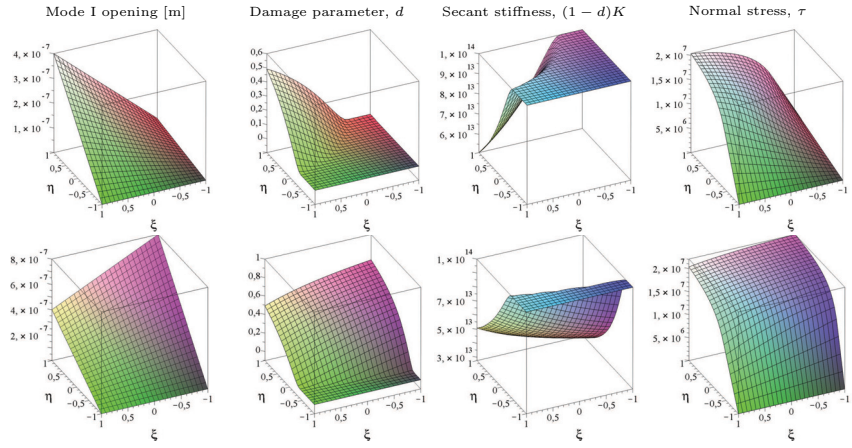

Figure 1: The mode I opening, damage parameter, secant stiffness and normal stress are shown for two different mode I opening configurations in natural coordinates.

It is seen that the surface for τ is concave-down. This means that the Newton-Cotes integration of τ is in general underestimated. $(1-d)K$ is neither concave-up or concave-down and therefore the error can be both positive and negative.

Different integration methods based on a composite Newton-Cotes trapez integration rule have been implemented into a user defined element routine of the cohesive element in Abaqus 6.10. They fall into two categories; evenly distributed integration points and adaptive placement of the integration points onto the damaged part of the element, see Figure 2. The damaged part of the element is defined as the smallest rectangular area that contains the crack front. Results of the methods are presented for 4, 9, 25 and 10 integration points for the evenly distributed integration points and 9 and 36 integration points for the adaptive placement of integration points. The new integration methods are only active when damage is developing in the element. Before and after damage the regular 4 point Newton-Cotes integration is used.

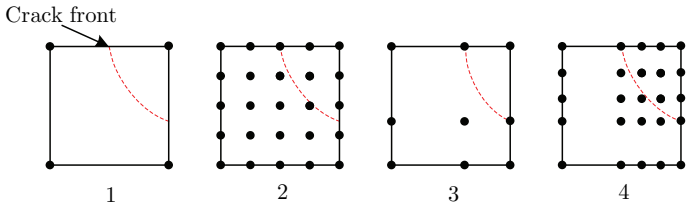

Figure 2: Location of integration points for the Newton-Cotes integration points for evenly distributed integration points (1 and 2) and placement of integration points in the damaged zone (3 and 4).

It is difficult to exactly quantify the error introduced with different integration methods because it is dependent on the opening configuration of the element, which in relation to a real structure depends on mesh, elements size, material properties and boundary conditions. In order to get an indication of the magnitude of error introduced by the different integration methods the error is determined for the opening configuration in Table 1 as it is scaled from 0.1 to 1 for a 1mm × 1mm element. The progression of the crack front for this opening is shown in Figure 3.

Node no.	z
5	$4 \cdot 10^{-6}$ m
6	$4 \cdot 10^{-4}$ m
7	$4 \cdot 10^{-3}$ m
8	$4 \cdot 10^{-4}$ m

Table 1: Out-of-plane displacements of nodes. All other nodal displacements are zero.

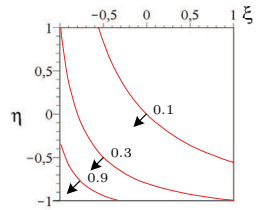

Figure 3: Crack front progression at scale factor equal 0.1, 0.3 and 0.9.

In Figure 4 the integration error is presented for the τ and $(1-d)K$. From these results it is evident that the integration error is significant.

Analysis results

The integration methods are tested on a 3D solid finite element model. The model is a DCB specimen with mechanical properties of UD glass-epoxy. The dimensions $h \times l \times w = 5\text{mm} \times 110\text{mm} \times 23\text{mm}$ with a precrack length of 46mm. In the simulations a mesh with cohesive elements of 0.5mm is used. The fracture mechanical properties used are $G_{Ic} = 613 J/m^2$,

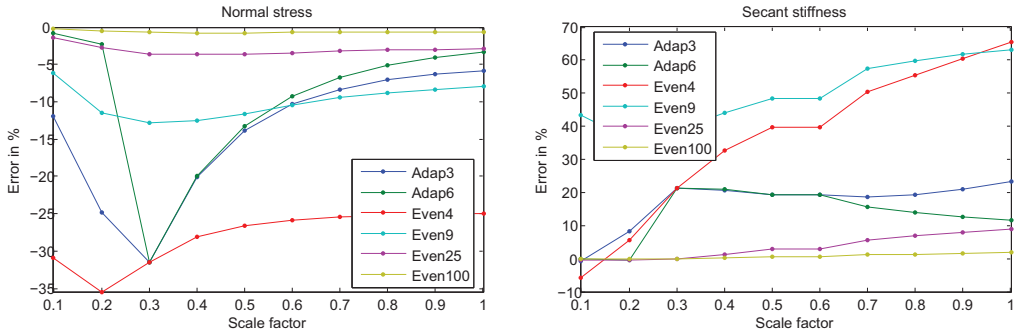

Figure 4: Graphs showing the error of integrated normal stress and secant stiffness as it develops when the nodal displacement in Table 1 are scaled from 0.1 to 1.

$G_{IIc} = 2252J/m^2$, mode I onset stress = 12MPa , mode II onset stress = 22MPa and the opening penalty stiffness = 10^8MPa and penetration penalty stiffness = 10^8MPa.

Table 2: Total number of iterations.

Integration method	Iterations 0.5mm
Evenly 4	741
Evenly 100	223
Adaptive 9	not converged

There is a clear speed advantage of using a higher number of integration points where it is seen that there is almost a reduction in the number of iterations by a factor of 4. Furthermore, the structural response is smoother with significantly smaller oscillations.

List of References

[1] G. Barenblatt. *The Mathematical Theory of Equilibrium Cracks in Brittle Fracture*, volume 7 of *Advances in Applied Mechanics*, pages 55–129. Elsevier, 1962.

[2] P. P. Camanho, C. G. Davila, and M. F. de Moura. Numerical Simulation of Mixed-Mode Progressive Delamination in Composite Materials. *Journal of Composite Materials*, 37(16):1415–1438, August 2003.

[3] C. G. Dávila, P. P. Camanho, and A. Turon. Cohesive Elements For Shells. Technical report, 2007.

[4] D. S. Dugdale. Yielding of steel sheets containing slits. *Journal of the Mechanics and Physics of Solids*, 8(2):100–104, May 1960.

[5] A. Turon, P. P. Camanho, J. Costa, and C. G. Dávila. A damage model for the simulation of delamination in advanced composites under variable-mode loading. *Mechanics of Materials*, 38(11):1072–1089, November 2006.

[6] A. Turon, C. Davila, P. Camanho, and J. Costa. An engineering solution for mesh size effects in the simulation of delamination using cohesive zone models. *Engineering Fracture Mechanics*, 74(10):1665–1682, July 2007.

Proceedings of the 24th Nordic Seminar on Computational Mechanics
J. Freund and R. Kouhia (Eds.)

A residual based a posteriori error estimator for post-processed MITC plate elements

Lourenço Beirão da Veiga[1], Jarkko Niiranen[2], and Rolf Stenberg[3]

(1)Dipartimento di Matematica "F. Enriques", Università di Milano, via Saldini 50, 20133 Milano, Italy, lourenco.beirao@unimi.it
(2)Department of Civil and Structural Engineering, Aalto University School of Engineering, P.O. Box 12100, 00076 AALTO, Finland, jarkko.niiranen@aalto.fi
(3)Department of Mathematics and Systems Analysis, Aalto University School of Science, P.O. Box 11100, 00076 AALTO, Finland, rolf.stenberg@aalto.fi

Summary. This contribution presents a residual based *a posteriori* error estimator for the post-processed MITC finite element methods approximating the solution of the Reissner–Mindlin plate bending problem. The error estimator utilizes a post-processing method improving the accuracy of the deflection approximation of the original MITC method.

Key words: Reissner–Mindlin plates, MITC finite element methods, *a posteriori* error estimates

Introduction

For thin plate structures, the most commonly used models in engineering applications are the Kirchhoff–Love and Reissner–Mindlin plate models; the latter, in particular, being capable of modelling a wide range of applications of moderately thick plate structures as well. Regarding finite element approximations, the MITC family [1, 3, 6] is propaply the most reputable method. *A posteriori* error analysis of the MITC elements for adaptive mesh refinements has been recently accomplished in [4, 5]. This paper presents a corresponding error indicator with reliability and efficiency results [2] for the post-processed MITC methods [6].

Reissner–Mindlin plate model

Let Ω be a polygonal domain in $\mathbb{R}^2$ representing the midsurface of a plate of thickness t. We assume that the boundary Γ of Ω is a union of five disjoint sets defined as $\Gamma = \Gamma_{C_H} \cup \Gamma_{C_S} \cup \Gamma_{S_H} \cup \Gamma_{S_S} \cup \Gamma_F$, with each set above being a finite union of connected components. The plate is (respectively hard and soft) clamped on $\Gamma_{C_H} \cup \Gamma_{C_S}$, (respectively hard and soft) simply supported on $\Gamma_{S_H} \cup \Gamma_{S_S}$ and free on Γ_F. For simplicity, we assume that all boundary conditions are homogeneous, and that the union of the clamped and simply supported parts has a positive measure in the sense that the rigid body motions of the plate can be neglected. Finally, let the plate be subjected to a vertical loading f which already includes the standard scaling by t^3.

The variational spaces of kinematically admissible deflections and rotations are defined, according to the boundary conditions listed above, as

$$W = \{v \in H^1(\Omega) \ | \ v = 0 \text{ on } \Gamma_{\mathrm{C_H}} \cup \Gamma_{\mathrm{C_S}} \cup \Gamma_{\mathrm{S_H}} \cup \Gamma_{\mathrm{S_S}}\}, \tag{1}$$

$$\boldsymbol{V} = \{\boldsymbol{\eta} \in [H^1(\Omega)]^2 \ | \ \boldsymbol{\eta} \cdot \boldsymbol{n} = 0 \text{ on } \Gamma_{\mathrm{C_H}} \cup \Gamma_{\mathrm{C_S}}, \ \boldsymbol{\eta} \cdot \boldsymbol{\tau} = 0 \text{ on } \Gamma_{\mathrm{C_H}} \cup \Gamma_{\mathrm{S_H}}\}, \tag{2}$$

with $\boldsymbol{\tau}$ denoting the unit tangent to Γ obtained by an anti-clockwise rotation of the outward normal $\boldsymbol{n}$. The scaled bending bilinear form is defined as

$$a(\boldsymbol{\phi},\boldsymbol{\eta}) = (\mathcal{A}\boldsymbol{\varepsilon}(\boldsymbol{\phi}),\boldsymbol{\varepsilon}(\boldsymbol{\eta})) = \frac{1}{6}\{(\boldsymbol{\varepsilon}(\boldsymbol{\phi}),\boldsymbol{\varepsilon}(\boldsymbol{\eta})) + \frac{\nu}{1-\nu}(\operatorname{div}\boldsymbol{\phi},\operatorname{div}\boldsymbol{\eta})\}, \tag{3}$$

with $\mathcal{A}$ denoting the (scaled) fourth order tensor of the bending moduli, $\boldsymbol{\varepsilon}$ denoting the symmetric gradient and ν standing for Poisson's ratio and $(\cdot,\cdot)$ standing for the standard scalar product in $L^2(\Omega)$. The Reissner–Mindlin plate bending problem can be now written in the following form:

Variational formulation. *Find the deflection $w \in W$ and the rotation $\boldsymbol{\beta} \in \boldsymbol{V}$ such that*

$$a(\boldsymbol{\beta},\boldsymbol{\eta}) + t^{-2}(\nabla w - \boldsymbol{\beta}, \nabla v - \boldsymbol{\eta}) = (f,v) \quad \forall (v,\boldsymbol{\eta}) \in W \times \boldsymbol{V}. \tag{4}$$

The shear force is defined as $\boldsymbol{q} = (\nabla w - \boldsymbol{\beta})/t^2 \in \boldsymbol{Q} = [L^2(\Omega)]^2$.

MITC finite elements

In what follows, by $\mathcal{C}_h$ we denote the triangulation of $\overline{\Omega}$, and by $\mathcal{E}_h$ the set of all its edges. As usual, for the mesh size we use the notation $h = \max_{K\in\mathcal{C}_h} h_K$, where h_K is the diameter of element K. The space of polynomials of degree k on K is denoted by $P_k(K)$. By C we denote positive constants independent of both the thickness t and the mesh size h.

The finite element subspaces $W_h \subset W$ and $\boldsymbol{V}_h \subset \boldsymbol{V}$ are defined as

$$W_h = \{v \in W \ \mid \ v_{|K} \in P_k(K) \ \ \forall K \in \mathcal{C}_h\}, \tag{5}$$

$$\boldsymbol{V}_h = \{\boldsymbol{\eta} \in \boldsymbol{V} \ \mid \ \boldsymbol{\eta}_{|K} \in [P_k(K)]^2 \oplus [B_{k+1}(K)]^2 \ \ \forall K \in \mathcal{C}_h\}, \tag{6}$$

with the polynomial degree $k \geq 2$ and the local "bubble function space" $B_{k+1}(K) = \{bp \ \mid \ p \in \tilde{P}_{k-2}(K),\ b \in P_3(K),\ b_{|E} = 0 \ \ \forall E \subset \partial K\}$, where $\tilde{P}_{k-2}(K)$ denotes the space of homogeneous polynomials of degree $k-2$ on the element K and E denotes an edge to K. We denote the rotated Raviart–Thomas space of order $k-1$ by

$$\boldsymbol{Q}_h = \{\boldsymbol{r} \in \boldsymbol{H}(\operatorname{rot},\Omega) \ \mid \ \boldsymbol{r}_{|K} \in [P_{k-1}(K)]^2 \oplus (y,-x)\tilde{P}_{k-1}(K) \ \ \forall K \in \mathcal{C}_h\}. \tag{7}$$

Note that the requirement $\boldsymbol{Q}_h \subset \boldsymbol{H}(\operatorname{rot},\Omega)$ implies that the tangential components of functions in $\boldsymbol{Q}_h$ are continuous along inter element boundaries. Next, we define the reduction operator $\boldsymbol{R}_h : [H^1(\Omega)]^2 \to \boldsymbol{Q}_h$, with $\boldsymbol{R}_K = \boldsymbol{R}_{h|K}$, by the conditions

$$\langle(\boldsymbol{R}_K\boldsymbol{\eta} - \boldsymbol{\eta})\cdot\boldsymbol{\tau}_E, p\rangle_E = 0 \quad \forall p \in P_{k-1}(E) \quad \forall E \subset \partial K, \tag{8}$$

$$(\boldsymbol{R}_K\boldsymbol{\eta} - \boldsymbol{\eta}, \boldsymbol{p})_K = 0 \quad \forall \boldsymbol{p} \in [P_{k-2}(K)]^2, \tag{9}$$

where $\boldsymbol{\tau}_E$ denotes a unit tangent to E. The notations $(\cdot,\cdot)_K$ and $\langle\cdot,\cdot\rangle_E$ stand for the standard inner products in $L^2(K)$ and $L^2(E)$, respectively.

Method. *[3] Find the deflection $w_h \in W_h$ and the rotation $\boldsymbol{\beta}_h \in \boldsymbol{V}_h$ such that*

$$a(\boldsymbol{\beta}_h,\boldsymbol{\eta}) + t^{-2}(\boldsymbol{R}_h(\nabla w_h - \boldsymbol{\beta}_h), \boldsymbol{R}_h(\nabla v - \boldsymbol{\eta})) = (f,v) \quad \forall (v,\boldsymbol{\eta}) \in W_h \times \boldsymbol{V}_h. \tag{10}$$

The discrete shear force is defined as $\boldsymbol{q}_h = \boldsymbol{R}_h(\nabla w_h - \boldsymbol{\beta}_h)/t^2 = (\nabla w_h - \boldsymbol{R}_h\boldsymbol{\beta}_h)/t^2 \in \boldsymbol{Q}_h$.

For smooth solution fields, the following optimal *a priori* error estimate holds:

Theorem 1. *[3] Let the solution of the Variational formulation be sufficiently regular. For the error of the solution obtained by the Method, there exists a positive constant C such that*

$$||w - w_h||_{H^1(\Omega)} + ||\boldsymbol{\beta} - \boldsymbol{\beta}_h||_{H^1(\Omega)} + t||\boldsymbol{q} - \boldsymbol{q}_h||_{L^2(\Omega)} + ||\boldsymbol{q} - \boldsymbol{q}_h||_{\boldsymbol{V}'} \tag{11}$$

$$\leq Ch^k\big(||w||_{H^{k+1}(\Omega)} + ||\boldsymbol{\beta}||_{H^{k+1}(\Omega)} + ||\boldsymbol{q}||_{H^{k-1}(\Omega)} + t||\boldsymbol{q}||_{H^k(\Omega)}\big). \tag{12}$$

Next, we briefly review the post-processing procedure introduced and analyzed in [6]. First, we define an interpolation operator into the discrete deflection space W_h as follows:

Definition. *Let a and E, respectively, be a vertex and an edge of a triangle K. The interpolation operator $I_h : H^s(\Omega) \to W_h$, $s > 1$, $I_K = I_{h|K} \ \forall K \in \mathcal{C}_h$, is defined by the conditions*

$$\begin{aligned}(v - I_K v)(a) &= 0 \ \forall a \in K, &(13)\\ \langle v - I_K v, p\rangle_E &= 0 \ \forall p \in P_{k-2}(E) \ \forall E \subset K, &(14)\\ (v - I_K v, p)_K &= 0 \ \forall p \in P_{k-3}(K). &(15)\end{aligned}$$

In the post-processing, we use the splitting $P_{k+1}(K) = P_k(K) \oplus \widehat{W}(K) \oplus \overline{W}(K)$ with

$$\begin{aligned}\widehat{W}(K) &= \{v \in P_{k+1}(K) \ | \ I_K v = 0, \ (v,p)_K = 0 \ \forall p \in \tilde{P}_{k-2}(K)\}, &(16)\\ \overline{W}(K) &= \{v \in P_{k+1}(K) \ | \ I_K v = 0, \ \langle v,p\rangle_E = 0 \ \forall p \in \tilde{P}_{k-1}(E) \ \forall E \subset K\}. &(17)\end{aligned}$$

Post-processing scheme. *For each triangle $K \in \mathcal{C}_h$, find the local post-processed finite element deflection $w^*_{h|K} \in P_{k+1}(K) = P_k(K) \oplus \widehat{W}(K) \oplus \overline{W}(K)$ such that $I_h w^*_{h|K} = w_{h|K}$,*

$$\begin{aligned}\langle \nabla w^*_h \cdot \boldsymbol{\tau}_E, \nabla \hat{v} \cdot \boldsymbol{\tau}_E\rangle_E &= \langle (\boldsymbol{\beta}_h + t^2 \boldsymbol{q}_h) \cdot \boldsymbol{\tau}_E, \nabla \hat{v} \cdot \boldsymbol{\tau}_E\rangle_E \ \forall E \subset \partial K, \ \forall \hat{v} \in \widehat{W}(K), &(18)\\ (\nabla w^*_h, \nabla \bar{v})_K &= (\boldsymbol{\beta}_h + t^2 \boldsymbol{q}_h, \nabla \bar{v})_K \ \forall \bar{v} \in \overline{W}(K). &(19)\end{aligned}$$

It should be pointed out that the post-processed deflection is conforming since $(\boldsymbol{\beta}_h + t^2 \boldsymbol{q}_h) \cdot \boldsymbol{\tau}$ is continuous along inter element boundaries. Furthermore, it holds that $\boldsymbol{\beta}_h + t^2 \boldsymbol{q}_h = \nabla w_h + (I - \boldsymbol{R}_h)\boldsymbol{\beta}_h$. With respect to the convergence rate of Theorem 1 for the original deflection approximation, an improvement of order $\mathcal{O}(h + t)$ holds for the convergence rate of the post-processed deflection:

Theorem 2. *[6] For a convex fully clamped plate, there exists a positive constant C such that*

$$\|w - w^*_h\|_1 \leq C(h + t)h^k\big(||w||_{H^{k+2}(\Omega)} + ||\boldsymbol{\beta}||_{H^{k+1}(\Omega)} + ||\boldsymbol{q}||_{H^{k-1}(\Omega)} + t||\boldsymbol{q}||_{H^k(\Omega)}\big). \quad (20)$$

Finally, we define a mesh dependent norm coupling the deflection and the rotation as

$$|||(\boldsymbol{\eta}, v)|||^2 = ||\boldsymbol{\eta}||^2_{H^1(\Omega)} + \sum_{K \in \mathcal{C}_h} \frac{1}{t^2 + h_K^2} ||\nabla v - \boldsymbol{\eta}||^2_{L^2(K)}. \quad (21)$$

Proposition. *[2] There exists a positive constant C such that*

$$|||(\boldsymbol{\beta} - \boldsymbol{\beta}_h, w - w^*_h)||| \leq Ch^k\big(||w||_{H^{k+2}(\Omega)} + ||\boldsymbol{\beta}||_{H^{k+1}(\Omega)} + ||\boldsymbol{q}||_{H^{k-1}(\Omega)} + t||\boldsymbol{q}||_{H^k(\Omega)}\big). \quad (22)$$

A posteriori error estimates

Let first the moment operator be defined as $\boldsymbol{m}(\boldsymbol{\phi}) = \mathcal{A}\boldsymbol{\varepsilon}(\boldsymbol{\phi})$ and let a new approximation for the shear force be defined as $\boldsymbol{q}^*_h = (\nabla w^*_h - \boldsymbol{\beta}_h)/t^2$. Then we define the following local error indicators, for all elements K and edges E of the mesh $\mathcal{C}_h$:

$$\begin{aligned}\tilde{\eta}^2_K &= h_K^2(h_K^2 + t^2)||f + \operatorname{div} \boldsymbol{q}_h||^2_{L^2(K)} + h_K^2||\mathbf{div}\, \boldsymbol{m}(\boldsymbol{\beta}_h) + \boldsymbol{q}_h||^2_{L^2(K)}, &(23)\\ \eta^2_E &= h_E(h_E^2 + t^2)|||[\![\boldsymbol{q}_h \cdot \boldsymbol{n}]\!]||^2_{L^2(E)} + h_E|||[\![\boldsymbol{m}(\boldsymbol{\beta}_h)\boldsymbol{n}]\!]||^2_{L^2(E)}, &(24)\\ \eta^2_{C_S,E} &= h_E|||[\![\boldsymbol{\tau} \cdot \boldsymbol{m}(\boldsymbol{\beta}_h)\boldsymbol{n}]\!]||^2_{L^2(E)}, &(25)\\ \eta^2_{S_H,E} &= h_E|||[\![\boldsymbol{n} \cdot \boldsymbol{m}(\boldsymbol{\beta}_h)\boldsymbol{n}]\!]||^2_{L^2(E)}, \quad \eta^2_{S_S,E} = h_E|||[\![\boldsymbol{m}(\boldsymbol{\beta}_h)\boldsymbol{n}]\!]||^2_{L^2(E)}, &(26)\\ \eta^2_{F,E} &= h_E|||[\![\boldsymbol{m}(\boldsymbol{\beta}_h)\boldsymbol{n}]\!]||^2_{L^2(E)} + h_E(h_E^2 + t^2)|||[\![\boldsymbol{q}_h \cdot \boldsymbol{n}]\!]||^2_{L^2(E)}, &(27)\end{aligned}$$

where $[\![\cdot]\!]$ represents the standard jump operator which is assumed to be equal to the function value on boundary edges. Moreover, for each $K \in \mathcal{C}_h$ let us define the consistency terms

$$(\sigma_K^*)^2 = \frac{t^4}{t^2 + h_K^2} ||\boldsymbol{q}_h^* - \boldsymbol{q}_h||^2_{L^2(K)} \ , \qquad (\sigma_K')^2 = ||\mathrm{rot}\,(I - \boldsymbol{R}_h)\boldsymbol{\beta}_h||^2_{L^2(K)}. \tag{28}$$

Then, for any element $K \in \mathcal{C}_h$, the local error indicator is defined as

$$\begin{aligned}\eta_K = \Big(\tilde{\eta}_K^2 + \frac{1}{2}\sum_{E\in I(K)} \eta_E^2 + \sum_{E\in C_S(K)} \eta_{C_S,E}^2 + \sum_{E\in S_H(K)} \eta_{S_H,E}^2 \\ + \sum_{E\in S_S(K)} \eta_{S_S,E}^2 + \sum_{E\in F(K)} \eta_{F,E}^2 + (\sigma_K')^2 + (\sigma_K^*)^2\Big)^{1/2},\end{aligned} \tag{29}$$

where $I(K)$ denotes the edges of the element K lying in the interior of Ω, while $C_S(K)$, $S_H(K)$, $S_S(K)$ and $F(K)$ represent the edges of K on $\Gamma_{\mathrm{C_S}}$, $\Gamma_{\mathrm{S_H}}$, $\Gamma_{\mathrm{S_S}}$ and Γ_{F}, respectively. Finally, the global error indicator is defined as

$$\eta_h = \Big(\sum_{K\in\mathcal{C}_h} \eta_K^2\Big)^{1/2}. \tag{30}$$

The following reliability end efficiency results show that the error estimator proposed can be used as a basis for adaptive mesh refinements and error estimation:

Theorem 3. *[2] There exist positive constants C and C' such that*

$$\begin{aligned}&|||(\boldsymbol{\beta} - \boldsymbol{\beta}_h, w - w_h^*)|||^2 + t^2||\boldsymbol{q} - \boldsymbol{q}_h||^2_{L^2(\Omega)} \\ &\quad + t^4||\mathrm{rot}\,(\boldsymbol{q} - \boldsymbol{q}_h)||^2_{L^2(\Omega)} + ||\boldsymbol{q} - \boldsymbol{q}_h||^2_{\boldsymbol{V}'} \le C\eta_h^2,\end{aligned} \tag{31}$$

$$\begin{aligned}\eta_h^2 \le C'\big(&|||(\boldsymbol{\beta} - \boldsymbol{\beta}_h, w - w_h^*)|||^2 + t^2||\boldsymbol{q} - \boldsymbol{q}_h||^2_{L^2(\Omega)} \\ &+ t^4||\mathrm{rot}\,(\boldsymbol{q} - \boldsymbol{q}_h)||^2_{L^2(K)} + ||\boldsymbol{q} - \boldsymbol{q}_h||^2_{\boldsymbol{V}'} + \mathrm{osc}(f)^2\big).\end{aligned} \tag{32}$$

References

[1] K.-J. Bathe, F. Brezzi, and M. Fortin. Mixed-interpolated elements for Reissner–Mindlin plates. *Int. J. Num. Meths. Eng.*, 28:1787–1801, 1989.

[2] L. Beirão da Veiga, J. Niiranen, and R. Stenberg. A posteriori error analysis for the post-processed MITC plate elements. In preparation.

[3] F. Brezzi, M. Fortin, and R. Stenberg. Error analysis of mixed-interpolated elements for Reissner–Mindlin plates. *Math. Mod. Meth. Appl. Sci.*, 1:125–151, 1991.

[4] C. Carstensen and J. Hu. A posteriori error analysis for conforming MITC elements for Reissner–Mindlin plates. *Math. Comp.*, 77:611–632, 2008.

[5] J. Hu and Y. Huang. A posteriori error analysis of finite element methods for Reissner–Mindlin plates. *SIAM J. Numer. Anal.*, 47:4446–4472, 2010.

[6] M. Lyly, J. Niiranen, and R. Stenberg. Superconvergence and postprocessing of MITC plate elements. *Comp. Meths. Appl. Mech. Engrg.*, 196:3110–3126, 2007.

Proceedings of the 24th Nordic Seminar on Computational Mechanics
J. Freund and R. Kouhia (Eds.)

Acceleration of large self consistent iterations with the quasi-Newton method

Kurt Baarman[1], Timo Eirola[1], Ville Havu[2]

Aalto University
(1)Institute of Mathematics, FI-00076 Aalto, Finland, kurt.baarman@aalto.fi
(2)Department of Applied Physics, FI-00076 Aalto, Finland, ville.havu@aalto.fi

Summary. The quasi-Newton method provides quick and reliable acceleration of self consistent iterations for systems where the Jacobian is unavailable. The inverse Jacobian is approximated by a low rank matrix that makes the iteration suitable for large systems.

Key words: quasi-Newton method, Broyden's update, fixed point iteration, self consistent field iteration

Introduction

Several applications of computational science and engineering, such as plasticity and electronic structure calculations, result in systems of nonlinear equations. When the system size is small and the Jacobian of the nonlinear system is available Newton-like methods offer an efficient solution method. However, for large systems or when the Jacobian is unavailable it is no longer possible to use methods that rely on the Jacobian.

The prototype nonlinear system of equations is the fixed point problem, find $\boldsymbol{x} \in \mathbb{R}^n$ such that

$$g(\boldsymbol{x}) = \boldsymbol{x}, \tag{1}$$

where $g : \mathbb{R}^n \to \mathbb{R}^n$. The fixed point problem can easily be transformed into the self consistent field problem, find $\boldsymbol{x} \in \mathbb{R}^n$ such that

$$f(\boldsymbol{x}) = \boldsymbol{0}, \tag{2}$$

where $f(\boldsymbol{x}) := \boldsymbol{x} - g(\boldsymbol{x})$.

Given an initial guess, $\boldsymbol{x}_0$, equation (2) can be solved by a sufficiently under relaxed fixed point iteration

$$\boldsymbol{x}_{k+1} = \boldsymbol{x}_k - \beta g(\boldsymbol{x}_k). \tag{3}$$

Here $\beta \in (0, 1]$ is the under relaxation parameter. Unfortunately, for several systems $\beta \ll 1$ is necessary for the method to converge, and the rate of convergence suffers. For large systems the evaluation of (2) becomes very expensive, and the convergence rate of the fixed point iteration (3) becomes prohibitively slow.

The number of evaluations of (2) can be reduced by using an accelerator to improve rate of convergence. Electronic structure calculations are often accelerated by Pulay's method [5]. However, while Pulay's method usually converges quickly, it sometimes fails to converge [4, 1, 2]. The secant condition based quasi-Newton method provides a method that is nearly as fast as Pulay's method, while offering improved robustness.

The quasi-Newton method

If the Jacobian of f is unavailable, it is not possible to use Newton's method to solve (2). Instead a quasi-Newton method, where an approximate inverse Jacobian, $\boldsymbol{G}$, is substituted in place of the exact inverse Jacobian. The result of the evaluation of (2) can be used to improve $\boldsymbol{G}$. The quasi-Newton method then becomes

$$\boldsymbol{x}_{k+1} = \boldsymbol{x}_k - \beta \boldsymbol{G}_k \boldsymbol{f}_k, \tag{4}$$

where we set $\boldsymbol{f}_k = f(\boldsymbol{x}_k)$, and use $\boldsymbol{G}_0 = \sigma \boldsymbol{I}$ as the initial approximation of the inverse Jacobian.

There are several available updates for $\boldsymbol{G}$, and Broyden's type 2 update offers a robust low rank update scheme [3, 4, 1]. Broyden's second update is based on requiring that $\boldsymbol{G}_{k+1}$ satisfies the secant condition

$$\boldsymbol{G}_{k+1} \Delta \boldsymbol{f}_k = \Delta \boldsymbol{x}_k \tag{5}$$

in the recently evaluated direction, where $\Delta \boldsymbol{x}_k = \boldsymbol{x}_{k+1} - \boldsymbol{x}_k$ and $\Delta \boldsymbol{f}_k = \boldsymbol{f}_{k+1} - \boldsymbol{f}_k$. It is simultaneously required that $\boldsymbol{G}_{k+1}$ does not change in directions orthogonal to the evaluated direction

$$\boldsymbol{G}_{k+1} \boldsymbol{q} = \boldsymbol{G}_k \boldsymbol{q} \quad \forall \boldsymbol{q} \text{ such that } \boldsymbol{q}^T \Delta \boldsymbol{f}_k = 0. \tag{6}$$

Together these requirements result in the type 2 update formula

$$\boldsymbol{G}_{k+1} = \boldsymbol{G}_k + (\Delta \boldsymbol{x}_k - \boldsymbol{G}_k \Delta \boldsymbol{f}_k) \frac{\Delta \boldsymbol{f}_k^T}{\Delta \boldsymbol{f}_k^T \Delta \boldsymbol{f}_k}. \tag{7}$$

For large systems $\boldsymbol{G}_k$ cannot be directly computed, instead the low rank structure of $\boldsymbol{G}_k$ must be exploited.

The quasi-Newton method provides quick and reliable acceleration. It turns out that the rate of convergence is nearly the same for Pulay's method and the quasi-Newton method. Broyden's update also makes the quasi-Newton method more robust, and it often converges when Pulay's method fails to reach a solution. Furthermore, the convergence rate of the quasi-Newton method is relatively smooth, and the control parameters, β and σ, can be dynamically adjusted to increase performance of the accelerator.

References

[1] K. Baarman, T. Eirola, and V. Havu. Robust acceleration of self consistent field calculations in density functional theory. *J. Chem. Phys.*, 134:134109, 2011.

[2] K. Baarman and J. VandeVondele. A compariston of accelerators for direct energy minimization in electronic structure calculations. *J. Chem. Phys.*, 134:244104, 2011.

[3] H.-r. Fang and Y. Saad. Two classes of multisecant methods for nonlinear acceleration. *Numer. Linear Algebra Appl.*, 16:197, 2009.

[4] L. D. Marks and D. R. Luke. Robust mixing for ab initio quantum mechanical calculations. *Phys. Rev. B*, 78:075114, 2008.

[5] P. Pulay. Convergence acceleration in iterative sequences: The case of SCF iteration. *Chem. Phys. Lett.*, 73:393, 1980.

Proceedings of the 24th Nordic Seminar on Computational Mechanics
J. Freund and R. Kouhia (Eds.)

A discontinuous Galerkin multiscale method for first order hyperbolic equations

Mats G. Larson[1], Axel Målqvist[2], and Robert Söderlund[3]

(1)Professor, Department of Mathematics, Umeå University, S-901-87 Umeå, Sweden, mats.larson@math.umu.se
(2)Assistant Professor, Department of Information Technology, Uppsala University, Sweden, axel.malqvist@it.uu.se
(3)Research Assistant, Department of Mathematics, Umeå University, S-901-87 Umeå, Sweden, robert.soderlund@math.umu.se

Summary. Multiscale problems appear in many applications in the engineering sciences, for instance, composite materials, porous media flow, and fluid mechanics. A common feature of multiscale problems is that they are very computationally challenging and often impossible to solve to an acceptable tolerance, with standard methods, using only one mesh.

Over the last fifteen years several numerical methods have been proposed for solving partial differential equations with rapidly varying coefficients, see e.g. [2, 3]. In a series of papers [5, 6, 4] we have developed an adaptive variational multiscale method (AVMS), and in the present paper we adopt the framework presented in [5], using discontinuous Galerkin basis functions. The method is applied to a hyperbolic model problem with multiscale features in the advection coefficient.

Key words: multiscale, discontinuous Galerkin, hyperbolic problem

Introduction

We seek the concentration u such that,

$$\dot{u} + \operatorname{div}(\boldsymbol{\sigma} u) = f, \qquad \text{in } \Omega \times I,$$

where $I = (0, T)$ is the time interval, f is a source term, and $\boldsymbol{\sigma}$ is a given advection field.

We use a discontinuous Galerkin method of first order, as described in [1], to solve the problem and for some suitable forms $q(\cdot,\cdot)$, $l(\cdot)$ the method reads: find $u_h \in \mathcal{V}_h$ such that

$$\begin{aligned} (\dot{u}_h, v) + q(u_h, v) &= l(v), && \forall v \in \mathcal{V}_h, \forall t \in I, \\ (u_h(t_{n-1}), v) &= (u_{n-1}, v), && \forall v \in \mathcal{V}_h, \end{aligned}$$

where $u_n = u(t_n)$, and u_{n-1} is assumed to be known. Now we introduce the variational multiscale method for this problem: Find $u_h = u_c + u_f$, where $u_c \in \mathcal{V}_c$, $u_f \in \mathcal{V}_f$ such that

$$\begin{aligned} (\dot{u}_c + \dot{u}_f, v_c + v_f) + q(u_c + u_f, v_c + v_f) &= l(v_c + v_f), && \forall v_c \in \mathcal{V}_c, \forall v_f \in \mathcal{V}_f, \forall t \in I, \\ (u_c(t_{n-1}) + u_f(t_{n-1}), v_c + v_f) &= (u_{n-1}, v_c + v_f), && \forall v_c \in \mathcal{V}_c, \forall v_f \in \mathcal{V}_f. \end{aligned}$$

We split this equation into two parts and use an L^2-orthogonal split of the coarse and fine scale

which cancel the terms $(\dot{u}_c, v_f)$, and $(\dot{u}_f, v_c)$

$$\begin{aligned}
(\dot{u}_c, v_c) + q(u_c + u_f, v_c) &= l(v_c), && \forall v_c \in \mathcal{V}_c, \forall t \in I,\\
(u_c(t_{n-1}), v_c) &= (u_{n-1}, v_c), && \forall v_c \in \mathcal{V}_c,\\
(\dot{u}_f, v_f) + q(u_f, v_f) &= l(v_f) - q(u_c, v_f), && \forall v_f \in \mathcal{V}_f, \forall t \in I,\\
(u_f(t_{n-1}), v_f) &= (u_{n-1}, v_f), && \forall v_f \in \mathcal{V}_f.
\end{aligned}$$

We use the partition of unities $\{\varphi_i\}_{i\in\mathcal{N}}$ and $\{\chi_i\}_{i\in\mathcal{N}}$, where $\{\varphi_i\}_{i\in\mathcal{N}}$ are the basis functions for $\mathcal{V}_c$, and where $\chi_i = \frac{1}{d+1}$ on $\text{supp}(\varphi_i)$, and split the fine scale equation into three parts

$$\begin{aligned}
(\dot{u}_{f,l,i}, v_f) + q(u_{f,l,i}, v_f) &= l(\chi_i v_f), && \forall v_f \in \mathcal{V}_f, \forall t \in I,\\
(u_{f,l,i}(t_{n-1}), v_f) &= 0, && \forall v_f \in \mathcal{V}_f,\\
(\dot{u}_{f,0,i}, v_f) + q(u_f, v_f) &= 0, && \forall v_f \in \mathcal{V}_f, \forall t \in I,\\
(u_{f,0,i}(t_{n-1}), v_f) &= (\chi_i u_{n-1}, v_f), && \forall v_f \in \mathcal{V}_f,\\
(\dot{\mathcal{T}}\varphi_i, v_f) + q(\mathcal{T}\varphi_i, v_f) &= -q(\varphi_i, v_f), && \forall v_f \in \mathcal{V}_f, \forall t \in I,\\
(\mathcal{T}\varphi_i(t_{n-1}), v_f) &= 0 && \forall v_f \in \mathcal{V}_f.
\end{aligned}$$

It is important to note that these fine scale problems are decoupled from each other and are all solved on patches ω_i localized around $\text{supp}(\varphi_i)$, which are considerably smaller than the entire domain Ω. If $u_c = \sum_{i\in\mathcal{N}} \alpha_i \varphi_i$, then $u_f = \sum_{i\in\mathcal{N}} \left(u_{f,l,i} + u_{f,0,i} + \alpha_i \mathcal{T}\varphi_i\right)$ and we get the following for the coarse scale equation

$$\begin{aligned}
(\dot{u}_c, v_c) + q(u_c + \mathcal{T}u_c, v_c) &= l(v_c) - q(u_{f,l} + u_{f,0}, v_c), && \forall v_c \in \mathcal{V}_c, \forall t \in I,\\
(u_c(t_{n-1}), v_c) &= (u_{n-1}, v_c), && \forall v_c \in \mathcal{V}_c,
\end{aligned}$$

where $\mathcal{T}u_c = \sum_{i\in\mathcal{N}} \alpha_i \mathcal{T}\varphi_i$, $u_{f,l} = \sum_{i\in\mathcal{N}} u_{f,l,i}$, and $u_{f,0} = \sum_{i\in\mathcal{N}} u_{f,0,i}$.

We focus on how to construct the patches ω_i in order to efficiently and accurately compute the local fine scale solutions. Two types of patches are considered, symmetric patches that increases in size symmetrically around $\text{supp}(\varphi_i)$, and directed patches that increase in size along the advection field $\boldsymbol{\sigma}$, see Figure 1. Convergence results that clearly shows the efficiency of using directed patches are found in Figure 2-3.

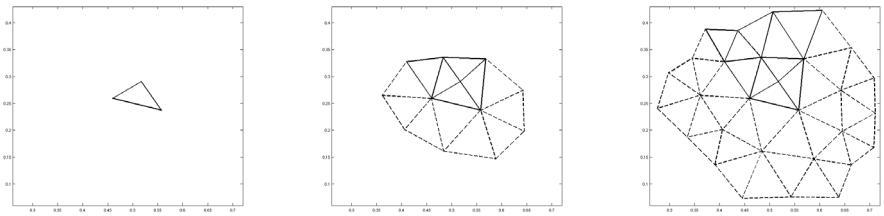

Figure 1. Symmetric (dashed) and directed (solid) type patches as they increase in size. In this illustration we have used $\boldsymbol{\sigma} = [0, 1]$. Note that the directed patches are subsets of the symmetric patches.

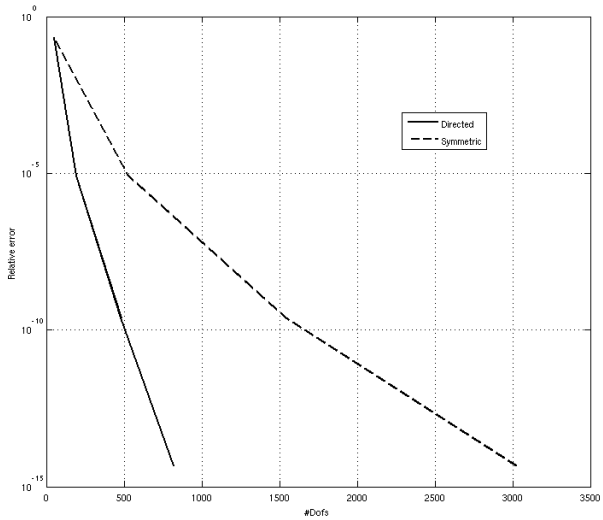

Figure 2. Convergence in H^1-norm of $T\varphi_i$ for the two different kind of patches.

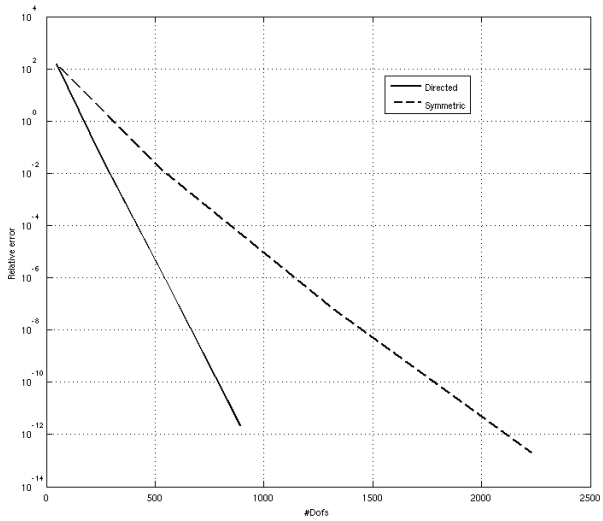

Figure 3. Convergence in H^1-norm of the global solution $u_c + u_f$ for the two different kind of patches.

References

[1] F. Brezzi, L. D. Marini, and E. Süli, *Discontinuous Galerkin methods for first-order hyperbolic problems,* NA-04/02, Oxford University Computing Laboratory, 2004.

[2] Y. R. Efendiev, T. Y. Hou, and X. H. Wu, *Convergence of a nonconforming multiscale finite element method*, SIAM J. Num. Anal., 37 (2000), pp. 888–910.

[3] T. J. R. Hughes, *Multiscale phenomena: Green's functions, the Dirichlet-to-Neumann formulation, subgrid scale models, bubbles and the origins of stabilized methods,* Comput. Methods Appl. Mech. Engrg. 127, (1995), 387–401.

[4] M. G. Larson and A. Målqvist, *Adaptive variational multiscale method of convection-diffusion problems, Comm. Num. Methods Engrg.,* 25, (2009), 65–79.

[5] M. G. Larson and A. Målqvist, *Adaptive variational multiscale methods based on a posteriori error estimation: Energy norm estimates for elliptic problems,* Comput. Methods Appl. Mech. Engrg. 196 (2007) 2313-2324.

[6] M. G. Larson and A. Målqvist, *A mixed adaptive variational multiscale method with applications in oil reservoir simulation,* (to appear in Math. Models Methods Appl. Sci.)

Proceedings of the 24th Nordic Seminar on Computational Mechanics
J. Freund and R. Kouhia (Eds.)

On the emergence of asymmetric waves in the Mindlin–Engelbrecht–Pastrone model.

Kert Tamm[1], Andrus Salupere[2]

CENS, Institute of Cybernetics at Tallinn University of Technology, Akadeemia tee 21 12618 Tallinn, (1)kert@cens.ioc.ee, (2)salupere@ioc.ee

Summary. The subject of the present numerical study is the 1D wave propagation in the microstructured solids making use of the Mindlin–Engelbrecht–Pastrone model. The main focus is on the emergence of asymmetry between waves propagating in the opposite directions.

Key words: Solitary waves, dispersion, nonlinearity, microstructured solids, pseudospectral methods

Introduction

In the present work a model derived by Jüri Engelbrecht and Franco Pastrone [1, 4] is applied to describe wave propagation in nonlinear dispersive media with microstructure. In this model the microelement is taken as a deformable cell with an additional assumption that the deformation gradient is small. The later allows one to express microdeformation in terms of macrodisplacement. Balance laws are formulated separately for the macro- and microscale.

The main goals of the present study are: (i) to solve model equations numerically under localised initial conditions and periodic boundary conditions, (ii) to describe and analyse the emergence of asymmetry between waveprofiles propagating in the opposite directions in the nonlinear cases.

Mindlin–Engelbrecht–Pastrone model

In order to clarify the principal essence and the role of the parameters of the model, we repeat here the basic steps of modeling (see [1, 4] and references therein for details). In the 1D case the Lagrangian L is expressed as: $L = K - W$, where the kinetic energy is $K = \frac{1}{2}\rho u_t^2 + \frac{1}{2} I \varphi_t^2$ and the free (potential) energy can be expressed as $W = W(u_x, \varphi, \varphi_x)$. Here I is the microinertia, φ – the microdeformation, u – the macrodisplacement, ρ – the macroscale density, and partial derivatives are denoted by subscripts. Equations of motion are derived by making use of Euler–Lagrange equations and the free energy as follows:

$$W = \frac{A}{2}u_x^2 + \frac{B}{2}\varphi^2 + \frac{C}{2}\varphi_x^2 + D\varphi u_x + \frac{N}{6}u_x^3 + \frac{M}{6}\varphi_x^3. \tag{1}$$

Here A, B, C, D are material parameters responsible for the linear part of the model and N, M for the nonlinearity. For further analysis dimensionless variables $X = \frac{x}{L_o}$, $T = \frac{\sqrt{A}t}{\sqrt{\rho}L_o}$, $U = \frac{u}{U_o}$, and parameters $\delta = \frac{l_o^2}{L_o^2}$, $\varepsilon = \frac{U_o}{L_o}$ are introduced [3, 4]. Here U_o and L_o are the amplitude and the wavelength of the initial excitation, and l_o is the characteristic scale of the microstructure.

Making use of change of variables one arrives at dimensionless equations of motion

$$\begin{aligned} U_{TT} &= \frac{DL_o}{AU_o}\varphi_X + \frac{NU_o}{AL_o}U_X U_{XX} + U_{XX}, \\ \varphi_{TT} &= \frac{C\rho}{AI}\varphi_{XX} - \frac{B\rho L_o^2}{AI}\varphi - \frac{D\rho U_o L_o}{AI}U_X + \frac{M\rho}{AIL_o}\varphi_X\varphi_{XX}. \end{aligned} \tag{2}$$

Equations (2) are referred to as the full system of equations (the FSE for short) below. Making use of the slaving principle (see [1] for details) allows one to derive a single hierarchical equation in terms of macrodisplacement U from the FSE:

$$U_{TT} - bU_{XX} - \frac{\mu}{2}\left(U_X^2\right)_X = \delta\left(\beta U_{TT} - \gamma U_{XX} + \frac{\lambda\sqrt{\delta}}{2}U_{XX}^2\right)_{XX}. \tag{3}$$

Constants in equation (3) in terms of material and geometrical parameters are $b = 1 - \frac{D^2}{AB}$, $\mu = \frac{NU_o}{AL_o}$, $\beta = \frac{ID^2}{\rho l_o^2 B^2}$, $\gamma = \frac{CD^2}{AB^2 l_o^2}$, $\lambda = \frac{D^3 MU_o}{AB^3 l_o^3 L_o}$. Equation (3) can be considered as an approximation of the FSE (2) and are referred to as the hierarchical equation (HE) below.

Numerical scheme and material parameters

In the present paper the material parameters are combined into two parameters

$$\gamma_A^2 = 1 - b = \frac{D^2}{AB}, \qquad \gamma_1^2 = \frac{\gamma}{\beta} = \frac{\rho C}{AI}. \tag{4}$$

One can interpret γ_1 as the dimensionless speed of short waves and $\sqrt{1-\gamma_A^2}$ as the dimensionless speed of long waves. Parameters γ_A^2 and γ_1^2 combine the linear material parameters in (1) describing macro- and microstructure and interaction between those [1, 5]. Parameters describing nonlinearity in macro– and microscale (μ and λ in (3), respectively) are not combined in here.

The used parameter values are

$$\begin{aligned} &\gamma_A^2 = 0.02\ldots 0.98,\ \gamma_1^2 = 0.02\ldots 0.98,\ A = 117\cdot 10^9,\ D = 5\cdot 10^9, \\ &N = 1\cdot 10^{11},\ M = 5\cdot 10^{10},\ \rho = 8950,\ I = 4475. \end{aligned} \tag{5}$$

Free energy parameter B is used to control the value of γ_A^2 and parameter C to control the value of γ_1^2 from 0.02 up to 0.98. Geometrical parameters are $L_o = 25, \quad l_o = 1$.

In the present paper the pseudospectral method (PSM) based on the discrete Fourier transform (DFT) [2, 6] is applied for the numerical solving of eqs. (2) and (3). The regular PSM algorithm is derived for $u_t = \Phi(u, u_x, u_{2x}, \ldots, u_{mx})$ type equations. In our case, however, we have also a mixed partial derivative term $\delta\beta U_{TTXX}$ in the HE (3) and thus the standard PSM has to be modified [6, 7]. Therefore we rewrite the HE (3) so that all partial derivatives with respect to time are in the left-hand side of the HE and introduce a new variable $\Phi = U - \delta\beta U_{XX}$. After that, making use of properties of the DFT, one can express the variable U and its spatial derivatives in terms of the new variable Φ:

$$U = \mathrm{F}^{-1}\left[\frac{\mathrm{F}(\Phi)}{1+\delta\beta k^2}\right], \qquad \frac{\partial^m U}{\partial X^m} = \mathrm{F}^{-1}\left[\frac{(\mathrm{i}k)^m \mathrm{F}(\Phi)}{1+\delta\beta k^2}\right], \tag{6}$$

where F denotes the Fourier transform and F^{-1} the inverse Fourier transform. Finally, equation (3) can be rewritten in terms of the variable Φ

$$\Phi_{TT} = bU_{XX} + \frac{\mu}{2}\left(U_X^2\right)_X - \delta\left(\gamma U_{XX} - \frac{\lambda\sqrt{\delta}}{2}U_{XX}^2\right)_{XX}. \tag{7}$$

In equation (7) all partial derivatives of U with respect to X are calculated in terms of Φ by using expression (6) and therefore one can apply the PSM for numerical integration of equation (7). The FSE (2) is reduced to the system of first-order differential equations which are solved by the standard PSM without any further modifications.

The HE (3) and FSE (2) are solved under localized initial conditions and periodic boundary conditions $U(X,0) = U_o \mathrm{sech}^2 B_o\,(X - 64\pi)\,,\ U(X,T) = U(X + 128m\pi, T),\ m = 1, 2, \ldots,$ i.e., the total length of the spatial period is 128π. For the amplitude and the width of the initial pulse we use the values $U_o = 1$ and $B_o = \pi/2$. Initial phase speed is taken to be zero. For the FSE (2) two more initial conditions are needed for the microdeformation. We assume that at $T = 0$ the microdeformation and the corresponding velocity are zero, i.e., $\varphi(X,0) = 0$ and $\varphi_T(X,0) = 0$. The integration interval is from zero to $T_f = 180$. In all considered cases two solitary waves that propagate in opposite directions emerge from the initial pulse, however, the spatial period is long enough and the time interval short enough to avoid interactions between emerged solitary waves regardless of periodic boundary conditions.

Results, discussion and conclusions

The dispersion type for the HE can be determined by the sign of quantity $\Gamma = 1 - \gamma_A^2 - \gamma_1^2$, (see [1] for details). If Γ is positive, we have the normal dispersion case, if negative, we have the anomalous dispersion case and if it is equal to zero, we have the dispersionless case. Only the results corresponding to the dispersionless case are presented here and therefore $\gamma_1^2 = 1 - \gamma_A^2$. It should be noted that the FSE has one additional dispersion curve – so called optical (higher frequency) branch.

Under used initial and boundary conditions the initial pulse at $X = 64\pi$ splits into two waves propagating in the opposite directions. Previous studies have shown that in the nonlinear cases these waves evolve differently (see [7] and references therein).

In Fig. 1 waveprofiles for the HE (left panel) and for the FSE (right panel) are plotted at $T_f = 180$ for $\gamma_A^2 = 0.5$ and $\gamma_1^2 = 0.5$. The right pulses are propagating to the right and the left pulses to the left. We introduce a new quantity A_Σ characterising the difference between the waves propagating in opposite directions (normalised against the number of grid points)

$$A_\Sigma = A_\Sigma^l - A_\Sigma^r, \quad A_\Sigma^l = \sum_1^{n/2} \frac{2|U_i|}{n}, \quad A_\Sigma^r = \sum_{n/2+1}^{n} \frac{2|U_i|}{n}, \tag{8}$$

where upper index r denotes the wave propagating to the right, l – the wave propagating to the left, respectively and n – the number of grid points. The quantity A_Σ^l is related to the area of the left pulse ($0 \le X < 64\pi$) and A_Σ^r to the area of the right pulse ($64\pi \le X < 128\pi$).

In the linear cases $A_\Sigma^l = A_\Sigma^r$ for the HE as well as for the FSE and the quantity $A_\Sigma = 0$. In the nonlinear cases, however, $A_\Sigma^l \neq A_\Sigma^r$. In Fig. 2 quantity A_Σ is plotted against parameter γ_A^2 at $T_f = 180$. In general A_Σ increases with increasing γ_A^2. The higher the γ_A^2 the faster the A_Σ increases. Compared to the initial value at $\gamma_A^2 = 0.02$, the quantity A_Σ is increased by 39%, 115% and 195% for the HE and by 22%, 64% and 115% for the FSE at $\gamma_A^2 = 0.5$, 0.8, 0.9, respectively. At low values of γ_A^2 the difference between the HE and FSE is negligible (less than 5% at $\gamma_A^2 = 0.3$ and below). However, the difference between the HE and FSE increases with increasing γ_A^2. Values of A_Σ for the HE exceed these for the FSE by 13%, 32% and 37% at $\gamma_A^2 = 0.5$, 0.8, 0.9, respectively.

It is interesting to note that the additional oscillations emerging in the FSE as a result of the presence of the optical dispersion branch (see Fig. 1) are more prominent for the higher the values of parameter γ_A^2. These oscillations cause the quantities A_Σ^l and A_Σ^r to increase with increasing γ_A^2. However, the quantity A_Σ (that measure the strength of asymmetry) is greater for the HE (where the oscillations do not exist).

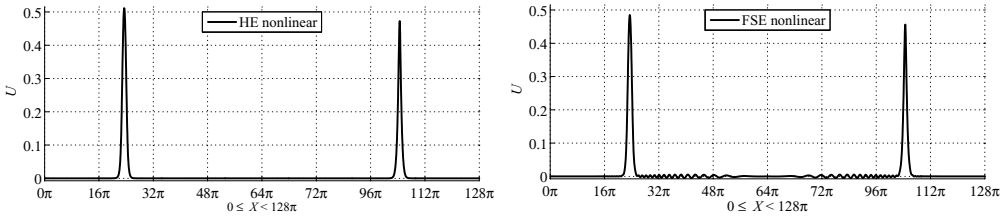

Figure 1. Waveprofiles at $T = 180$ and $\gamma_A^2 = 0.5$ in the dispersionless case.

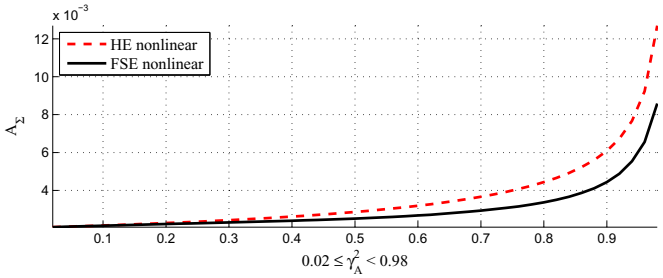

Figure 2. Quantity A_Σ against γ_A^2 at $T = 180$ in the dispersionless case.

To summarise the results we can conclude: (i) the model equations were solved numerically under localised initial conditions and periodic boundary conditions, (ii) in the linear cases the waves propagating to the opposite directions are symmetric with respect to $X = 64\pi$ but in nonlinear cases asymmetric, (iii) under used material parameters the quantity $A_\Sigma^l > A_\Sigma^r$ in the nonlinear cases, (iv) A_Σ increases faster for the HE than for the FSE with increasing γ_A^2, (v) similar asymmetry exists in dispersive cases as well.

Acknowledgments

The research is supported by Estonian Science Foundation Grant No. 7035.

References

[1] J. Engelbrecht, A. Berezovski, F. Pastrone, and M. Braun. Waves in microstructured materials and dispersion. *Philosophical Magazine*, 85(33–35):4127–4141, 2005.

[2] B. Fornberg. *A practical guide to pseudospectral methods.* Cambridge University Press, Cambridge, 1998.

[3] J. Janno and J. Engelbrecht. An inverse solitary wave problem related to microstructured materials. *Inverse Problems*, 21:2019–2034, 2005.

[4] J. Janno and J. Engelbrecht. Solitary waves in nonlinear microstructured materials. *Journal of Physics A: Mathematical and General*, 38:5159–5172, 2005.

[5] T. Peets, M. Randrüüt, and J. Engelbrecht. On modelling dispersion in microstructured solids. *Wave Motion*, 45(4):471–480, 2008.

[6] A. Salupere. The pseudospectral method and discrete spectral analysis. In E. Quak and T. Soomere, editors, *Applied Wave Mathematics*, pages 301–334, Berlin, 2009. Springer.

[7] K. Tamm. *Wave Propagation and Interaction in Mindlin-Type Microstructured Solids: Numerical Simulation.* PhD thesis, Tallinn University of Technology, 2011.

Proceedings of the 24th Nordic Seminar on Computational Mechanics
J. Freund and R. Kouhia (Eds.)

Analysis of volume average relations in continuum mechanics

Aylin Ahadi and Per Lidström

Division of Mechanics, Lund University, P.O. Box 118, S-22100 Lund, Sweden,
aylin.ahadi@mek.lth.se , per.lidstrom@mek.lth.se

Summary. In this paper the volume average relations related to the multilevel modelling process are analyzed and the concept of average consistency is investigated both analytically and numerically.

Key words: volume average relations, computational homogenization, continuum mechanics

Introduction

Volume average relations have become important in applied continuum mechanics due to the growing interest in a numerical procedure known as computational homogenization. This averaging technique, using for instance the unit cell or representative volume element as reference configuration, is useful when considering macroscopic engineering components for which micro-structural features and heterogeneities are of importance. The technique makes it possible to obtain a transition of the mechanical properties from the local, microscopic, to the global, macroscopic, length scale. Various versions of these procedures, presented in a number of papers by Ref. [1-4], among others, have been used by several authors dealing with the modelling of materials for which the microstructure plays an important role for the global behaviour. The basic ideas underlying these procedures rest on the general assumption that the principles of continuum mechanics may be used on the global as well as the local scale, and that these scales are thermo-mechanically interconnected by solving a boundary value problem on the local scale equipped with some suitable constraints, kinematical or others, originating from the global scale. The solution to this boundary value problem is volume averaged in order to obtain the thermo-mechanical response on the global scale.

The RVE as a ”constitutive equation”

As a concrete example we may consider a multilevel model of a cantilever beam with fixed support at one end and loaded by a force $\boldsymbol{W}$ at the other end according to figure 1. below. This is called our global structure. Conventionally, the problem of finding the equilibrium transplacement of the beam is obtained by introducing constitutive equations for the beam material. If the beam is inhomogeneous, involving a mixture of different materials, then a finite

element formulation of the equilibrium equations may lead to problems with the accuracy of the subsequent computation. An alternative analysis of this problem may be done by using a multilevel calculation involving two models; one for the global structure, such as the cantilever beam, and one for the local structure in the shape of a RVE. This RVE, denoted by $\mathcal{R}_\kappa(\hat{X})$, represents a 'close-up picture' of the beam material and gives a detailed representation of it in terms of constitutive equations.

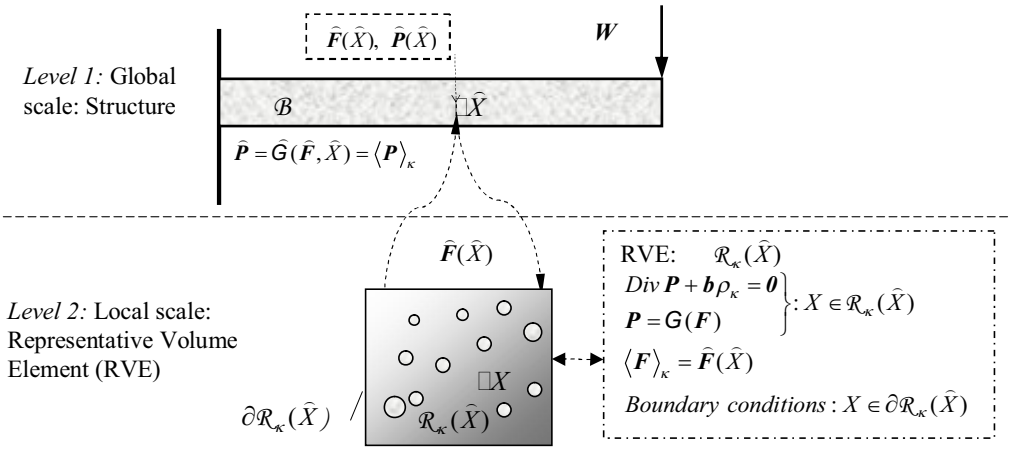

Figure 1. Multi-level model.

Here $\boldsymbol{P} = \boldsymbol{P}(X)$ denotes the first Piola-Kirchhoff stress tensor, $\boldsymbol{b} = \boldsymbol{b}(X)$ is body force field and $\rho_\kappa = \rho_\kappa(X)$ is the mass density in the reference placement of the RVE. The volume average of the deformation gradient is defined by

$$\langle \boldsymbol{F} \rangle_\kappa = \frac{1}{v(\mathcal{R}_\kappa(\hat{X}))} \int_{\mathcal{R}_\kappa(\hat{X})} \boldsymbol{F}(X)\, dv(X) \tag{1}$$

where $v(\mathcal{R}_\kappa(\hat{X}))$ is the volume of the RVE. From the solution to the constrained boundary value problem we obtain the stress tensor $\boldsymbol{P}$ and its volume average may be calculated as

$$\langle \boldsymbol{P} \rangle_\kappa = \langle \boldsymbol{P} \rangle_\kappa(\hat{X}) = \frac{1}{v(\mathcal{R}_\kappa(\hat{X}))} \int_{\mathcal{R}_\kappa(\hat{X})} \boldsymbol{P}(X)\, dv(X) \tag{2}$$

The volume average $\langle \boldsymbol{P} \rangle_\kappa$ is brought back to the global structure. In this way the RVE serves as a 'constitutive equation' for the beam material and one may formally write $\hat{\boldsymbol{P}}(\hat{X}) = \hat{\mathsf{G}}(\hat{\boldsymbol{F}}, \hat{X}) = \langle \boldsymbol{P} \rangle_\kappa(\hat{X})$, where $\hat{\boldsymbol{P}}$ denotes the global stress and $\hat{\mathsf{G}}$ denotes the 'constitutive response function' for the beam material. The equilibrium conditions for the beam are then checked. If they are not fulfilled a change of the equilibrium transplacement of the beam is made and the process is repeated. By this iterative procedure called computational homogenization a unique equilibrium transplacement of the beam may eventually be obtained.

The constrained boundary value problem is obviously over-determined in the sense that, in general, if the displacement vector $\boldsymbol{u}$ or the traction vector $\boldsymbol{t}_\kappa$, are prescribed on the boundary together with $\hat{\boldsymbol{F}}$ then the problem will have no solution. Consequently we cannot choose $\boldsymbol{u}$ and $\boldsymbol{t}_\kappa$ arbitrarily and we have to relax our boundary conditions. There are several ways of doing

this, including so-called 'periodic boundary condition'. For different formulations the global stress will be different. The question then arises which formulation should be used? One guideline for this choice could be the requirement of *average consistency*. It seems reasonable to require that the multilevel modelling procedure should, as far as possible, result in continuum mechanical relations which maintain as much as possible of their general appearance and structure during an averaging procedure.

The continuum mechanical relations

$$\boldsymbol{F} = \boldsymbol{R}\boldsymbol{U}\,,\quad \boldsymbol{C} = \boldsymbol{F}^T\boldsymbol{F}\,,\quad \boldsymbol{B} = \boldsymbol{F}\boldsymbol{F}^T\,,\quad J = \det\boldsymbol{F}$$

$$\boldsymbol{P} = J\boldsymbol{T}\boldsymbol{F}^{-T}\,,\quad \boldsymbol{K} = J\boldsymbol{T}\,,\quad \boldsymbol{S} = J\boldsymbol{F}^{-1}\boldsymbol{T}\boldsymbol{F}^{-T}\,,\quad \boldsymbol{T}^T = \boldsymbol{T}\,,\quad \boldsymbol{P}\boldsymbol{F}^T = \boldsymbol{F}\boldsymbol{P}^T\,,\quad \boldsymbol{S}^T = \boldsymbol{S} \tag{3}$$

where $\boldsymbol{T}$ is the Cauchy stress, $\boldsymbol{K}$ is the Kirchhoff stress and $\boldsymbol{S}$ is the second Piola-Kirchhoff stress tensor, are said to be *volume average consistent* if

$$\langle \boldsymbol{R}\boldsymbol{U}\rangle_\kappa = \langle \boldsymbol{R}\rangle_\kappa \langle \boldsymbol{U}\rangle_\kappa\,,\quad \langle \boldsymbol{C}\rangle_\kappa = \langle \boldsymbol{F}\rangle_\kappa^T \langle \boldsymbol{F}\rangle_\kappa\,,\quad \langle \boldsymbol{B}\rangle = \langle \boldsymbol{F}\rangle_\kappa \langle \boldsymbol{F}\rangle_\kappa^T\,,\quad \langle J\rangle_\kappa = \det\langle \boldsymbol{F}\rangle_\kappa \tag{4a}$$

$$\langle \boldsymbol{P}\rangle_\kappa = \langle J\rangle_\kappa \langle \boldsymbol{T}\rangle \langle \boldsymbol{F}\rangle_\kappa^{-T}\,,\quad \langle \boldsymbol{K}\rangle_\kappa = \langle J\rangle_\kappa \langle \boldsymbol{T}\rangle\,,\quad \langle \boldsymbol{S}\rangle_\kappa = \langle J\rangle_\kappa \langle \boldsymbol{F}\rangle_\kappa^{-1} \langle \boldsymbol{T}\rangle \langle \boldsymbol{F}\rangle_\kappa^{-T} \tag{4b}$$

$$\langle \boldsymbol{T}\rangle^T = \langle \boldsymbol{T}\rangle\,,\quad \langle \boldsymbol{P}\rangle_\kappa \langle \boldsymbol{F}\rangle_\kappa^T = \langle \boldsymbol{F}\rangle_\kappa \langle \boldsymbol{P}\rangle_\kappa^T\,,\quad \langle \boldsymbol{S}\rangle_\kappa^T = \langle \boldsymbol{S}\rangle_\kappa \tag{4c}$$

where the volume averages of a quantity Φ are defined according to

$$\langle \Phi\rangle = \frac{1}{v(\mathcal{R})}\int_{\mathcal{R}} \phi(x)\,dv(x)\,,\quad \langle \Phi\rangle_\kappa = \frac{1}{v(\mathcal{R}_\kappa)}\int_{\mathcal{R}_\kappa} \Phi(X)\,dv(X) \tag{5}$$

$\langle \Phi\rangle$ is called the *spatial volume average* and $\langle \Phi\rangle_\kappa$ the referential volume average of the quantity Φ. Inconsistencies may appear in connection with, for instance, the polar decomposition of the deformation gradient, i.e. $\langle \boldsymbol{F}\rangle_\kappa = \langle \boldsymbol{R}\boldsymbol{U}\rangle_\kappa \neq \langle \boldsymbol{R}\rangle_\kappa \langle \boldsymbol{U}\rangle_\kappa$. The inconsistence may be quantified by *inconsistency ratio* I defined by

$$I(\boldsymbol{R}\boldsymbol{U}) = \frac{\left|\langle \boldsymbol{R}\boldsymbol{U}\rangle_\kappa - \langle \boldsymbol{R}\rangle_\kappa \langle \boldsymbol{U}\rangle_\kappa\right|}{\left|\langle \boldsymbol{R}\boldsymbol{U}\rangle_\kappa\right|} \tag{6}$$

The volume average relations in (4) are analyzed and the concept of average consistency is investigated for three type of boundary conditions - the periodical, affine and anti-periodical boundary condition. It can be shown analytically, see Ref. [5], that average stress relations in (4b) and (4c) are fulfilled, assuming the periodical boundary condition, whereas the average relations in (4a) are in general not average consistent. Therefore these relations were investigated also numerically.

Numerical investigation

The numerical example consists of a square shaped RVE and as a constitutive law a hyper elastic material of Neohookean type is assumed. For large strain hyper elastic material the Cauchy stress can be derived from the strain energy function given by the deformation gradient. The logarithmic strain is introduced as a strain measure as $\boldsymbol{\varepsilon} = \ln \boldsymbol{V}$, where $\boldsymbol{V} = \left(\boldsymbol{F}\boldsymbol{F}^T\right)^{1/2}$ is the left stretch tensor. The inhomogeneities are introduced and periodic boundary conditions are applied. The displacement is prescribed on the two vertical boundaries of the RVE, where as the horizontal boundaries are traction free. The periodic boundary conditions are applied as constrains, which reduces the number of equation. In figure.1 the deformed shape of the RVE is presented. Result for different inconsistency ratio for both homogeneous and in homogeneous RVE, are seen in table 1.

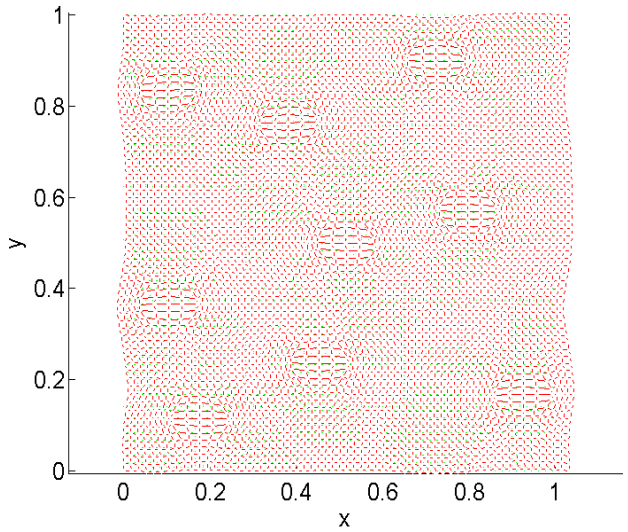

Figure 2. Inhomogeneous RVE subjected to periodic boundary condition.

Table 1. Inconsistency ratios

Average relations	Homogeneous material	Inhomogeneous material
Kirshhoff stress, $\boldsymbol{K}$	3.31×10^{-9}	6.03×10^{-5}
Cauchy stress, $\boldsymbol{T}$	1.63×10^{-9}	3.28×10^{-5}
1st Piola-Kirshhoff stress, $\boldsymbol{P}$	3.32×10^{-9}	6.03×10^{-5}
2nd Piola-Kirshhoff stress, $\boldsymbol{S}$	3.14×10^{-9}	7.63×10^{-5}
Right Cauchy-Green tensor, $\boldsymbol{C}$	2.87×10^{-10}	2.66×10^{-5}
Left Cauchy-Green tensor, $\boldsymbol{B}$	3.55×10^{-10}	2.30×10^{-5}
decomposition $\boldsymbol{F}=\boldsymbol{VR}$	5.71×10^{-11}	2.22×10^{-6}
decomposition $\boldsymbol{F}=\boldsymbol{RU}$	6.11×10^{-11}	2.72×10^{-6}

References

[1] R. Hill, On constitutive macro-variables for heterogeneous solids in finite strain. *Proc. R. Soc. Lond. A*., **326**: 131-147, 1972.

[2] J. Mandel, *Plasticité classique et viscoplasticité*. Springer-Verlag, Vienna, 1971. (CISM lecture Notes, Udine, Italy).

[3] K.S Havner, A discrete model for the prediction of subsequent yield surfaces in polycrystalline plasticity. *Int J. Solids Structures*, **7**:719-730, 1971.

[4] P. Suquet, Elements of Homogenization for Inelastic Solid Mechanics. In, *Homogenization Techniques for Composite Mechanics*, 193 – 278, 1987.

[5] A. Ahadi, P.Lidström, On Analysis of volume average relations in continuum mechanics, *Division of Mechanics, Lund University*, 2011.

Proceedings of the 24th Nordic Seminar on Computational Mechanics
J. Freund and R. Kouhia (Eds.)

Chloride transport in concrete modeled by the FE^2-method

F. Nilenius[1,2,†], F. Larsson[2], K. Lundgren[1], and K. Runesson[2]

(1)Department of Civil and Environmental Engineering, Chalmers University of Technology, Sven Hultins gata 8A, 412 96 Göteborg, Sweden
(2)Department of Applied Mechanics, Chalmers University of Technology, Hörsalsvägen 7B, 412 96 Göteborg, Sweden
(†) filip.nilenius@chalmers.se

Summary. An FE^2-method is employed for modeling diffusion of chloride ions in concrete. Concrete is considered on the mesoscale, within a representative volume element (RVE), as a heterogeneous composite material consisting of the cement paste, ballast and the interfacial transition zone (ITZ). In addition, the proposed model accounts for the fact that the diffusion of chloride ions is cross-coupled to the diffusion of moisture.

Key words: chloride ions, concrete, diffusion, FE^2, moisture.

Introduction

Chloride ions are harmful for concrete structures as the ions can initiate corrosion of embedded reinforcement bars. Modeling and simulation of chloride diffusion is therefore of interest in order to be able to predict time spans at which corrosion may be initiated.

In this contribution, a FE^2-method for coupled chloride-moisture diffusion is proposed where the strongly heterogeneous mesoscale structure of concrete is accounted for. The model is based on the concept of a representative volume element (RVE) where the mesoscale constituents of concrete in terms of cement paste, ballast and the interfacial transition zone (ITZ) are contained. Here, the ITZ is interface between the cement paste and the ballast, having much higher porosity than the bulk cement paste. In the model it is assumed that the cement paste is permeable, the ballast is impermeable and the ITZ is highly permeable.

An algorithm for generating the mesoscale structure of concrete has been developed and examples of generated structures are shown in Figure 1. Main control parameters of the algorithm are ballast content and sieve curve. Note though, that since the modelled geometry is in 2D, it will not exactly correspond to concrete with a given (3D) sieve curve.

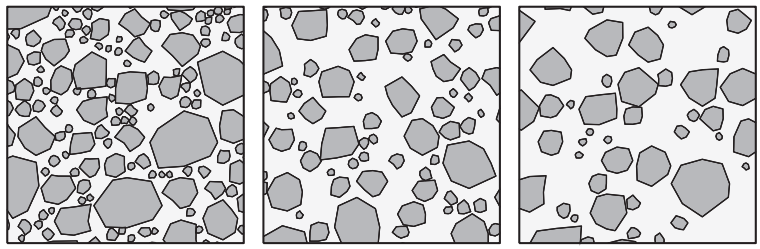

(a) $n_b \approx 60\%$ (b) $n_b \approx 50\%$ (c) $n_b \approx 40\%$

Figure 1: Examples of different mesoscale structures generated by the algorithm. n_b denotes the ballast fraction.

Computationally, the approach is to introduce the RVE in the Gauss-points on the macroscale domain in a so-called FE^2-algorithm, with its principal structure depicted in Figure 2. In this manner, the idea is to let the RVE serve as a constitutive model for the macroscale.

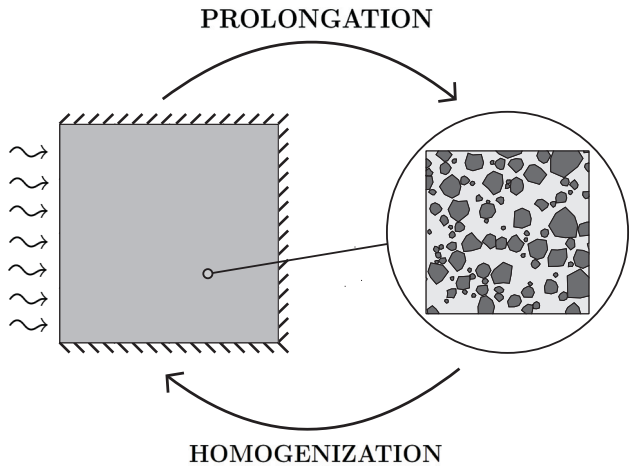

Figure 2: The RVE (right) is introduced in the Gauss-points on the macroscale (left). Macroscale quantities of $\bar{H}$ and $\bar{C}$ are used to set up Dirichlet boundary conditions (prolongation), a boundary value problem on the RVE is solved, and the solution is homogenized and sent back to the macroscale.

Problem formulation

The FE^2-framework used in this work was developed in Larsson et al. [1] for transient heat flow and is here adopted for coupled diffusion phenomena. Mathematically, the problem is formulated using the mass conservation laws stating that

$$\partial_t \Phi_{\mathrm{H}} + \boldsymbol{\nabla} \cdot \boldsymbol{J}_{\mathrm{H}} = 0 \quad \text{in } \Omega \times [0,T] \tag{1}$$

$$\partial_t \Phi_{\mathrm{C}} + \boldsymbol{\nabla} \cdot \boldsymbol{J}_{\mathrm{C}} = 0 \quad \text{in } \Omega \times [0,T] \tag{2}$$

where $\Omega \subset \mathbb{R}^3$ is an arbitrary spatial domain of unit thickness bounded by Γ, and where $\boldsymbol{\nabla}$ is the spatial gradient with respect to coordinates $\boldsymbol{x}$ in Ω. $\Phi_{\mathrm{H}}(\boldsymbol{x},t)$ and $\Phi_{\mathrm{C}}(\boldsymbol{x},t)$ denote the

moisture and chloride ion content, respectively, and $\boldsymbol{J}_{\mathrm{H}}(\boldsymbol{x},t)$ and $\boldsymbol{J}_{\mathrm{C}}(\boldsymbol{x},t)$ denote the moisture- and chloride ion flux, respectively. The explicit choice of constitutive relations for the cement paste, used on the meso-scale, for the flux vectors is taken from Ababneh et al. [2]:

$$\boldsymbol{J}_{\mathrm{H}}(H,C;\boldsymbol{\nabla}H,\boldsymbol{\nabla}C) = -D_{\mathrm{H}}(H)\boldsymbol{\nabla}H - \varepsilon_{\mathrm{C}}D_{\mathrm{C}}(H,C)\boldsymbol{\nabla}C \tag{3}$$

$$\boldsymbol{J}_{\mathrm{C}}(H,C;\boldsymbol{\nabla}H,\boldsymbol{\nabla}C) = -\varepsilon_{\mathrm{H}}D_{\mathrm{H}}(H)\boldsymbol{\nabla}H - D_{\mathrm{C}}(H,C)\boldsymbol{\nabla}C \tag{4}$$

where H is the relative humidity in the cement pores and C is the chloride concentration. Furthermore, D_{H} and D_{C} are diffusive coefficients and ε_{H} and ε_{C} are coupling parameters.

Numerical example

In Figure 3, a numerical example of a two scale (FE^2) simulation is presented.

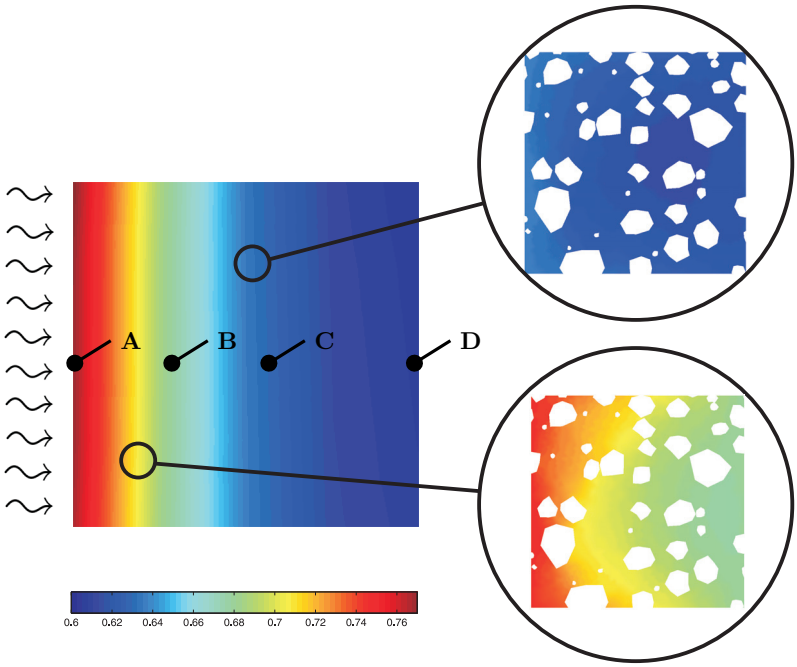

Figure 3: Snapshot of transient solution to $\bar{H}$, for a given time step. The smooth solution on the macroscale (left) is obtained by homogenization of the non-smooth RVE responses (right).

In Figures 4 and 5, the time evolution of $\bar{H}$ and $\bar{C}$ are presented from FE^2-simulations as shown in Figure 3.

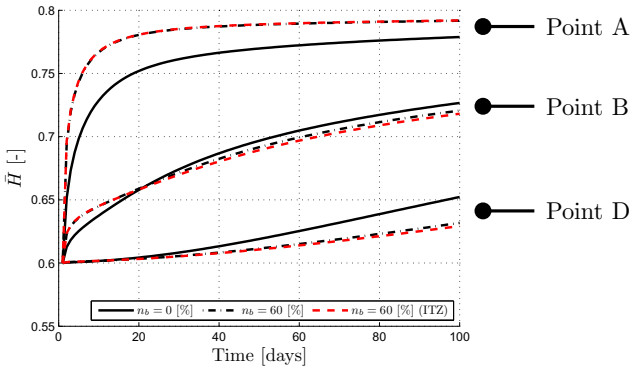

Figure 4: Time evolution of $\bar{H}$ for varying values of n_b in the RVE, in different points in the macroscale domain. The red line has the ITZ included in the RVE. Point A,B and D are defined in Figure 3.

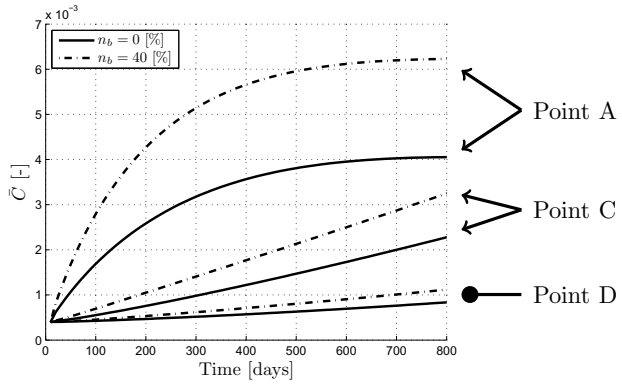

Figure 5: Time evolution of $\bar{C}$ for varying values of n_b in the RVE, in different points in the macroscale domain. Point A,C and D are defined in Figure 3.

Conclusions

By employing a FE^2-method for modeling transport phenomena in concrete, the strongly heterogeneous structure of the material can be accounted for. This method enables modeling of concrete as a heterogeneous material by actually consider it as a composition of three materials, namely the cement paste, ballast and ITZ.

References

[1] F. Larsson, K. Runesson, F. Su, Variationally consistent computational homogenization of transient heat flow, *International Journal for Numerical Methods in Engineering*, Vol. 81, No 13, pp 1659–1686, 2009.

[2] A. Ababneh, F. Benboudjema, Y. Xi, Chloride Penetration in Nonsaturated Concrete, *Journal of Materials in Civil Engineering*, Vol. 15, No 2, pp 183-191, 2003.

Proceedings of the 24th Nordic Seminar on Computational Mechanics
J. Freund and R. Kouhia (Eds.)

Multiscale modeling of porous media

Carl Sandström*, Fredrik Larsson, Håkan Johansson and Kenneth Runesson

*Department of Applied Mechanics
Chalmers University of technology
SE-412 96 Göteborg, Sweden
e-mail: carl.sandstrom@chalmers.se

Summary. Homogenization of a Stokes flow in an open pore system is studied. The homogenization results in a Darcy flow on the macroscale. On the heterogeneous subscale, a (possibly nonlinear) Stokes flow problem is formulated on a Representative Volume Element (RVE). As a coupling between the macroscale and the subscale, the macroscale pressure gradient is used. The prolongation of the Darcy flow fulfills the Variationally Consistent Macrohomogeneity Condition.

Key words: porous media, FE^2, computational homogenization

Introduction

Porous materials are present in many natural as well as engineered structures e.g sandstone which contains oil and different kinds of filters. On the subscale, the material has a strongly heterogeneous composition consisting of a solid matrix with fluid filled pores, while on the macroscale the material is often modeled as homogeneous using an averaged constitutive relation. Due to the complexity of the substructure in this kind of materials, it is difficult to make an accurate model on the macroscopic level, thus exploring the possibilities of a multiscale approach is a natural step, see e.g [1].

On the macroscale a Darcy flow is present which is solved using the Finite Element Method. However, instead of using a conventional constitutive relation associating the seepage velocity to the pressure gradient, another Finite Element problem is solved in each Gausspoint in order to produce the velocity given the pressure gradient. The problem solved in each Gausspoint is referred to as the subscale problem. This problem consists of a Stokes flow that is solved for on a Representative Volume Element (RVE)[2] which is geometrically a representation of the substructure of the porous medium. The solution to the subscale problem is homogenized and the result is returned to the macroproblem. The procedure presented in this work is a generalization of classic homogenization, following along the lines in [3].

Fully resolved Stokes flow

Consider a fully resolved domain Ω consisting of an open pore system Ω^{F} and solid obstacles which are assumed to be rigid. The boundary Γ^{F} is the part of $\Gamma := \partial\Omega$ which intersects the boundary of Ω^{F}, i.e. the part of Γ where fluid can enter or exit the domain. Furthermore, the boundary Γ^{int} is introduced as the part of $\partial\Omega^{\mathrm{F}}$ which is contained inside Ω, i.e. the boundaries of the obstacles in the porous domain.

The strong form of the Stokes flow on the fully resolved domain is then given as

$$-\boldsymbol{\nabla}\cdot\boldsymbol{\sigma}\left(\boldsymbol{l},\ p\right)=\mathbf{0} \qquad \text{in } \Omega^{\mathrm{F}} \tag{1a}$$

$$\boldsymbol{\nabla}\cdot\boldsymbol{v}=0 \qquad \text{in } \Omega^{\mathrm{F}} \tag{1b}$$

$$\boldsymbol{t}\overset{\text{def}}{=}\boldsymbol{\sigma}\cdot\boldsymbol{n}=-\hat{p}\boldsymbol{n} \qquad \text{on } \Gamma_{\mathrm{P}}^{\mathrm{F}} \tag{1c}$$

$$\boldsymbol{v}=\hat{v}_n\boldsymbol{n} \qquad \text{on } \Gamma_{\mathrm{V}}^{\mathrm{F}} \tag{1d}$$

$$\boldsymbol{v}=\mathbf{0} \qquad \text{on } \Gamma_{\mathrm{int}}^{\mathrm{F}} \tag{1e}$$

where $\boldsymbol{\sigma}$ is the Caucy stress tensor and $\boldsymbol{l}$ is the velocity gradient tensor. Furthermore, $\hat{p}$ is the prescribed pressure on $\Gamma_{\mathrm{P}}^{\mathrm{F}}$ and $\hat{v}_n$ is the prescribed velocity normal to the boundary $\Gamma_{\mathrm{V}}^{\mathrm{F}}$. In standard fashion, the total stress is split up into a (generally nonlinear) deviatoric part $\boldsymbol{\sigma}^{\mathrm{v}}$ and a hydrostatic pressure part p as

$$\boldsymbol{\sigma}(\boldsymbol{l})=\boldsymbol{\sigma}^{\mathrm{v}}(\boldsymbol{l})-p\boldsymbol{I} \tag{2}$$

We proceed by splitting the pressure p into a smooth macroscale part p^{M} and a fluctuating, non-smooth subscale part p^{S}. The weak form of the problem is given as that of finding $(\boldsymbol{v},\ p^{\mathrm{M}},\ p^{\mathrm{S}})\in\mathcal{V}\times\mathcal{P}_{\mathrm{F}}^{\mathrm{M}}\times\mathcal{P}_{\mathrm{F}}^{\mathrm{S}}$ such that

$$\int_{\Omega^{\mathrm{F}}}\boldsymbol{\sigma}^{\mathrm{v}}(\boldsymbol{l}):[\delta\boldsymbol{v}\otimes\boldsymbol{\nabla}]-\boldsymbol{\nabla}p^{\mathrm{M}}\cdot\boldsymbol{v}+p^{\mathrm{S}}(\boldsymbol{\nabla}\cdot\boldsymbol{v})\mathrm{d}V=0 \tag{3a}$$

$$\int_{\Omega^{\mathrm{F}}}\delta p^{\mathrm{S}}\left[\boldsymbol{\nabla}\cdot\boldsymbol{v}\right]-\boldsymbol{v}\cdot\boldsymbol{\nabla}\delta p^{\mathrm{M}}\mathrm{d}V=-\int_{\Gamma_{\mathrm{V}}^{\mathrm{F}}}\hat{v}_n\delta p^{\mathrm{M}}\mathrm{d}S \tag{3b}$$

holds for all $\delta\boldsymbol{v}\in\mathcal{V}^0$ and all $(\delta p^{\mathrm{S}},\ \delta p^{\mathrm{M}})\in\mathcal{P}_{\mathrm{F}}^{\mathrm{S},0}\times\mathcal{P}_{\mathrm{F}}^{\mathrm{M},0}$. Here, we introduced the linear trail spaces $\mathcal{V}^0\times\mathcal{P}_{\mathrm{F}}^{\mathrm{S},0}\times\mathcal{P}_{\mathrm{F}}^{\mathrm{M},0}$.

Homogenization and separation of scales

To proceed, we consider the case that the we want to solve the Stokes flow problem in the previous section on two connected scales; the macroscale Ω and the subscale $\Omega_\square$. The subscale domain $\Omega_\square$ is referred to as a Representative Volume Element (RVE) and represent the subscale geometry and fluid properties. Furthermore, the macroscale pressure p^{M} is assumed to vary linearly inside each RVE, thus first order homogenization is adopted. On the macroscale, the smooth pressure $\bar{p}$ is introduced and the macroscale and subscale are connected by the respective pressure gradients, i.e. $\boldsymbol{\nabla}\bar{p}=\boldsymbol{\nabla}p^{\mathrm{M}}$ where $\bar{p}$ exists on the entire Ω and p^{M} exists on the RVE only.

For the subsequent homogenization, the intrinsic volume averaging for an arbitrary function f is introduced as

$$\langle f\rangle_\square=\frac{1}{|\,\Omega_\square^{\mathrm{F}}\,|}\int_{\Omega_\square^{\mathrm{F}}}f\,\mathrm{d}V \tag{4}$$

Using Equation 4, the weak form in Equation 3 can be restated as that of finding $(\boldsymbol{v},\ p^{\mathrm{M}},\ p^{\mathrm{S}})\in\mathcal{V}\times\mathcal{P}_{\mathrm{F}}^{\mathrm{M}}\times\mathcal{P}_{\mathrm{F}}^{\mathrm{S}}$ such that

$$\int_{\Omega^{\mathrm{F}}}\phi\left\langle\boldsymbol{\sigma}^{\mathrm{v}}(\boldsymbol{l}):[\delta\boldsymbol{v}\otimes\boldsymbol{\nabla}]+p^{\mathrm{S}}(\boldsymbol{\nabla}\cdot\boldsymbol{v})\right\rangle_\square\mathrm{d}V=\int_{\Omega^{\mathrm{F}}}\phi\left\langle\boldsymbol{\nabla}p^{\mathrm{M}}\cdot\boldsymbol{v}\right\rangle_\square\mathrm{d}V \tag{5a}$$

$$\int_{\Omega^{\mathrm{F}}}\phi\left\langle\delta p^{\mathrm{S}}\left[\boldsymbol{\nabla}\cdot\boldsymbol{v}\right]\right\rangle_\square\mathrm{d}V=0 \tag{5b}$$

$$-\int_{\Omega}\phi\left\langle\boldsymbol{v}\cdot\boldsymbol{\nabla}\delta p^{\mathrm{M}}\right\rangle_\square\mathrm{d}V=-\int_{\Gamma_{\mathrm{V}}}\phi\left\langle\left\langle\hat{v}_n\delta p^{\mathrm{M}}\right\rangle\right\rangle_\square\mathrm{d}V \tag{5c}$$

for all $\delta\boldsymbol{v} \in \mathcal{V}^0$ and all $(\delta p^{\mathrm{S}},\ \delta p^{\mathrm{M}}) \in \mathcal{P}_{\mathrm{F}}^{\mathrm{S},0} \times \mathcal{P}_{\mathrm{F}}^{\mathrm{M},0}$ where $\phi = \frac{|\Omega_{\square}^{\mathrm{F}}|}{|\Omega_{\square}|}$ is the porosity and $\bar{\boldsymbol{w}}$ is the seepage velocity defined as

$$\bar{\boldsymbol{w}} = \phi \, \langle \boldsymbol{v} \rangle_{\square}$$

In Equation 5c, we introduced the surface average $\langle\langle \bullet \rangle\rangle$ required for the homogenization of velocity boundary conditions.

The macroscale problem

Using the definition of the seepage velocity and Equation 5c together with the condition that $\boldsymbol{\nabla}\bar{p} = \boldsymbol{\nabla} p^{\mathrm{M}}$, the macroscale equation is given as

$$-\int_{\Omega^{\mathrm{F}}} \bar{\boldsymbol{w}}(\boldsymbol{\nabla}\bar{p}) \cdot \boldsymbol{\nabla}\delta\bar{p} \, \mathrm{d}V = -\int_{\Gamma_{\mathrm{D}}^{\mathrm{F}}} \hat{w}_n \delta p^{\mathrm{M}} \mathrm{d}S \tag{6}$$

which is identified as the weak form of the continuity equation. Thus, the macroscale problem is a Darcy flow where $\bar{\boldsymbol{w}}(\boldsymbol{\nabla}\bar{p})$ is evaluated on the subscale.

The subscale problem

From Equations 5a and 5b, the subscale problem is given as that of finding $(\boldsymbol{v},\, p^{\mathrm{S}}) \in \mathcal{V}_{\square} \times \mathcal{P}_{\square}^{\mathrm{S}}$ such that

$$\frac{1}{|\,\Omega_{\square}\,|} \int_{\Omega_{\square}^{\mathrm{F}}} \boldsymbol{\sigma}^{\mathrm{v}}(\boldsymbol{l}) : [\delta\boldsymbol{v} \otimes \boldsymbol{\nabla}] - p^{\mathrm{S}} \, [\boldsymbol{\nabla} \cdot \delta\boldsymbol{v}] \, \mathrm{d}V = \frac{1}{|\,\Omega_{\square}\,|} \left(-\int_{\Omega_{\square}^{\mathrm{F}}} \delta\boldsymbol{v} \cdot \boldsymbol{\nabla}\bar{p} \, \mathrm{d}V + \int_{\Gamma^{\mathrm{F}}} \boldsymbol{t}^{\mathrm{S}} \cdot \delta\boldsymbol{v} \, \mathrm{d}S \right) \tag{7a}$$

$$\frac{1}{|\,\Omega_{\square}\,|} \int_{\Omega_{\square}^{\mathrm{F}}} \delta p^{\mathrm{S}} \, [\boldsymbol{\nabla} \cdot v] \, \mathrm{d}V = 0 \tag{7b}$$

for all $\delta\boldsymbol{v} \in \mathcal{V}_{\square}^0$ and all $\delta p^{\mathrm{S}} \in \mathcal{P}_{\square}^{\mathrm{S},0}$.

As a special case, we now consider periodic boundary conditions, whereby we assume $\boldsymbol{v} \in \mathcal{V}_{\square}$ and $p^{\mathrm{S}} \in \mathcal{P}_{\square}^{\mathrm{S}}$ to be periodic and the subscale traction $\boldsymbol{t}^{\mathrm{S}}$ to be anti-periodic. Note that the boundary integral in Equation 7a is a result from the decomposition of Ω into RVEs $\Omega_{\square}$. It can be shown that for periodic boundary conditions, this boundary integral vanish, thus assuring equilibrium.

Numerical results

The example below illustrates how a RVE is used as a constitutive model in a macroscopic problem. On the left hand side of the macroscale domain (the L shaped domain), a pressure of 100 Pa is applied while on the north most part of the domain a pressure of 0Pa is used, resulting in a flow through the domain. Along the walls, a Neumann condition is used to prevent seepage in the normal direction. On the subscale, the macroscopic pressure gradient is used as a body-load along with periodic boundary conditions.

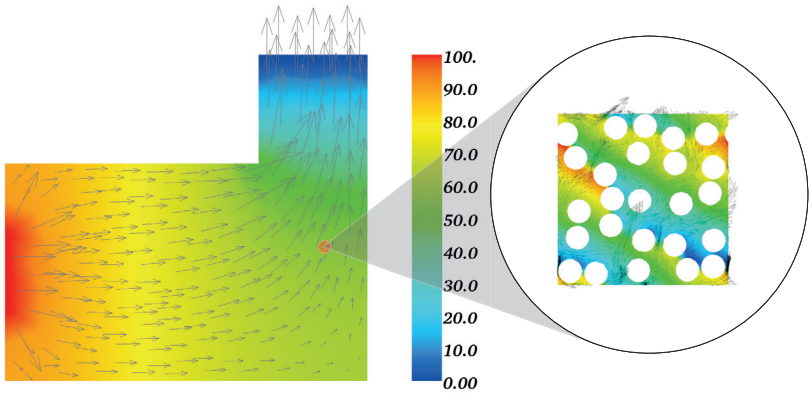

Figur 1. The domain on the left is the macroscale domain exposed to a pressure gradient. In each Gauss point, the pressure gradient is imposed on a RVE in order to compute the seepage velocity.

Conclusions and outlook

It is shown how a Stokes flow in an open pore system is turned into a two-scale problem consisting of a Darcy flow on the macroscale and a Stokes flow on the subscale. The method described herein is capable of performing coupled subscale-macroscale computations involving non-linear fluids.

Future work includes an extension to a deformable solid matrix which calls for a transition from 2D to 3D. Moreover, since concurrent multiscale is computationally expensive, an incorporation of adaptive techniques is of interest.

References

[1] E. Sánchez-Palencia, *Non-homogeneous media and vibration theory.* Springer-Verlag, 1980.

[2] T. I. Zohdi and P. Wriggers, *An introduction to computational micromechanics.* Springer-Verlag, 2008.

[3] F. Larsson, K. Runesson, and F. Su, "Variationally consistent computational homogenization of transient heat flow," *International Journal for Numerical Methods in Engineering*, 2009.

Proceedings of the 24th Nordic Seminar on Computational Mechanics
J. Freund and R. Kouhia (Eds.)

Minimizing structure-borne noise of rotating machinery in the room of a light-weight building

Bin Niu[1], Niels Olhoff[1], and Jan Balle Larsen[2]

(1) Department of Mechanical and Manufacturing Engineering, Aalborg University, DK-9220 Aalborg, Denmark, {bni, no}@m-tech.aau.dk
(2) Grundfos Management A/S, DK-8850 Bjerringbro, Denmark, janballelarsen@grundfos.com

Summary. This article deals with the problem of minimizing the structure-borne noise level in a room transmitted from unbalanced rotating machinery. The machine is mounted via resilient mounts on the roof of the room. The resilient mounts will be optimized for the noise reduction. A generalized formulation using the mobility and impedance is developed for analysis and optimization of the system consisting of the machine, resilient mounts, the floor plate and the room cavity. Numerical examples are provided for validation of the method.

Key words: rotating machine, structure-borne noise, resilient mounts, light-weight building

Introduction

Rotating machinery is often installed in buildings for various applications such as in central heating and ventilation systems. The machinery is normally mounted on a floor of the storey via some resilient mounts. Due to the existence of dynamic forces of e.g. mechanical, fluid dynamic or electro-magnetic origin, the rotating machinery may be considered a source that within a given range of excitation frequencies excites forced vibration of the foundation, and thereby the floors and walls, etc., of the building. The transmission of such vibrations through the building may result in undesirable sound emission. The minimization of vibration and noise transmission is studied in this paper.

Analysis formulation

The mobility and impedance approach is adopted to analyze the installation system of the machinery. The transmitted force $\mathbf{F}^d$ from the machine to the floor plate can be found in our previous work Ref. [1]. Furthermore, using the modal approach, and assuming weak coupling, the equation for the acoustic pressure in the room is given by

$$p = \mathbf{Z}_a \mathbf{C} \mathbf{Y}_s \mathbf{g}^d \tag{1}$$

where $\mathbf{Z}_a$ is the uncoupled acoustic modal impedance matrix, $\mathbf{C}$ the structural-acoustic mode shape coupling matrix, $\mathbf{Y}_s$ the uncoupled structural modal mobility matrix, and $\mathbf{g}^d$ is the generalized modal force given by

$$\mathbf{g}^d = \int_{S_f} \mathbf{\Phi} \mathbf{F}^d dS \tag{2}$$

In Eq. (2), $\mathbf{\Phi}$ denotes the uncoupled vibration mode shape functions of the floor plate, and S_f is the surface area of the floor plate. Detailed derivation of modal impedance and mobility matrices is available in Refs. [1] and [2].

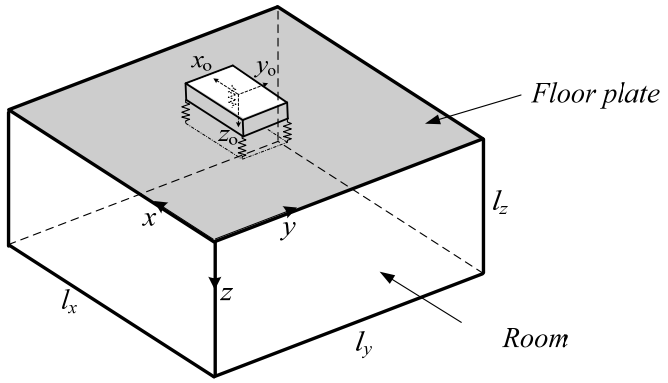

Figure 1. A schematic illustration of the machine installation via resilient mounts on the building floor connected with an acoustic cavity.

Modeling of resilient mounts

A convenient way to isolate vibration of machinery is to use polymer or rubber-like material as resilient mounts, which are called mass-less compression mounts. A novel periodic mount in Ref. [3] termed as periodic shear mount is applied in the computation as a comparison, where the rubber-like material is in a shear deformation mode rather than compression mode. The acoustic pressure using different resilient mounts will be compared to determine the optimum selection for the installation of machinery.

Numerical examples

As indicated in Figure 1, the border of the enclosure consists of five acoustically rigid walls and a simply supported flexible plate on the remaining side, where an unbalanced rotating machine is installed. The material and geometric parameters of the structure and acoustic medium are given in Tables 1 and 2.

Figure 2 shows the acoustic pressure at the central point inside the cavity for softer and stiffer compression resilient mounts, and for the rigid connection as a comparison. The comparison of acoustic pressure at the central point is given in Figure 3 for three cases using rigid connection, compression mount and periodic shear mount.

Table 1. Material parameters of the building floor plate.

Young's modulus E	6×10^9 Pa
Poisson's ratio v	0.1
length l_x	6 m
width l_y	4 m
thickness h	0.05m
Mass density ρ	455 kg/m^3
Damping ratio ζ	0.01

Table 2. Material parameters of the acoustic medium (air) in the room.

Mass density ρ_a	1.21 kg/m^3
Phase speed	343 m/s
length l_x	6 m
width l_y	4 m
height l_z	3 m
Damping ratio ζ_a	0.01

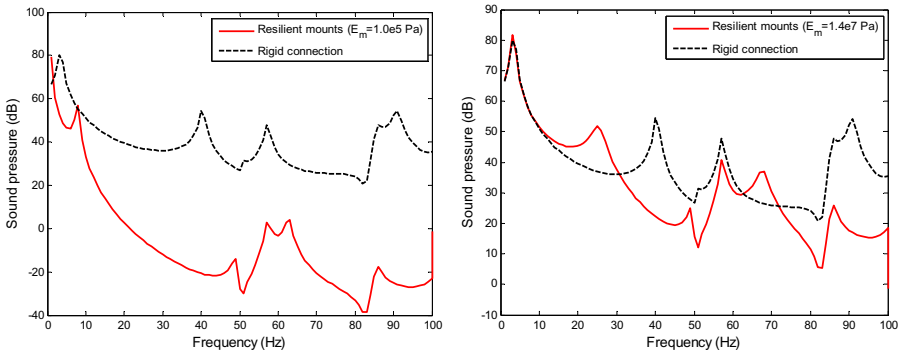

(a) (b)

Figure 2. Acoustic pressure at the central point inside the cavity: (a) softer compression resilient mounts, (b) stiffer compression resilient mounts.

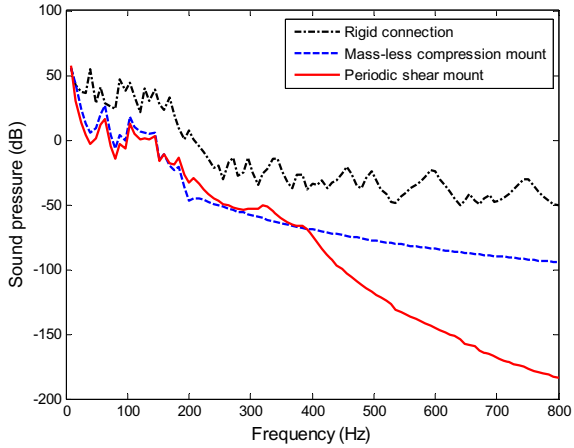

Figure 3. Acoustic pressure at the central point inside the cavity using rigid connection, mass-less compression mounts and periodic shear mounts.

Conclusions

In comparison with designs without resilient mounts, it is found that a relatively soft resilient mount generally reduces the transmission of vibration and noise from the unbalanced machinery. The periodic shear mount can provide more considerable reduction in the higher frequency range.

Acknowledgements

This work has been funded by the EU InterReg Project “Silent Spaces” and Aalborg University. This support is gratefully acknowledged.

References

[1] B. Niu and N. Olhoff, Design optimization of foundation for rotating machinery against standing-wave vibration in a building, *Proceedings of COMPDYN 2011, M. Papadrakakis, M. Fragiadakis, V. Plevris (eds.), Corfu, Greece,* 26-28 May 2011.

[2] S.M. Kim and M.J. Brennan, A compact matrix formulation using the impedance and mobility approach for the analysis of structural-acoustic systems, *Journal of Sound and Vibration*, 223 (1):97-113, 1999.

[3] W. Jung, Z. Gu and A. Baz, Mechanical filtering characteristics of passive periodic engine mount, *Finite Elements in Analysis and Design*, 46 (9):685-697, 2010.

Proceedings of the 24th Nordic Seminar on Computational Mechanics
J. Freund and R. Kouhia (Eds.)

Design optimization of a light-weight robotic arm under structural constraints

Shaoping Bai and Lelai Zhou

Department of Mechanical and Manufacturing Engineering
Aalborg University, Aalborg, Denmark
e–mail: {shb,lzh}@m-tech.aau.dk

Summary. This paper proposed a new approach of the design optimization of lightweight robotic arms, where robot kinematics, dynamics, drive-train design and strength analysis by means of finite element analysis (FEA) are considered. Constraints are formulated on the basis of kinematic performance, dynamic requirements and structural strength constraints, with the objective to minimize the weight. The proposed approach is demonstrated with a design example of a five degree-of-freedom lightweight arm for assistive applications.

Key words: integrated robot design, lightweight robots, Complex method, robot optimization with FEA.

Introduction

Light and strong robotic arms are desirable for assistive applications due to concerns of safety and energy efficiency. Optimization is an effective approach to achieve a lightweight design, while different constraints can be considered. The constraints typically considered in reported works include the kinematics and dynamics performance, the drive train requirements, etc. [1–3]. The structural constraints such as stress and deformation, on the other hand, are rarely considered.

In this work, an optimization method is developed for the design of lightweight robotic manipulators by addressing the influence of strength constraints, with an objective to minimize the weight of the robot. The structural dimensions of a robotic arm are taken as variables in the design optimization, in addition to the parameters of the drive-trains. Constraints on the kinematics, drive-train dynamics and structural strength are considered. The paper shows that the integrated optimization method can contribute to further reducing the arm weight.

A 5-dof robotic arm

The light-weight robotic arm considered in this paper has five degrees of freedom (dof), with two dof at the shoulder, one at the elbow, and two at the wrist, as shown in Fig. 1(a). A modular approach is adopted in the design. Each joint is built with CPU series gearboxes of Harmonic Drive^{TM} and Maxon motors, which are mounted inside the joint housings.

The structural parts of the robotic arm are to be optimized in this method, in addition to the drive-train optimization. Figure 1(b) shows some parameterized dimensions of the robotic arm. These dimensions fall into two groups: the assembling dimensions including the link lengths of the upper arm l_1 and the lower arm l_2. The assembling dimensions determine the robotic arm's kinematic performance, while the structural dimensions affect the arm structural strength.

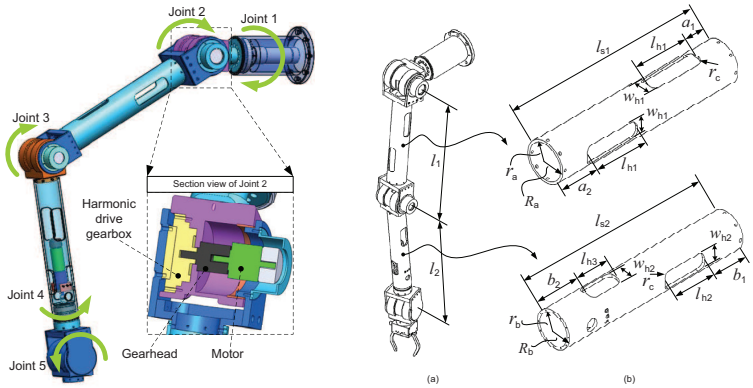

Figure 1. (a) CAD Rendering of a 5-dof light-weight anthropomorphic arm, (b) parameterized dimensions

Integrated design optimization

The objective of the design optimization is to minimize the total mass of the light-weight robotic arm. The task is to find the lightest combination of motors and gearboxes for all five joints and the optimal link lengths that fulfill all constraints associated with the kinematic, strength and drive-train constraints. The optimization will minimize the total mass which includes the masses of motors (m_m), gears (m_g) and the robotic arm structure (m_{arm}). Skipping derivations, the objective function, $f(\mathbf{x})$, is defined as

$$\min_{\mathbf{x}} \; f(\mathbf{x}) = \sum_{i=1}^{n} \{m_m(\mathbf{u}_m) + m_g(\mathbf{u}_g)\}_i + m_{arm}(\mathbf{u}_d), \quad \mathbf{x} = [\mathbf{u}_m, \mathbf{u}_g, \mathbf{u}_d] \tag{1}$$

$$s.t. \quad S_{max} < S_y, \quad D_{max} < D_{lim} \tag{2}$$

$$GCI \geq C_{min} \tag{3}$$

$$\tau_{rms} \leq T_m, \quad \tau_p \leq T_m^{max}, \quad n_p \leq N_m^{max} \tag{4}$$

$$\tau_{rmc} \leq T_g, \quad \tau_g \leq T_g^{max}, \quad n_g \leq N_g^{max} \tag{5}$$

where design variables of $\mathbf{x}$ include the index numbers of motors $\mathbf{u}_m = [u_{m,1}, \ldots, u_{m,n}]$ and gearboxes $\mathbf{u}_g = [u_{g,1}, \ldots, u_{g,n}]$, relative to databases containing commercially available components, and an array of dimensional variables $\mathbf{u}_d$ consisting of index numbers of discretized dimensions.

The constraints specified in eqs. (2)–(5) stand for the structural constraints, kinematics constraint, requirements for motor and gearbox selections, respectively. In these constraints, the left-hand sides are calculated values, namely, the maximum stress (S_{max}) and deformation (D_{max}), kinematic performance GCI, rated torque (τ_{rms}/τ_{rmc}), peak torque (τ_p/τ_g) and peak velocity (n_p/n_g) for motors/gears, while the right-hand sides are their corresponding limits, either specified in the product catalogs or by users. Note that GCI is a kinematic performance of manipulability, evaluated in terms of global conditioning number of the robot Jacobian.

So far, we have formulated the design problem as a discrete optimization problem, which can be solved by commercial available codes. We select a non-gradient method called Complex for this purpose. The implementation is outlined in the next section.

Procedure of optimization

The design optimization problem is solved by the Complex method [4], a method suitable for nonlinear and discrete optimization problems. With this method, a number of points (sets of

Table 1. Results of design optimization.

Joint	Initial		Case A		Case B	
	Motor	Gearbox	Motor	Gearbox	Motor	Gearbox
1	RE 40	CPU 17	RE 30	CPU 14	EC 32	CPU 14
2	RE 35	CPU 17	RE 25	CPU 14	RE 25	CPU 14
3	RE 35	CPU 17	RE 30	CPU 14	RE 30	CPU 14
4	RE 35	Gearhead	RE 25	Gearhead	RE 25	Gearhead
5	RE 35	CPU 17	RE 25	CPU 14	RE 25	CPU 14
Ratio	$r = 0.5$		$r = 0.6$		$r = 0.6$	
Weight	16.7 [kg]		8.3 [kg]		9.92 [kg]	
$[l_1, r_a, r_b, w_{h1}]$ mm	[500, 31, 27, 20]		[600, 34, 29, 40]		—	

Case A: Robot optimization with structural constraints
Case B: Robot optimization without structural constraints

design variables) will be evaluated against the objective function. The set of design variables minimizing the objective function is denoted as the best point $\mathbf{x}_b$, while the one maximizing the objective function is denoted as the worst point $\mathbf{x}_w$. The worst point is replaced in each iteration with a better point until the optimization converges, i.e., the difference between the worst and best values is less than a user-defined tolerance.

The optimization method is implemented as a design optimization platform containing three modules, which include the kinematic simulation, the dynamic simulation, the FEA module. Among them, the kinematics simulation module is used to conduct the kinematics analysis of the robot system. Kinematics performance such as global conditioning index (GCI), etc., is evaluated in this module. The dynamics module runs the dynamic analysis of the robotic multibody system. The FEA module deals with the static and dynamic structural analysis. The optimization is implemented in Matlab which oversees all modules.

In this work, a group of four trajectories within the robot workspace was used to conduct kinematics and dynamics simulations for the robotic arm. With the defined trajectories, the end-effector moves either horizontally or vertically. The end-effector remains horizontal during all the movement.

The payload is defined as a point mass of 5 kg. In the structural analysis, the design payload is multiplied by a safety factor of 2. The structure parts of this robot are made of aluminium, so the yield strength $S_y = 280$ MPa. The deflection limit at the end-effector is set to $D_{lim} = 5$ mm.

Results of design optimization

Optimized designs of structural dimensions and drive-train for the robotic arm are listed in Table 1. As shown in the optimization results of Case A, the minimum mass of the robotic arm is 8.3 kg, a mass reduction to 50% of the initial design being achieved.

The convergence of the objective function are depicted in Fig. 2(a), both the best value (black dot) and worst value (gray dot) from the Complex algorithm are shown. The solution to the optimal result is achieved at 6500 iterations with 150 population sizes. The tolerance of convergence is set to 0.0001.

A practical concern is the time-consuming FEA calculation. To improve the efficiency, FEA simulations were conducted in batch mode for all the discrete structural dimensions and the results consisting of maximum stress, deformation and mass are stored in a database file. In each iteration of the optimization, the program will re-load the FEA results instead of running FEA simulation. Adopting this approach leads to the computational time reduced from more than 10 days for one case to 10 minutes only.

The lengths of the upper arm link l_{s1} and lower arm link l_{s2} converge following the convergence of the link length ratio r. The optimized structural dimensions of the robotic arm are

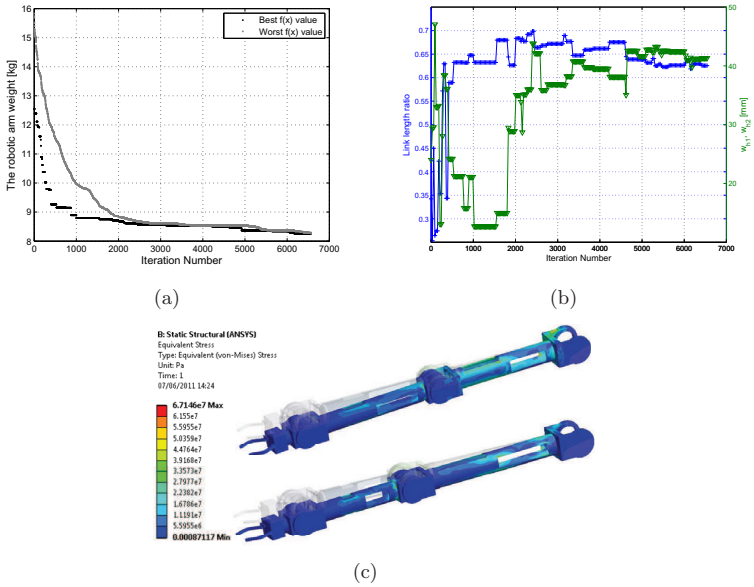

Figure 2. (a) Convergence of the objective function, (b) convergence of structural dimensions, (c) von-Mises stress with the original (top) and optimized (bottom) designs

shown in Table 1. The convergence plots of the length ratio and widths of the opening slots are depicted in Fig. 2(b). Note that to reduce calculation, w_{h1} is made identical to w_{h2} in this work. Upon the optimized structural dimensions in Table 1, FEA is conducted separately for the original and optimized robotic arm designs, with the von-Mises element stress being depicted in Fig. 2(c).

The optimization results were compared with the results from a method reported in [3]. An additional case, Case B, in which structural constraints are not considered, is included. The results are summarized in Table 1. It is seen that a significant mass reduction is achieved with the optimization under the constraint of strength, which reduces the mass of the upper and lower arm links by 1.7 kg. The comparison reveals that the new method can contribute to reduce further the robot mass without degrading the performance of the robot.

Discussion and conclusions

An integrated approach for the design of light-weight robotic arms was proposed in this work. Selections of structural dimensions, motors and gearboxes were formulated as a discrete optimization problem, which was solved by a non-gradient optimization method. The results show that the method can achieve an optimal design with minimum mass, while satisfying the constraints on kinematics, drive-train and structural strength.

The inclusion of the robot structural strength in the optimization benefits the robot design in several aspects. Firstly, the mass can be effectively reduced by applying the static strength constraint, as did in this work. Secondly, this approach can also address the fatigue limit, a major concern in robot design, by either specifying a minimum stress or conducting fatigue simulation in FEA module.

References

[1] P. Chedmail and M. Gautier, "Optimum choice of robot actuators," *J. Eng. Indus.*, vol. 112, pp. 361–367, 1990.

[2] Z. Shiller and S. Sundar, "Design of robotic manipulators for optimal dynamic performance," in *Proc. IEEE Int. Conf. Robot. Autom.*, 1991, pp. 344–349.

[3] L. Zhou, S. Bai, and M. R. Hansen, "Design optimization on the drive train of a light-weight robotic arm," *Mechatronics*, vol. 21, no. 3, pp. 560–569, 2011.

[4] M. J. Box, "A new method of constrained optimization and a comparison with other methods," *Comp. J.*, no. 8, pp. 42–52, 1965.

Proceedings of the 24th Nordic Seminar on Computational Mechanics
J. Freund and R. Kouhia (Eds.)

Thickness optimization of fiber reinforced composite laminates with the discrete material optimization method

Søren N. Sørensen and Erik Lund

Department of Mechanical and Manufacturing Engineering, Aalborg University, DK-9220 Aalborg East, Denmark, e-mail: sns@m-tech.aau.dk and el@m-tech.aau.dk

Summary. This paper presents a novel method for large-scale multi-material topology optimization of fiber reinforced composite structures subject to certain manufacturing constraints. The method concerns simultaneous determination of thickness (i.e. a varying integer number of plies with predefined thicknesses) and fiber orientation (among a finite set) throughout laminate structures with fixed outer geometries. The conceptual combinatorial/integer problem is relaxed to a continuous problem and solved on basis of the so-called Discrete Material Optimization method, explicitly including the manufacturing constraints as a large number of sparse linear constraints. An example is solved and results agree with the expected outcome.

Key words: multi-material topology optimization, fiber reinforced composite laminates, optimal design, manufacturing constraints, discrete material optimization

Introduction

Fiber reinforced composite laminates are applied in a variety of high performance structures because the stiffness to weight ratio along the fibers surpasses e.g. steel and aluminum alloys. The basis of this paper is laminated structures where the outer geometry for some reason is fixed which could be the case for e.g. wind turbine blades. Weight reduction while maintaining sufficient stiffness of such structures implies that the thickness of the laminate must vary inwards in an optimal manner. The individual plies/layers in the laminate are typically chosen among a finite set of materials with finite sets of fiber angles, e.g. Carbon/Glass Fiber Reinforced Polymer (CFRP/GFRP) with [0°, +45°, −45°, 90°] fiber orientation. The task for the designer is simultaneously to determine thickness (i.e. a varying integer number of plies with predefined thicknesses) and fiber orientation (among a finite set) throughout the entire laminate. In a finite element discretized domain, the problem is therefore conceptually a combinatorial multi-material topology optimization problem. This paper presents a novel method that treats this problem.

The optimized design is typically subject to certain manufacturing constraints (MC): To accommodate application of prepregs, large regions/patches within the layers of the total geometry/laminate must be identical (MC1); to prevent failure such as delamination and matrix cracking problems, changes in thickness cannot be too abrupt (MC2) and the number of identical contiguous plies should not be too high (MC3). Explicit inclusion of these manufacturing constraints in the topology optimization problem while preventing intermediate void in the monolithic laminates yields an optimized starting point for detailed post processing before true realization may take place. Stress constraints and failure criteria are not considered explicitly in this work. Avoiding intermediate void and fulfilling MC1-MC3 will, however, implicitly reduce the risk of failure.

Recent work on simultaneous material distribution and orientation has been summarized in [2]. Heuristic and genetic algorithms are frequently applied and well suited for combinatorial/integer problems, see e.g. [4] and [5]. Heuristic and genetic algorithms do, however, rely on extensive amounts of finite element analyses, and despite the ever-increasing parallelizeable computational power, it is unacceptably computationally expensive to apply such methods for large-scale optimization problems.

In this paper, the combinatorial/integer thickness optimization problem is relaxed thus allowing application of gradient based state-of-the-art optimizers as e.g. SNOPT [3] that is used in this work. Based on the so-called Discrete Material Optimization method [6], prevention of intermediate void and MC1-MC3 are explicitly included in the optimization problem as a large number of sparse linear constraints. The paper is organized as follows: General formulation of the optimization problem, an illustrative example with results, concluding remarks, and a list of references.

Problem formulation

The method to be presented takes basis in multi-phase minimization of compliance, c, through the density approach, see [1], in which the constitutive properties of all layers in all Equivalent Single Layer (ESL) shell elements in the discretized domain are functions of the densities.

$$\boldsymbol{E}_{ij} = \boldsymbol{E}_0 + \frac{\rho_{ij}}{1+p(1-\rho_{ij})} \sum_{k=1}^{n^c} \frac{x_{ijk}}{1+q(1-x_{ijk})} (\boldsymbol{E}_k - \boldsymbol{E}_0) \quad , \quad \forall (i,j) \tag{1}$$

In (1), index i concerns a specific ESL shell element, index j concerns a specific layer in an ESL element, and index k concerns a specific material candidate. $\boldsymbol{E}$ is a constitutive matrix, $\rho \in [0,1]$ is the topology variable (density), $x \in [0,1]$ is a candidate material variable, p and q are penalization powers for the variables, and n^c is the number of specific candidate materials. $\boldsymbol{E}_0$ is massless and significantly more compliant than all $\boldsymbol{E}_k$. The parameterization in (1) utilizes the material interpolation scheme RAMP (Rational Approximation of Material Properties) [7] and is a convenient way to enforce identical material candidate selection within predefined regions of the design domain (patches), possibly mixed with void (i.e. zero valued topology variables, ρ) only.

The chosen parameterization in (1) implies that the mass constraint is non-linear as well.

$$\sum_{i=1}^{n^e} \sum_{j=1}^{n^l} \rho_{ij} V_{ij} \sum_{k=1}^{n^c} x_{ijk} \varrho_k \leq \overline{M} \tag{2}$$

In (2), ϱ_k is the mass density for candidate material k, n^e is the number of elements, n^l is the number of layers, V_{ij} is the volume of layer j in element i, and $\overline{M}$ is the allowable mass.

Let index P concern a specific patch and $n^{pa} \in \mathbb{Z}$, $1 \leq n^{pa} \leq n^e$, denote the number of predefined, non-overlapping patch domains, Ω_P, together containing all ESL shell element domains, ω_i. To enforce candidate material continuity within the patches (MC1), $x_{ijk} \equiv y_{Pjk}$ for element domains ω_i within patch domains Ω_P. All variables, x_{ijk} and ρ_{ij} ($n^e \cdot n^l \cdot n^c + n^e \cdot n^l$), are used in the finite element analyses. Only substitute variables, y_{Pjk}, and ρ_{ij} ($n^{pa} \cdot n^l \cdot n^c + n^e \cdot n^l$) enter the optimizer. Sensitivities for the substitute variables that govern candidate material selection within the patches P, are determined as the summation of sensitivities concerning elements i contained in patches P.

$$\frac{\partial c}{\partial y_{Pjk}} = \sum_i \frac{\partial c}{\partial x_{ijk}} \quad , \quad \forall (P,j,k) \tag{3}$$

Equation (4) ensures at most 100% of one of the candidate materials in the patches.

$$\sum_{k=1}^{n^c} y_{Pjk} = 1 \quad , \quad \forall (P,j) \tag{4}$$

Letting index $j = 1$ represent the fixed layers with full density, i.e. $\rho_{i1} = 1$, preventing intermediate void throughout the monolithic laminate is achieved with (5).

$$\rho_{ij} \geq \rho_{i(j+1)} \quad , \quad \forall i \quad , \quad j = 2,3,\ldots,n^l - 1 \tag{5}$$

Suppose element $(i+1)$ is a neighbour to element (i) in a stencil-like manner. A limit on thickness change (MC2) is specified in (6) where $S \in \mathbb{Z}$ is the slope limit, $0 \leq S \leq n^l - 1$.

$$-S \leq \sum_{j=1}^{n^l} \rho_{ij} - \sum_{j=1}^{n^l} \rho_{(i+1)j} \leq S \tag{6}$$

Combined with (4), the constraints for contiguity (MC3) enforce at most $(n^l - 1)$ contiguous identical candidate materials. The contiguity limit is denoted $CL \in \mathbb{Z}$, $1 \leq CL \leq n^l - 1$.

$$0 \leq \sum_{j=n}^{n+CL} y_{Pjk} \leq CL \quad , \quad \forall (P,k) \quad , \quad n = 1,2,\ldots,n^l - CL \tag{7}$$

Example and results

Figure 1 illustrates the setup, a 2D cantilever plate. Because of symmetry, only half of the plate is considered (grey). The grey plate is discretized as 39×26 square elements in seven layers.

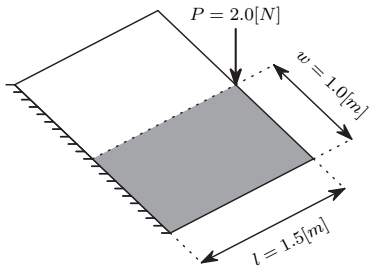

Figure 1: Setup, a 2D cantilever plate.

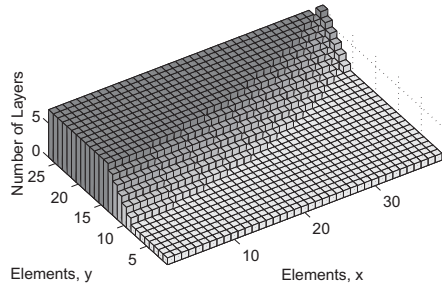

Figure 2: Optimized density distribution.

The plate is discretized using isoparametric degenerated 9-node ESL shell elements with five degrees of freedom per node. The material is orthotropic with $E_x = 34GPa$, $E_y = E_z = 8.2GPa$, $\nu = 0.29$, $G_{xy} = G_{xz} = 4.5GPa$, $G_{yz} = 4.0GPa$, and $\varrho = 1910.0kg/m^3$. A layer has thickness $t = 1mm$. Maximum mass, M_{max}, is $20.055kg$. A single patch implies that the material must

be oriented identically on layer basis along one of the four distinct orientations $[0°, \pm 45°, 90°]$. The total number of variables in the example is $39 \cdot 26 \cdot 7 \cdot 5 = 35,490$.

The presented topology optimization problem is linearized and solved sequentially, using SNOPT with an adaptive update scheme that repeatedly scales (5) and reduces move limits on basis of oscillation of the objective function value, c. The problem is solved in two consecutive steps. Step 1 converges without penalization. Step 2 continues with constant penalization.

Table 1 summarizes the results of a cantilever plate subject to: $\overline{M} = 0.5 \cdot M_{max}$, $S = 1$, $CL = 2$. Table 2 denotes the fiber angle distribution throughout the layers, counter-clockwise is positive. Layer 1 (the bottom layer in figure 2) is fixed, i.e. enforced full density.

	# Iter	*p/q*	*c*
Step 1	72	0.0/0.0	0.2374E-02
Step 2	50	5.0/2.0	0.2390E-02

Table 1: Summary of results.

Layer #	1	2	3	4	5	6	7
Fiber Angle [°]	0	0	45	0	45	0	0

Table 2: Fiber angles.

Figure 2 illustrates the optimized density distribution. The result is completely binary, $x_{ijk} \in \{0, 1\}$ and $\rho_{ij} \in \{0, 1\}$.

Concluding remarks

A novel method for simultaneous determination of material distribution and fiber orientation in a composite laminate subject to a variety of manufacturing constraints has been presented. The method is applicable for designs of composite structures with a fixed outer geometry but may also be used for thickness optimization of structures with a fixed plane of symmetry. In the example, the optimized density distribution and fiber orientation are in nice agreement with the moment distribution in a cantilever beam/plate. The SLP strategy with a heuristic update scheme causes large variations in the required number of iterations until convergence and the non-convexity of the posed optimization problem entails the risk of sub-optimal local minima. Although the presented example results in a binary design, this is not always the case. The sensitivity of different settings for the adaptive update scheme is elaborated in future work.

References

[1] M.P. Bendsøe and O. Sigmund. *Topology Optimization - Theory, Methods and Applications*. Springer Verlag, Berlin Heidelberg, 2003

[2] H. Ghiasi, F. Kazem, D. Pasini, and L. Lessard. Optimum stacking sequence design of composite materials part II: Variable stiffness design. *Composite Structures*, 93(1):1–13, 2010

[3] P.E. Gill, W. Murray, and M.A. Saunders. SNOPT: An SQP algorithm for large-scale constrained optimization. *SIAM Review*, 47(1):99–131, 2005

[4] W. Hansel, A. Treptow, W. Becker, and B. Freisleben. A heuristic and a genetic topology optimization algorithm for weight-minimal laminate structures. *Composite Structures*, 58(2):287–294, 2002

[5] J.S. Kim, C.G. Kim, and C.S. Hong. Optimum design of composite structures with ply drop using genetic algorithm and expert system shell. *Composite Structures*, 46(2):171–187, 1999

[6] J. Stegmann and E. Lund. Discrete material optimization of general composite shell structures. *International Journal for Numerical Methods in Engineering*, 62(14):2009–2027, 2005

[7] M. Stolpe and K. Svanberg. An alternative interpolation scheme for minimum compliance topology optimization. *Structural and Multidisciplinary Optimization*, 22(2):116–124, 2001

Proceedings of the 24th Nordic Seminar on Computational Mechanics
J. Freund and R. Kouhia (Eds.)

Block aggregation for strength criteria in multi-material topology design of laminates

Erik Lund

Department of Mechanical and Manufacturing Engineering, Aalborg University, Fibigerstraede 16, DK-9220 Aalborg East, Denmark, el@m-tech.aau.dk

Summary. The objective of this paper is to present an approach for multi-material topology optimization of laminated composite structures where strength constraints are taken into account together with other global structural performance measures. The topology design problem considered contains very many design variables, and when strength criteria are included in the problem, a very large number of criteria functions must be considered in the optimization problem to be solved. Thus, block aggregation methods are introduced, such that global strength measures are obtained. These formulations are illustrated for multi-material laminated design problems where the maximum failure index is minimized while compliance and mass constraints are taken into account.

Key words: topology optimization, failure, block aggregation, global strength measures, laminated composites.

Introduction

Laminated composite structures are being used in many different engineering applications due to their superior strength and stiffness characteristics. In order to fully exploit the weight saving potential of these multilayered structures, it is necessary to tailor the laminate layup and behavior to the given structural needs. In many applications the glass or carbon fiber reinforced polymers (FRP) are combined with core materials (foam, balsa tree, etc.) in parts of the structure in order to introduce sandwich structures, which may yield better structural performance for a given cost than monolithic fiber-reinforced polymer structures. In this work the combinatorial problem of proper choice of material and fiber orientation is formulated as a material selection problem using the so-called Discrete Material Optimization (DMO) approach developed by the authors [1]. This approach relaxes the discrete material selection problem to a continuous formulation using interpolation schemes with penalization, i.e., the material properties are computed as weighted sums of properties of candidate materials, which may be different kinds of fiber reinforced materials associated with given fiber angles together with core materials. The DMO approach has been used for global measures such as stiffness, mass, cost, eigenfrequencies, and buckling load factors of linear and geometrically nonlinear problems, and in this work local measures of performance in terms of strength criteria are included.

Parameterization

The approach relies on newly developed interpolation schemes, see [2] for compliance problems, that are generally applicable for interpolation between an arbitrary number of pre-defined candidate materials. Here the "generalized SIMP scheme" is used where the material property of interest, for example the constitutive matrix $\mathbf{C}^{eff}$, is computed in the following way, when there

are n_c candidate materials to choose between, each characterized by its constitutive matrix $\mathbf{C}_i$:

$$\mathbf{C}^{eff} = \sum_{i=1}^{n^c} x_i^p \mathbf{C}_i, \quad 0 \le \underline{x}_i \le x_i \le \overline{x}_i \le 1, \quad \sum_{i=1}^{n^c} x_i = 1 \tag{1}$$

Thus, design variables x_i are directly associated with candidate material i, and the penalization power p is used to enforce a unique choice of material at the end of the optimization.

This parameterization can be applied element-wise for each layer in the finite element model consisting of layered shell finite elements, but typically larger patches of elements, associated with the same parameterization, are used. A large number of sparse linear constraints to enforce the selection of at most one material in each design domain is introduced, but these constraints are handled effectively using the SNOPT optimization package [3] using either SLP or SQP.

Strength criteria

The inclusion of strength criteria introduces a large number of highly nonlinear (local) constraints which in combination with the many design variables introduced by the DMO approach yield a computationally challenging optimization problem. The failure criteria used for FRP materials are normally defined in the material coordinate system 1-2-3, and the procedure applied for computing effective failure indices (FI_{eff}) with the above DMO parameterization is the following:

1. Assemble the element stiffness matrices using $\mathbf{C}^{eff} = \sum_{i=1}^{n^c} x_i^p \mathbf{C}_i$
2. Solve the linear elastic static problem ($\mathbf{KD} = \mathbf{F}$) for displacements $\mathbf{D}$
3. Failure analysis postprocessing:
   - For each element (ElemNo) extract the element displacement vector $\mathbf{d}$ from $\mathbf{D}$:
     - For each layer (LayerNo):
       - Compute strain vector $\boldsymbol{\epsilon}$ in structural coordinate system
       - For each candidate material i:
         - Transform $\boldsymbol{\epsilon}$ to material coordinate system 1-2-3 of the candidate material $\Rightarrow \boldsymbol{\epsilon}_i^{1-2-3}$ and evaluate failure index $\mathrm{FI}_i(\boldsymbol{\epsilon}_i^{1-2-3})$
       - Failure index FI_{eff} (ElemNo, LayerNo, top/bottom) $= \sum_{i=1}^{n^c} x_i \, \mathrm{FI}_i(\boldsymbol{\epsilon}_i^{1-2-3})$

The maximum strain criterion is used for the examples in this paper, but many other failure criteria used for laminated composites have also been implemented and can be applied. The inclusion of strength criteria introduces a large number of criterion values (number of elements $\times$ number of layers per element $\times$ 2). In order to reduce the amount of functions to include in the mathematical programming problem, globalization functions are used. In this work global strength measures (see, e.g., [4, 5, 6]) are obtained by using Kreisselmeier-Steinhauser (KS) functions, but other globalization functions like the p-norm are also being investigated.

The efficiency of using global strength approaches decreases when a large number of values are lumped into a single global value, but this problem can be handled by associating a global strength measure with each patch used for the parameterization. The approach has similarities with the block aggregation approach [6] and the regional stress measure approach [5] used for single-material structural topology optimization problems with stress constraints.

The number of FI values, n^{FI}, to include for each patch may be defined by the user, and for each patch j, $j = 1, \ldots, n^P$, a KS function $f(\mathbf{x})^j$ is computed:

$$f(\mathbf{x})^j \;=\; \frac{1}{\rho}\ln\left[\sum_{k=1}^{n^{FI}} e^{\rho\, f_k^j}\right] \quad \text{or} \quad f(\mathbf{x})^j \;=\; f^{j,max} + \frac{1}{\rho}\ln\left[\sum_{k=1}^{n^{FI}} e^{\rho\,(f_k^j - f^{j,max})}\right] \tag{2}$$

where $\ln = \log_e$, the scalar ρ typically is between 2 and 200 (50 is used), and $f^{j,max}$ is the largest FI value among $f_k^j(\mathbf{x})\,,\ k = 1, \ldots, n^{FI}$. The latter KS definition has numerical advantages.

Mathematical programming problems

With the introduction of global strength measures for each patch of the design domain, the problem of minimizing the mass M with strength constraints (together with other constraints, like compliance C) are directly formulated as

$$\begin{aligned}
&\text{Objective :} && \min_{\mathbf{x}} \;\; M \\
&\text{Subject to :} && f(\mathbf{x})^j \le 1, \quad j = 1, \ldots, n^P \\
&&& (C \le \overline{C}) \\
&&& \sum_{i=1}^{n^c} x_i = 1 \text{ for all design domains} \\
&&& 0 < \underline{x_i} \le x_i \le \overline{x_i} < 1,\ i = 1, \ldots, I
\end{aligned} \tag{3}$$

where I is the total number of DMO design variables and $\overline{C}$ a compliance constraint.

Similarly, in case of minimizing the maximum failure index FI with a mass constraint (and perhaps other constraints), the problem is reformulated using a bound formulation:

$$\begin{aligned}
&\text{Objective :} && \min_{\mathbf{x},\,\beta} \;\; \beta \\
&\text{Subject to :} && f(\mathbf{x})^j \le \beta, \quad j = 1, \ldots, n^P \\
&&& M \le \overline{M} \\
&&& (C \le \overline{C}) \\
&&& \sum_{i=1}^{n^c} x_i = 1 \text{ for all design domains} \\
&&& 0 < \underline{x_i} \le x_i \le \overline{x_i} < 1,\ i = 1, \ldots, I
\end{aligned} \tag{4}$$

In both cases the optimization problem must be solved by an algorithm that in an efficient way can handle the many linear constraints ($\sum x_i = 1$) generated by the DMO parameterization scheme used. The examples considered have been solved using a SLP approach where SNOPT [3] is used to solve the LP sub-problems.

Example and concluding remarks

The approach is shortly demonstrated in the following for multi-material design of a generic main spar from a wind turbine blade subjected to the maximum flapwise bending load case. The midsection of the main spar is divided into 16 patches, each consisting of 10 layers of equal thickness. The candidate materials are GFRP oriented at 0°, 45°, −45°, and 90°, GFRP ±45° biax mats, and foam material. The objective has been to minimize the failure index in the main spar while fulling compliance and mass constraints. 1/5 of the design domain should be filled with foam material. The FE model and the parameterization are seen on Figure 1, and the results are listed in Table 1. Both constraints are active for the final design.

The candidate material associated with the largest design variable is listed in the table. In general, a distinct choice of material is obtained in most of the design domain, and the

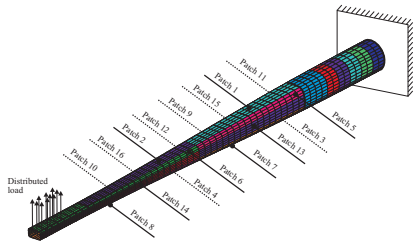

Figure 1. Generic main spar from wind turbine blade.

Table 1. Results of optimization.

Patch \ Layer	L1	L2	L3	L4	L5	L6	L7	L8	L9	L10
P1	90°	0°	0°	0°	0°	0°	0°	0°	0°	0°
P2	90°	0°	0°	0°	0°	0°	0°	0°	0°	0°
P3	0°	0°	0°	0°	0°	0° / 90°	0°	0°	0°	0°
P4	0°	0°	0°	0°	0°	0°	0°	0°	0°	0°
P5	90°	foam	foam	foam	0°	0° *	0°	0° *	0°	0°
P6	-45°	45°	45°	90°	0°	0°	0°	0°	0°	45°
P7	45° *	45° *	foam	45° *	0°	0°	0°	0°	0°	0°
P8	-45°	0°	0°	0°	0°	0°	0°	0°	0°	0°
P9	90° *	foam *	foam	foam	foam	foam	foam	-45° *	-45° *	0°
P10	45°	45°	0°	0°	0°	0°	0°	0°	0°	45°
P11	90°	90° *	90° *	0° *	0°	0°	0°	45°	45° *	0°
P12	90°	-45°	-45°	90°	foam	foam	0°	0°	-45°	-45°
P13	90°	foam	foam	foam	foam	foam	foam	foam	foam	0°
P14	0°	0°	0°	0°	0°	0°	0°	0°	45°	45°
P15	90°	foam	foam	foam	foam	foam	foam	foam	foam	0°
P16	0°	0°	0°	0°	0°	0°	0°	0°	0°	biax45

presented approach is a step towards efficient handling of local failure criteria in topology design of multi-material laminated composite structures.

References

[1] J. Stegmann and E. Lund. Discrete material optimization of general composite shell structures. *International Journal for Numerical Methods in Engineering*, 62(14):2009–2027, 2005.

[2] C.F. Hvejsel and E. Lund. Material interpolation schemes for unified topology and multi-material optimization. *Structural and Multidisciplinary Optimization*, 43:811–825, 2011.

[3] P.E. Gill, W. Murray and M.A. Saunders. SNOPT: An SQP algorithm for large-scale constrained optimization. *SIAM Review*, 47(1):99–131, 2005.

[4] P. Duysinx and O. Sigmund. New development in handling stress constraints in optimal material distribution. In: *Proc. 7th AIAA/USAF/NASA/ISSMO symposium on multidisciplinary analysis and optimization. A collection of technical papers (held in St. Louis, Missouri)*, 3:1501-1509, 1998.

[5] C. Le, J. Norato, T. Bruns, C. Ha and D. Tortorelli. Stress-based topology optimization for continua. *Structural and Multidisciplinary Optimization*, 41:605–620, 2010.

[6] J. París, J., F. Navarrina, I. Colominas and M. Casteleiro. Block aggregation of stress constraints in topology optimization of structures. *Advances in Engineering Software*, 41:433–441, 2010.

Rakenteiden Mekaniikka (Journal of Structural Mechanics)
Vol. 44, No 3, 2011, pp. 218-230

Optimal design of stiffened plate using metamodeling techniques

Ossi Heinonen and Sami Pajunen

Summary. In this article mass minimization of a stiffened plate is reported. From the actual finite element model of the plate, surrogate models are constructed using response surface methodology and the Kriging method. Estimation of the structural response is carried out using three different design of experiment models. As a numerical example a typical off-shore structure is optimized with respect to stress constraint equations. The optimization procedure is based on the standard NLPQL algorithm with iteratively moving response estimation window.

Key words: design of experiments, response surface methodology, Kriging method, metamodeling, optimization

Ossi Heinonen, Sami Pajunen
Tampere University of Technology
Department of Mechanics and Design
P.O. Box 589, 33101 Tampere
ossi.heinonen@tut.fi, sami.pajunen@tut.fi

Proceedings of the 24th Nordic Seminar on Computational Mechanics
J. Freund and R. Kouhia (Eds.)

Buckling of plates with cut-outs made of non-isotropic materials[1]

Alexandr V. Lebedev[2], Andrei L. Smirnov[3]

St. Petersburg State University
198504, 28 University Ave, St. Petersburg, Russia
(2) privater@mail.ru, (3) a_l_smirnov@mail.ru

Summary. Buckling of non-homogeneous elastic thin structures weakened with holes is considered. The purpose of the study is to analyze the effect of area of the rectangular or circular holes on buckling under compression of rectangular or circular plates made of isotropic, orthotropic and transversal-isotropic material.

Key words: non-isotropic plates buckling, non-homogeneous plates buckling

Introduction

The research refers to buckling analysis of non-homogeneous (weakened with holes or cut-outs) isotropic or non-isotropic (orthotropic and transverse isotropic) thin-walled elastic plates. The purpose of the study is to examine the effect of the area and proportions of rectangular or circular holes on critical loading of rectangular or circular plates. In the report we limit ourselves with analysis of plates under external compressive loadings. The plates are considered to be thin enough to apply 2D Kirchhoff-Love theory [1]. Mathematically buckling problems for plates with cutouts are reduced to solution of the boundary value problems for non-simply connected domain, which are solved in the research with analytical and/or numerical methods including the Bubnov-Galerkin method [2] and FEM.

Buckling of isotropic plates

Rectangular plates

We start with analysis of isotropic thin plate under axial compressive load. The load directed along the lateral faces of the plate, which are of the length a, the side ends have the length b and $a \geqslant b$, side ratio $r = a/b$. Here only boundary conditions of simply supported type are considered. The free edges of the central hole are parallel to the plate sides and for the square hole have the length d.

For uniform shells the buckling load may be found analytically [1], for shells with holes the results obtained by means of Bubnov-Galerkin method are reported in [2]. Here we compare them with the results of the numerical analysis of the problem by means of FEM package ANSYS. The most important and interesting is the effect of the hole area on critical buckling loadings and buckling modes.

In Fig. 1a one can see the effect of the plate sides ratio on the critical loading for a plate with the relative thickness $h = 0.01$ and the Poisson coefficient $\nu = 0.3$, where q_0 and q_{cr} are critical

[1]The research was supported by grant N 10–01–00244-a from Russian Foundation for Basic Research.

buckling load for a homogeneous plate and for a plate with the square hole respectively, n — the number of waves in transversal direction, $d = 0.1$. It appeared that the critical buckling

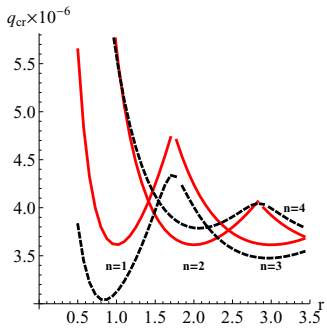

(a) Effect of the plate side ratio on critical loadings for the plates with hole $d = 0.1$ (dashed lines) and homogeneous plate.

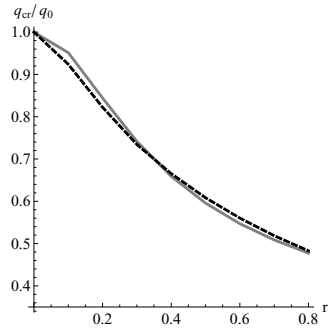

(b) Effect of the hole area on critical loadings for circular plate with circular hole radius r.

Figure 1: Buckling of isotropic plates.

loadings may either increase or decrease. Presumably the effect when "mechanical buckling strengths of the perforated plates, contrary to expectation, increase rather than decrease as the hole sizes grow larger" was firstly reported in [4]. In our research it was found that, for example, for axially compressed rectangular plate for buckling nodes with odd wave numbers the critical loading decreases with the hole area and increases for even wave numbers [5]. The explanation of this phenomenon is in the initial compressive stresses developing in the narrow strips between the hole and the plate edges. One should remember that a hole not only affects the plate stiffness but also influences on the initial stress-strain state. These initial stresses are higher for the stronger supports of the lateral edges of the plate and they increase with the Poisson ratio. That leads to the growth of the critical load.

The ratio of the hole sides plays an important role. For buckling under axial loading for all cases the extension of the hole in the axial direction leads to decreasing of the critical loading. For a hole elongated in the transversal direction the width of a strip is smaller and the intensity of the initial stresses is higher and the critical loading increases. The change of the ratio may also cause the switch of the buckling modes.

Circular plates

For the circular plate (radius R) with the central circular hole (radius r) under radial compressive load q the dependence of the critical load on the hole area is more predictable. The main effect has the decreasing of the plate stiffness with the hole area and the critical load goes down monotonously with the hole area. In Fig. 1b we compare numerical results for the critical loadings (dashed lines) and those obtained in [3] by method of initial parameters (solid lines).

Buckling of orthotropic plates

The buckling behavior of non-isotropic plates has some specific features. As an example we consider buckling of a plate made of orthotropic material with Young modules E_x, and E_y, Poisson ratios ν_{xy} and ν_{yx} and shear modulus G. Since we wish to study the effect of non-

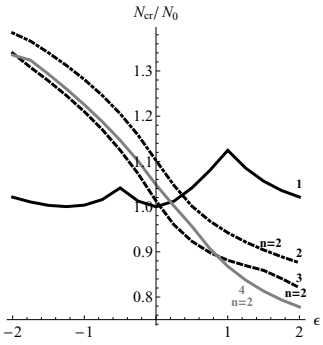

(a) Rectangular plate $r = 2$: 1 – homogenous plate, 2,3,4 – plate with central square hole area $S^* = 0.01; 0.04; 0.09$ respectively.

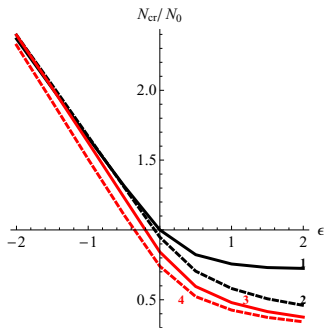

(b) Circular plate $R = 1$: 1 – homogenous plate, 2,3,4 – plate with central circular hole $r = 0.1; 0.2; 0.3$ respectively.

Figure 2: Buckling of orthotropic plates

isotropy on the buckling load we assume that

$$E_x = E_0(1+|\epsilon|)^{\operatorname{sign}\epsilon}, E_y = E_0(1+|\epsilon|)^{-\operatorname{sign}\epsilon},$$
$$\nu_{xy} = \nu_0(1+|\epsilon|)^{\operatorname{sign}\epsilon}, \tag{1}$$
$$E_x\nu_{yx} = E_y\nu_{xy} = E_0\nu_0, G = E_0/(2(1+\nu_0)).$$

So, for small ϵ this material is almost isotropic. For positive ϵ the material is stiffer in the x-direction, for negative ϵ — in the y-direction.

Rectangular plates

The effect of orthotropy on buckling load of the rectangular plate with a central square hole with different hole area $S^* = d^2$ under axial compression is shown in Fig. 2a, where N_0 and N_{cr} are critical buckling loads for plates without and with a hole respectively. Even for relatively small hole the effect of non-isotropy is very significant: if the plate becomes stiffer in the axial direction and softer in transversal the critical buckling loading decreases very speedy with $\epsilon > 0$ and for the plate stiffer in the transverse direction the critical buckling loading increases. One more time it underlines the crucial effect for buckling of the initial stresses "carried by the narrow side strips of material along the plate boundaries" [4].

Circular plates

Similar the critical loading for a orthotropic circular plate with a central circular hole under radial compression depends on the material properties. Here the important effect has the initial stresses in the circumferential direction. For materials (1) stiffer in the circumferential direction ($\epsilon < 0$) the critical load increases (see Fig. 2b).

Buckling of transversally isotropic plates

Finally we consider buckling behavior of transversally isotropic plates with the following elastic modules:

$$E_x = E_y = E_0(1+|\epsilon|)^{\operatorname{sign}\epsilon}, E_z = E_0(1+|\epsilon|)^{-\operatorname{sign}\epsilon},$$
$$\nu_{xy} = \nu_{yx} = \nu_0(1+|\epsilon|)^{\operatorname{sign}\epsilon}, \tag{2}$$
$$E_x\nu_{yx} = E_y\nu_{xy} = E_z\nu_{xz} = E_0\nu_0, G = E_0/(2(1+\nu_0)).$$

For positive ϵ the material is stiffer in the x, y-direction (in plane), for negative ϵ — in the z-direction (along the thickness).

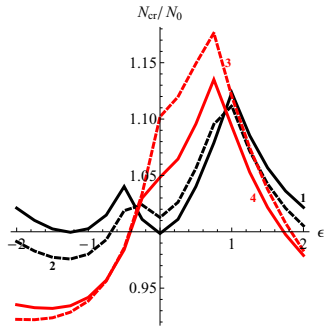

(a) Rectangular plate $r = 2$: 1 – homogenous plate, 2,3,4 – plate with central square hole area $S^* = 0.01; 0.04; 0.09$ respectively.

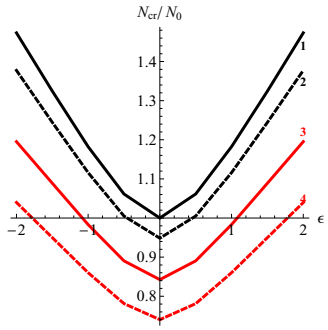

(b) Circular plate $R = 1$: 1 – homogenous plate, 2,3,4 – plate with central circular hole $r = 0.1; 0.2; 0.3$ respectively.

Figure 3: Buckling of the transversally isotropic plates

Rectangular plates

For rectangular transversally isotropic plates, the effect of the material is shown in Fig. 3a. For the materials stiffer in plane ($\epsilon > 0$) the buckling load is higher and the buckling mode essentially depends on the stiffness parameter. For small ϵ the critical load is also increases with the hole area.

Circular plates

For the transversally isotropic circular plates the change of the ratio of in plane and in thickness Young modules leads to increasing of the critical buckling load. The critical buckling load monotonously decreases with the hole area.

Conclusions

The presence of the hole or cut-outs may lead to either increasing or decreasing of the critical buckling load for the compressed plates depending on the boundary conditions, geometric parameters of the plate and the hole and material property. For the rectangular plates the principal effect has the stresses in the lateral strips. For buckling of circular plates the material properties play the key role.

References

[1] N. A. Alfutov, *Fundamentals of buckling analysis of elastic systems*. M.: Machinostroyenie, 1991 (in Russian).

[2] I. N. Preobrazhensky, *Buckling and vibrations of plates and shells with the holes*. M.: Machinostroyenie, 1981 (in Russian).

[3] C. G. Chizgevsky, *Analysis of circular and annular plates*, Machinostroyenie, 1977 (in Russian).

[4] W. L. Ko, *Behavior of Rectangular Plates With Different Central Cutouts*, Dryden Flight Research Center, NASA report, 1998.

[5] A. V. Lebedev, Effects of the cut-outs on buckling of rectangular elastic plates under axial compression. *Vestnik St.Petersburg University* 1(4), 77-83, 2009 (in Russian).

Proceedings of the 24th Nordic Seminar on Computational Mechanics
J. Freund and R. Kouhia (Eds.)

Eigenfrequencies in moving material problems: practical challenges

Juha Jeronen

University of Jyväskylä, Mattilanniemi 2 (Agora), 40014 Jyväskylä, Finland, juha.jeronen@jyu.fi

Summary. Axially moving materials are encountered in many applications, for example tape and optical drives, band saws, and some manufacturing processes such as those for paper and steel. Analysis of the complex eigenfrequencies of time-harmonic vibrations in the linear regime for small transverse displacement is a common tool to obtain insight into the stability and vibration characteristics of the system. In the talk, we consider practical challenges that are encountered in this analysis. The issues are viewed in the light of the examples of the moving ideal string, and the moving panel submerged into axially flowing ideal fluid.

Key words: eigenfrequencies, numerics, moving materials, ideal string, panel

Introduction

Much research into axially moving materials such as strings and beams, described by second- and fourth-order partial differential equations respectively, has been performed during the last slightly over one hundred years, beginning with the seminal paper by Skutch in 1897 [20]. Some classical examples of this research are Archibald and Emslie 1958 [1], Miranker 1960 [12], Swope and Ames 1963 [21], and Simpson 1973 [19]. Also the very extensive research, e.g. [13, 14, 15, 16, 23, 24, 27, 10, 11], by the group of C. D. Mote deserves a mention.

The most important result from the literature is that axially moving materials are inherently unstable, sharing some behavioural characteristics, and some mathematical form, with axially compressed beams and plates. The axial transport velocity plays the role of an effective axial load.

In the paper making community, there is interest into the problems of transverse vibration and stability of axially moving materials, because paper machines contain so-called open draws, where the paper web travels without mechanical support. The model is often geometrically linearized in the small displacement regime. This simplifies the analysis significantly, and allows the decoupling of the in-plane and out-of-plane displacements (as is well-known from classical Kirchhoff plate theory).

Because paper is a very light material, the fluid-structure interaction (FSI) with the surrounding air becomes important to consider. The interaction effects may change both the eigenfrequencies and the critical velocity of the system [17, 18, 7, 26, 8, 9].

In our own research, we have analyzed the static stability (the buckling problem) of moving isotropic and orthotropic rectangular plates with SFSF boundary conditions in vacuum [3, 2]. For the simpler case of cylindrical deformation, we have studied the FSI aspects in the ideal fluid framework. We have introduced a semi-analytical functional solution for the aerodynamic pressure difference over the panel surface, by using ideas from thin airfoil theory. This has been performed for both the steady-state [4] and dynamic [5] cases. In both, we have allowed for axial motion of the surrounding fluid.

Eigenfrequencies

Consider the small transverse free vibrations of an axially moving, tensioned string moving through two pinholes. The governing PDE and its boundary conditions (BCs) are

$$mw_{tt} + 2mV_0 w_{xt} + (mV_0^2 - T_0)w_{xx} = 0 \,, \qquad w(-\ell, t) = w(\ell, t) = 0 \,, \tag{1}$$

where w is the transverse displacement, m is mass per unit length, V_0 is the axial velocity, T_0 is the tension applied at the ends of the string, and the x and t subscripts denote derivatives. The symbol ℓ denotes the half-length of the span.

For the eigenfrequency analysis (and dynamic stability analysis) of a linear model, it is standard [6] to use a complex-valued time-harmonic trial function

$$w(x, t) := \exp(st)\, W(x) \,, \tag{2}$$

where s is the complex eigenfrequency and $W(x)$ is the eigenshape. The eigenfrequency problem is to find pairs (s, W) such that (2) satisfies (1). In the continuous case, there are a countably infinite number of eigenvalues, which form the eigenfrequency spectrum of the problem.

For the panel problem, we have

$$mw_{tt} + 2mV_0 w_{xt} + (mV_0^2 - T_0)w_{xx} + Dw_{xxxx} - q_f(w) = 0 \,, \tag{3}$$

where D is the bending rigidity of the panel ([22], p. 5) and q_f is the aerodynamic reaction, expressed as an integrodifferential operator (for details, see [5]). The customary boundary conditions are the simply supported (pinned) ones, i.e.

$$w(-\ell, t) = w(\ell, t) = w_{xx}(-\ell, t) = w_{xx}(\ell, t) = 0 \,.$$

It should be noted for both problems that if $V_0 \neq 0$, in general also the eigenshapes $W(x)$ will be complex-valued (see e.g. [27]).

Discretization and solution

As is usual, we discretize the PDE in space first. In this study, we used Fourier–Galerkin for both problems. Additionally, for the ideal string problem, we used standard linear FEM, and derived the analytical solution for comparison.

After space discretization of (1) or (3), using n degrees of freedom, we have

$$\mathbf{M}_2 \mathbf{f}''(t) + \mathbf{M}_1 \mathbf{f}'(t) + \mathbf{M}_0 \mathbf{f}(t) = 0 \,, \tag{4}$$

where $\mathbf{M}_j$ are matrices in $\mathbb{R}^{n \times n}$, the primes denote time derivatives, and $\mathbf{f}(t) : \mathbb{R} \to \mathbb{R}^n$ is the vector-valued solution function for the Galerkin coefficients. We assume that the basis for our Galerkin discretization is chosen such that it fulfills the appropriate boundary conditions identically. The matrices $\mathbf{M}_2$ and $\mathbf{M}_0$ are symmetric, and $\mathbf{M}_1$ is skew-symmetric (antisymmetric).

In the standard way, define $\mathbf{u}(t) := [\mathbf{f}'(t)\ \mathbf{f}(t)]^T$. We obtain $\mathbf{u}'(t) = \mathbf{M}\mathbf{u}(t)$, where

$$\mathbf{M} = \begin{bmatrix} -\mathbf{M}_2^{-1}\mathbf{M}_1 & -\mathbf{M}_2^{-1}\mathbf{M}_0 \\ \mathbf{1} & \mathbf{0} \end{bmatrix} \,. \tag{5}$$

Here $\mathbf{1}$ is the $n \times n$ identity matrix, and $\mathbf{0}$ denotes an $n \times n$ matrix of zeroes. The matrix $\mathbf{M} \in \mathbb{R}^{2n \times 2n}$. Now, choose the trial $\mathbf{f}(t) := \mathbf{F} \exp(st)$, insert to (4), multiply from the left by $\mathbf{M}_2^{-1}$, and discard the common scalar factor $\exp(st)$. We obtain the flutter equation

$$\mathbf{L}(s)\, \mathbf{F} := \left(s^2 + \mathbf{M}_2^{-1}\mathbf{M}_1 s + \mathbf{M}_2^{-1}\mathbf{M}_0\right)\, \mathbf{F} = 0 \,, \tag{6}$$

where $\mathbf{L}(s) \in \mathbb{C}^{n\times n}$. The problem is to find pairs $(s, \mathbf{F}) \in (\mathbb{C}, \mathbb{C}^n)$ such that (6) is satisfied nontrivially. We easily see that values of s making $\mathbf{L}(s)$ singular are the eigenvalues of $\mathbf{M}$. Thus we solve $\mathbf{Mx} = s_j\mathbf{x}$, obtaining $2n$ solutions $s_1, s_2, \ldots, s_{2n}$.

Finally, the corresponding eigenmodes can be obtained from the SVD of $\mathbf{L}(s) = \mathbf{U\Sigma V}$, performed separately for each solution $s = s_j$. In practice, for each s_j, the null space of $\mathbf{L}(s_j)$ is one-dimensional. It is easy to show that the column of $\mathbf{V}$ corresponding to the zero diagonal entry in $\mathbf{\Sigma}$ (for a given s_j) contains the Galerkin coefficients for the corresponding eigenmode.

The practical challenges

The solution process described above is well-known; the main topic of the talk are its practical challenges. The first challenge is that the s_j are returned in a random order, although the problem is continuous. Thus, in order to plot the evolution of the s_j as lines in the parameter space, one needs to track the modes as the parameter values are changed.

Another important challenge is the identification of correct solutions. It is fairly easily seen, by comparing to the analytical solution, that both numerical solutions of the ideal string problem have a qualitative problem. The eigenvalues of the ideal string are known to be purely imaginary for all parameter values; however, the numerical solutions suggest flutter bifurcations. These occur above the critical velocity, but as there are indications that the critical velocity of the ideal string may not represent an instability (see [25]), the appearance of such numerical artefacts should be considered in order to determine the range where the numerical solutions are valid.

In the talk, these issues are illustrated and partial solutions are suggested.

References

[1] F. R. Archibald and A. G. Emslie. The vibration of a string having a uniform motion along its length. *ASME Journal of Applied Mechanics*, 25:347–348, 1958.

[2] N. Banichuk, J. Jeronen, M. Kurki, P. Neittaanmäki, T. Saksa, and T. Tuovinen. On the limit velocity and buckling phenomena of axially moving orthotropic membranes and plates. *International Journal of Solids and Structures*, 48(13):2015–2025, 2011.

[3] N. Banichuk, J. Jeronen, P. Neittaanmäki, and T. Tuovinen. On the instability of an axially moving elastic plate. *International Journal of Solids and Structures*, 47(1):91–99, 2010.

[4] N. Banichuk, J. Jeronen, P. Neittaanmäki, and T. Tuovinen. Static instability analysis for travelling membranes and plates interacting with axially moving ideal fluid. *Journal of Fluids and Structures*, 26(2):274–291, 2010.

[5] N. Banichuk, J. Jeronen, P. Neittaanmäki, and T. Tuovinen. Dynamic behaviour of an axially moving plate undergoing small cylindrical deformation submerged in axially flowing ideal fluid. *Journal of Fluids and Structures*, In Press, Corrected Proof:–, 2011.

[6] V. V. Bolotin. *Nonconservative Problems of the Theory of Elastic Stability*. Pergamon Press, New York, 1963.

[7] Y. B. Chang and P. M. Moretti. Interaction of fluttering webs with surrounding air. *TAPPI Journal*, 74(3):231–236, 1991.

[8] T. Frondelius, H. Koivurova, and A. Pramila. Interaction of an axially moving band and surrounding fluid by boundary layer theory. *Journal of Fluids and Structures*, 22(8):1047–1056, 2006.

[9] A. Kulachenko, P. Gradin, and H. Koivurova. Modelling the dynamical behaviour of a paper web. Part I. *Computers & Structures*, 85:131–147, 2007.

[10] C. C. Lin and C. D. Mote. Equilibrium displacement and stress distribution in a two-dimensional, axially moving web under transverse loading. *ASME Journal of Applied Mechanics*, 62:772–779, 1995.

[11] C. C. Lin and C. D. Mote. Eigenvalue solutions predicting the wrinkling of rectangular webs under non-linearly distributed edge loading. *Journal of Sound and Vibration*, 197(2):179–189, 1996.

[12] W. L. Miranker. The wave equation in a medium in motion. *IBM Journal of Research and Development*, 4:36–42, 1960.

[13] C. D. Mote. Divergence buckling of an edge-loaded axially moving band. *International Journal of Mechanical Sciences*, 10:281–195, 1968.

[14] C. D. Mote. Dynamic stability of an axially moving band. *Journal of the Franklin Institute*, 285(5):329–346, May 1968.

[15] C. D. Mote. Dynamic stability of axially moving materials. *Shock and Vibration Digest*, 4(4):2–11, 1972.

[16] C. D. Mote. Stability of systems transporting accelerating axially moving materials. *ASME Journal of Dynamic Systems, Measurement, and Control*, 97:96–98, 1975.

[17] A. Pramila. Sheet flutter and the interaction between sheet and air. *TAPPI Journal*, 69(7):70–74, 1986.

[18] A. Pramila. Natural frequencies of a submerged axially moving band. *Journal of Sound and Vibration*, 113(1):198–203, 1987.

[19] A. Simpson. Transverse modes and frequencies of beams translating between fixed end supports. *Journal of Mechanical Engineering Science*, 15:159–164, 1973.

[20] Rudolf Skutch. Uber die bewegung eines gespannten fadens, weicher gezwungen ist durch zwei feste punkte, mit einer constanten geschwindigkeit zu gehen, und zwischen denselben in transversal-schwingungen von gerlinger amplitude versetzt wird. *Annalen der Physik und Chemie*, 61:190–195, 1897.

[21] R. D. Swope and W. F. Ames. Vibrations of a moving threadline. *Journal of the Franklin Institute*, 275:36–55, 1963.

[22] S. P. Timoshenko and S. Woinowsky-Krieger. *Theory of plates and shells*. New York : Tokyo : McGraw-Hill, 2nd edition, 1959. ISBN 0-07-085820-9.

[23] A. G. Ulsoy and C. D. Mote. Analysis of bandsaw vibration. *Wood Science*, 13:1–10, 1980.

[24] A. G. Ulsoy and C. D. Mote. Vibration of wide band saw blades. *ASME Journal of Engineering for Industry*, 104:71–78, 1982.

[25] Y. Wang, L. Huang, and X. Liu. Eigenvalue and stability analysis for transverse vibrations of axially moving strings based on hamiltonian dynamics. *Acta Mech Sinica*, 21:485–494, 2005.

[26] Y. Watanabe, K. Isogai, S. Suzuki, and M. Sugihara. A theoretical study of paper flutter. *Journal of Fluids and Structures*, 16(4):543–560, 2002.

[27] J. A. Wickert and C. D. Mote. Classical vibration analysis of axially moving continua. *ASME Journal of Applied Mechanics*, 57:738–744, 1990.

Proceedings of the 24th Nordic Seminar on Computational Mechanics
J. Freund and R. Kouhia (Eds.)

Simplified buckling analysis of imperfection sensitive reinforced concrete columns

Noël Challamel[1] and Jostein Hellesland[2]

(1)Professor of Civil Engineering, Université Européenne de Bretagne, University of South Brittany UBS, LIMATB, Centre de Recherche, Rue de Saint Maudé, BP92116, 56321 Lorient cedex – France, Email : noel.challamel@univ-ubs.fr; on sabbatical leave, Mechanics Division, Department of Mathematics, University of Oslo, P.O. Box 1053, Blindern, NO-0316 Oslo - Norway
(2)Professor of Structural Mechanics, Mechanics Division, Department of Mathematics, University of Oslo, P.O. Box 1053, Blindern, NO-0316 Oslo – Norway, Email: jostein.hellesland@math.uio.no

Summary. This article deals with the mathematical modeling by damage mechanics of the buckling and post-buckling of structural systems such as reinforced concrete columns. Imperfection sensitivity is found for such a class of structural elements.

Key words: reinforced concrete columns, buckling, softening, limit point, imperfection analysis

Introduction

It is accepted that slender reinforced concrete columns must be designed taking into account the second order effects produced by the axial loads on the deformed member. The main international rules, including for instance Eurocode 2, are based on this concept for the design of reinforced concrete columns. Various methods based on empirical or theoretical approaches have been published in the past, that all introduced some necessary realistic imperfections through additional geometrical eccentricities (see recently Mari and Hellesland [1]). There are numerous textbooks devoted to the elastic or inelastic buckling of columns (see for instance Bažant and Cedolin [2]). But the link between imperfection sensitive structural models and the buckling phenomena of reinforced concrete columns was not clearly highlighted in the authors' point of view, at least not from simple physically based models. In this paper, we will show, using a simple softening one-dimensional model based on continuum damage mechanics (CDM theory), that the buckling of reinforced concrete columns is associated with a limit load which decreases with the imperfection considered. Furthermore, we will derive a universal load-imperfection relationship that can be useful for structural design (Koiter's ½ power law, see [3]). The problem handled in this study is not so different from the *elastica* problem of a softening column, as already numerically investigated by Oden and Childs [4], Wang [5] or Brojan et al [6]. These authors also noticed that buckling of softening systems may lead to the imperfection sensitivity phenomenon. However, our study is based on continuum damage

mechanics arguments, specifically applied to a simplified model of a cantilever reinforced concrete column, in which all material nonlinearities are concentrated in a nonlinear softening spring at the column base. Though simplified, this column will still give some qualitatively useful results. In particular, the specific imperfection sensitivity law that we find in this study is significantly different from the ones highlighted in the studies cited above.

Single-degree-of-freedom model

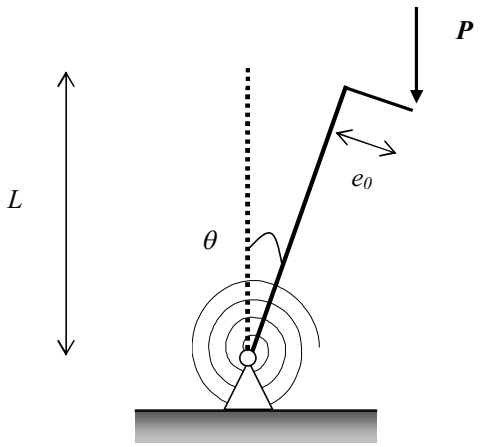

Figure 1. Discrete spring-mass model.

We adopt a simple nonlinear inelastic single-degree-of-freedom system (Fig. 1). The spring is assumed to behave with a damage law defined by:

$$M = k_0(1-D)\theta \tag{1}$$

where M is the bending moment, θ is the rotation of the spring, D is the damage variable, which is a measure of the integrity of the spring. D evolves between 0 for a virgin (undamaged) spring and 1 for the totally broken spring. k_0 is the initial stiffness of the spring. The damage loading function of this model is postulated as (see also Challamel et al [7]):

$$f(\theta, D) = \frac{|\theta|}{\theta_Y} - 2D \tag{2}$$

where θ_Y is the rotation associated with the maximum moment in the spring. For a monotonic increasing evolution of the rotation, which this study is limited to, the loading function is vanishing, i.e. $f(\theta, D) = 0$. The resulting monotonic moment – rotation curve becomes parabolic with a maximum reached for the rotation θ_Y. The equilibrium of the system can readily be obtained in the geometrically exact form as:

$$M = PL\sin\theta + Pe_0\cos\theta \tag{3}$$

Considering Eq. (1), Eq. (2) and Eq. (3), the general nonlinear load-rotation relationship can be written as:

$$p = \frac{\theta\left(1 - \dfrac{|\theta|}{2\theta_Y}\right)}{\sin\theta + e_0^* \cos\theta} \qquad \text{with} \qquad p = \frac{PL}{k_0} \text{ and } e_0^* = \frac{e_0}{L} \tag{4}$$

This relationship is shown in Fig. 2 for different initial eccentricities e_0^*. We note that it has a symmetrically unstable bifurcation $\left(e_0^* = 0\right)$ with softening branches. From an asymptotic expansion of Eq. (4), it can be expressed by:

$$e_0^* = 0 \quad \Rightarrow \quad p = 1 - \frac{|\theta|}{2\theta_Y} + \ldots \tag{5}$$

The interesting result is that the post-buckling branches at the bifurcation point intersect with a sharp angle, even if the system is a symmetrical one in the absence of additional eccentricities. This type of bifurcation is generally present for unsymmetrical bifurcation and it is notable here that this phenomenon occurs due to the specific damage evolution in the inelastic spring.

Imperfection analysis

Unlike the symmetrical behaviour for the perfect case, the behaviour in presence of an imperfection is unsymmetrical, as seen in Fig. 2.

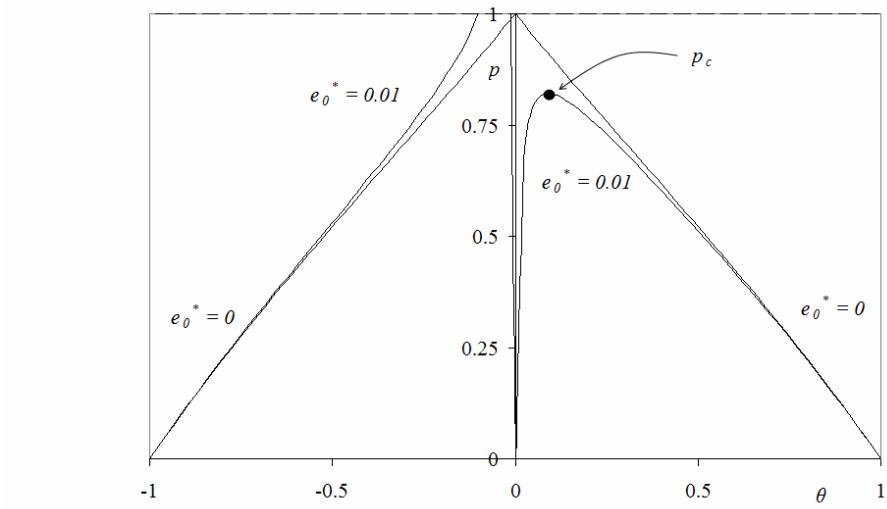

Figure 2. Bifurcation diagram; $\theta_Y = 0.5$; $e_0^* \in \{0;0.01\}$

It can be shown that the limit load p_c of the imperfect problem as defined in Fig. 2, can be expressed for sufficiently small eccentricities by:

$$p_c = 1 - \sqrt{\frac{2}{\theta_Y}}\sqrt{e_0^*} + \ldots \tag{6}$$

This can be cast in the form of a universal rule. One recognizes that this is the same as Koiter's ½ power law (see Koiter [3] or Bažant and Cedolin [2]). However, this extreme sensitivity of the limit load with respect to the eccentricities (or more generally with some imperfections) is generally found in asymmetrical structural systems as pointed out by Bažant and Cedolin [2]. It is remarkable in the present damage problem that this strong imperfection sensitivity appears in an initially symmetrical structural problem, where some angular bifurcation points control the perfect system.

Conclusions

It has been shown using a simple continuum damage mechanics single-degree-of-freedom system, that imperfection sensitivity may arise in buckling of reinforced concrete columns. A new engineering equation has been presented for the limit load-dependence on the imperfection.

We are now extending the analysis to the continuum column problem, where the complete post-failure analysis has certainly to include some non-locality.

Acknowledgements

The research leading to these results has received funding from the European Community's Seventh Framework Programme (FP7/2007-2013) under grant agreement n° PIEF-GA-2010-271610 STABELAS.

References

[1] Mari A.R. and Hellesland J., Lower slenderness limits for rectangular reinforced concrete columns, *J. Struct. Eng.*, 131, 1, 85-95, 2005.

[2] Bažant Z.P. and Cedolin L., *Stability of structures – Elastic, Inelastic, Fracture, and Damage Theories*, Dover Publications, Inc., New-York, 2003.

[3] Koiter W.T., *Over de stabiliteit van het elastische evenwicht*, dissertation, Delft, Holland, The Netherlands, 1945 (in Dutch).

[4] Oden J.T. and Childs S.B., Finite deflection of a nonlinearly elastic bar, *J. Appl. Mech.*, 69, 48-52, 1970.

[5] Wang C.Y., Global buckling load of a nonlinearly elastic bar, *Acta Mechanica*, 119, 229-234, 1996.

[6] Brojan M., Puksic A. and Kosel F., Buckling and post-buckling of a nonlinearly elastic column, *ZAMM*, 87, 7, 518-527, 2007

[7] Challamel N., Lanos C. and Casandjian C., Creep failure of a simply-supported beam through a uniaxial Continuum Damage Mechanics model, *Acta Mechanica*, 192, 1-4, 213-234, 2007.

Proceedings of the 24th Nordic Seminar on Computational Mechanics
J. Freund and R. Kouhia (Eds.)

Unexpected behavior of linearized eigenvalue problem in the context of stability analysis

Alexis Fedoroff, Reijo Kouhia

Aalto University, P.O. Box 12100, 00076 Aalto, FINLAND,
alexis.fedoroff@aalto.fi, reijo.kouhia@aalto.fi

Summary. In this article we aim to demonstrate some unexpected behavior of the critical solution of a non-linear eigenvalue problem if linearization with respect to the critical parameter is used as an approximative method to find the critical point.

Key words: non-linear eigenvalue problem, polynomial approximation of non-linear eigenvalue problem, stability analysis

Introduction

Polynomial approximation with respect to the critical parameter (and in particular linear approximation) of a non-linear eigenvalue problem, evaluated at the origin, is currently the most widespread method used in stability analysis. As a matter of fact linear approximation is currently the only possibility in commercial finite element programs. The reason is that linearization is fast, robust and simple to use compared to other methods, such as path following methods with singularity check (Riks, 1974) or direct computation of augmented non-linear eigenvalue problem (Keener and Keller, 1973), (Moore and Spence, 1980), (Wriggers and Simo, 1990), (Mäkinen et al., 2011).

As far as highly non-linear problems are concerned, even though the critical value given by the linear approximation is too erroneous to be used for engineering applications, the approximated critical mode has usually been considered as reliable. In other words the minimum positive critical mode given by the linear approximation would be suitable to use as initial imperfection for imperfection analysis or together with the approximated critical value as a starting point for direct computation of the of augmented non-linear problem. However, in this paper we shall demonstrate that there are situations when the minimum positive critical mode given by the linear approximation is *not* approximating the minimum positive critical mode of the full non-linear problem, but rather a mode that is associated with higher positive eigenvalue, negative or even non-real eigenvalue. We shall define that in such a situation the linearized approximation is *degenerate*. If such a situation occurs, then all attempts to perform imperfection analysis using a degenerate critical mode or direct computation of augmented non-linear eigenvalue problem starting from a degenerate critical mode will obviously give erroneous results.

We shall first consider the non-linear eigenvalue problem and the linear approximation thereof at a very general level, then give some practical examples of unexpected behavior of the linear approximation.

The non-linear eigenvalue problem

Consider a non-linear eigenvalue problem, where the entries of the matrix $\boldsymbol{A}$ depend smoothly on the critical parameter.

$$\boldsymbol{A}|_{\lambda^{\mathrm{nl}}}\, \boldsymbol{q}^{\mathrm{nl}} = 0 \tag{1}$$

The solution eigenpair for equation (1) is $(\lambda^{\mathrm{nl}}, \boldsymbol{q}^{\mathrm{nl}})$. Consider then a polynomial approximation at the origin with respect to the critical parameter:

$$\sum_{i=0}^{k} \frac{\lambda^{\mathrm{pol}\, i}}{i!} \left.\frac{\mathrm{d}^i \boldsymbol{A}}{\mathrm{d}\lambda^i}\right|_0 \boldsymbol{q}^{\mathrm{pol}} = 0 \tag{2}$$

The solution eigenpair for that polynomial approximation is noted $(\lambda^{\mathrm{pol}}, \boldsymbol{q}^{\mathrm{pol}})$. In figure 1 we have represented graphically the behavior of a non-linear eigenvalue problem and the linear approximation. The influence of non-linearity on the critical value can be depicted most effectively in the matrix space $\mathrm{R}^{n\times n}$. In that space the set of points for which the matrix is singular (rank deficient 1) can be viewed as a smooth n^2-1 manifold $\mathscr{M}$. The set $\mathscr{I}$ corresponds to the graph of the non-linear matrix valued function $\boldsymbol{A} : \lambda \mapsto \boldsymbol{A}|_\lambda$, and the intersection between $\mathscr{M}$ and $\mathscr{I}$ corresponds to the singular matrix $\boldsymbol{A}|_{\lambda^{\mathrm{nl}}}$. In a similar way, the intersection between the manifold $\mathscr{M}$ and the linearized function corresponds to the singular matrix $\boldsymbol{A}|_0 + \lambda^{\mathrm{lin}}\, \boldsymbol{A}'|_0$. If the dependence of the matrix $\boldsymbol{A}$ on the parameter is highly non-linear, as in the example case depicted in figure 1, it is natural that the relative error between the critical value λ^{ln} and λ^{lin} is very important.

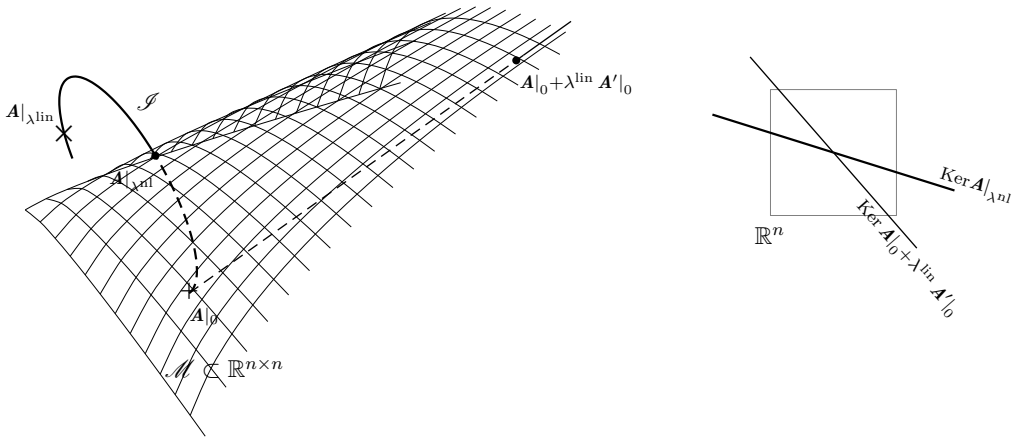

Figure 1. Left: graphic representation of the criticality manifold $\mathscr{M}$ and the set $\mathscr{I}$ given by the (non-linearly) parameter dependent matrix $\boldsymbol{A}|_\lambda$ as well as the linear approximation thereof. Right: Eigenspaces for the non-linear eigenvalue problem and the linear approximation.

However, as we can see on the picture on the right in figure 1, the eigenspace of the non-linear problem $\mathrm{Ker}\boldsymbol{A}|_{\lambda^{\mathrm{nl}}}$ and the eigenspace of the approximation $\mathrm{Ker}\ \boldsymbol{A}|_0 + \lambda^{\mathrm{lin}}\ \boldsymbol{A}'|_0$ are rather distant from each other. The linearized eigenvalue problem shall be called degenerate if the relative error between the eigenmodes $1 - \langle \boldsymbol{q}^{\mathrm{lin}}, \boldsymbol{q}^{\mathrm{nl}} \rangle$ is higher than a user defined threshold level.

Application to bifurcation problems in mechanics

In the field of mechanics stability analysis of quasi-static discrete or discretized systems is traditionally analyzed using the Dirichlet (or energy) criterion (Koiter, 1976) although a full understanding of stability phenomena requires a time dependent approach (Knops and Wilkes, 1974). Hence the non-linear eigenvalue problem issued from a quasi-static mechanical system can be given as a criticality condition subject to equilibrium condition:

$$\begin{cases} \boldsymbol{J}|_{(\boldsymbol{p}^{\mathrm{nl}},\lambda^{\mathrm{nl}})}\,\boldsymbol{q}^{\mathrm{nl}} &= 0 \\ \boldsymbol{f}(\boldsymbol{p}^{\mathrm{nl}},\lambda^{\mathrm{nl}}) &= 0 \end{cases} \tag{3}$$

where $\boldsymbol{p}^{\mathrm{nl}}, \boldsymbol{q}^{\mathrm{nl}}, \lambda^{\mathrm{nl}}$ denote respectively the state variable, the eigenmode and the critical parameter at the critical point. The vector valued function $\boldsymbol{f}$ denotes the defining function of the equilibrium equation and the matrix $\boldsymbol{J}$ denotes the Jacobian of that defining function. Assuming that in the neighborhood of the origin the jacobian of the defining function is invertible, we can find a function $\boldsymbol{p} : \lambda \mapsto \boldsymbol{p}(\lambda)$ via the implicit function theorem and linearize equation (3) at the origin with respect to the critical parameter:

$$\begin{cases} \left[\boldsymbol{J}|_{(\boldsymbol{0},0)} + \lambda^{\mathrm{lin}}\left(\partial_{\boldsymbol{p}}\boldsymbol{J}|_{(\boldsymbol{0},0)}\,(\boldsymbol{p}'|_0) + \partial_\lambda \boldsymbol{J}|_{(\boldsymbol{0},0)}\right)\right]\boldsymbol{q}^{\mathrm{lin}} &= 0 \\ \partial_{\boldsymbol{p}}\boldsymbol{f}|_{(\boldsymbol{0},0)}\,(\boldsymbol{p}'|_0) + \partial_\lambda \boldsymbol{f}|_{(\boldsymbol{0},0)} &= 0 \end{cases} \tag{4}$$

where $\boldsymbol{q}^{\mathrm{lin}}, \lambda^{\mathrm{lin}}$ denote respectively linear approximation of the the eigenmode and the critical parameter at the critical point, and as we have previously showed, there might be situations where the linearized eigenvalue problem (4) is degenerated.

Clearly this degenerate character has to do with non-linearity of the eigenvalue problem in the neighborhood of the origin, as can be seen from figure 1. However, as we start analyzing applied problems, given by equation (3), we have to be cautious what non-linearity we are talking about. In bifurcation problems the primary equilibrium path can be, indeed, quasi-linear and still we have a degenerate linear approximation. It is not even the non-linearity of the secondary equilibrium path in the neighborhood of the critical point that affects the degenerate character of the linear approximation, but rather the non-linearity of the jacobian in the neighbourhood of the origin. Therefore it is not easy to predict the degenerate character of the linear approximation by examining only the bifurcation diagram of the equilibrium path.

Considering observations made on simulations of mechanical structures, it seems that the degenerate character of the linear approximation is closely related to a possible mode interaction in a given structure. Intuitively it makes sense that if the switch from one critical mode to another occurs at a given geometric parameter value when full non-linear analysis is used, then if linear approximation is used instead the mode switch would happen for a slightly different geometric parameter. Therefore all structures that lie within that "gap" with respect to the geometric parameter will show a degenerate linear approximation of the eigenvalue problem.

Figure 2 shows a practical example of what can happen when analyzing out-of-plane buckling of initially plane truss structures. Lateral sway of the top chord has been prevented at node points in order to reflect the lateral stiffening provided by purlins and roof sheeting. We can clearly see that the eigenmode given by the linearized approximation is characterized mainly by flexural buckling of the top chord. On the other hand the eigenmode given by the full non-linear solution is characterized by rigid body motion of the compressed diagonals combined with flexural buckling.

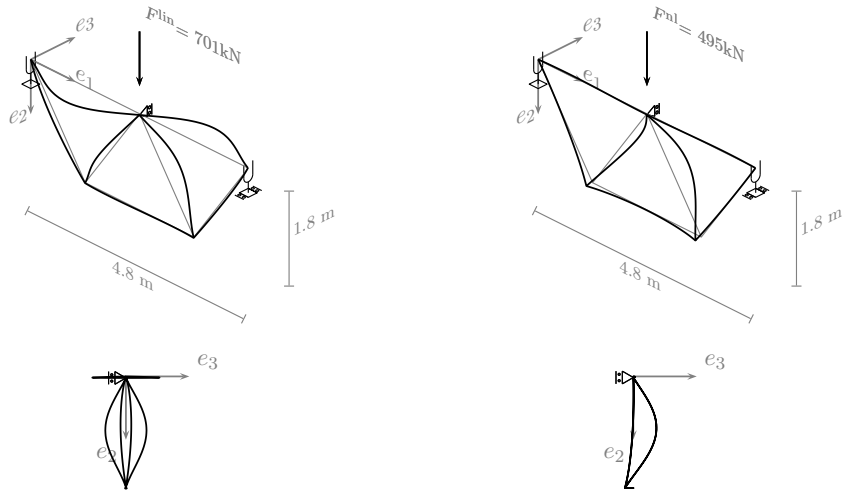

Figure 2. An example of degenerate linear approximation for a Warren truss with 4 diagonals, all members $60 \times 60 \times 3$ closed steel cross-sections. Left picture: result of the linear approximation analysis. Right picture: result of the full non-linear analysis

Conclusions

Numeric analysis of bifurcation problems using linear approximation of the eigenvalue problem can possibly lead to large errors not only for the eigenvalue but also for the eigenmode. In the latter case the linearized eigenvalue problem is called degenerate and the linearized result is useless for engineering considerations.

References

Keener J, Keller H. (1973), "Perturbed bifurcation theory", *Archive for Rational Mechanics and Analysis*, 50:159-175.

Koiter, W. (1976), "A basic open problem in the theory of elastic stability", *Applications of Methods of Functional Analysis to Problems in Mechanics*, Lecture Notes in Mathematics, Springer Berlin / Heidelberg 503:366-373.

R.J. Knops, E.W. Wilkes, (1973) "Theory of elastic stability" S. Flügge (ed.), *Handbuch der Physik*, VI a/3, Springer 125-302

Moore G., Spence A. (1980), "The calculation of turning points of non-linear equations", *SIAM Journal of Num. Analysis*, 17 567-576.

Mäkinen J., Kouhia R., Fedoroff A., Marjamäki H. (2011), "Direct computation of critical equilibrium states for spatial beams and frames", *International Journal for Numerical Methods in Engineering*, accepted for publishing on 17 April 2011.

Riks E. (1974), "The incremental solution of some basic problems in elastic stability", Technical Report NLR TR 74005 U, National Aerospace Laboratory, The Netherlands.

Wriggers P., Simo J.C. (1990), "A general Procedure for the Direct Computation of Turning and Bifurcation Problems", *Computer Methods in Applied Mechanics and Engineering* 30:155-176.

Rakenteiden Mekaniikka (Journal of Structural Mechanics)
Vol. 44, No 3, 2011, pp. 172-185

Static instability analysis of an elastic band travelling in the gravitational field

Nikolay Banichuk, Juha Jeronen, Tytti Saksa and Tero Tuovinen

Summary. Static instability analysis is performed for an axially moving elastic band, which is travelling at a constant velocity in a uniform gravitational field between two supports. The buckling of the band is investigated with the help of admitting small transverse deflections. The model of a thin elastic beam (panel) subjected to bending, centrifugal forces and nonhomogeneous tension (including a gravitational term) is used. Buckling analysis and estimation of the critical velocities of elastic instability are based on variational principles and variational inequalities. As a result, explicit formulas for upper and lower limits for critical velocities are found. It is shown analytically that a critical velocity always exists. The critical buckling modes are found, first, by solving the original differential equation directly, and, secondly, by energy minimization. The buckling modes and corresponding critical velocities are found and illustrated with some numerical examples. The gravitational force is shown to have a major effect on the buckled shape, but a minor effect on the critical velocity.

Key words: stability, paper industry, paper, elasticity, gravitation, partial differential equations, optimization

Nikolay Banichuk
Institute for problems in mechanics, Russian Academy of Sciences
Prospekt Vernadskogo 101, 119526 Moscow, Russia
banichuk@ipmnet.ru

Juha Jeronen, Tytti Saksa, Tero Tuovinen
University of Jyväskylä
P.O. Box 35 (Agora), 40014 University of Jyväskylä, Finland
juha.jeronen@jyu.fi, tytti.saksa@jyu.fi, tero.tuovinen@jyu.fi

Proceedings of the 24th Nordic Seminar on Computational Mechanics
J. Freund and R. Kouhia (Eds.)

The equations of motion and the power theorem in multibody dynamics

Per Lidström

Division of mechanics, Lund University, P.O. Box 118, S-22100, Lund, Sweden
per.lidstrom@mek.lth.se

Summary. A power theorem for a multibody system is derived

Key words: multibody dynamics, equations of motion, power theorem

Introduction

Consider a *multibody* $\mathcal{B}$ consisting of N *rigid* or *elastic* bodies (parts): $\mathcal{B}^\alpha$, $\alpha = 1,...,N$. The *transplacement* of a part is given by a mapping $x = \chi^\alpha(t,q;X)$, $(t,q;X) \in \mathbb{R}\times\mathbb{R}^n\times\mathcal{B}_0^\alpha$ where $\mathcal{B}_0^\alpha$ is a reference placement for part $\mathcal{B}^\alpha$ and $q = (q^1,q^2,...,q^n) \in \Omega \subseteq \mathbb{R}^n$ are *configuration coordinates*.

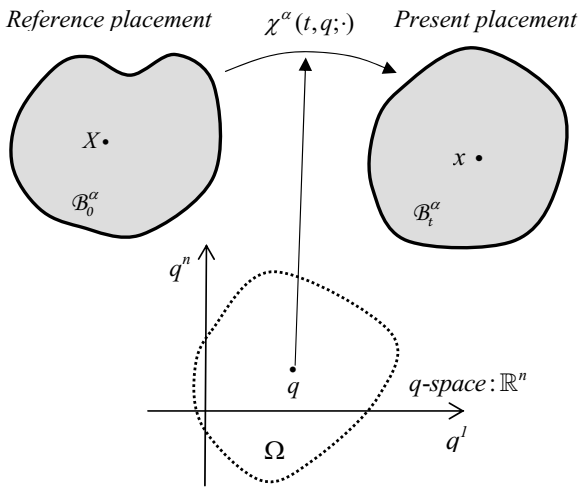

Figure 1. Transplacement of multibody part.

A central issue in multibody dynamics is the formulation of geometrical or kinematical constraints representing conditions on the relative motions between parts of the mechanical system and the associated formulation of the equations of motion, see Lidström [1,2]. In general, the kinematical (bilateral) constraint will lead to a system of first order ordinary differential equations

$$g_0 + g\,\dot{q} = 0_{m\times 1}$$

where $g_0 = g_0(t,q) \in \mathbb{R}^{m\times 1}$ and $g = g(t,q) \in \mathbb{R}^{m\times n}$ are the *constraint matrices*. A formulation of the equations of motion for the constrained mechanical system may, for instance, be obtained by invoking the *Lagrange - d'Alembert equations of motion*,

$$\frac{d}{dt}\left(\frac{\partial T}{\partial \dot{q}}\right) - \frac{\partial T}{\partial q} - Q = 0_{1\times n}$$

where $T = T(t,q,\dot{q})$ is the kinetic energy of the multibody, $Q = Q(t,q,\dot{q}) \in \mathbb{R}^{1\times n}$ is the so-called *sum of the generalized forces* acting on the multibody due to internal, contact and body forces. One part of Q is the force $Q^{kc} = Q^{kc}(t,q,\dot{q}) \in \mathbb{R}^{1\times n}$ due to the kinematical constraints. The so-called '*nonholonomic principle*' states that

$$Q^{kc} = \lambda^T g$$

where the '*multipliers*' $\lambda = \lambda(t) \in \mathbb{R}^{m\times 1}$ represent components of constraint forces and moments. A justification of the nonholonomic principal may be based on the *principle of virtual power.*

The initial value problem for the motion of a constrained multibody system may be written

$$\begin{cases} \ddot{q}^T M_2 - Q^{sum} = 0_{1\times n} \\ g_0 + g\dot{q} = 0_{m\times 1} \\ q(0) = q_0, \quad \dot{q}(0) = \dot{q}_0 \end{cases} \tag{1}$$

where $g_0(0,q_0) + g(0,q_0)\dot{q}_0 = 0_{m\times 1}$. In (1) M_2 is the *mass matrix* and Q^{sum} is the *sum of the generalized forces* on the multibody. This sum may be written

$$Q^{sum} = Q^{res} + Q^{kc} \tag{2}$$

where $Q^{res} = Q^{cif} + Q^{i} + Q^{ec} + Q^{b} + Q^{ric}$ is the *residual generalized force*, Q^{cif} is the *complementary inertia force* and Q^{i}, Q^{ec} and Q^{b} are the *generalized force* due to internal, external contact and body forces, respectively. Furthermore, $Q^{ric} = Q^{ic} - Q^{kc}$ is the reduced internal contact force, i.e. internal contact forces not including the constraint forces. The internal generalized contact forces may be written

$$Q^{ic} = \frac{1}{2}\sum_{\alpha,\beta=1}^{N} I^{\alpha\beta} \tag{3}$$

where the *mechanical interaction* $I^{\alpha\beta}$ between parts $\mathcal{B}^\alpha$ and $\mathcal{B}^\beta$ is given by

$$I^{\alpha\beta} = Q^{\alpha\beta} + Q^{\beta\alpha}, \quad Q_k^{\alpha\beta} = \int_{S_t^{\alpha\beta}} \boldsymbol{x}_k^\alpha \cdot \boldsymbol{t}^{\alpha\beta} da(x), \quad \alpha \neq \beta, \quad k = 1,...,n \tag{4}$$

$S_t^{\alpha\beta}$ is the contact surface between parts $\mathcal{B}^\alpha$ and $\mathcal{B}^\beta$, $\boldsymbol{x}_k^\alpha(t,q,x) = \dfrac{\partial \chi^\alpha}{\partial q^k}(t,q(t);X)$ and $\boldsymbol{t}^{\alpha\beta}$ is the traction vector acting on $\mathcal{B}^\alpha$ from $\mathcal{B}^\beta$.

The power theorem

We split the generalized forces, except for the internal contact forces Q^{ic} into one conservative and one non-conservative part, i.e.

$$Q^i + Q^{ec} + Q^b = Q^{con} + Q^{non} \tag{5}$$

where Q^{con} is a *conservative force* with potential $V = V(t,q)$, i.e.

$$Q_k^{con} = -\frac{\partial V}{\partial q^k} \tag{6}$$

and Q^{non} is the *non conservative generalized force* containing the non-conservative parts of the left hand side in (5). If the specific body force is conservative with the potential V_b, then the potential $V = V(t,q)$ will contain the sum $V_e + V_b$ where V_e is the elastic energy, which for a *St. Venant-Kirchhoff material* is given by ($\lambda^\alpha, \mu^\alpha$ Lame moduli)

$$V_e = \sum_{\alpha=1}^{N} \left(\int_{\mathcal{B}_0^\alpha} \left(\frac{1}{2}\lambda^\alpha (\mathrm{tr}\boldsymbol{E}^\alpha)^2 + \mu^\alpha \left|\boldsymbol{E}^\alpha\right|^2 \right) dv(X) \right) \tag{7}$$

The *mechanical energy*, *E*, of the multibody is defined by

$$E = \sum_{k=1}^{n} p_k \dot{q}^k - L \tag{8}$$

where $L = L(t,q,\dot{q})$ is the *Lagrangian* and $p_k = \dfrac{\partial L}{\partial \dot{q}^k}$ are the components of the so-called *generalized momentum*. The *power expended by forces maintaining the kinematical constraints* is defined by

$$P^{kc} = Q^{kc}\dot{q} \tag{9}$$

Proposition 1

$$P^{kc} = -g_0^T \lambda \tag{10}$$

which implies that for a multibody with homogeneous constraints $P^{kc} = 0$.

The constraint forces supporting homogeneous constraints are thus powerless. The powers P^{ic} and P^{ric} expended by the internal and residual internal contact forces, respectively are defined by $P^{ic} = Q^{ic}\dot{q}$, $P^{ric} = Q^{ric}\dot{q}$ and $P^{ic} = P^{ric} + P^{kc}$.

Theorem 1 (*The Power Theorem*)

$$P^{non} + P^{ric} + P^{kc} - \frac{\partial L}{\partial t} = \dot{E} \tag{11}$$

where P^{non} is *the power expended by the nonconservative forces*, i.e. $P^{non} = Q^{non}\dot{q}$. For a multibody with homogeneous constraints $P^{non} + P^{ric} - \frac{\partial L}{\partial t} = \dot{E}$.

Theorem 2 The initial value problem (1) is equivalent to

$$\begin{cases} M_2\ddot{q} - Q_c^{resT} + g^T\Gamma^{-1}(\frac{\partial \overline{g}}{\partial \overline{q}}\dot{\overline{q}})\dot{\overline{q}} = 0_{n\times 1} \\ q(0) = q_0, \quad \dot{q}(0) = \dot{q}_0 \end{cases} \tag{12}$$

where $g_0(0,q_0) + g(0,q_0)\dot{q}_0 = 0_{m\times 1}$ and

$$Q_c^{res} = Q^{res}R^T, \quad R = I_{n\times n} - P, \quad P = g^T\Gamma^{-1}gM_2^{-1} \in \mathbb{R}^{n\times n} \text{ and } \Gamma = gM_2^{-1}g^T \in \mathbb{R}^{m\times m}$$

Q_c^{res} is called the *constrained residual generalized force*. The matrices R and P are projections, i.e. $R^2 = P^2 = I_{n\times n}$ and $P \neq 0_{n\times n}$. Furthermore, $range(g^T)$ is a linear subspace of $range(P)$. The Lagrangian multipliers (constraint forces) are given by

$$\lambda = -(\Gamma^{-1}gM_2^{-1}Q^{resT} + \Gamma^{-1}(\frac{\partial \overline{g}}{\partial \overline{q}}\dot{\overline{q}})\dot{\overline{q}}) \tag{13}$$

and then, according to (10)

$$P^{kc} = -g_0^T\Gamma^{-1}(gM_2^{-1}Q^{resT} - (\frac{\partial \overline{g}}{\partial \overline{q}}\dot{\overline{q}})\dot{\overline{q}}) \tag{14}$$

References

[1] Lidström P.; On the Equations of Motion in Multibody Dynamics. Published online in *Mathematics and Mechanics of Solids*.

[2] Lidström P.; On the Equations of Motion in Constrained Multibody Dynamics. Published online in *Mathematics and Mechanics of Solids*.

Proceedings of the 24th Nordic Seminar on Computational Mechanics
J. Freund and R. Kouhia (Eds.)

Numerical simulation of dynamic Brazilian disc test on rock

Timo Saksala[1], Mikko Hokka[2], Veli-Tapani Kuokkala[2] and Jari Mäkinen[1]

(1)Department of Mechanics and Design, Tampere University of Technology, P.O. Box 589, FI-33101, Tampere, Finland, timo.saksala@tut.fi, jari.m.makinen@tut.fi
(2)Department of Materials Science, Tampere University of Technology, P.O. Box 589, FI-33101, Tampere, Finland, mikko.hokka@tut.fi, veli-tapani.kuokkala@tut.fi

Summary. This paper presents a numerical method for simulating the dynamic Brazilian disc test on rock using the Split Hopkinson Pressure Bar apparatus (SHPB). The method includes a material model based on viscoplasticity and damage mechanics for rock and a FEM based explicit time marching technique for simulating the dynamics of the SHPB apparatus. Simulation results are verified experimentally on the Kuru granite.

Key words: dynamic Brazilian disc test, split Hopkinson pressure bar, FEM, rock fracture

Introduction

The tensile strength of brittle materials, such as rock and concrete, is usually much, up to 15 times, lower than their compressive strength. Moreover, both strengths display a significant loading rate hardening effect, which is particularly pronounced for the tensile strength. Therefore, a numerical model aiming at realistic prediction of rock behaviour under dynamic loading conditions should take the loading (strain) rate sensitivity into account. The dynamic tensile strength of rock can be indirectly measured using the Split Hopkinson Pressure Bar apparatus with the so-called Brazilian disc (BD) specimens [1].

This paper presents some preliminary results on an on-going project at TUT, the purpose of which is to provide experimental data on the dynamic tensile strength and failure modes of the Kuru granite. The data is used in (dynamic) calibration and verification of the material model for the rock under low-velocity impact loadings [2]. The main application of the model is the simulation of percussive rock drilling.

In the numerical simulations the failure mode and the dynamic tensile strength predicted with the present modelling approach are compared to the results of the experimental work carried out at the Department of Materials Science of TUT.

Principle of the SHBP apparatus with a Brazilian disc sample

The principle of the SHPB test apparatus with the Brazilian disc sample is shown schematically in Figure 1.

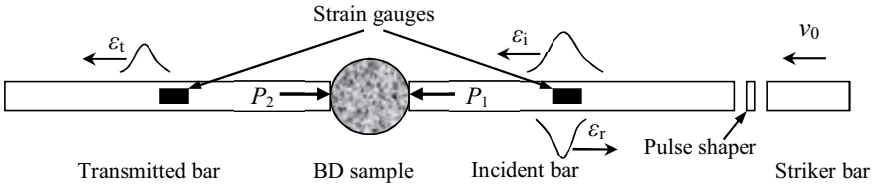

Figure 1. Schematic picture of the SHPB setup for the dynamic BD test.

The striker bar impacts the free end of the incident bar generating a compressive stress wave (incident pulse), which travels through the incident bar and the BD sample causing its diametrical splitting. The incident, transmitted and reflected pulse strains, ε_i, ε_t, ε_r, respectively, are measured as a function of time by the strain gages indicated in Figure 1. Moreover, a pulse shaper of relatively soft material (copper, rubber) is utilized in order to reach the dynamic stress equilibrium by increasing the rise time of the incident stress pulse. The indirect tensile strength of the specimen can be calculated, based on the elasticity solution of the quasi-static problem, as

$$\sigma_T = 2P / \pi LD \tag{1}$$

where P is the force acting on the specimen with length L and diameter D. The dynamic forces acting on both sides of the BD specimen are calculated using Equations (2) [1]

$$P_1 = A_b E_b (\varepsilon_i + \varepsilon_r), \quad P_2 = A_b E_b \varepsilon_t \tag{2}$$

where A_b and E_b are the cross-sectional area and Young's modulus of the bars, respectively.

Theory of the simulation model

Constitutive model for rock

The constitutive model for rock is based on the consistent viscoplasticity and isotropic damage concept. The viscoplastic stress states are indicated by the Drucker-Prager and Rankine type of yield criteria formulated in the principal stress space as

$$\begin{aligned} f_{\mathrm{DP}}(\boldsymbol{\sigma}, \kappa_{\mathrm{DP}}, \dot{\kappa}_{\mathrm{DP}}) &= \sqrt{J_2} + \alpha_{\mathrm{DP}} I_1 - k_{\mathrm{DP}} c(\kappa_{\mathrm{DP}}, \dot{\kappa}_{\mathrm{DP}}) \\ f_{\mathrm{MR}}(\boldsymbol{\sigma}, \kappa_{\mathrm{MR}}, \dot{\kappa}_{\mathrm{MR}}) &= \sqrt{\textstyle\sum_{i=1}^{3} \langle \sigma_i \rangle^2} - f_{\mathrm{t}}(\kappa_{\mathrm{MR}}, \dot{\kappa}_{\mathrm{MR}}) \end{aligned} \tag{3}$$

where c, f_t are the cohesion and the tensile strength of the material, respectively, and κ_{MR}, κ_{DP} are the internal variables in tension and compression, respectively. The cohesion and tensile strength are rate dependent as follows:

$$c = c_0 + h_{\mathrm{DP}} \kappa_{\mathrm{DP}} + s_{\mathrm{DP}} \dot{\kappa}_{\mathrm{DP}}, \quad f_{\mathrm{t}} = f_{\mathrm{t0}} + h_{\mathrm{MR}} \kappa_{\mathrm{MR}} + s_{\mathrm{MR}} \dot{\kappa}_{\mathrm{MR}} \tag{4}$$

where h_{DP}, h_{MR} are the plastic (softening) moduli in compression and tension, respectively, and s_{DP}, s_{MR} are the viscosity moduli in compression and tension, respectively. Generally, the viscosity moduli depend on the loading rate and should thus be formulated accordingly if the hardening effects are to be realistically predicted in a wide range of loading rates. In the present preliminary study, however, constant values were assumed.

In the damage part of the model the standard phenomenological isotropic (scalar) damage model is employed with a typical exponential damage function

$$\omega_t = 1 - \left(1 - A_t + A_t \exp\left(-\beta_t \varepsilon^{vp}_{eqvt}\right)\right) \tag{5}$$

where A_t, β_t are the parameters controlling the final value and the initial slope of the damage variable ω_t, respectively, and ε^{vp}_{eqvt} is a cumulative equivalent viscoplastic strain that serves as a history variable. The damage variable defined in (5) operates only on the positive part of the principal stress vector. Thus, the damage model governs the softening and stiffness degradation in tension while the viscoplastic softening law (4) governs the softening in compression.

The values of the softening moduli are determined based on the fracture energies G_{Ic} and G_{IIc} as $\beta_t = f_{t0}h_e/G_{Ic}$ and $h_{DP} = -f_{c0}^2 h_e/2G_{IIc}$ where f_{c0} is uniaxial compressive strength and h_e is a characteristic length of a finite element. Mesh objective and realistic dissipation is obtained through this choice of the softening moduli values. In tension $h_{MR} = 0$.

As for the stress return mapping, it is performed independently of damage in a standard manner in the effective stress space.

The microstructural heterogeneity of the rock has a major influence on its failure processes. Here, the statistical method based on the Weibull distribution is selected for characterising the rock strength heterogeneity at the mesoscopic level.

SHPB simulation model

The SHPB test setup with the BD sample of rock is modeled as described in Figure 2.

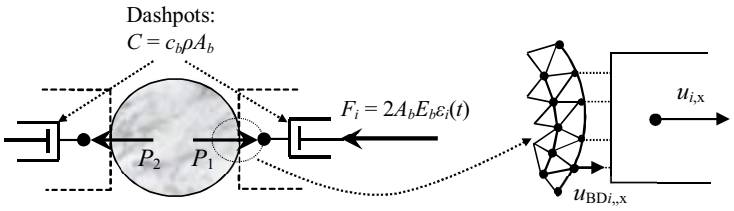

Figure 2. Principle of the dynamic BD test simulation model.

As the purpose is to simulate the dynamic BD test on rock, the bars of the SHPB apparatus are modeled by two nodes (see Figure 2) with one degree of freedom in each. This simplification requires viscous dashpots, with the impedance $C = c_b \rho A_b$, attached to the nodes so as to simulate long bars. The incident pulse is modelled as an external strain pulse, $\varepsilon_i(t)$, applied to the incident node. The contacts between the BD sample and the incident and transmitter nodes (bars) are modelled in a standard manner by imposing contact constraints, of form $u_{ix} - u_{BDi,x} = b_i$, between these nodes and the edge nodes of the discretized BD sample (see Figure 2).

The equations of motion of the incident and transmitted nodes are attached to the discretized equations of motion of the BD sample. The contact constraints are imposed with the forward increment Lagrange multiplier method and the explicit modified Euler time integrator is employed in solving the response of the system in time [2].

Numerical example

The method presented above was applied in the dynamic 2D (plane stress) simulation of a BD specimen with dimensions L = 16 mm and D = 40.5 mm. The bar lengths of the SHPB apparatus are $L_i = L_t$ = 1.2 m and L_{sb} = 0.2 m (striker bar). The diameter of the bars is 22 mm.

The initial velocity of the striker bar is 11.2 m/s. The BD sample is discretized with 4348 CST elements each having the maximum side length of 1 mm. The external strain pulse $\varepsilon_i(t)$ is taken from an experiment conducted with a rubber pulse shaper. The material properties chosen for the Kuru granite are: E = 60 GPa, ν = 0.2, ρ = 2600 kg/m^3, f_{t0} = 13 MPa, f_{c0} = 230 MPa, G_{Ic} = 100 N/m^2 and G_{IIc} = 10G_{Ic}. The viscosity moduli values are set s_{DP} = s_{MR} = 0.07 MPa·s.

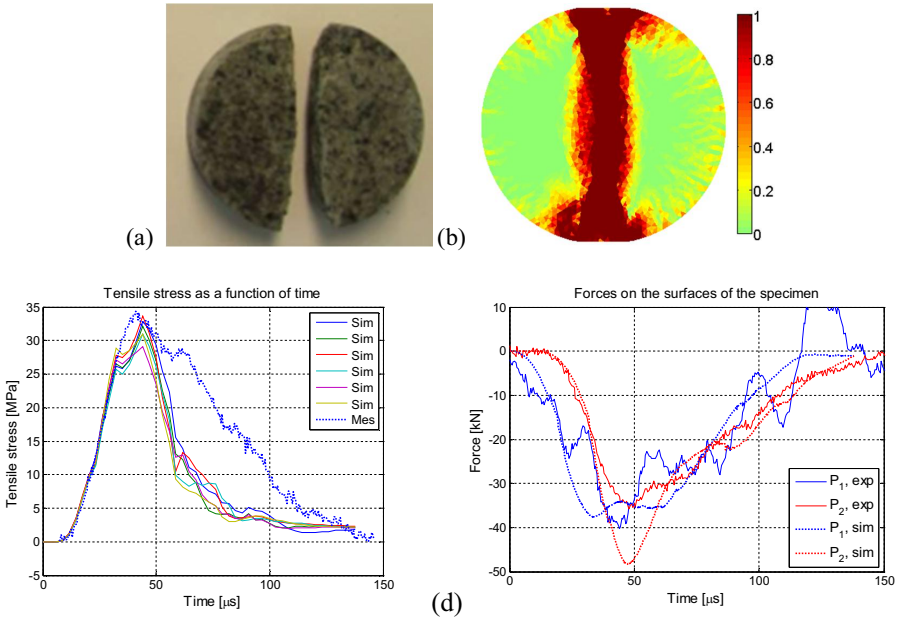

Figure 3. Experimental (a) and simulated (b) failure modes, tensile stress at the center of the specimen (c) and forces on the contact surfaces of the specimen (d).

According to the results shown in Figure 3, the present model predicts the correct failure mode, i.e., the diametrical splitting in tension. The experimental dynamic forces P_1 and P_2 are fairly well matched with the simulated ones. As for the tensile strength in Figure 3c, the simulated and quasi-experimental curves are close to each other during loading but deviate substantially during unloading. The reason for this deviation is that the simulated stresses are recorded within a patch of six triangles at the centre of the disc while the experimental curves are calculated using the experimental force P_1 and the quasi-static Equation (1). The maximum tensile stress of 34 MPa is, however, closely predicted by the simulation model. As the quasi-static tensile strength of the Kuru granite is ~13 MPa, strong loading rate sensitivity is evidenced in the test.

References

[1] Q.Z. Wang, W. Li, X.L. Song, A Method for Testing Dynamic Tensile Strength and Elastic Modulus of Rock Materials Using SHPB, *Pure and Applied Geophysics*, 163(5-6):1091-1100, 2006.

[2] T. Saksala, Damage–viscoplastic consistency model with a parabolic cap for rocks with brittle and ductile behavior under low-velocity impact loading, *International Journal for Numerical and Analytical Methods in Geomechanics*, 34(13):1362–1386, 2010.

Proceedings of the 24th Nordic Seminar on Computational Mechanics
J. Freund and R. Kouhia (Eds.)

Sensitivity analysis of Snelson-type tensegrity booms due to member loss

Seif Dalil Safaei, Anders Eriksson, and Gunnar Tibert

KTH Mechanics, 10044 Stockholm, Sweden, tibert@kth.se

Summary. Tensegrity structures are spatial reticulate systems in a state of self-stress. Although the concept of tensegrity has received significant attention, the application of these structures is limited. This paper is concerned with the effects of element loss on the stiffness and natural frequencies of Snelson-type tensegrity booms. The effect of module length is evaluated for the constant structural length, diameter and axial stiffness of the elements.

Key words: Snelson-type tensegrity boom, element loss, non-linear static analysis, modal analysis.

Introduction

Tensegrity structures are structures composed of tension and compression elements in equilibrium [1]. Tensegrity structures have several advantages: (i) they have low mass, making them suitable for many applications, (ii) the elements could have the role of sensors, actuators or both of them, and (iii) the non-contacting compression members make them interesting as deployable structures. A tensegrity structure usually has a number of members depending on its application and size. Some members critically affect the stiffness and strength of the structure. The failure of these elements could significantly reduce the stiffness and strength and create large non-linear vibrations. Failures could be cable rupture, strut buckling, or a faulty joint. For example, a critical element should not be selected as sensor or actuator for control of the shape of the structure. The analysis for finding the critical elements can be seen on static and dynamic levels. Shekastehband et al. [2] study the sensitivity analysis of tensegrity grids considering material and geometrical non-linearity. Korkmaz et al. [3] study several damage scenarios and introduce active control for self-repair. Ben Kahla al. [4] investigate the influence of sudden cable rupture in a beam-like tensegrity not considering the influence of external loads.

Snelson-type tensegrity boom

Figure 1 shows a Snelson-type tensegrity boom. Having one state of self-stress and one mechanism for any number of stages is the unique property of this structure. The method from [5] is implemented for form-finding.

Analysis

A linearized dynamic model of the structure is written as:

$$\mathbf{M}\ddot{\mathbf{u}} + \mathbf{C}\dot{\mathbf{u}} + \mathbf{K}\mathbf{u} = \mathbf{f} \tag{1}$$

where $\mathbf{M}, \mathbf{K}$, $\mathbf{C}$, $\mathbf{f}$ and are mass, damping, tangent stiffness matrices, and external force vector, respectively. $\ddot{\mathbf{u}}$, $\dot{\mathbf{u}}$, and $\mathbf{u}$ are acceleration, velocity and displacement vectors. For the non-linear

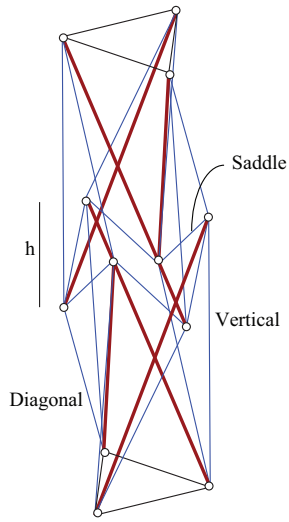

Figure 1. Snelson-type tensegrity boom

equilibrium analysis in this study, the bar element stiffness formulation by [6] was used. A consistent mass matrix formulation is used. To understand the vibration behavior, an investigation of the first mode of natural frequency is necessary. The modal analysis is conducted by ignoring the damping term and the vector of external force. Assuming a small harmonic motion of the form $\mathbf{u} = \bar{\mathbf{u}}\sin(\omega t)$, with ω as the frequency of system and $\bar{\mathbf{u}}$ as the amplitude vector:

$$\mathbf{K}\bar{\mathbf{u}} = \omega^2\mathbf{M}\bar{\mathbf{u}} \tag{2}$$

The eigenvalue analysis of the matrix $\mathbf{M}^{-1}\mathbf{K}$ give the natural modes of the vibration.

Numerical examples

The boom structures are assumed to have following properties: truss radius $R = 0.577$ m, truss length $L = 20$ m. Carbon Fiber Reinforced Plastic (CFRP) is selected as material for the compressive members, because of its high strength and stiffness. The Young's modulus, Poisson's ratio, and density of CFRP are $E = 536$ GPa, ν =0.39, and $\rho = 1840\,\mathrm{kg/m^3}$. Zylon with ultimate strength $\sigma_u = 5.8$ GPa, $E = 180$ GPa and $\rho = 180\,\mathrm{kg/m^3}$ is selected for cable elements. The radius of cables is 6.2 mm. The outer and inner radii of the struts are 29.2 and 27 mm. The stage overlap in Snelson boom is 1.93 m. Here, two cases with 10 and 5 equally spaced number of modules are considered. The radius, axial stiffness of the elements and overlap part (h) are the same. The structures are pre-stressed to have 50 kN force in struts.

The element removal is performed only for pre-stressed case with no external load (no self-weight). Due to symmetry, one element of each type (diagonal cable, vertical cable, saddle cable and strut) is removed in each module. The following conclusions can be drawn out from Tables 1 and 2:

- Normally it is expected that the elements in lower modules, close to base, have more effect on the stiffness and natural frequencies of the structure. Tables 1 and 2 shows this idea is not valid. For example, one can compare the effect on displacement and frequency from rupture of diagonal cables in modules 4 and 8.

- Most damage is inflicted by removing the saddle cables on the lower modules.
- Element removal for the case with 5 modules is less risky than element removal in the 10-module boom.

Table 1. Displacement (m) from prestressed geometry / first natural mode of frequency (Hz) for various element removals of the boom with 10 modules. The frequency for the first mode of the boom with all elements is 4.11 (Hz).

Modules	Diagonal cables	Vertical cables	Saddle cables	Struts
1 (bottom)	0.74 / 2.31	3.06 / 0.37	2.57 / 0.13	Collapse
2	0.63 / 2.51	0.75 / 1.11	2.71 / 0.17	Collapse
3	0.54 / 2.41	0.90 / 2.63	2.21 / 0.26	1.63 / 0.06
4	0.45 / 3.23	0.74 / 3.10	2.44 / 0.34	1.35 / 0.08
5	0.53 / 2.87	0.66 / 3.31	2.42 / 0.50	1.73 / 0.34
6	0.31 / 3.87	0.55 / 3.57	1.99 / 0.76	1.45 / 0.45
7	0.39 / 3.55	0.50 / 3.78	1.12 / 0.90	0.87 / 0.29
8	0.13 / 4.10	0.37 / 3.92	1.14 / 0.90	0.64 / 0.39
9	0.23 / 4.03	0.34 / 3.82	0.85 / 1.74	0.58 / 0.63
10 (top)	0.27 / 4.09	0.47 / 3.94	0.38 / 4.10	0.32 / 3.762

Table 2. Displacement (m) from prestressed geometry / first natural mode of frequency (Hz) for various element removals of the boom with 5 modules. The frequency for the first mode of the boom with all elements is 4.05 (Hz).

Modules	Diagonal cables	Vertical cables	Saddle cables	Struts
1 (bottom)	0.41 / 3.08	1.92 / 0.75	1.28 / 0.36	0.41 / 3.08
2	0.32 / 3.43	0.59 / 2.86	1.43 / 0.17	0.63 / 0.22
3	0.37 / 3.19	0.50 / 3.35	1.22 / 0.73	0.95 / 0.45
4	0.16 / 4.03	0.46 / 3.74	0.86 / 1.80	0.57 / 0.92
5 (top)	0.29 / 3.95	0.50 / 3.34	0.38 / 4.03	0.31 / 3.59

Figure 2 shows the undeformed and deformed configurations of the studied tensegrity booms. As shown, removal of the strut and saddle cables lead to a "buckled" configuration.

Conclusions

The study in this paper was concerned with the investigation into the effects of member loss on the structural integrity of the Snelson-type tensegrity boom in a pre-stressed state and without the presence of the external loads. The study shows that for the same structural length, the case with lower number of module has higher resistance against element damage. Also the structure with higher number of modules is more sensitive to damage of saddle cables.

References

[1] Motro,R. and Raducanu,V. *Tensegrity systems.* International Journal of Space Structures, 18 (2), 2003.

[2] Shekastehband, B. and Abedi, K. and Chenaghlou, M. R. Sensitivity analysis of tensegrity systems due to member loss. *Journal of Constructional Steel Research, 67(9), 2011.*

[3] Korkmaz, S. and Bel Hadj Ali, N. and Smith, I. F. C. Determining control strategies for damage tolerance of an active tensegrity structure. *Engineering Structures, 33(6), 2011.*

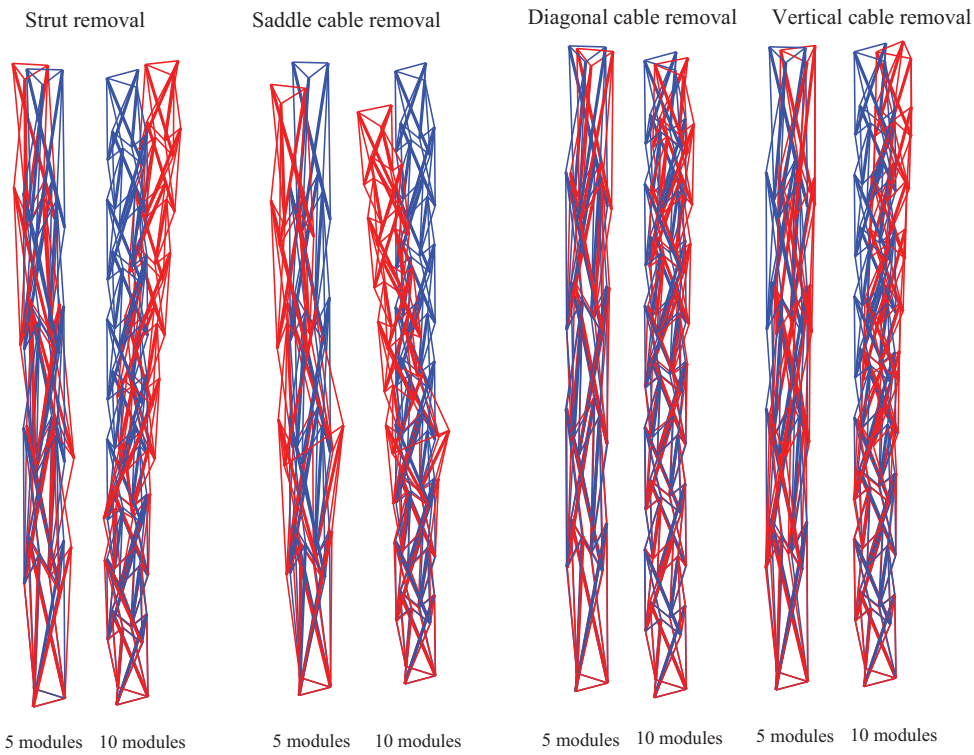

Figure 2. Undeformed (blue) and deformed (red) configuration of Snelson-type tensegrity boom due to several cases of element removals.

[4] Ben Kahla, N. and Moussa, B. Effect of a cable rupture on tensegrity systems. *International Journal of Space Structures, 17(1), 2002.*

[5] Nishimura, Y. *Static and dynamic analyses of tensegrity structures,* PhD thesis, University of California at San Diego, La Jolla, CA, USA, 2000.

[6] Guest, S. The stiffness of prestressed frameworks: A unifying approach. *International Journal of Solids and Structures, 43(3-4), 2006.*

Proceedings of the 24th Nordic Seminar on Computational Mechanics
J. Freund and R. Kouhia (Eds.)

Three-dimensional solid elements employing slopes in the absolute nodal coordinate formulation

Alexander Olshevskiy[1], Oleg Dmitrochenko[2] and Chang-Wan Kim[1]

(1)Department of Mechanical Engineering, Konkuk University1 Hwanyang-Dong, Gwangjin-Gu, 143-701, Seoul, Korea, dsmsoft@rambler.ru
(2)Department of Mechanical Engineering Lappeenranta University of Technology Skinnarilankatu 34, 53850 Lappeenranta, Finland, dmitroleg@rambler.ru

Summary. Two new solid finite elements employing the absolute nodal coordinate formulation are presented. This formulation leads to the constant mass matrix and the non-linear stiffness matrix. The discussed solid eight node brick and the tetrahedral element use translations of nodes and finite slopes as a set of nodal coordinates. The interpolation of the displacement field using incomplete cubic polynomials provides the absence of the shear locking effect. Several examples of numerical simulation are given

Key words: absolute nodal coordinate formulation, flexible multibody dynamics, large displacements, finite element method

Introduction

Many researchers have contributed in adapting the FEM for solving problems with large deformations and large overall motion. One of the approaches in this area is the floating reference frame formulation [1]. The local displacements of a flexible body are considered to be small, and large deformations cannot be simulated. The incremental finite element approach [2] uses infinitesimal rotation angles as nodal variables and leads to the linearized equations of kinematics. The rigid-body displacements cannot be described exactly. The large rotation vector formulation uses finite rotation angles and allows simulating an arbitrary rigid-body motion correctly [3]. The absolute nodal coordinate formulation (ANCF) was introduced by Shabana [4]. In the ANCF the elements use absolute coordinates of nodes and their spatial derivatives (slopes) as nodal degrees of freedom in the global reference frame. As a result, the mass matrix and the gravity forces vector are constant, and the centrifugal and Coriolis inertia forces vanish. The expressions describing the elastic forces vector can be quite very cumbersome. Many different finite elements employing the ANCF exist were developed [5, 6, 7, 8]. In the most of existing three-dimensional solid element types, only translational degrees of freedom are used. Using the finite slopes allows avoiding the effect of shear locking. In this paper, solid elements with eight and four nodes using translations of nodes and finite slopes are considered.

Elements formulation

The nodal coordinates of the 3-D elements with eight and four nodes are shown in the Fig. 1.

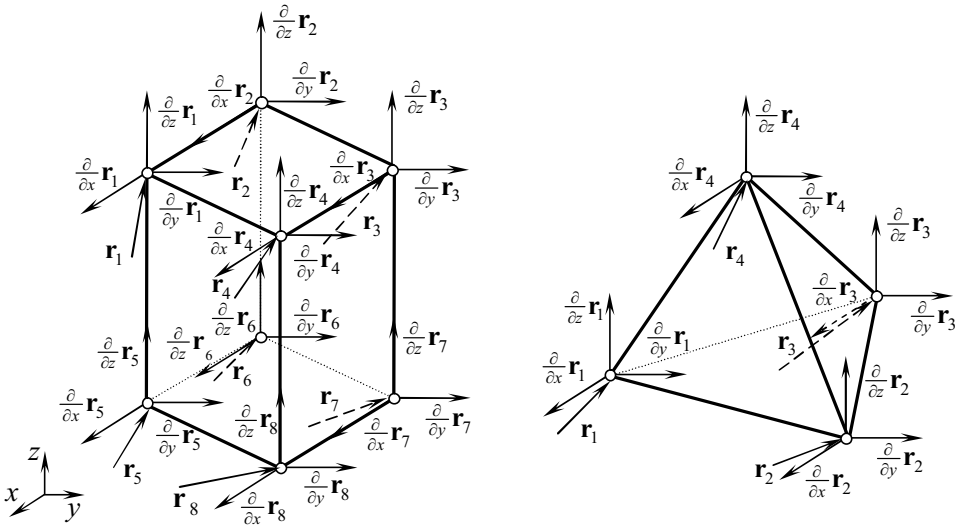

Figure 1. 3-D solid elements using translations of nodes and finite slopes.

The position of an arbitrary point P within the element is determined by a global vector $\mathbf{r}$, which is calculated as a product of the shape functions matrix $\mathbf{S}$ and the vector of nodal coordinates $\mathbf{e}$ as follows:

$$\mathbf{r} = \mathbf{S} \cdot \mathbf{e} = \underbrace{[s_{11}\mathbf{I} \quad \cdots \quad s_{1c}\mathbf{I} \,\vdots\, \cdots \,\vdots\, s_{n1}\mathbf{I} \quad \cdots \quad s_{nc}\mathbf{I}]}_{\mathbf{S}} \cdot \underbrace{\{\mathbf{r}_{11}^{\mathrm{T}} \quad \cdots \quad \mathbf{r}_{1c}^{\mathrm{T}} \,\vdots\, \cdots \,\vdots\, \mathbf{r}_{n1}^{\mathrm{T}} \quad \cdots \quad \mathbf{r}_{nc}^{\mathrm{T}}\}^{\mathrm{T}}}_{\mathbf{e}}. \tag{1}$$

The shape functions for the brick element are the generalization of the shape functions for the 2-D quadrilateral element [9]. For the tetrahedral element, the shape function set is based on the shape functions described by Bazeley [9, 10].

Elastic forces formulation

The energy accumulated in the volume of the deformed element is determined by the integral:

$$U = \frac{1}{2} \iiint_V \boldsymbol{\varepsilon}^{\mathrm{T}} \cdot \mathbf{E} \cdot \boldsymbol{\varepsilon} \, \mathrm{d}x\mathrm{d}y\mathrm{d}z \,. \tag{2}$$

where $\boldsymbol{\varepsilon}$ is a Voigt representation of the nonlinear Green-Lagrange strain tensor, $\mathbf{E}$ is a elastic matrix including Young's modulus E and Poisson's ratio v. The generalized elastic forces vector $\mathbf{Q}$ is calculated as a gradient of the strain energy U:

$$\mathbf{Q} = \frac{\partial U}{\partial \mathbf{e}}. \tag{3}$$

Equations of motion

Kinetic energy of the element is calculated by differentiating equation (1) with respect to time as follows:

$$T = \frac{1}{2}\iiint_{V} \rho\, \dot{\mathbf{r}}^{T} \cdot \dot{\mathbf{r}}\, dxdydz, \tag{4}$$

where $\dot{\mathbf{r}}$ is the velocity of an arbitrary point within the element volume, ρ is the density and V is the volume of the element. The mass matrix is defined as follows:

$$\mathbf{M} = \iiint_{V} \rho\, \mathbf{S}^{T} \cdot \mathbf{S}\, dxdydz. \tag{5}$$

The equations of motion are constructed using the mass matrix **M**, nonlinear elastic nodal forces vector **Q** and the external forces vector $\mathbf{Q}_e$ as follows:

$$\mathbf{M}\ddot{\mathbf{e}} + \mathbf{Q} = \mathbf{Q}_e \tag{6}$$

Numerical simulation example

Several test problems, such as a motion of the flexible pendulum (Fig. 2) and large deflection of the cantilever beam were simulated. The results of simulations were validated by comparing with analytical solutions and the results obtained using commercial software.

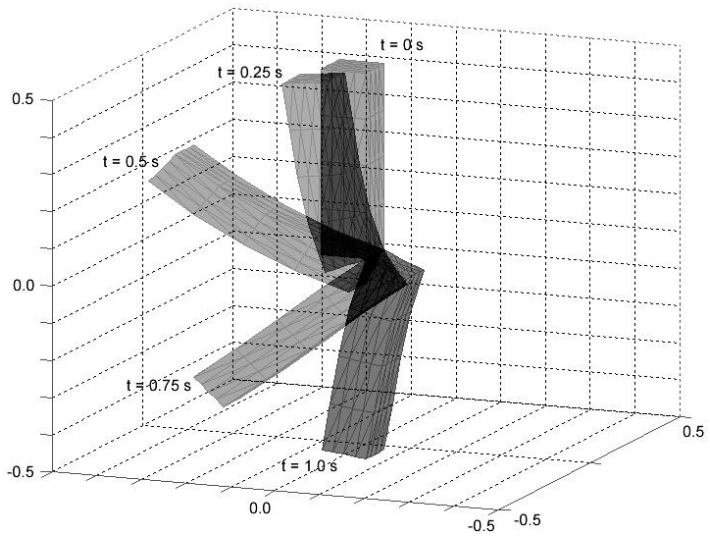

Figure 2. A motion of the flexible pendulum.

References

[1] Song J.O., Haug E.J. Dynamic analysis of planar flexible mechanisms. *Computer Methods in Applied Mechanics and Engineering* 24:359–381, 1980

[2] Belytschko T., Hsieh B.J. Nonlinear transient finite element analysis with convected coordinates. *Int. Journal for Numerical Methods in Engineering* 7: 255–271, 1973.

[3] Simo J.C. A finite strain beam formulation. The three-dimensional dynamic problem, Part I, *Computer Methods in Applied Mechanics and Engineering* 49:55–70, 1985.

[4] Shabana A. A. An absolute nodal coordinate formulation for the large rotation and large deformation analysis of flexible bodies, Rep. MBS96-1-UIC, Dept. of Mech. Eng., Univ. of Illinois at Chicago (1996)

[5] Dombrowski S. von. Analysis of large flexible body deformation in multibody systems using absolute coordinates. *Multibody System Dynamics*, 8:409–432, 2002.

[6] Dmitrochenko O., Yoo Wan-Suk, Pogorelov D. Helicoseir as shape of a rotating chain (II): 3D theory and simulation using ANCF. *Multibody System Dynamics* 15(2): 181–200,2006.

[7] Dmitrochenko O. N., Pogorelov D. Yu. Generalization of Plate Finite Elements for Absolute Nodal Coordinate Formulation. *Multibody System Dynamics* 10(1): 17–43.

[8] Dmitrochenko O. Mikkola A. Two Simple Triangular Plate Elements Based on the Absolute Nodal Coordinate Formulation. *Journal of Computational and Nonlinear Dynamics* Vol. 3(4), 2008.

[9] Zienkiewicz O. C, Taylor R. L. *The finite element method, fourth ed., Solid and Fluid Mechanics*, vol. 2, McGraw-Hill Book, NewYork, 1991.

[10] Bazeley G.P., Cheung Y.K., Irons B.M., Zenkiewicz O.C. Triangular elements in bending - conforming and non-conforming solutions. *Proc. 1st Conf. Matrix Methods in Structural Mechanics, Vol.AFFDL-TR-66-90*, 547-76, 1966.

Proceedings of the 24th Nordic Seminar on Computational Mechanics
J. Freund and R. Kouhia (Eds.)

On the characteristic based split (CBS) method in an arbitrary Lagrangian Eulerian (ALE) framework

Miikka Mikkola

Tampere University of Technology, Mechanics and Design, P.O. Box 589, FI-33101, miikka.mikkola@tut.fi

Summary. This text describes the basis and resulting equations of the characteristic based split (CBS) method in an arbitrary Lagrangian-Eulerian (ALE) framework. A new kind of perspective is that material can be compressible and the results are obtained in tensor form.

Key words: characteristic based split, arbitrary Lagrangian-Eulerian, compressible

Introduction

The characteristic based split (CBS) method is usually a finite element based method for solving compressible and incompressible fluid mechanics problems or e.g. viscoelastic solid mechanics problems. The method leads directly to an appropriate stabilizing diffusion in the streamwise direction, similar to the streamline upwind Petrov-Galerkin (SUPG) method, but has also the advantage that the LBB incompressibility restriction for pressure and velocity interpolation is circumvented, which means that elements do not lock. However, the CBS method is based on a fractional step method which is only first order accurate in time. Second order time accuracy can be obtained using artificial compressibility (AC) method with dual time stepping (DTS). One of the latest reviews of the method is in Ref. [1] and more details of the method are fully explained in Ref. [3].

An arbitrary Lagrangian-Eulerian (ALE) formulation of the CBS method is derived in Ref. [3] and explained also in Ref. [2]. In both cases it is used in the context of incompressible free surface flows. This text describes shortly a derivation of the CBS method equations in compressible case using tensor notation and also explains the basis of the method in continuum mechanics terms. Material coordinates are used instead of characteristic coordinates, because the material point trajectories are coincident with the characteristic curves.

A generic conservation equation

Integral form of the conservation equation for a scalar variable ϕ transported by material is:

$$\frac{\mathrm{D}}{\mathrm{D}t}\left[\int_{\Omega}\phi\,\mathrm{d}\Omega\right]=\int_{\Gamma}\mathbf{D}\cdot\mathbf{n}\,\mathrm{d}\Gamma+\int_{\Omega}s\,\mathrm{d}\Omega \tag{1}$$

where **D** is diffusive flux, s is source term and the time derivative is the material time derivative. Using the Reynolds transport theorem and the Gauss divergence theorem, the following spatial (Eulerian) conservation equation in the strong conservation form is obtained:

$$\frac{\partial\phi}{\partial t}+\mathrm{div}(\phi\mathbf{v})=\mathrm{div}(\mathbf{D})+s \tag{2}$$

where **v** is material velocity. The first term is the spatial time derivative of ϕ and it can be expressed in terms of the material time derivative, denoted as $\dot{\phi}$, using the chain rule. As a result the following Eulerian equation is obtained:

$$\dot{\phi}+\phi\,\mathrm{div}(\mathbf{v})=\mathrm{div}(\mathbf{D})+s \tag{3}$$

This equation is in a self-adjoint form for which the Galerkin method can be used to obtain numerical approximation without spurious oscillations, but there is not a direct method for approximating the material time derivative in an Eulerian mesh.

An explicit characteristic Galerkin method in an updated ALE framework

A referential domain with reference coordinate vector $\boldsymbol{\chi}$ is introduced. This ALE domain and also the material domain are chosen to be coincident with the spatial domain at every current instant of time t^{n+1}. Because of this choice, the following equations describe the relation between material coordinate vector **X**, ALE coordinate vector $\boldsymbol{\chi}$ and spatial coordinate vector **x**:

$$\mathbf{X}=\boldsymbol{\chi}(\mathbf{X},t^{n+1})=\mathbf{x}(\mathbf{X},t^{n+1}) \tag{4}$$

Using this choice and the chain rule the referential particle velocity is obtained as follows:

$$\mathbf{v}=\dot{\mathbf{x}}=\left.\frac{\partial\mathbf{x}}{\partial t}\right|_{\boldsymbol{\chi}}+\underbrace{\frac{\partial\mathbf{x}}{\partial\boldsymbol{\chi}}}_{\mathbf{I}}\cdot\left.\frac{\partial\boldsymbol{\chi}}{t}\right|_{\mathbf{X}}=\hat{\mathbf{v}}+\left.\frac{\partial\boldsymbol{\chi}}{\partial t}\right|_{\mathbf{X}}\qquad\Leftrightarrow\qquad\left.\frac{\partial\boldsymbol{\chi}}{\partial t}\right|_{\mathbf{X}}=\mathbf{v}-\hat{\mathbf{v}} \tag{5}$$

where $\hat{\mathbf{v}}$ is defined as mesh velocity. A referential particle displacement vector $\boldsymbol{\delta}$ from previous to current time step in the updated ALE domain is approximated using the trapezoidal rule:

$$\boldsymbol{\delta}=\boldsymbol{\chi}(\mathbf{X},t^{n+1})-\boldsymbol{\chi}(\mathbf{X},t^{n})=\int_{t^n}^{t^{n+1}}\left.\frac{\partial\boldsymbol{\chi}}{\partial t}\right|_{\mathbf{X}}\mathrm{d}t=\int_{t^n}^{t^{n+1}}\mathbf{v}(\boldsymbol{\chi}(\mathbf{X},t),t)-\hat{\mathbf{v}}(\boldsymbol{\chi}(\mathbf{X},t),t)\,\mathrm{d}t\approx\frac{1}{2}\left(\left[\mathbf{v}-\hat{\mathbf{v}}\right]_{\chi}^{n+1}+\left[\mathbf{v}-\hat{\mathbf{v}}\right]_{\chi-\delta}^{n}\right)\Delta t \tag{6}$$

where the following kind of notation is used:

$$
\begin{aligned}
&[\mathbf{v}]_{\chi}^{n+1} = \mathbf{v}\left(\boldsymbol{\chi}\left(\mathbf{X}, t^{n+1}\right), t^{n+1}\right) \\
&[\mathbf{v}]_{\chi}^{n} = \mathbf{v}\left(\boldsymbol{\chi}\left(\mathbf{X}, t^{n+1}\right), t^{n}\right) \\
&[\mathbf{v}]_{\chi-\boldsymbol{\delta}}^{n} = \mathbf{v}\left(\boldsymbol{\chi}\left(\mathbf{X}, t^{n+1}\right) - \boldsymbol{\delta}, t^{n}\right) = \mathbf{v}\left(\boldsymbol{\chi}\left(\mathbf{X}, t^{n}\right), t^{n}\right)
\end{aligned}
\tag{7}
$$

Using a second order Taylor expansion about the current referential position, an approximation for any variable $\circ$ at the previous referential position is obtained:

$$
[\circ]_{\chi-\boldsymbol{\delta}}^{n} \approx [\circ]_{\chi}^{n} - \frac{\partial [\circ]_{\chi}^{n}}{\partial \boldsymbol{\chi}} \cdot \boldsymbol{\delta} + \frac{1}{2} \frac{\partial^2 [\circ]_{\chi}^{n}}{\partial \boldsymbol{\chi} \partial \boldsymbol{\chi}} : (\boldsymbol{\delta} \otimes \boldsymbol{\delta}) = [\circ]_{\chi}^{n} - \frac{\partial [\circ]_{\chi}^{n}}{\partial \mathbf{x}} \cdot \boldsymbol{\delta} + \frac{1}{2} \frac{\partial^2 [\circ]_{\chi}^{n}}{\partial \mathbf{x} \partial \mathbf{x}} : (\boldsymbol{\delta} \otimes \boldsymbol{\delta}) \tag{8}
$$

Using equation (8) to the equation (6) and ignoring second order derivative terms the following approximation is obtained for the referential particle displacement vector:

$$
\boldsymbol{\delta} \approx \frac{1}{2} \left([\mathbf{v} - \hat{\mathbf{v}}]_{\chi}^{n+1} + [\mathbf{v} - \hat{\mathbf{v}}]_{\chi}^{n} - \frac{\partial [\mathbf{v} - \hat{\mathbf{v}}]_{\chi}^{n}}{\partial \mathbf{x}} \cdot [\mathbf{v} - \hat{\mathbf{v}}]_{\chi}^{n} \Delta t \right) \Delta t \tag{9}
$$

An approximation for the material time derivative of ϕ in the updated ALE domain is obtained in similar way as the approximation for the referential particle displacement vector was obtained is equation (6):

$$
\dot{\phi} \approx \frac{1}{\Delta t} \int_{t^n}^{t^{n+1}} \phi(\boldsymbol{\chi}(\mathbf{X}, t), t) \, \mathrm{d}t \approx \frac{[\phi]_{\chi}^{n+1} - [\phi]_{\chi-\boldsymbol{\delta}}^{n}}{\Delta t} \approx \frac{1}{2} \left([\dot{\phi}]_{\chi}^{n+1} + [\dot{\phi}]_{\chi-\boldsymbol{\delta}}^{n} \right) \tag{10}
$$

The material time derivative of ϕ is now solved from the conservation equation (3) and substituted to the last form of the equation (10). Approximation (8) is then used to all terms which refer to referential particle position at previous time step. All third order exponent terms of Δt and also third and higher order spatial derivatives are ignored only after the substitution.

The final step in the derivation is to approximate all the unknown terms which refer to the current time step n+1 by their values from the previous time step n. As a result the following fully explicit characteristic based approximation for the conservation equation (3) is obtained:

$$
\frac{\phi^{n+1} - \phi^{n}}{\Delta t} = \left[\frac{\partial \phi}{\partial \mathbf{x}} \cdot \hat{\mathbf{v}} - \operatorname{div}(\phi \mathbf{v}) + \operatorname{div}(\mathbf{D}) + s \right]^{n} - \frac{1}{2} \frac{\partial}{\partial \mathbf{x}} \left[\frac{\partial \phi}{\partial \mathbf{x}} \cdot \hat{\mathbf{v}} - \operatorname{div}(\phi \mathbf{v}) + \operatorname{div}(\mathbf{D}) + s \right]^{n} \cdot (\mathbf{v} - \hat{\mathbf{v}})^{n} \Delta t \tag{11}
$$

The subscripts referring to referential particle position are not needed anymore as all the terms refer to current position and all the domains were chosen to be instantaneously coincident. Equation (11) is an approximation for the self-adjoint equation (3). Galerkin method can thus be used to obtain numerical approximation. The last term in equation (11) is a stabilizing term which effectively stabilizes the spurious oscillations that could otherwise occur.

The characteristic based split

When the scalar variable ϕ is density ρ and there is no diffusive or source terms, a stabilized conservation of mass equation is obtained. Convective term appears due to the mesh velocity. Equation (11) was derived using tensor calculus with right derivatives and divergences. Therefore the scalar variable ϕ, a zero order tensor, can be directly replaced by a vector variable.

When the vector variable is mass flux $\mathbf{U}=\rho\mathbf{v}$, diffusive term is Cauchy stress $\boldsymbol{\sigma}$ and source term is body force $\rho\mathbf{g}$ the stabilized conservation of momentum equation is obtained.

The first part of the split is to decompose Cauchy stress $\boldsymbol{\sigma}$ into deviatoric part $\boldsymbol{\tau}$ and spherical part, which defines the physical pressure p. Mass flux term in the conservation of mass equation and pressure term in the conservation of momentum equation are the only terms which are not treated explicitly. This is controlled by two dimensionless parameters θ_1 and θ_2. Then a fractional step method is used in which the mass flux increment is split into two parts $\Delta\mathbf{U}=\Delta\mathbf{U}^{*}+\Delta\mathbf{U}^{**}$. All the pressure terms are removed from part $\Delta\mathbf{U}^{*}$ and included in part $\Delta\mathbf{U}^{**}$. Density correction is solved between these two mass flux correction steps. Details including boundary conditions and time step restrictions are explained in Ref. [3]. As a result the following three equations are obtained which are the first three steps of the characteristic based split scheme:

$$\Delta\mathbf{U}^{*}=\left[\frac{\partial\mathbf{U}}{\partial\mathbf{x}}\cdot\hat{\mathbf{v}}-\operatorname{div}(\mathbf{U}\otimes\mathbf{v})+\operatorname{div}(\boldsymbol{\tau})+\rho\mathbf{g}\right]^{n}\Delta t-\frac{1}{2}\frac{\partial}{\partial\mathbf{x}}\left[\frac{\partial\mathbf{U}}{\partial\mathbf{x}}\cdot\hat{\mathbf{v}}-\operatorname{div}(\mathbf{U}\otimes\mathbf{v})+\rho\mathbf{g}\right]^{n}\cdot(\mathbf{v}-\hat{\mathbf{v}})^{n}\Delta t^{2} \tag{12}$$

$$\Delta\rho=\left[\frac{\partial\rho^{n}}{\partial\mathbf{x}}\cdot\hat{\mathbf{v}}^{n}-\operatorname{div}\left(\mathbf{U}^{n}+\theta_1\Delta\mathbf{U}^{*}-\theta_1\frac{\partial p^{n+\theta_2}}{\partial\mathbf{x}}\Delta t\right)\right]\Delta t+\frac{1}{2}\frac{\partial}{\partial\mathbf{x}}\left[\frac{\partial\rho}{\partial\mathbf{x}}\cdot\hat{\mathbf{v}}-\operatorname{div}(\mathbf{U})\right]^{n}\cdot\hat{\mathbf{v}}^{n}\Delta t^{2} \tag{13}$$

$$\Delta\mathbf{U}^{**}=-\frac{\partial p^{n+\theta_2}}{\partial\mathbf{x}}\Delta t+\frac{1}{2}\frac{\partial^{2}p^{n}}{\partial\mathbf{x}\partial\mathbf{x}}\cdot(\mathbf{v}-\hat{\mathbf{v}})^{n}\Delta t^{2} \tag{14}$$

Additional equations are needed to enclose the problem. For example the constitutive equation for Newtonian fluid, which can be compressible or incompressible, is:

$$\boldsymbol{\tau}=\boldsymbol{\sigma}^{\mathrm{dev}}=2\mu\,\mathbf{d}^{\mathrm{dev}} \tag{15}$$

where μ is dynamic viscosity and $\mathbf{d}^{\mathrm{dev}}$ is the deviatoric part of the rate-of-deformation tensor which depends only on the velocity gradient. In the case of near incompressibility density increment is linearly proportional to pressure increment as follows:

$$\Delta\rho=\frac{\rho}{K}\Delta p \tag{16}$$

where K is bulk modulus. Otherwise an equation of state is needed. Also stabilized conservation equations of other variables convected by material can be easily added after the three steps. Depending on the nature of the problem these can be e.g. conservation of energy equation, turbulence equations or constitutive equation more complicated than (15).

References

[1] P. Nithiarasu, R. Codina and O.C. Zienkiewicz, The Characteristic-Based Split (CBS) scheme—a unified approach to fluid dynamics, *International Journal for Numerical Methods in Engineering*, 66(10):1514-1546, 2006.

[2] P.Nithiarasu, An arbitrary Lagrangian Eulerian (ALE) formulation for free surface flows using the characteristic-based split (CBS) scheme, *International Journal for Numerical Methods in Engineering*, 48(12):1415-1428, 2005.

[3] O.C. Zienkiewicz, R.L.Taylor and P. Nithiarasu, *The Finite Element Method for Fluid Dynamics*, Butterworth-Heinemann, 2005.

Proceedings of the 24th Nordic Seminar on Computational Mechanics
J. Freund and R. Kouhia (Eds.)

Investigation of the steady state vibration of flexibly supported rigid rotors attenuated by a new controllable damping element

Jaroslav Zapoměl[1], and Petr Ferfecki[2]

(1)VŠB-Technical University of Ostrava, Department of Mechanics, 17.listopadu 15, Ostrava-Poruba, Czech Republic, jaroslav.zapomel@vsb.cz
(2)VŠB-Technical University of Ostrava, Center of Advanced Innovation Technologies, 17.listopadu 15, Ostrava-Poruba, Czech Republic, petr.ferfecki@vsb.cz

Summary. Lateral vibration of rotors can be significantly reduced if damping devices are added to the coupling elements between the rotor and the stationary part. For this purpose a new semiactive damping element has been proposed. It works on the principle of squeezing two concentric films of classical oil and magnetorheological liquid, whose flow is sensitive on magnetic induction. The damping effect is controlled by the change of the electric current generating magnetic field. The computational simulations prove that the proposed damping element makes possible to extend the speed intervals, in which the rotors can be operated.

Key words: rotors, vibration damping, new damping element, magnetorheological fluid

Introduction

Lateral vibration of rotors induced by imbalance forces can be reduced if damping devices are added to their coupling elements. To achieve their optimum performance their damping effect must be controllable.

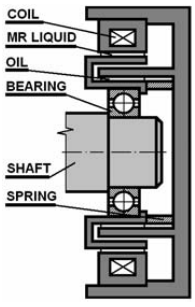

Figure 1. Scheme of the proposed damping element.

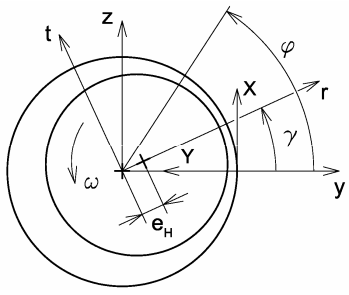

Figure 2. The coordinate system.

For this purpose a new damping element has been proposed. In fact, it is a combination of a classical and magnetorheological squeeze film dampers (Fig.1). As resistance against the flow of magnetorheological fluid depends on magnetic induction, the change of the current generating magnetic field can be used to control the damping force.

Mathematical model of the proposed controllable semiactive damping element

In the developed mathematical model of the proposed damping element the classical and magnetorheological oils are represented by newtonian and Bingham materials and the yield shear stress depends on magnetic induction. Further it is assumed that parameters of the damping element make possible to consider it as short. The pressure distribution in the oil layers is governed by Reynolds equations

$$\frac{\partial^2 p_{CO}}{\partial Z^2} = \frac{12\eta}{h_{CO}^3}\dot{h}_{CO}, \tag{1}$$

$$h_{MR}^3\left(p'_{MR}\right)^3 + 3\left(h_{MR}^2\,\tau_y - 4\eta_B\,\dot{h}_{MR}Z\right)\left(p'_{MR}\right)^2 - 4\tau_y^3 = 0 \qquad \text{for} \qquad p'_{MR} < 0\,. \tag{2}$$

p_{CO}, p_{MR}, p'_{MR} denote the pressure and the pressure gradient in the axial direction in the layers of the classical and magnetorheological liquids, h_{CO}, h_{MR} are the thicknesses of the classical and magnetorheological oil films [1], η, η_B are the dynamic and Bingham viscosities of the oils, τ_y is the yield shear stress, Z is the axial coordinate (Fig.2) and $\dot{(\cdot)}$ denotes the first derivative with respect to time. As Reynolds equation (2) has multiple solutions, the seeked one, which has the physical meaning, must be real and must satisfy condition (3) [2]

$$p'_{MR} < -\frac{2\,\tau_y}{h_{MR}}\,. \tag{3}$$

In the simplest design case the outer and inner rings of the magnetorheological part of the damping element can be considered as a divided core of an electromagnet. Then the dependence of the yield shear stress on magnetic induction can be approximately expressed [3]

$$\tau_y = k_y\left(\frac{N\,I}{2h_{MR}}\right)^{n_y}. \tag{4}$$

k_y and n_y are the material constants of the magnetorheological liquid, N is the number the coil turns and I is the electric current.

In the developed mathematical model it is assumed that in the areas where the thicknesses of the lubricating films rises with time ($\dot{h}_{CO} > 0$, $\dot{h}_{MR} > 0$) a cavitation takes place. The pressure in these regions remains constant and equal to the pressure in the ambient space. The damping force is then calculated by integration of the pressure distributions p_{DCO}, p_{DMR} in the cavitated and noncavitated regions around the circumference and along the length of the damping element

$$F_{dy} = -2\,R_{CO}\int_0^{2\pi}\int_0^{\frac{L}{2}} p_{DCO}\cos\varphi\,dZ\,d\varphi - 2\,R_{MR}\int_0^{2\pi}\int_0^{\frac{L}{2}} p_{DMR}\cos\varphi\,dZ\,d\varphi\,, \tag{5}$$

$$F_{dz} = -2\,R_{CO}\int_0^{2\pi}\int_0^{\frac{L}{2}} p_{DCO}\sin\varphi\,dZ\,d\varphi - 2\,R_{MR}\int_0^{2\pi}\int_0^{\frac{L}{2}} p_{DMR}\sin\varphi\,dZ\,d\varphi \tag{6}$$

R_{CO} and R_{MR} are the radii of the layers of the classical and magnetorheological oils, L is the damping element length and φ denotes the circumferential coordinate (Fig.2).

The equations of motion of the investigated rotor

The investigated rotor is considered as absolutely rigid (Fig.3). It is coupled with the stationary part by rolling element bearings and squirrel springs. The damping layers of the new damping element are placed between the outer rings of the bearings and the stationary part. The rotor turns at constant angular speed, is loaded by its weight and is excited by the disc unbalance. The squirrel springs are prestressed to be eliminated their deflection caused by the rotor weight.

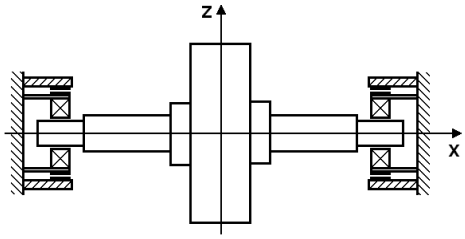

Figure 3. Investigated rotor system.

In the computational model the system is considered to be symmetric. Lateral vibration of the rotor is then governed by a set of two nonlinear equations of motion

$$m_R \ddot{y} + b_P \dot{y} + 2k_D y = 2F_{dy}(y, z, \dot{y}, \dot{z}) + m_R e_T \omega^2 \cos(\omega t + \psi_o), \tag{7}$$

$$m_R \ddot{z} + b_P \dot{z} + 2k_D z = 2F_{dz}(y, z, \dot{y}, \dot{z}) + m_R e_T \omega^2 \sin(\omega t + \psi_o). \tag{8}$$

m_R is the rotor mass, b_P is the external damping coefficient, k_D is the squirrel spring stiffness, ω is the angular rotation speed, e_T is the eccentricity of the rotor unbalance, t is the time, ψ_o is the phase shift, y, z are displacements of the rotor centre and ($\ddot{}$) denote the second derivatives with respect to time.

Results of the computer simulations

The response characteristics referred to the case when the rotor is attenuated only by classical squeeze film dampers (or by the proposed damping element without being filled with the magnetorheological fluid) and corresponding dependences of amplitude of the force transmitted into the stationary part are drawn in Fig. 4 and 5. The decreasing width of the damper clearance (in μm in Fig. 4 and 5) rises reduction of the vibration but also considerably increases the force transmitted into the stationary part. Not to exceed the required maximum amplitude of the rotor vibration, which is 70 μm, the width of the damper gap must be 100 μm and this leads to amplitude of the transmitted force of 2.2 kN at the speed of rotation of 400 rad/s. Results in Fig. 7 are referred to the steady state vibration of the rotor if the proposed damping elements are applied and if the current is controlled in dependence on the speed of the rotor rotation according to the diagram in Fig.6. The amplitude of the vibration remains less than 70 μm and the maximum force amplitude does not exceed the value of 450 N. This clearly demonstrates the contribution of the controlled damping elements to enhanced behaviour of the rotor system.

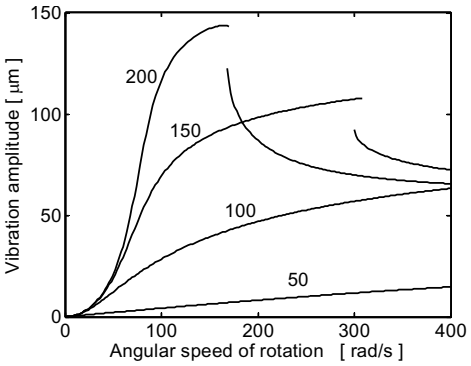

Figure 4. The system response characteristic.

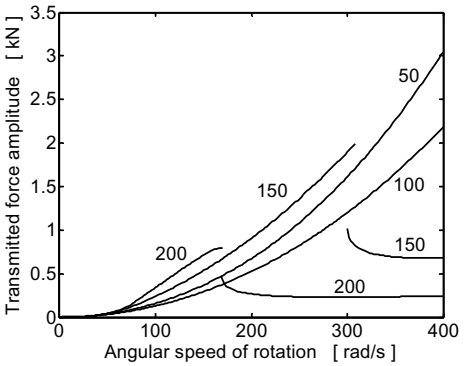

Figure 5. Force-rotational speed dependence.

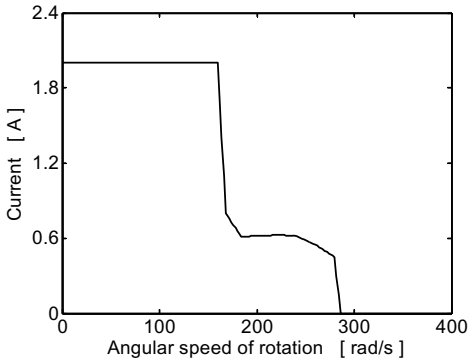

Figure 6. Current controll.

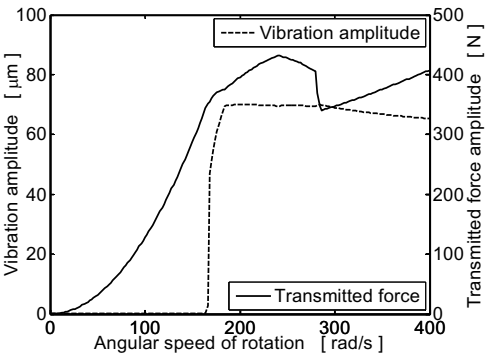

Figure 7. The system vibration/force response.

Conclusions

Results of the computational simulations show that the damping effect of the proposed damping element can be controlled by the change of applied electric current. This makes possible to achieve the optimum compromise between reduction of the rotor vibration and magnitude of the force transmitted into the stationary part by changing the damping effect.

This work was supported by the research projects P101/10/0209 and MSM 6198910027.

References

[1] E. Krämer, *Dynamics of Rotors and Foundations*, Springer-Verlag, 1993.

[2] J. Zapoměl, P. Ferfecki, L. Čermák, A computational method for determination of a frequency response characteristic of flexibly supported rigid rotors attenuated by short magnetorheological squeeze film dampers, *Applied and Computational Mechanics*, 5(1): 101-110, 2011.

[3] W. Kordonsky, Elements and devices based on magnetorheological effect, *Journal of Intelligent Material Systems and Structures*, 4(1):65-69, 1993.

Proceedings of the 24th Nordic Seminar on Computational Mechanics
J. Freund and R. Kouhia (Eds.)

On non-dimensional groups for characterization of energy absorption of tubes at constant crushing velocity

Jonas Dahl

Department of Mechanical and Manufacturing Engineering, Aalborg University,
Fibigerstræde 16, DK-9220 Aalborg East, Denmark, jda@m-tech.aau.dk

Summary. This paper introduces non-dimensional groups that cluster results on energy absorption of tubes crushed at constant velocity. This is part of a general work that aims to find optimal tube dimensions that maximize energy absorption based on tube material, crushing velocity, etc.

Key words: Progressive buckling, Global buckling, Crushing of tubes.

Introduction

The energy absorption capacity of tubes is vital for a number of applications related to crashworthiness and blast protection. The research in collapse of structural members is extensive and the monograph [1], which features hundreds of references, provides an excellent overview of this field. In the present study we are looking at tubes that are crushed axially with a constant quasi-static velocity between two rigid plattens. In most studies the non-dimensional radius R/L, and non-dimensional wall-thickness $t/2R$ are used for the description of tube geometry. Here L, R, and t denote the length, radius, and wall-thickness of the tube, respectively. In this paper it is shown that by grouping the geometry parameters, such that one of the independent variables explicitly refers to the volume of the tube, the absorbed energy at significant nominal strains, such that plastic buckling is observed, group nicely and general observations regarding optimal R/L values can be made.

Modeling

A hollow circular tube of length L, radius R, and thickness t is placed between two rigid plattens, see figure 1. The bottom rigid plate is stationary, while the top plate moves towards the bottom plate with a velocity that is smoothly ramped up from zero to V thus crushing the tube with a constant nominal strain rate after an initial smooth acceleration. The tube material is assumed isotropic with moderate strain rate sensitivity and conventional J_2 flow rule is used. It is assumed that the material has enough ductility to withstand the deformations without fracture. The material constants are representative of an aluminium alloy: initial yield stress $\sigma_Y = 250$ MPa, Young's modulus $E = 70$ GPa, density $\rho = 2700$ kg/m^3, and Poisson's ratio $\nu = 0.27$. Nominal strain $\bar{\epsilon}$ is defined as the displacement of the top rigid plane divided by the initial length of the tube $\bar{\epsilon} = \Delta/L$. The finite strain version of the commercially available dynamic finite element code ABAQUS / Explicit 6.10 [3] is employed for the calculations. The tube is modeled using 4-noded quadrilateral 3D shell elements (S4R) with 7 integration points through the thickness using reduced integration and hourglass control. The rigid plattens are modeled using discrete rigid elements. To model welded connections between the plattens and the tube all displacements and rotations of the bottom nodes of the tube are constrained, and the displacements in the x-y

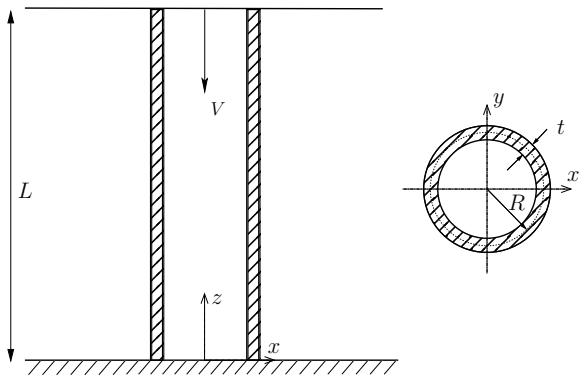

Figure 1. Cross-sectional views of the tube and the rigid plattens.

plane and all rotations of the top nodes of the tube are constrained This allows for movement of the top nodes in the z-direction. The top nodes of the tube and the top rigid plate are applied a velocity in the negative z-direction which is smoothly ramped up from zero to the final velocity V over one tenth of the total simulation time using the ABAQUS function *smooth step*. Any contact between the rigid plattens and the buckled tube walls is enforced using the *contact pair* contact algorithm in ABAQUS/Explicit with standard settings, and self-contact of the tube is obtained using the standard *self-contact* algorithm with standard settings. Friction is neglected. To initiate buckling, imperfections are introduced in the form of the lowest elastic eigenmodes of the tube, which include both global and local modes. The eigenmodes are scaled with equal weights such that the maximum amplitude of each mode equals ξ/n, where n is the number of eigenmodes and ξ is the scaling. In this study, a total of 25 modes shapes are used, and ξ is taken to be $L/1000$ which is considered to be representative of realistic imperfections. Numerical results indicate that the absorbed energy is a relatively weak function of the imperfections as long as imperfections are present ($\xi \neq 0$). The constant velocity $V/(c_0\epsilon_Y) = 1$, which is essentially quasi-static in the sense that the total kinetic energy amounts to only a small fraction of the total strain energy, is used in all simulations in this paper.

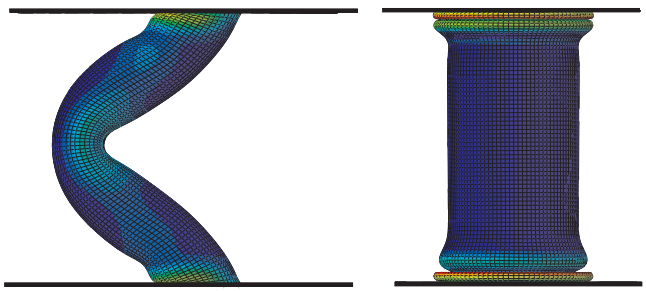

Figure 2. Global (left - $R/L = 0.07$) and progressive (right - $R/L = 0.15$) buckling modes at 0.4 nominal strain. The mass of the tubes are identical and $AL/L^3 = 0.0134$. The color range represents equivalent plastic strain.

Results

The simulation described above is carried out a number of times for different tube geometries. Each simulation is stopped when the top platten has reached a position equivalent to 0.4 nominal strain ($\bar{\epsilon} = 0.4$). At this strain level substantial plastic buckling has begun for all tubes. At this point the energy dissipated in plastic straining E_p is evaluated.

It is well known that the tubes buckle in a global or a progressive mode depending on parameters, see fig. 2. By grouping the geometry parameters, such that one of these explicitly refers to the non-dimensional material volume of the tube AL/L^3, the non-dimensional energy absorbed per volume $Ep/(AL\sigma_Y)$ collapses approximately into one curve for each AL/L^3 value, see figure 3. Here $A = \pi((R+t/2)^2 - (R-t/2)^2)$ denotes the cross-sectional area of the tube, such that AL is the material volume of the tube. It is seen that for each AL/L^3 value an optimum R/L ratio exists for which the amount of dissipated energy is maximum. This optimum is closely liked to the buckling modes. For R/L values larger than the optimum, the tubes buckle in progressive modes, whereas for smaller R/L values the tubes buckle in global modes. The energy dissipated by the optimum tube is significantly larger than that dissipated by tubes with much smaller or larger R/L ratios.

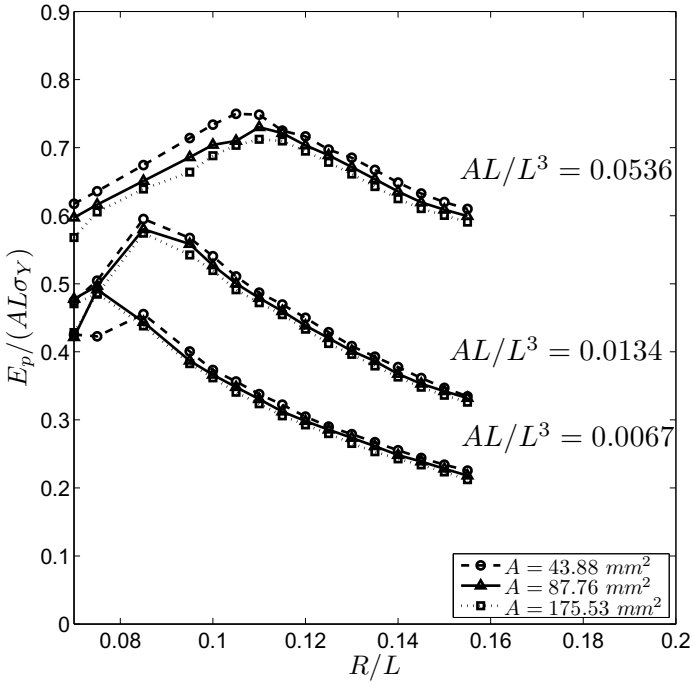

Figure 3. Energy dissipated in plastic straining at 0.4 nominal strain.

Conclusions

It is shown that the introduced non-dimensional groups cluster results on energy absorption satisfactory and it is shown that there for given non-dimensional material volume AL/L^3 and velocity $V/(c_0\epsilon_Y)$ exists an optimum non-dimensional radius R/L that maximizes energy absorption. The optimum R/L ratio is a function of crushing velocity as well as the nominal strain at which the dissipated energy is evaluated, hence rather detailed information regarding the expected crushing conditions are necessary to optimize energy absorption in a practical design situation. A future paper will elaborate on how crushing velocity, conveniently expressed in non-dimensional form $V/(c_0\epsilon_Y)$, affects the dissipated energy depending on the quasi-static buckling mode.

The results presented here are valid for *constant* velocity crushing. In most realistic events, however, the tube will absorb all, or a substantial fraction, of the kinetic energy of the top platten. This makes the crushing velocity a function of time. Therefore, future research is aimed at including the inertia of the top platten in the analysis, and investigations of when a constant crushing velocity assumption is valid.

References

[1] N. Jones *Structural Impact*, Cambridge University Press, 1. paper back edition, 1997.

[2] D.G. Vaughn, J.M. Canning and J.W. Hutchinson. Coupled plastic wave propagation and column buckling, *Journal of Applied Mechanics*, 72, 1-8, 2005.

[3] ABAQUS *ABAQUS/Explicit User's Manual Version 6.10*, ABAQUS Inc., 2010.

Proceedings of the 24th Nordic Seminar on Computational Mechanics
J. Freund and R. Kouhia (Eds.)

Reduction of traffic-induced vibrations at high-tech facility using trenches

Peter Persson, Kent Persson, and Göran Sandberg

Division of Structural Mechanics, Lund University, Box 118, 221 00 Lund, Sweden,
peter.persson@construction.lth.se.

Summary. This extended abstract presents a parametric study on trenches. The influence of using trenches to reduce vibration levels induced by traffic was investigated by means of the finite element method. A harmonic unit load was applied on a modeled road and the vibration levels were evaluated at different distances. The vibration levels were scaled to represent a realistic traffic load. An RMS-value was used to evaluate the reduction of the vibration levels using various parameters of the trench.

Key words: dynamic analysis, finite element method, wave propagation, vibration isolation

Introduction

MAX-lab is a national laboratory operated jointly by the Swedish Research Council and Lund University. The present laboratory consists of three facilities (three storage rings): Max I, Max II, Max III and one electron pre-accelerator, Max Injector. A new facility, MAX IV, is needed to improve material science such as nanotechnology.

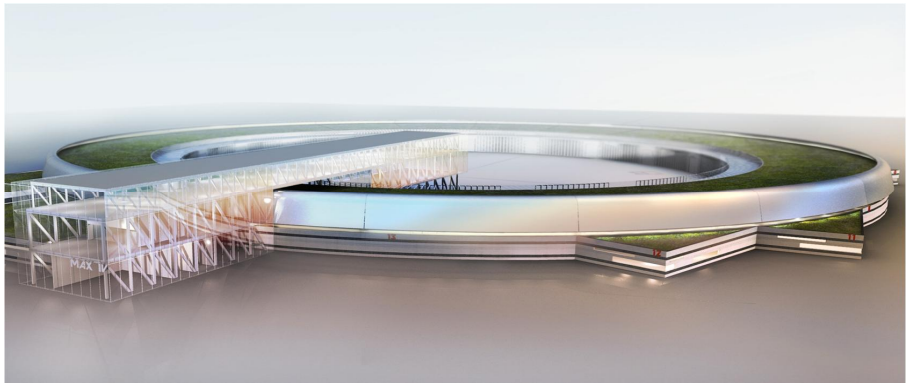

Figure 1. 3D view of the main building of MAX IV facility.

Several studies, analytical as well as numerical, have been performed to investigate the influence of a trench as a method to reduce ground vibrations, e.g. [1-2]. This numerical investigation considers several soil layers in combination with a measured traffic load and the vibrations are evaluated at several points at the location of the facility, on top of the soil.

MAX IV facility

MAX IV will mainly consist of a main storage ring and a linear accelerator, Linac, that will provide short pulses of electrons to it. The Linac will be built as an underground tunnel next to the main storage ring. The MAX IV facility will be about 100 times more efficient than already existing synchrotron facilities, i.e. it will be the next generation synchrotron facility. The floor of the storage ring building will mainly be constituted of a concrete structure that is built on soil consisting of different clay tills and sedimentary bedrock, shale. The inner and the outer diameter of the main building are approximately 140 m and 220 m respectively and the height is 12 m, see Figure 1. The facility is exposed to both to harmonic and transient loading. The harmonic loading is typically working machines and transient excitations are mainly traffic from the nearby roads and other human activities in the building such as walking. The main storage ring is controlled by a large number of magnets that are distributed along the ring. The main concern is that vibrations at the magnets will increase the vibration of the electron beam, which is used for measurements. Since the quality of the measurement is dependent on the precision of the synchrotron light, a very strict requirement regarding the vibration levels of the magnets is specified. The strict requirement is especially put in the vertical direction. The vibration levels must be less than 26 nm RMS-value during one second in the frequency span of 5-100 Hz.

Objective and method

MAX IV was previously analysed by the finite element method in, [3-4]. In those reports it was concluded from the analyses that the material parameters of the soil have a significant influence on the vibration levels in the facility. Therefore, changes of the soil could be an adequate method to minimize the vibration levels. One way is to build a trench between the highway, which is the main source of outdoor vibrations, and the facility. The main objective of this study is to investigate the effect of a trench on the traffic induced vibrations. The aim is to establish realistic finite element models that predict the reduction of vibrations with high accuracy. The vibrations were analysed by means of a dynamic finite element method, [5-6].

Materials

Since the soil is exposed to loads with low magnitude the materials were modelled as linear elastic isotropic materials. The road is assumed to be constituted by asphalt covering a layer of pavement material (UGM). The soil consists of two different layers, each with a different type of clay till. The soil rests on the bedrock consisting of shale. Table 1 summarizes the material data which were determined by consultant companies involved in the MAX IV project.

Table 1. Material data.

Material	Thickness [m]	MoE [MPa]	Poisson's ratio	Density [kg/m^3]	Loss factor
Asphalt	0.15	5000	0.25	2600	0.10
UGM	0.5	315	0.2	2300	0.10
Upper clay till	12	378	0.48	2125	0.10
Lower clay till	4	1136	0.48	2125	0.10
Shale	-	8809	0.40	2600	0.04

FE-model

A model with the state of plane strain was made to investigate the influence of a trench, see Figure 2. The shale was modelled with a thickness of 100 m. To consider the real extension of the soil as well as the bedrock, infinite elements were used along those boundaries. Interfaces between different material layers are assumed to have full interaction. The investigation was made with steady-state analysis. The excitation was applied as a concentrated harmonic unit load positioned at the center of the road.

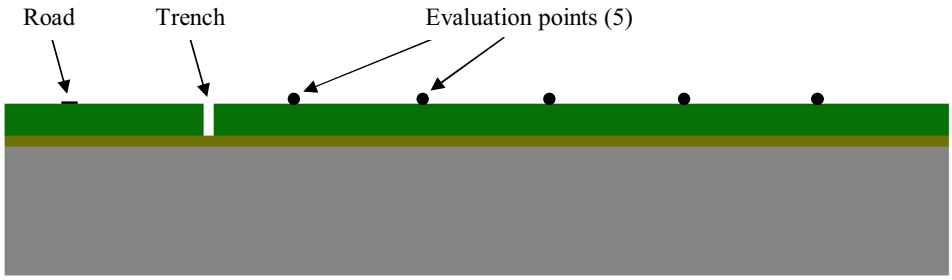

Figure 2. 2D FE-model, state of plane strain (not showing the full extension of the bedrock).

Results and conclusions

The displacements were scaled with a frequency dependent factor to consider the frequency content in the traffic load. The frequency dependent complex amplitude of the vertical displacements was evaluated 100, 150, 200, 250 and 300 m from the road. An RMS-value was calculated for every evaluation point and then the average RMS-value was used for comparisons. A set of geometric base parameters for the trench was determined. The base position of the trench was chosen to be at the middle point, between the road and the facility. The base depth of the trench was at the same depth as the interface between the upper and lower clay till layer and the base width was set to 1 m. Totally, three parameters were varied, one at the time. Several analyses were made to investigate the influence of a trench between the road and the location of the facility. In Figure 3a it is shown that an optimal position of the trench is 30 m from the road and the worst positions are either close to the road or close to the facility.

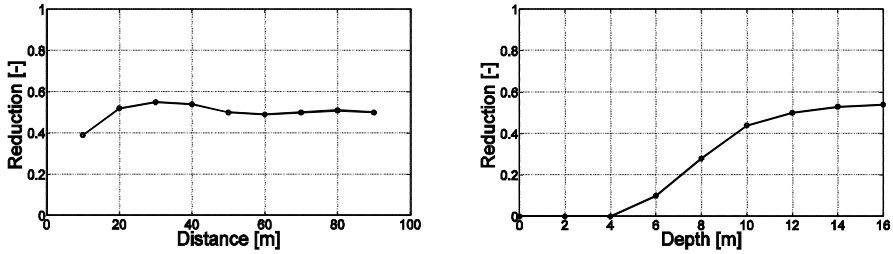

a) b)

Figure 3. Reduction of the average RMS-value for all evaluation points. a) Various distances between the road and the trench. b) Various depths of the trench.

In Figure 3b it is shown that the depth of the trench should be greater than 6 m to show a significant reduction of the vibration levels at the facility. The maximum gradient is found between the depths of 6 and 10 m. In the case with a trench deeper than 10 m, the waves in the bedrock seem to be dominating. From the calculations it was concluded that a deeper trench gives larger reduction of the vibration levels than a wider trench, keeping the volume constant.

Several further investigations regarding trenches are ongoing. The influence of in-filled trenches will also be investigated. Known materials will be investigated as well as parametric studies on material parameters, such as wave-speeds and impedance. To validate the 2D FE-model a 3D FE-model will also be analysed.

Acknowledgements

The Silent Spaces project, a part of the EU program Interreg IVA, is gratefully acknowledged for the financial support.

References

[1] M. Adam, O. von Estorff, Reduction of train-induced building vibrations by using open and filled trenches, Computers and Structures, 83(1):11-24, 2005.
[2] L. Andersen, S.R.K. Nielsen, Reduction of ground vibrations by means of barriers or soil improvement along a railway track, Soil Dynamics and Earthquake Engineering, 25(7-10):701-716, 2005.
[3] P. Persson, Analysis of Vibrations in High-Tech Facility, Report TVSM-5164, Division of Structural Mechanics, Lund University, 2010.
[4] P. Persson, K. Persson, Analysis of Dynamic Soil-Structure Interaction at High-Tech Facility, Proceedings of NSCM-23: the 23rd Nordic Seminar on Computational Mechanics, Stockholm, 2010.
[5] N. S. Ottosen, H. Petersson, Introduction to the finite element method, Prentice Hall, Harlow, 1992.
[6] A. K. Chopra, Dynamics of structures, Prentice Hall, Upper Saddle River, 1995.

Proceedings of the 24th Nordic Seminar on Computational Mechanics
J. Freund and R. Kouhia (Eds.)

Analysis of vibration reduction at high-tech facility by stabilising the soil

Ola Flodén, Kent Persson, and Göran Sandberg

Division of Structural Mechanics, Lund University, Box 118, 221 00 Lund,
ola.floden@construction.lth.se

Summary.

The new synchrotron radiation research facility MAX IV will have strict vibration tolerances in order to obtain good measurement precision. To satisfy the tolerances, a number of different design features have been investigated. One of the methods is to stabilise the soil under the building with cement. This paper investigates the influence of changing parameters related to the stabilisation by performing steady-state analyses with use of the finite element method.

Key words: vibration analysis, finite element method, soil-structure

Introduction

MAX-lab is a national laboratory operated jointly by the Swedish Research Council and Lund University. Today, the facilities for synchrotron radiation research consist of three storage rings, MAX I-III, and one electron accelerator, MAX Injector. Accelerated electrons are emitted into the storage rings, where magnets steer the electrons along the path of the rings. When the high-energy electrons are accelerated inside the storage rings, they emit synchrotron light which is used for studying materials at nanometer level. A new facility, MAX IV, will be built to improve the performance. The design is shown in Figure 1. For more information on the MAX-lab facilities, see [1].

MAX IV facility

MAX IV will consist of an underground linear accelerator and two storage rings with diameters of 30 m and 170 m respectively. The precision of the measurements will depend on the stability of the synchrotron light beams and this leads to demands on the vibration levels in the building. For the large storage ring, the vibration tolerance is set to 26 nm RMS-value during 1 s regarding frequencies in the range of 5-100 Hz and 260 nm for 0-100 Hz. For frequencies below 5 Hz, the vibrations can be compensated by active systems, which lead to the increased tolerance for lower frequencies. Vibrations arise from different sources, mainly from the nearby highway E22 and from internal excitations like walking.

Figure 1. Design of the MAX-IV facility.

The MAX IV facility will be built on a location where the soil consists of two different clay tills above sedimentary shale bedrock. The large storage ring building will have a concrete floor with research stations upon it and the electron beam will be placed in a concrete tunnel.

To reduce the vibration levels, a number of different features to the design have been proposed and one of them is to stabilise the underlying soil, which is accomplished by mixing the soil with cement. In the preliminary design, a 4 m thick stabilisation divided into two layers is included beneath the large storage ring. The stiffness of the stabilisation depends on the amount of cement.

Objective and method

In this investigation, the objective was to analyse how the material properties and geometry of the stabilised soil affect the vibration levels in the storage ring building caused by both external and internal loads. The analyses were carried out using the finite element method and steady-state analysis, for more information see [2-3]. The aim was to establish how changes in the stabilised soil influence the vibration levels in a 2D-model of a cross-section of the ring.

Material properties

The wave-lengths in the soil and bedrock are long compared to local variations and the materials were therefore modelled as linear-elastic and isotropic. For more information about elasto-dynamic modelling of materials see [4]. The material properties and layer thicknesses are presented in Table 1. The data presented for the stabilised soil were used in a reference model.

Table 1. Material data.

Material	Young's modulus [MPa]	Poisson's ratio	Density [kg/m^3]	Damping ratio	Thickness [m]
Shale	8000	0.3	2400	0.02	-
Lower clay	900	0.45	2200	0.05	5
Upper clay	300	0.48	2100	0.05	12
Lower stab. soil	2000	0.2	2100	0.02	3.4
Upper stab. soil	4000	0.2	2100	0.02	0.6
Concrete	30000	0.3	2400	0.02	-

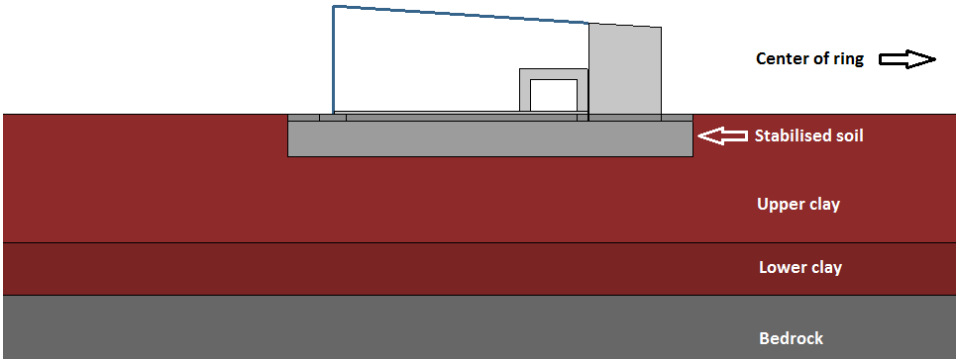

Figure 2. The 2D FE-model of the cross-section of the storage ring building.

Parametric studies

In the 2D-model of the storage ring building, see Figure 2, plane strain was assumed. The boundaries of the soil and bedrock were meshed with non-reflecting elements. Two different loads were applied to the model, one on the soil representing excitations from the highway and one on the concrete floor representing human walking.

As an initial step, two different parametric studies were carried out, one study with varying Young's modulus of the lower stabilisation layer and one study with varying thickness of the stabilised soil. RMS-values are calculated in three evaluation points on the storage ring floor and tunnel and the parameter studies are evaluated in terms of reduction of the RMS-values. Reduction levels in the vertical direction from the Young's modulus study are shown in Figure 3a. The reduction levels are in comparison with the reference model.

When varying the thickness of the stabilised soil, only the lower layer thickness was altered. The results were evaluated in the same manner as for the Young's modulus parameter study and the result is shown in Figure 3b. In this case, the reduction levels are in comparison with a model without the lower stabilisation layer (t = 0 m).

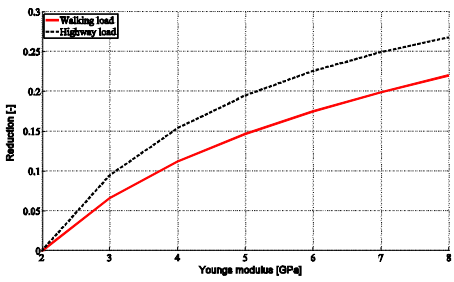

a) Young's modulus.

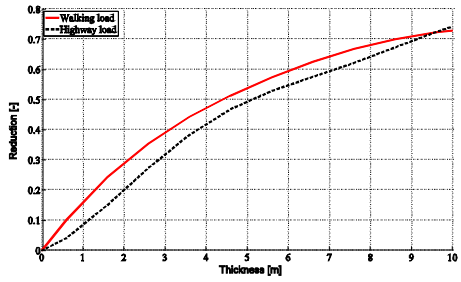

b) Thickness.

Figure 3. Vibration reduction levels from the parametric studies.

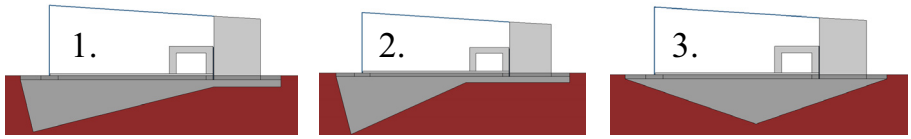

Figure 4. Analysed geometries of the stabilisation cross-section.

Table 2. Vibration reduction levels of the different cross-section models.

Cross-section	Floor-load	Highway-load
1	0.05	0.10
2	-0.02	0.04
3	0.21	0.02

Cross-section geometry

As expected, the parametric studies showed that the vibration levels could be reduced by increasing the Young's modulus of the stabilised soil or increasing the depth, but the drawback of both methods is the increased use of cement. As the next step in the analysis, the possibility to reduce the vibrations by distributing the same material in other geometries was investigated. The tested cross-section geometries are shown in Figure 4 and the reduction levels compared to the reference model are shown in Table 2.

Conclusions

The geometries investigated so far have been subjectively selected. A more intelligent way would be to perform an optimisation with the RMS-value as objective and some variables of the stabilisation geometry as design variables. This, as well as testing the optimal cross-section geometries in a 3D-model of the storage ring building will be done in order to conclude how the vibration levels could be reduced by altering the cross-section geometry of the stabilised soil.

Acknowledgements

The research is supported by the Silent Spaces project, a part of the EU program Interreg IVA.

References

[1] MAX-lab, Lund University, *http://www.maxlab.lu.se.*
[2] N. S. Ottosen, H. Petersson, Introduction to the finite element method, Prentice Hall, Harlow, 1992.
[3] A. K. Chopra, Dynamics of structures, Prentice Hall, Upper Saddle River, 1995.
[4] L. Andersen, DCE Lecture Notes No.3: Linear Elastodynamic Analysis, Aalborg University, 2006.

Proceedings of the 24th Nordic Seminar on Computational Mechanics
J. Freund and R. Kouhia (Eds.)

Interaction of vocal fold and vocal tract oscillations

Atte Aalto[1], Daniel Aalto[2], Jarmo Malinen[1], and Martti Vainio[3]

(1)Dept. of Mathematics and Systems Analysis, Aalto SCI, aaalto@cc.hut.fi, jmalinen@cc.hut.fi
(2)Institute of Mathematics, Åbo Akademi, daniel@iki.fi
(3)Institute of Behavioural Sciences (Phonetics), University of Helsinki, martti.vainio@helsinki.fi

Summary. We study the mechanical feedback coupling between the human vocal folds and vocal tract (VT) by simulating fundamental frequency glides over the lowest VT resonance. In the classical source–filter theory of speech production, the vocal folds produce a signal which is filtered by the resonator, vocal tract without any feedback. We have developed a computational model of the vocal folds and the VT that also includes a counter pressure from the VT to the vocal folds. This coupling gives rise to new computational observations (such as modal locking) that can be established experimentally.

Key words: Speech modelling, vocal folds model, flow induced vibrations, modal locking

Introduction

According to the classical source–filter theory of vowel production, the source (i.e., the *glottis*, meaning the aperture between vocal folds) operates independently of the filter (i.e., the vocal tract (VT)) whose resonances modulate the harmonic contents of the resulting sound, see [1, 2]. It is well known that this theory is adequate for modelling a wide range of phenomena in speech production. However, when the vocal folds' oscillation frequency f_0 (a.k.a. the *fundamental frequency*) is near the lowest VT resonance F_1 (i.e., the first *formant frequency*), the vocal folds' oscillations are affected by the acoustics of the VT as is observed in the computational and experimental works [3, 4, 5]. Such phenomena appear, e.g., in soprano singers phonation.

We use the computational model developed in [6, 7] to simulate f_0-glides on a steady vowel. The model includes an additional aerodynamic load from the resonator (filter) that is fed back to the vocal fold (source) equations of motion. In simulations we observe a strong and consistent modal locking between vocal folds oscillations and the acoustic vibrations in the VT. This phenomenon can also be detected in the preliminary experimental materials that we briefly introduce in the work.

Computational model

The model consists of three subsystems: vocal folds, glottal flow, and vocal tract. Since f_0–F_1 crossover typically occurs in females whereas the original model parameters corresponds to male physiology (see [7]), we have scaled the vocal fold masses by a factor of 0.253 and the stiffnesses by 0.836, see [8]. For details, model parameters, and numerical realisation, we refer to [6, 7].

Vocal folds

The vocal fold model in Fig. 1 consists of two wedge-shaped elements with two degrees of freedom. The distributed mass of these elements is reduced into three mass points and the

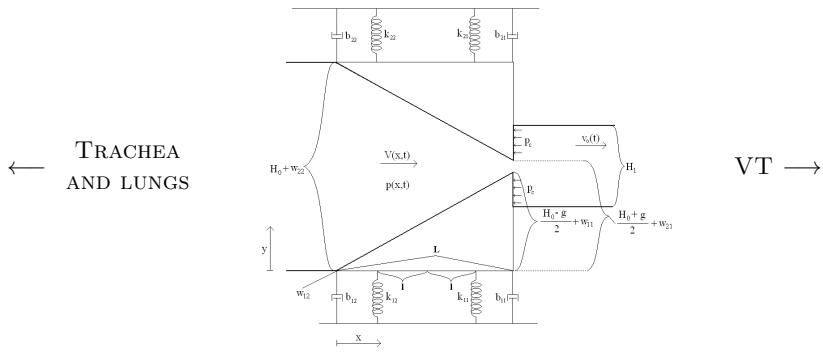

Figure 1. The geometry of the glottis model and the symbols used.

elastic support is approximated by two springs. The equations of motion for the vocal folds are

$$\begin{cases} \mathbf{M}_1\ddot{\mathbf{W}}_1(t) + \mathbf{B}_1\dot{\mathbf{W}}_1(t) + P\mathbf{K}_1\mathbf{W}_1(t) = -\mathbf{F}(t), \\ \mathbf{M}_2\ddot{\mathbf{W}}_2(t) + \mathbf{B}_2\dot{\mathbf{W}}_2(t) + P\mathbf{K}_2\mathbf{W}_2(t) = \mathbf{F}(t) \end{cases} \tag{1}$$

where $\mathbf{W}_j = (w_{j1}, w_{j2})^T$ are the displacements of the right and left endpoints of the j^{th} fold, $j = 1, 2$. The glottal opening at the narrowest point is denoted by ΔW_1. At the other end (towards the trachea), the opening is ΔW_2. These are given by (1) through $\left[\begin{smallmatrix}\Delta W_1 \\ \Delta W_2\end{smallmatrix}\right] = \mathbf{W}_2 - \mathbf{W}_1 + \left[\begin{smallmatrix} g \\ H_0\end{smallmatrix}\right]$. The parameter g is the glottal opening in neutral position. The mass, damping, and stiffness matrices are denoted by $\mathbf{M}_j$, $\mathbf{B}_j$, and $\mathbf{K}_j$. Control parameter P is used for simulating f_0-glides.

During the glottal open phase (when $\Delta W_1(t) > 0$), the load terms of (1) are given by $\mathbf{F} = (F_{A,1}, F_{A,2})^T$ that are given below in Eq. (3). During the glottal closed phase (when $\Delta W_1(t) < 0$), there are no aerodynamic forces apart from the acoustic counter pressure from the VT. Instead, there is a nonlinear spring force for the elastic collision of the vocal folds, given by the Hertz impact model (see, e.g., [9]), $\mathbf{F} = \begin{bmatrix} k_H|\Delta W_1|^{3/2} - \frac{H_0 - H_1/2}{2L}\frac{H_1}{2}h \cdot p_c \\ \frac{H_0 - H_1/2}{2L}\frac{H_1}{2}h \cdot p_c \end{bmatrix}$.

Glottal flow

An incompressible 1D flow through the glottal opening with velocity v_o is described by

$$\dot{v}_o(t) = \frac{1}{C_{iner} h H_1}\left(p_{sub} - \frac{C_g}{\Delta W_1(t)^3} v_o(t)\right) \tag{2}$$

motivated by the Hagen–Poiseuille law. The parameter p_{sub} is the subglottal pressure and h is the width of the rectangular flow channel. The parameter C_{iner} regulates the flow inertia, and C_g regulates the viscous pressure loss in the glottis.

In the glottis, the flow velocity $V(x,t)$ is assumed to satisfy the mass conservation law $H(x,t)V(x,t) = H_1 v_o(t)$ for static incompressible flow where $H(x,t) = \Delta W_2(t) + \frac{x}{L}(\Delta W_1(t) - \Delta W_2(t))$, $x \in [0, L]$ is the height of the flow channel inside the glottis. The pressure $p(x,t)$ in the glottis is given by the Bernoulli law $p(x,t) + \frac{1}{2}\rho V(x,t)^2 = p_{sub}$ for static flow.

This pressure and the VT counter pressure p_c are reduced to a force pair $(F_{A,1}, F_{A,2})^T$ where $F_{A,1}$ affects at the narrow end of the glottis ($x = L$) and $F_{A,2}$ at the wide end ($x = 0$). This reduction is carried out by using the total force and moment balance equations $F_{A,1} + F_{A,2} = h\int_0^L (p(x,t) - p_{sub})\,dx$ and $L \cdot F_{A,1} = h\int_0^L x(p(x,t) - p_{sub})\,dx - p_c \cdot h\frac{H_1}{2}\frac{H_0 - H_1/2}{2}$ that yield

$$\begin{cases} F_{A,1} &= \frac{1}{2}\rho v_o^2 hL\left(-\frac{H_1^2}{\Delta W_1(\Delta W_2 - \Delta W_1)} + \frac{H_1^2}{(\Delta W_1 - \Delta W_2)^2}\ln\left(\frac{\Delta W_2}{\Delta W_1}\right)\right) - \frac{H_1(H_0 - H_1/2)}{4L}hp_c, \\ F_{A,2} &= \frac{1}{2}\rho v_o^2 hL\left(\frac{H_1^2}{\Delta W_2(\Delta W_2 - \Delta W_1)} - \frac{H_1^2}{(\Delta W_1 - \Delta W_2)^2}\ln\left(\frac{\Delta W_2}{\Delta W_1}\right)\right) + \frac{H_1(H_0 - H_1/2)}{4L}hp_c. \end{cases} \tag{3}$$

Vocal tract

The VT is modelled by Webster's lossless horn equation $\Psi_{tt}(s,t) - \frac{c^2}{A(s)}\frac{\partial}{\partial s}\left(A(s)\frac{\partial \Psi(s,t)}{\partial s}\right) = 0$ where $\Psi(s,t)$ is a velocity potential, c is the sound velocity, $s \in [0, L_{VT}]$ is the distance from the glottis measured along the VT centreline, and L_{VT} is the length of the VT. The area function $A(\cdot)$ is the cross-sectional area of the VT. The sound pressure is given by $p = \rho\Psi_t$.

The resonator is controlled by the glottal flow velocity from (2) through the boundary condition $\Psi_s(0,t) = -v_o(t)$. The boundary condition at lips is $\Psi_t(L_{VT},t) + \theta c\Psi_s(L_{VT},t) = 0$ representing a frequency-independent acoustic resistance. The resonator exerts a counter pressure $p_c(t) = \rho\Psi_t(0,t)$ to (1) through (3), forming a feedback loop between the vocal folds and the VT.

Simulation and experimental results

We denote by $\tilde{f}_0$ the nominal frequency of the vocal fold oscillations if the feedback from the VT was removed. The actual, observed vocal fold oscillation frequency is denoted by f_0.

Frequency glides are simulated by quadratically increasing the parameter P in (1) so that $\tilde{f}_0$ increases linearly from 350 Hz to 810 Hz during a 2 s time interval. The spectrogram of the pressure at lips is shown in Fig. 2a with auxiliary lines showing the glide of $\tilde{f}_0$ and $F_1 = 647$ Hz. It is observed that f_0 coincides first with $\tilde{f}_0$, but then it suddenly jumps upwards to F_1 when it reaches about 470 Hz. The wave form of the glottal pulse near the transition is a superposition of two signals with frequencies $\tilde{f}_0$ and F_1. When $\tilde{f}_0$ exceeds F_1, then f_0 and $\tilde{f}_0$ coincide again. In the downward glide, a similar behaviour occurs as presented in Fig. 2b.

In the experiments, female subjects were asked to follow a target glide: a triangle wave sweep whose frequency grows from 170 Hz to 340 Hz linearly in logarithmic scale. In Fig. 3, a subject produces a rising glide of vowel /i/ for which 250 Hz $< F_1 <$ 300 Hz. Here the formant value has been measured from non-periodic phonation but it could also be obtained from the anatomy-based resonance analysis using MRI and FEM. Subjects use auditory, tactile, and proprioceptive feedback in controlling their phonation, and this is not modelled at all. A subject can start the corrective pitch regulation (e.g., near the modal locking) as early as 80 ms after a deviation from the given auditive target glide is perceived. Such corrective control actions may cause chaotic patterns such as the subphonation episode in Fig. 3.

Conclusions

We have introduced a simple model for simulating human vowel production. This model was used for studying the feedback effect from the vocal tract to the vocal folds in time domain complementing [4]. Qualitatively, the computational results are well in line with experiments: (1) in normal speech the vocal folds are not affected by the acoustics of the VT but (2) when

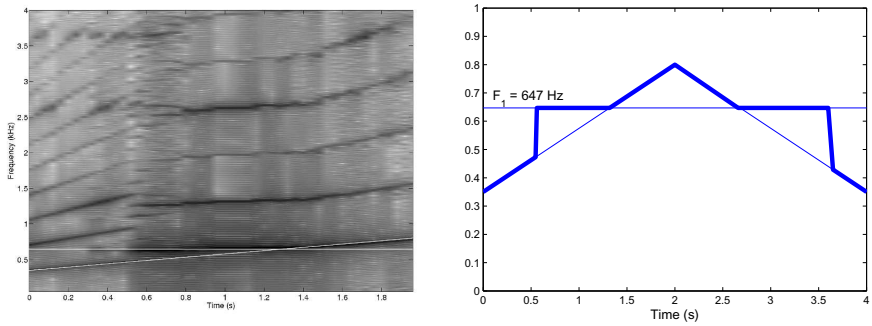

Figure 2. (a): Simulated f_0-glide upwards 350–810 Hz. (b): A sketch of the modal locking in an f_0-glide over F_1 first upwards and then downwards. The thick (thin) line shows f_0 (resp. $\tilde{f}_0$) during the glide.

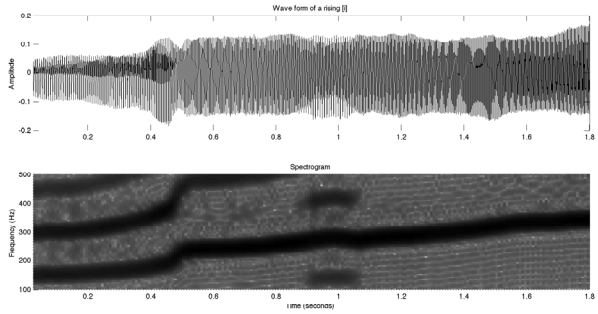

Figure 3. The wave form and the spectrogram (showing f_0) of a rising one octave glide with static vowel [i]. At 0.45–0.5 s a dip in amplitude coincides with a fast rise in f_0. At 0.9–1.06 s, subphonation occurs.

$|f_0 - F_1| < 100$ Hz, three kinds of instabilities are reported in [3]: fundamental frequency jumps, subharmonics, and chaotic behaviour. In simulations we have observed frequency jumps (of magnitude ≈170 Hz) at expected frequencies, and we propose that they are related to modal locking between the vocal fold and VT oscillations.

The experimental part of the work is in progress but some preliminary results are already available. It should be noted that the experimental results are complex: not all detected frequency jumps are due to the proposed coupling mechanism. Such jumps might occur because of register shifts, i.e., abrupt changes of the vibrating length of vocal folds. Subglottal formants may play a role at higher frequencies, and the muscle control may not be symmetric in falling and rising glides. Moreover, professional singers use at least following compensation mechanisms to avoid the coupling: change in F_1 by moving the tongue and pharynx configuration yet maintaining the vowel identifiable; reduction in the subglottal pressure inducing weaker glottal flow and hence weaker forces and weaker coupling; and a change to a more breathy phonation type.

References

[1] Chiba, T. and Kajiyama, M. *The Vowel, its Nature and Structure*. Tokyo-Kaiseikan Publishing Company Ltd., 1941.

[2] Fant, G. *The Acoustic Theory of Speech Production*. Moulton, The Hague, 1960.

[3] Titze, I., Riede, T., and Popolo, P. Nonlinear source-filter coupling in phonation: Vocal exercises, *Journal of the Acoustical Society of America*, 123(4):1902–1915, 2008.

[4] Titze, I. Nonlinear source-filter coupling in phonation: Theory, *Journal of the Acoustical Society of America*, 123(5):2733–2749, 2008.

[5] Hatzikirou H., Fitch W. T., and Herzel H. Voice Instabilities due to Source-Tract Interactions, *Acta Acustica united with Acustica*, 92:468–475, 2006.

[6] Aalto, A. *A low-order glottis model with nonturbulent flow and mechanically coupled acoustic load*, Master's thesis, TKK, Helsinki, 2009. `http://math.tkk.fi/research/sysnum/`

[7] Aalto, A., Alku, P., and Malinen, J. A LF-pulse from a Simple Glottal Flow Model, *MAVEBA2009 Proceedings*, Florence, Italy, 2009.

[8] Titze, I. Physiologic and acoustic differences between male and female voices, *Journal of the Acoustical Society of America*, 85(4):1699–1707, 1989.

[9] Horáček, J., Šidlof, P., and Švec, J. Numerical simulation of self-oscillations of human vocal folds with Hertz model of impact forces, *Journal of Fluids and Structures* 20:853–869, 2005.

Rakenteiden Mekaniikka (Journal of Structural Mechanics)
Vol. 44, No 3, 2011, pp. 231-242

On the self-excited vibrations of a viscoelastically covered cylinder in rolling contact using FE method

Anssi T. Karttunen and Raimo von Hertzen

Summary. As a result of ever-increasing speeds, the self-excited vibration of polymer-covered cylinders in rolling contact is becoming a more serious problem in many industrial processes. The vibration is generated by the viscoelastic behavior of the polymer covers. In this work, this vibration phenomenon, often referred to as barring, is studied using a two-dimensional rolling contact finite element model. The contact between two cylinders is modeled as a hard contact and the kinematic contact algorithm is used. The material parameters of the viscoelastic polymer cover of the other cylinder span a large relaxation spectrum. Readily available finite element software and tools are used for modeling and computations. The results show that strong barring vibration is a result of a resonance condition created in the rolling contact system. The vibration leads to the formation of a wave-like polygonal deformation pattern on the polymer-covered cylinder. The finite element model can provide detailed information on various phenomena, such as the nip waves, which have not been detected before by simplistic models.

Key words: polymer cover, viscoelasticity, barring, vibration, nip

Anssi T. Karttunen, Raimo von Hertzen
Aalto University School of Engineering, Department of Applied Mechanics
P.O. Box 14300, FI-00076 Aalto, Finland
anssi.karttunen@aalto.fi, raimo.von.hertzen@aalto.fi

Proceedings of the 24th Nordic Seminar on Computational Mechanics
J. Freund and R. Kouhia (Eds.)

Two phase flow in complicated geometries: Modeling the Frio data using improved computational meshes

Mika Juntunen[1] and Mary F. Wheeler[2]

(1) Aalto University, Institute of Mathematics, P.O. Box 11100, FI-00076 Aalto, Finland, mojuntun@gmail.com
(2) The University of Texas at Austin, 1 University Station C0200 Austin, Texas 78712-0027, USA, mfw@ices.utexas.edu

Summary. We study modeling two phase flow in complicated geometries. We use modern mesh generation techniques to improve the quality of the mesh and at the same time both reduce the number of elements and capture the geometry accurately. The generated meshes consist of orthogonally optimized general hexahedras. To model the flow in general hexahedras, we use the multipoint flux mixed finite element method (MFMFE) developed in [3]. As a test problem we use the Frio experiment data.

Key words: two phase flow, multipoint flux mixed finite method, MFMFE, finite element method, FEM, mesh generation

Introduction

The industry standard for modeling subsurface flow is either finite element or finite volume method. However, the representation of subsurface data is often poorly suited for such methods. The meshes used to represent data, such as permeability and porosity, are usually in corner point geometry and include collapsed hexahedra and even zero volume elements. Furthermore, the elements are often discontinuous. Yet another problem is that the meshes are often very dense, i.e. they have much more elements than needed for sufficient accuracy of finite element method.

In this article we use an auxiliary mesh generator to create the meshes for finite element simulations. The original data is used for acquiring the geometry, but the actual original elements are discarded. There is a wide selection of mesh generators to choose from. We use the GridPro mesh generator[1] because it applies modern, geometry based mesh generation and the generated meshes are optimized for flow problems. Due to an optimization strategy accurate solutions are attained with fewer elements and the stability of the computational method is improved.

The goal of this work is to demonstrate that by using better mesh generation it is possible to maintain fine geometrical details and at the same time improve the computational efficiency by decreasing the number of elements. As a test problem we use the Frio site which is located on the Gulf Coast, at South Liberty oil field, near Dayton, Texas, see [2]. There exist a substantial amount of well documented data for this experiment and the case is particularly well suited for our purposes due to the challenging geometry of the reservoir.

Mesh generation

The Frio data also offers a mesh for the problem. The mesh has $83 \times 62 \times 26 = 133796$ hexahedral elements with 32864 inactive elements, leaving 100932 active elements. The elements are given

[1]GridPro is developed by Program Development Company LLC, see *www.gridpro.com.*

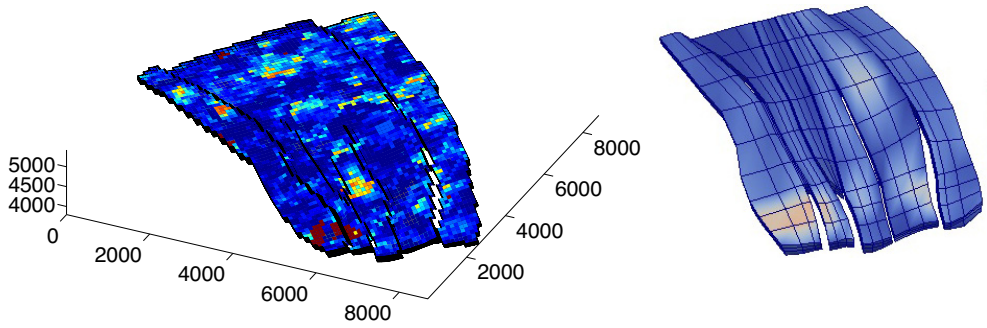

Figure 1. On the left, the original Frio geometry (100932 elements) and on the right a coarse approximation with 567 elements.

in corner point format, i.e. each element is defined by eight points in space. Since elements do not share the nodes, there are several small discontinuities between the elements. To use this data in finite element or finite volume simulation, the simulator needs to be able to handle the discontinuities or the unwanted discontinuities need to be removed. Either way, one must set a tolerance to tell which of the discontinuities are artifacts and which are real gaps.

In this work, we build a new mesh for the computational discretization with the GridPro mesh generator. The original data mesh provides the geometry for the mesh generation but the actual elements are discarded. This way we are able to produce even very coarse approximations without loosing significant geometrical details, see Figure 1. Furthermore, the computational meshes have smooth boundaries where the original data has jagged boundaries.

Numerical methods

The computational meshes used in this article consist of general hexahedra, i.e. the elements have eight corners but none of the faces is necessarily planar. This is also true for the data mesh so have not introduced any additional difficulties. To solve problem on general hexahedra accurately, one cannot use traditional finite volume methods, see e.g. [3]. Instead we use the multipoint flux mixed finite element method (MFMFE), developed in [3], that is shown to give accurate results on general hexahedra.

To simulate the reservoir we use the Integrated Parallel Accurate Reservoir Simulator (IPARS) developed at the University of Texas at Austin, at the Institute for Computational Sciences, at the Center for Subsurface Modeling. It has a collection of solvers, e.g. compositional flow and geomechanics, but in this work we only use the two-phase solver. We use the symmetric MFMFE with IMPES and allow for iterative coupling. We also allow for several saturation steps within one pressure step.

We will demonstrate with several numerical examples that using proper mesh generation it is possible to improve the computational mesh which yields faster and more reliable simulations. We will also discuss the data upscaling needed in coarser approximations.

Acknowledgements

The authors wish to thank Dr Peter Eiseman, President of Program Development Company LLC, for his support and for providing the GridPro mesh generator.

List of references

References

[1] Chen, Z., Huan, G., Ma, Y.: Computational methods for multiphase flows in porous media. Computational Science & Engineering. Society for Industrial and Applied Mathematics (SIAM), Philadelphia, PA (2006)

[2] Hovorka, S.D., Romero, M.L., Warne, A.G., Ambrose, W.A., Tremblay, T.A., Treviño, R.H., Sasson, D.: Sequestration of greenhouse gases in brine formations. Tech. rep., University of Texas at Austin, Bureau of Economic Geology, hypertext publication at: http://www.beg.utexas.edu/environqlty/co2seq/dispslsaln.htm (accessed December 20, 2005) (2000)

[3] Wheeler, M.F., Xue, G., Yotov, I.: Accurate cell-centered discretizations for modeling multiphase flow in porous media on general hexahedral and simplicial grids. SPE Reservoir Simulation Symposium, 21-23 February 2011, The Woodlands, Texas, USA (2011)

Rakenteiden Mekaniikka (Journal of Structural Mechanics)
Vol. 44, No 3, 2011, pp. 185-205

Simulation of a helicopter rotor flow

Juho Ilkko, Jaakko Hoffren and Timo Siikonen

Summary. Flowfield around the isolated main rotor of UH-60A helicopter was simulated to validate flow solver FINFLO for rotary wing applications. The computational model treated the four blades as rigid but hinged at their roots, and their dynamic movements resulting from the blade angle controls were solved interactively with the time-accurate flow solution that applies Reynolds-averaged Navier-Stokes equations. A hover case and a fast flight forward were studied with an overset grid system having around 20 million cells. With approximate modeling of appreciable blade elastic torsion, quite good agreement with the experimental and computational data taken from the literature was achieved.

Key words: helicopter rotor flow, CFD, fluid-structure interaction, multi-body dynamics

Juho Ilkko
Finflo Ltd.
Tekniikantie 12, 02150 Espoo, Finland
juho.ilkko@finflo.fi

Jaakko Hoffren
Patria Aviation Ltd.
Naulakatu 1, Tampere, Finland
jaakko.hoffren@patria.fi

Timo Siikonen
Aalto University School of Engineering
02015 Aalto, Finland
timo.siikonen@aalto.fi

Rakenteiden Mekaniikka (Journal of Structural Mechanics)
Vol. 44, No 3, 2011, pp. 279-291

Accuracy assessment of the Cartesian grid method for compressive inviscid flows using a simplified ghost point treatment

M. Asif Farooq, B. Müller

Summary. We introduce a new approach to treat ghost points near embedded boundaries to solve the 2D compressible Euler equations on a Cartesian grid. Solid wall boundary conditions are imposed by our new approach called simplified ghost point treatment for compressible inviscid flows with embedded boundaries. In the simplified ghost point treatment, we assume the solid boundary to lie in the middle between two grid points in the y-direction. Symmetry conditions are used to determine density, pressure, wall tangential, and wall normal velocity components at the ghost points. A cell-vertex finite volume formulation has been used to calculate transonic internal flows over a circular arc bump in a channel.

Key words: compressible Euler equations, Cartesian grid method, simplified ghost point treatment, cell-vertex finite volume method

M. Asif Farooq, B. Müller
Department of Energy and Process Engineering
Norwegian University of Science and Technology (NTNU)
Kolbjørn Hejes Vei 2 No-7491, Trondheim, Norway
asif.m.farooq@ntnu.no, bernhard.muller@ntnu.no

Proceedings of the 24th Nordic Seminar on Computational Mechanics
J. Freund and R. Kouhia (Eds.)

CFD study of roll damping of a winged bullet

Arttu Laaksonen

Aalto University School of Engineering, PO Box 14400, FI-00076 AALTO, Finland
arttu.laaksonen@aalto.fi

Summary. This article studies the roll damping of a bullet using computational fluid dynamics (CFD). Three different winged modifications based on a chosen bullet geometry are studied. The base geometry itself is also simulated to present comparison data. $SST\ k-\omega$ turbulence model is used and the boundary layer is solved by wall functions, which is proved reliable by validation process. The results show that the lengthened bullet with wings on the boat tail achieved the highest roll damping coefficients throughout the studied Mach number region.

Key words: roll damping, limited range projectile, flow simulation

Introduction

Bullets are usually spin-stabilized meaning that the rolling motion of the bullet around its longitudinal axis keeps the flight trajectory stable. Enhancing the damping of the roll is thus an effective way to make the bullet become unstable earlier and therefore limit its range. A bullet with a limited range but a decent accuracy until a chosen distance could be very useful for training use. This article studies three different winged bullet geometries with computational fluid dynamics (CFD) to compare their roll damping coefficient. A bullet with the same base geometry but without the wings is also studied to provide comparison data. This article is based on the author's master's thesis, see ref. [1] for detailed information.

Studied bullets

The studied bullet geometries are based on the American M33 bullet, see figure 1.

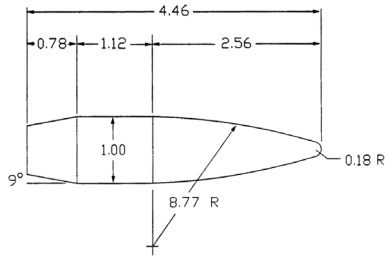

Figure 1. M33 bullet [2]. All dimensions in calibers, 1 cal = 12.95 mm.

Three different modified geometries were created. One bullet had wings on the ogive and two had wings on the boat tail. All modified geometries are presented in figure 2.

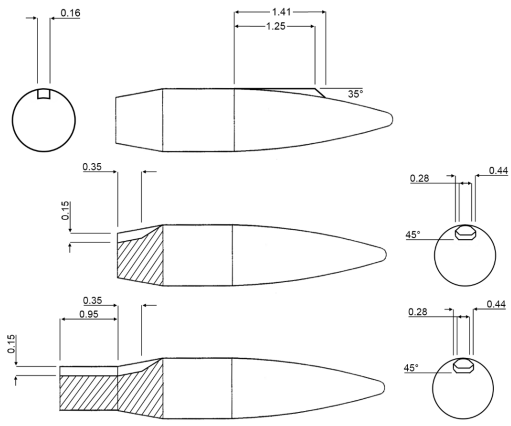

Figure 2. The studied bullet geometries: wings on the ogive (top), wings on boat tail (middle) and lengthened bullet with wings on boat tail and extension (bottom). All dimensions in calibers, 1 cal = 12.95 mm.

For simplicity all the pictures in figure 2 show only one wing/groove but in reality all the bullets had four wings at intervals of 90 degrees.

Methods

Turbulence model and boundary layer solving method were validated by simulating a bullet which had published experimental data [3] for comparison. After validation process RANS-based $SST\ k-\omega$ was chosen for the turbulence model and wall functions were proved reliable to solve the boundary layer.

Grids were created using Pointwise and had both structured and unstructured blocks. The grids for M33, ogive-winged, boat tail-winged and lengthened boat tail-winged bullet had 2.3M, 5.5M, 2.8M and 4.0M cells respectively.

The Ansys Fluent software was used for the flow simulations. Computations were performed on a desktop computer with a six-core Intel Xeon X5650 2.67 GHz processor and 12 GB of RAM. Some of the simulations were also performed on the Murska cluster of the IT Center for Science (CSC).

The bullets were studied at four supersonic Mach numbers ranging from Mach 2.7 to Mach 1.2. The rolling motion of the bullet was simulated by choosing a moving mesh-option in Fluent and giving a spin rate around longitudinal axis as an input. The spin rates are linearly related to the flow speed. In all simulations, the angle of attack was 0°. The studied Mach numbers and respective spin rates are presented in table 1.

Table 1. The studied flow situations.

Mach	Spin rate [rad/s]
1.2	-6707
1.7	-9501
2.2	-12296
2.7	-15090

Rolling moment coefficient was calculated from the simulation results. Roll damping coefficient is calculated from rolling moment coefficient by

$$C_{l_p} = \frac{\partial C_l}{\partial \hat{p}} \tag{1}$$

where $\hat{p}$ is the dimensionless spin rate, defined here by

$$\hat{p} = \frac{pd}{2V} \tag{2}$$

where p is the projectile spin rate, d is projectile maximum diameter and V is flow speed.

Results

Figure 3 presents roll damping coefficient for all bullets plotted as a function of Mach number.

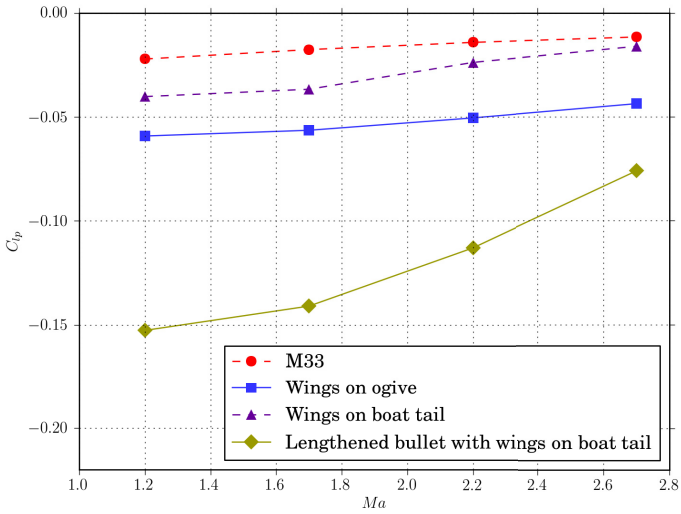

Figure 3. The roll damping coefficient for studied bullets as a function of Mach number.

The results show that the lengthened bullet with wings on the ogive achieved the highest roll damping coefficient throughout the studied region. The shorter bullet with wings on the boat tail proved to be unefficient at high Mach numbers as its roll damping coefficient is effectively equal to that of M33. This is due to flow separation before the grooves between the wings. In the lengthened bullet the flow attaches again further in the groove. The results of the bullet with wings on the ogive land between those of the other studied bullets. For further information on the results, see ref. [1].

References

[1] A. Laaksonen. Tutkimus luodin pyörimisen vaimenemisesta virtauslaskennan avulla (Study of the roll damping of a projectile using CFD methods) . Master's Thesis, Espoo, 2011.

[2] B. J. Guidos and S. K. Chung. Computational Flight Design of .50 Caliber Limited Range Training Ammunition. Army Research Laboratory, 1995, ARL-TR-662.

[3] P. Plostins, R. L. McCoy and B. A. Wagoner. Aeroballistic Performance of the 25mm M910 TPDS-T Range Limited Training Projectile. Ballistic Research Laboratory, 1991, BRL-MR-3886.

Proceedings of the 24th Nordic Seminar on Computational Mechanics
J. Freund and R. Kouhia (Eds.)

Electromechanics of polyurethane elastomers

A. Ask[1], M. Ristinmaa[1*], A. Menzel[1,2]

(1)Division of Solid Mechanics, Faculty of Engineering, Lund University
(2) Institute of Mechanics, Department of Mechanical Engineering,
Technische Universität Dortmund
∗ matti.ristinmaa@solid.lth.se

Summary. It is well known that electroactive polymers (EAP) deform under electric fields. An advantage of EAP is that it may undergo deformations much larger than those capable by electroactive ceramics, however at comparatively low forces. As common for polymers, EAP exhibit time-dependent material behavior, i.e. an electro-viscoelastic effect. In the modeling the deformation as well as the electric potential are introduced as global degrees of freedom, the internal variables accounting for the viscous response are incorporated at the so-called constitutive level. The proposed model is calibrated against experimental data, and a simple coupled finite element example is studied to show the applicability of the finite deformation electro-viscoelastic formulation proposed.

Key words: electro-viscoelasticity, electrostriction

Introduction

Electrostriction is the term used to describe an electrically activated deformation which is proportional to the square of the electric polarization in a dielectric material. In some dielectric elastomers this effect gives rise to deformations which are noticeable also on a macroscopic scale. A typical application utilizing dielectric elastomers is in actuators [2]. A thin film of the material is coated on both sides with compliant electrodes and then a potential difference is applied so that an electric field is generated through the elastomer. This will make the film contract in the thickness direction, i.e. perpendicularly to the field, and expand in the other two directions. The electromechanical response is in part due to the so-called Maxwell effect: opposite charges on the two electrodes give rise to attractive Coulomb forces between them. For some elastomers, there is additionally inherent electrostriction present, due to some electromechanical property of the material. This is true in the case of e. g. polyurethane (PU) elastomers, where the inherent electrostriction has been attributed to space charge impurities in the thin film samples.

In this contribution, the modeling of the inherent electromechanical behavior of PU elastomers is considered. Specifically, the behavior in the lower range of electric field strengths is studied, where the major part of the deformation of the PU has been demonstrated to be due to other causes than the Maxwell effect. Experimental evidence in the literature suggests that deformations of up to some 5–6% can be expected for this type of loading. A phenomenological constitutive model allowing for large deformations is developed [1]. The material behavior is separated into a coupled part which is essentially electroelastic, and a purely mechanical part, where the latter is taken to be viscoelastic as the elastomeric PU exhibits time dependent behavior during mechanical loading.

Basic equations

Kinematics

Let $\boldsymbol{\varphi}(\mathbf{X}, t)$ be a sufficiently smooth mapping transforming position vectors $\mathbf{X}$ of material particles in the reference configuration $\mathcal{B}_0$ to their position $\mathbf{x} = \boldsymbol{\varphi}(\mathbf{X}, t)$ in the current configuration $\mathcal{B}_t$ at time t. The deformation gradient tensor is then given by $\mathbf{F} = \boldsymbol{\nabla}_X \boldsymbol{\varphi}$. In addition, the deformation gradient is multiplicatively split into its volumetric, i.e. defined by the Jacobian $J = \det(\mathbf{F})$ and its isochoric part $\overline{\mathbf{F}} = J^{-1/3}\,\mathbf{F}$. For the viscous effects as discussed later on, an additional multiplicative decomposition is applied to the isochoric part into elastic and inelastic or rather viscous components

$$\overline{\mathbf{F}} = \overline{\mathbf{F}}_{e_\alpha} \cdot \mathbf{F}_{v_\alpha}\,, \tag{1}$$

where $\det(\mathbf{F}_{v_\alpha}) = 1$ is assumed. The format in (1) corresponds to a generalized Maxwell model extended to three dimensions and the large-strain regime. The parameter α denotes the number of viscous elements.

Balance equations

For electrostatics and in the absence of magnetic fields, free currents and free electric charges, the local referential balance equations for the electromagnetic field quantities are given by

$$\boldsymbol{\nabla}_X \times \mathbf{E} = \mathbf{0} \qquad \text{and} \qquad \boldsymbol{\nabla}_X \cdot \mathbf{D} = 0\,. \tag{2}$$

where the electric field is denoted by $\mathbf{E}$ and the electric displacement by $\mathbf{D}$, with respect to the reference configuration. A more careful description of the topic is found in [5], [8], see also the discussion in [6]. As the curl of the electric field is zero, it can be derived from a scalar potential ϕ as

$$\mathbf{E} = -\,\boldsymbol{\nabla}_X \phi\,. \tag{3}$$

At surfaces of discontinuity, including at the boundary $\partial\mathcal{B}_0$, the electric field and the electric displacement must fulfill the jump conditions

$$\mathbf{N} \cdot [\![\mathbf{D}]\!] = 0 \qquad \text{and} \qquad \mathbf{N} \times [\![\mathbf{E}]\!] = \mathbf{0}\,, \tag{4}$$

where brackets $[\![\,\bullet\,]\!]$ indicate a discontinuity and $\mathbf{N}$ is the outward unit normal of the referential surface. For the mechanical problem, in the absence of mechanical body forces and assuming a quasi-static setting, the referential local balance of linear momentum form reads

$$\boldsymbol{\nabla}_X \cdot \mathbf{T} = \mathbf{0}\,, \tag{5}$$

where $\mathbf{T}$ is the total nominal stress tensor, which also includes the electromagnetic force contribution. The boundary condition for the stress is represented by

$$[\![\mathbf{T}]\!] \cdot \mathbf{N} = \mathbf{0}\,. \tag{6}$$

Constitutive model

Based on equation (1), the following Cauchy-Green-type deformation tensors are introduced

$$\mathbf{C} = \mathbf{F}^{\mathrm{T}} \cdot \mathbf{F}\,, \qquad \overline{\mathbf{C}} = \overline{\mathbf{F}}^{\mathrm{T}} \cdot \overline{\mathbf{F}}\,, \qquad \mathbf{C}_{v_\alpha} = \mathbf{F}_{v_\alpha}^{\mathrm{T}} \cdot \mathbf{F}_{v_\alpha}\,. \tag{7}$$

The deformation tensors $\mathbf{C}_{v_\alpha}$ will be treated as internal variables accounting for the viscous behavior. Since $\det(\mathbf{F}_{v_\alpha}) = 1$, this implies $\det(\mathbf{C}_{v_\alpha}) = 1$. It is assumed that the material can be described by a free energy function $\Omega(\mathbf{F}, \mathbf{E}, \mathbf{C}_{v_\alpha})$ in terms of the deformation gradient,

the electric field vector, and internal variables as independent quantities. By introducing an augmented free energy function

$$\Omega^* = \Omega - \frac{1}{2}\,\epsilon_0\, J\, \mathbf{C}^{-1} : [\,\mathbf{E}\otimes\mathbf{E}\,] \tag{8}$$

where ϵ_0 is the electric permittivity of vacuum, it is straightforward to derive the stress and electric displacement as

$$\mathbf{T} = \frac{\partial\Omega^*}{\partial\mathbf{F}}\,, \qquad \mathbf{D} = -\,\frac{\partial\Omega^*}{\partial\mathbf{E}}\,. \tag{9}$$

Furthermore, it is assumed that the free energy Ω can be split additively into volumetric, isochoric long-term, non-equilibrium (viscous), electromechanical and electrical contributions as

$$\Omega(\mathbf{F},\mathbf{E},\mathbf{C}_{v_\alpha}) = \Omega_{\rm vol}(J) + \Omega_\infty(\overline{\mathbf{F}}) + \sum_\alpha \Omega_\alpha(\overline{\mathbf{F}},\mathbf{C}_{v_\alpha}) + \Omega_{\rm mel}(\overline{\mathbf{F}},\mathbf{E}) + \Omega_{\rm el}(\mathbf{E})\,. \tag{10}$$

The specific formats used are

$$\Omega_{\rm vol}(J) = \frac{1}{2}\,K\,[\,J-1\,]^2\,, \qquad \Omega_\infty(\overline{\mathbf{F}}) = \frac{1}{2}\,\mu\,[\,\overline{\mathbf{C}} : \mathbf{I} - 3\,]\,, \tag{11}$$

where $\mathbf{I}$ denotes the second-order identity tensor, together with

$$\Omega_\alpha(\overline{\mathbf{F}},\mathbf{C}_{v_\alpha}) = \frac{1}{2}\,\beta_\alpha\,\mu\,[\,\overline{\mathbf{C}} : \mathbf{C}_{v_\alpha}^{-1} - 3\,]\,, \quad \Omega_{\rm mel} = c_m\,\overline{\mathbf{C}} : [\,\mathbf{E}\otimes\mathbf{E}\,]\,, \quad \Omega_{\rm el} = c_e\,\mathbf{I} : [\,\mathbf{E}\otimes\mathbf{E}\,]\,. \tag{12}$$

The viscous part, needs to be further specified as the dissipation inequality places restrictions on the possible format of the evolution law of the internal variables given as

$$D = \sum_\alpha \boldsymbol{M}_{v_\alpha} : [\,\boldsymbol{C}_{v_\alpha}^{-1}\cdot\dot{\boldsymbol{C}}_{v_\alpha}\,] \geq 0\,. \qquad \text{where} \quad \boldsymbol{M}_{v_\alpha} = \rho_0\,\frac{\partial\Omega_\alpha}{\partial\boldsymbol{C}_{v_\alpha}^{-1}}\cdot\boldsymbol{C}_{v_\alpha}^{-1} \tag{13}$$

Above the Mandel-type quantity $\boldsymbol{M}_{v_\alpha}$ was introduced.

The format of the evolution law considered here resembles an approach commonly used in plasticity theory. Introduce the potential function

$$\Phi = [\,\frac{1}{2}\boldsymbol{M}_{v_\alpha}^{\rm dev} : \boldsymbol{M}_{v_\alpha}^{\rm dev^T}\,]^{1/2}\,. \tag{14}$$

Superscript dev here denotes the deviatoric part of the tensor. One possible format of the evolution law which does fulfill the dissipation inequality is then given by

$$\dot{\boldsymbol{C}}_{v_\alpha} = \dot\gamma_\alpha\,\boldsymbol{C}_{v_\alpha}\cdot\frac{\partial\Phi}{\partial\boldsymbol{M}_{v_\alpha}} = \dot\Gamma_\alpha\,\boldsymbol{C}_{v_\alpha}\cdot\boldsymbol{M}_{v_\alpha}^{\rm dev^T}\,, \tag{15}$$

where it was assumed that $\dot\gamma_\alpha = \dot\Gamma_\alpha\Phi$, where $\dot\Gamma_\alpha$ is a constant parameter.

Numerical examples

The weak form of the balance equations is linearized and discretized by adopting standard approaches as common for finite element applications. Since the electric field can be derived from a scalar potential in the static case and—by analogy with the deformation gradient—includes only first-order gradients, the discretization uses the same shape functions for the deformation $\boldsymbol{\varphi}$ and the electric potential ϕ, cf. [7].

The model is calibrated against experimental data provided by [4] for the viscoelastic part of the behavior and by [3] for the coupling coefficient c_m. The coefficient c_e is set to $c_e = 1$ due to lack of experimental data. It should be noted that its value does not affect the mechanical response. The material parameters used in the simulation are presented in Table 1.

Table 1. Material parameters.

Elastic	Viscoelastic
$\mu = 1.307$ MPa	$\beta_1 = 0.6260$, $\dot{\Gamma}_1 = 5.385\ \mathrm{s}^{-1}\ \mathrm{MPa}^{-1}$
Electromechanical	$\beta_2 = 0.1497$, $\dot{\Gamma}_2 = 1.021\ \mathrm{s}^{-1}\ \mathrm{MPa}^{-1}$
$c_\mathrm{m} = 1.763 \cdot 10^{-9}\ \mathrm{N\ V}^{-2}$	

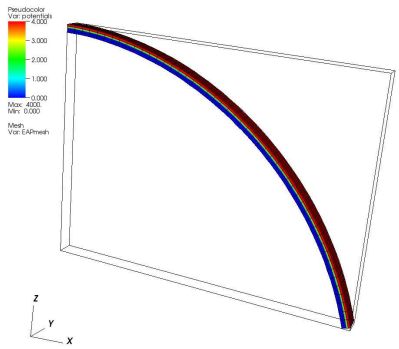

Figure 1. Deformation of the beam type actuator. The color indicates the value of the scalar potential

A finite element (FE) implementation is done in order to perform simulations using the established material model. A representative boundary value problem is then solved, e.g. Fig 1, which depicts a beam structure activated by electric loading in the form of a potential difference (potential values indicated in color). This type of structure and loading, though the example is academical, can still be said to be representative of actual applications, giving an indication of possible uses for material modeling of EAP from a continuum mechanics point of view in e.g. development and testing.

[1] Ask, A. and Menzel, A. and Ristinmaa, M. *Phenomenological modeling of viscous electrostrictive polymers*. Int. J. of Non-Linear Mechanics. doi: 10.1016/j.ijnonlinmec.2011.03.020

[2] Samatham R. et al., 2007. Active polymers: An Overview. *Electroactive Polymers for Robotic Applications*. London, Springer.

[3] Diaconu I., Dorohoi D.-O. and Ciobanu C., 2008. Electromechanical response of polyurethane films with different thickness. *Rom. Journ. Phys.*, **53**, 91-97.

[4] Johlitz, M. and Steeb, H. and Diebels, S. and Chatzouridou, A. and Batal, J. and Possart, W., 2007. Experimental and theoretical investigation of nonlinear viscoelastic polyurethane systems, *Journal of Materials Science*,**42**, 9894-9904.

[5] Maugin G.A., 1988. *Continuum Mechanics of Electromagnetic Solids*. (Amsterdam; North-Holland)

[6] Dorfmann A. and Ogden R.W., 2005. Nonlinear electroelasticity. *Acta Mechanica*. **174**. 167-183.

[7] Vu D.K., Steinmann P., and Possart G., 2007. Numerical modelling of non-linear electroelasticity. *International Journal for Numerical Methods in Engineering*. **70**, 685-704.

[8] Eringen A. C., 1989. *Mechanics of Continua.* 2nd edition. (Malabar; Krieger)

Proceedings of the 24th Nordic Seminar on Computational Mechanics
J. Freund and R. Kouhia (Eds.)

A unified solution attempt for the torsion problem

Jukka Aalto and Risto Syrjä
Aalto University, P.O. Box 12100, FI-00076 AALTO, jukka.aalto@aalto.fi

Summary. The possibility to consider Saint Venant's torsion [1] and warping torsion [2] problems together is discussed. Two separate boundary value problems for two warping functions are first presented. The solution of these equations is arranged so that center of twist of the cross section can be simultaneously determined. Equations for determining the normal stress and shear stresses in a cross section, if the corresponding stress resultants are known, are presented. Finite element solution of the problem is briefly described. The applicability of the method is demonstrated with numerical tests.

Key words: Saint Venant's torsion, warping torsion, finite elements

Assumptions

Let us consider torsion of a straight uniform beam. The axial displacement of the beam in the vicinity of the cross-section under consideration is assumed to be

$$u(x,y,z) = \varphi'(x)\psi(y,z) + \varphi'''\phi(y,z)\,, \tag{1}$$

where $\varphi(x)$ is the angle of twist, which is assumed to be locally a cubic function of the axial co-ordinate x. The functions $\psi(y,z)$ and $\phi(y,z)$, which define the distribution of the displacement in the cross-section, are called warping functions. Projection of the cross-section in the $y,z-$plane is assumed to rotate around the center of twist T like a rigid plate. Thus the transverse displacement components of the beam are

$$v(x,y,z) = -\varphi(x)(z - z_{\mathrm{T}}), \quad w(x,y,z) = \varphi(x)(y - y_{\mathrm{T}})\,. \tag{2}$$

Conventional assumptions of the beam theory, that the transverse normal stresses σ_y and σ_z vanish, are additionally made.

Boundary value problem for the warping functions

Using these assumptions and basic equations of linear elasticity, following boundary value problems

$$\begin{aligned} &\frac{\partial}{\partial y}[G(\frac{\partial \psi}{\partial y} - z + z_{\mathrm{T}})] + \frac{\partial}{\partial z}[G(\frac{\partial \psi}{\partial z} + y - y_{\mathrm{T}})] = 0 \quad \text{in } A, \\ &n_y(\frac{\partial \psi}{\partial y} - z + z_{\mathrm{T}}) + n_z(\frac{\partial \psi}{\partial z} + y - y_{\mathrm{T}}) = 0 \quad \text{on } s \end{aligned} \tag{3}$$

and

$$\frac{\partial}{\partial y}(G\frac{\partial \phi}{\partial y})+\frac{\partial}{\partial z}(G\frac{\partial \phi}{\partial z})+E\psi=0 \quad \text{in } A, \quad n_y\frac{\partial \phi}{\partial y}+n_z\frac{\partial \phi}{\partial z}=0 \quad \text{on } s \tag{4}$$

can be developed for the warping functions $\psi(y,z)$ and $\phi(y,z)$, respectively. Here A is the domain, s is the boundary and y_T and z_T are coordinates of the center of twist T.

Solution of the warping functions and the center of twist

Because y_T and z_T are unknowns, the boundary value problem (3) cannot, however, be solved as such. Therefore the warping function $\psi(y,z)$ is expressed as

$$\psi(y,z)=\bar{\psi}(y,z)+\psi_0-z_T y+y_T z\,, \tag{5}$$

where ψ_0 is constant. By substituting this into (3) it can be seen, that the boundary value problem for the new function $\bar{\psi}(y,z)$ is identical to (3), but with $y_T=z_T=0$. Unique solution for $\bar{\psi}(y,z)$ can be achieved, if its value at arbitrarily selected point y_0,z_0 is constrained to vanish. After $\bar{\psi}(y,z)$ is known the unknown parameters ψ_0, y_T and z_T can be determined based on the conditions $N=0$, $M_y=0$ and $M_z=0$ of pure torsion. The result is

$$\psi_0=-\frac{(ES)_{\bar{\psi}}}{(EA)},\; y_V=\frac{-(EI)_z(EI)_{z\bar{\psi}}+(EI)_{yz}(EI)_{y\bar{\psi}}}{(EI)_y(EI)_z-(EI)_{yz}^2},\; z_V=\frac{-(EI)_{yz}(EI)_{z\bar{\psi}}+(EI)_y(EI)_{y\bar{\psi}}}{(EI)_y(EI)_z-(EI)_{yz}^2}, \tag{6}$$

where (EA) is the axial stiffness, $(EI)_y,(EI)_z$ and $(EI)_{yz}$ are the bending stiffness's and

$$(ES)_{\bar{\psi}}=\int_A E\bar{\psi}dA,\; (EI)_{y\bar{\psi}}=\int_A Ey\bar{\psi}dA,\; (EI)_{z\bar{\psi}}=\int_A Ez\bar{\psi}dA. \tag{7}$$

The expressions (6) for the center of twist reduce to those of homogeneous cross-section, first presented by Trefftz (see Ref. [3]), by setting $E=\text{constant}$ and $(EI)_{yz}=0$. Unique solution for the warping function $\phi(y,z)$ is achieved, if its value at point y_0,z_0 is constrained to vanish.

Stresses from stress resultants

After the warping functions are known, the state of stress of the beam can be determined. In a cross-section, where the stress resultants: bi-moment B, its derivative B', total torque M_x and Saint Venant's torque $M_t=M_x-B'$ are known , the normal stress and the shear stresses can be obtained from

$$\begin{aligned}
&\sigma_x(y,z)=-\frac{EB}{(EI)_\psi}\psi(y,z),\\
&\tau_{xy}(y,z)=\tau_{xy}^t(y,z)+\tau_{xy}^w(y,z)\equiv\frac{GM_t}{(GI)_t}[\frac{\partial \psi}{\partial y}(y,z)-z+z_T]-\frac{GB'}{(EI)_\psi}\frac{\partial \phi}{\partial y}(y,z),\\
&\tau_{xz}(y,z)=\tau_{xt}^t(y,z)+\tau_{xz}^w(y,z)\equiv\frac{GM_t}{(GI)_t}[\frac{\partial \psi}{\partial z}(y,z)+y-y_T]-\frac{GB'}{(EI)_\psi}\frac{\partial \phi}{\partial z}(y,z),
\end{aligned} \tag{8}$$

where the superscripts t and w refer to the Saint Venant's and the warping shear stresses, respectively, and

$$(GI)_t=\int_A G[(\frac{\partial \psi}{\partial y}-z+z_T)(-z+z_T)+(\frac{\partial \psi}{\partial z}+y-y_T)(y-y_T)]dA,\quad (EI)_\psi=\int_A E\psi^2 dA \tag{9}$$

are the torsional and the warping stiffness. The problem of determining the typical stress resultants $M_x(x)$ and $B(x)$ of the beam is equivalent to that of warping torsion of thin-walled beams.

Finite element equations

The Poisson type boundary value problems for determining the functions $\bar{\psi}$ and ϕ are easily discretized. Because there is only one degree of freedom per node and the stiffness matrix corresponding to both problems is identical, the solution if very efficient. The stress resultants of the beam and the warping functions of the cross-section, can be solved in advance. After they are known, the state of stress of any cross-section of the beam can be determined using equations (8).

Example problem

Circular arch cross-section of Fig. 1 was analyzed using biquadratic iso-parametric finite elements both in the thin- ($t = 0{,}1a$) and the thick-walled ($t = a$) cases. One layer of 20 elements and 4 layers of 20 elements were used in the thin- and the thick-walled case, respectively. In the thin-walled case analytical solution based on warping torsion theory was used for comparison. Location of the center of twist T was first determined. In the thin-walled case the analytical and numerical result were $z_T = 1{,}623a$ and $z_T = 1{,}618a$, respectively, and in the thick-walled case the numerical result was $z_T = 1{,}246a$. Fig. 2 shows the distribution of (a) normal stress σ_x and (b) warping tangential shear stress $\tau^w_{x\theta}$ as function angle ϕ (see Fig. 1) obtained in the thin-walled case. The finite element results practically coincide with the analytical ones. Fig. 3 demonstrates distribution of (a) Saint Venant's shear stress $\tau^t_{x\theta}$ and (b) warping shear stress $\tau^w_{x\theta}$ obtained in the thick-walled case.

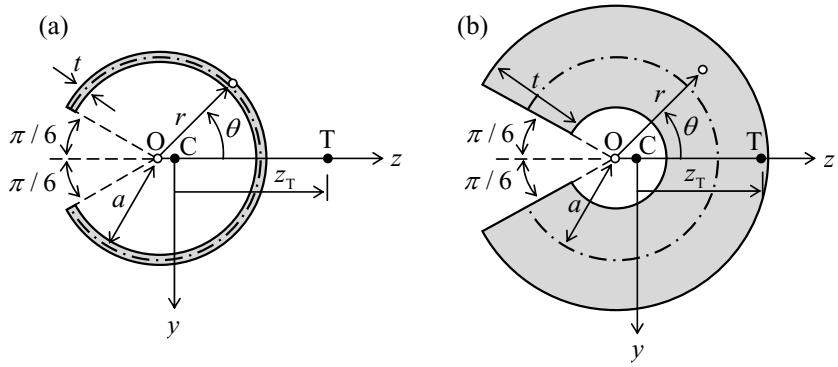

Figure 1. Circular arch cross section (a) thin $t = 0{,}1a$ and (b) thick $t = a$

Conclusions

The more or less intuitive solution approach presented above needs further substantiation. However numerical tests performed this far show that this strategy works both in connection with thin- and thick-walled cross-sections.

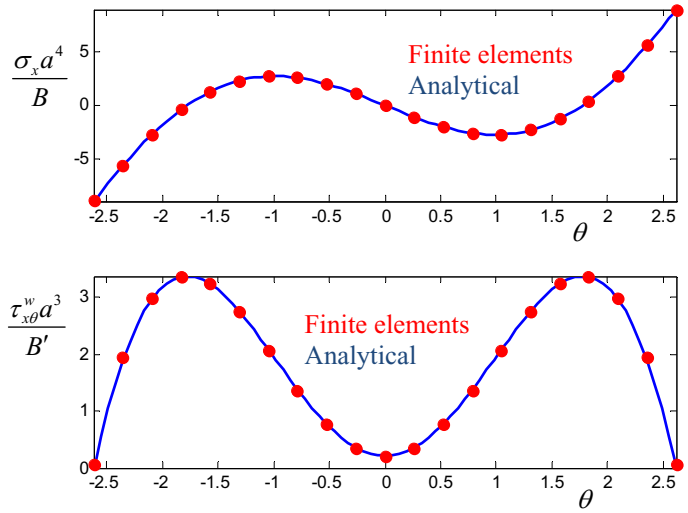

Figure 2. Comparison of numerical and analytical results for (a) normal stress σ_x and (b) warping shear stress $\tau^w_{x\theta}$; thin cross-section $t = 0{,}1a$.

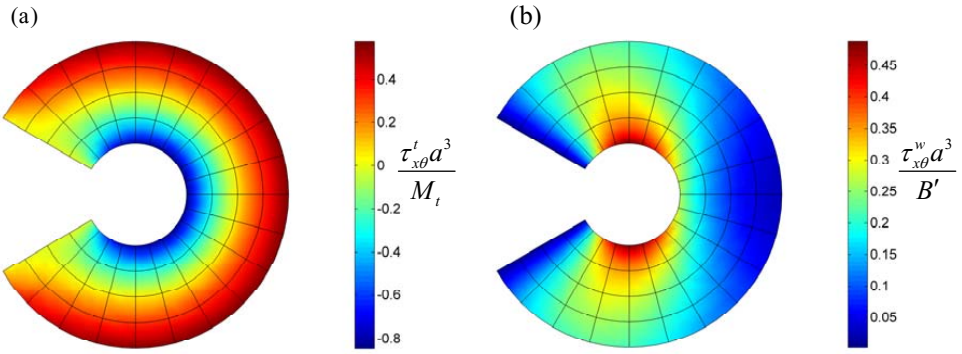

Figure 3. (a) Saint Venant's and (b) warping shear stresses; thick cross-section $t = a$.

Acknowledgements

Continual encouragement of emer. Prof. E.-M. Salonen to consider the torsion problem not as two separate problems but in a unified way is gratefully acknowledged.

References

[1] S.P. Timoshenko and J.N. Goodier, *Theory of Elasticity*, McGraw Hill, pp. 291-297, 1970.
[2] V.Z. Vlasov, *Thin-walled elastic beams*, Israel Program for Scientific Translations Ltd, 2nd Edition, pp. 3-51, 1963.
[3] K. Washizu, *Variational Methods in Elasticity and Plasticity,* Pergamon Press Ltd, 3rd Edition, p. 587, 1982.

Proceedings of the 24th Nordic Seminar on Computational Mechanics
J. Freund and R. Kouhia (Eds.)

Digital nomenclature code *dncm* for generation of finite-element kinematics

Oleg Dmitrochenko and Aki Mikkola

Lappeenranta University of Technology, Skinnarilankatu 34, 53850 Lappeenranta
Oleg.Dmitrochenko@LUT.fi, Aki.Mikkola@LUT.fi

Summary. A new system of identification of finite elements is proposed, the digital nomenclature code *dncm*. The topological and kinematic structure of an arbitrary finite element is represented by a multidigit code that reflects the topological structure of the element. The code of an element is based on dimension *d*, the number of nodes *n*, the number of scalar coordinates per node *c*, and a multiplier *m*. The introduced classification procedure enables description of previously undefined finite elements. The code allows for a systematic enumeration of finite elements and reflects interrelations and transformations between them. A universal procedure can be proposed to construct the geometrical and structural matrices of a finite element by its code *dncm*.

Key words: finite element analysis, nomenclature

Introduction

There are wide varieties of finite elements that have been developed in different physical areas such as structural analysis, fluid mechanics, electromagnetism, and coupled-field elements. This development work has been conducted by a large number of researchers, many working in FEA code development within the commercial sector. Given this commercial emphasis for much of the development, it is understandable that a conventional system of identification or numeration of finite elements does not exist. Because of this missing system of identification, authors usually describe finite elements in their papers with definitions such as 'constant-strain triangle', or 'drilling triangle'. This approach is acceptable if a single element or a few of them are discussed. However, if one needs to deal with many elements simultaneously and to describe their common features or interrelationships, the need for a short element designation becomes obvious.

Finite-element notations that have been employed in literature are as follows:

– by abbreviations, *e.g.* CFT, CST, LST, DKT, DKQ, BEAM189 *etc.*; this notation lacks information about nodes or coordinates to allow for reconstruction of the element;

– by number of nodes, *e.g.* quadrilaterals Q4, Q6, Q8, Q9, bricks B8, B20; the disadvantage of this approach is that there is no information about kinematics and nodal coordinates;

– by number of degrees of freedom, *e.g.* B4, B8, B12, B16 (beams), ANCF-B30, ANCF-B48; the problem here is that different elements can have exactly the same number of d.o.f.

In a recent research [1], a new classification called digital nomenclature code in the form *dnc* has been proposed for a systematic classification of conventional elements: *d* is the dimension; *n* is the number of nodes, and *c* is the number of coordinates (derivatives) per node. Further, it has been found that the kinematics of a great number of widely used elements are described in the form *dncm*.

The introduced nomenclature code allows for developing kinematic descriptions of new finite elements in a straightforward manner. This can be accomplished, in practise, with the help of a transformation procedure. In the transformation, some of the features from an original element are preserved.

Geometry and kinematics of basic *dnc* elements

A three-digit nomenclature *dnc* of a wide variety of finite elements is proposed using the following integer digits:

d is the (inner) dimension of the elements, it is equal to the number of arguments of the interpolation polynomial $Z^{dnc}(x,...)$; *e.g.* value 1 is associated with beams, 2 with plates *etc.*;

n is the number of nodes of the element;

c is the number of coordinates per node meant as the number of derivatives of the field variable *Z* starting with zeroth derivative: Z, $\frac{\partial}{\partial x}Z$, ...

Figures 1, 2, and 3 represent some of the commonly used simple finite elements in one-, two-, and three-dimensional cases.

Product *n* by *c* equals to the total number of degrees of freedom of element *dnc*: $D = n \cdot c$

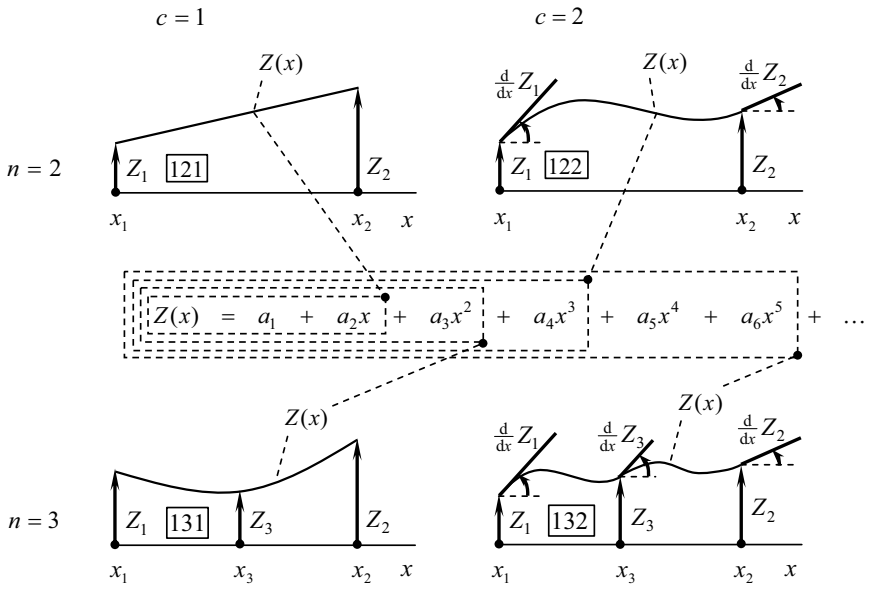

Figure 1. Basic 1D elements 1*nc* and their interpolation polynomials.

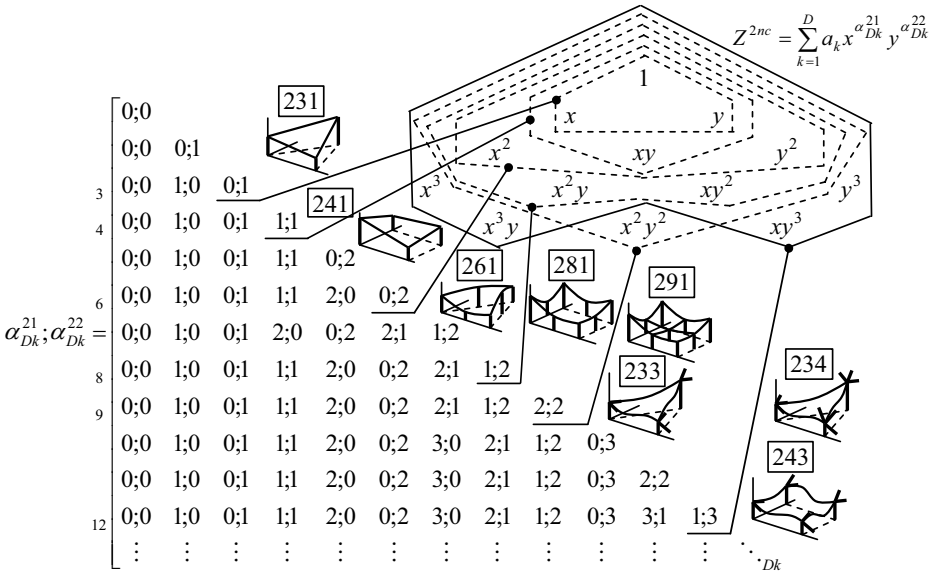

Figure 2. Basic 2D elements 2*nc* with Pascal triangle of polynomial terms and its matrix form

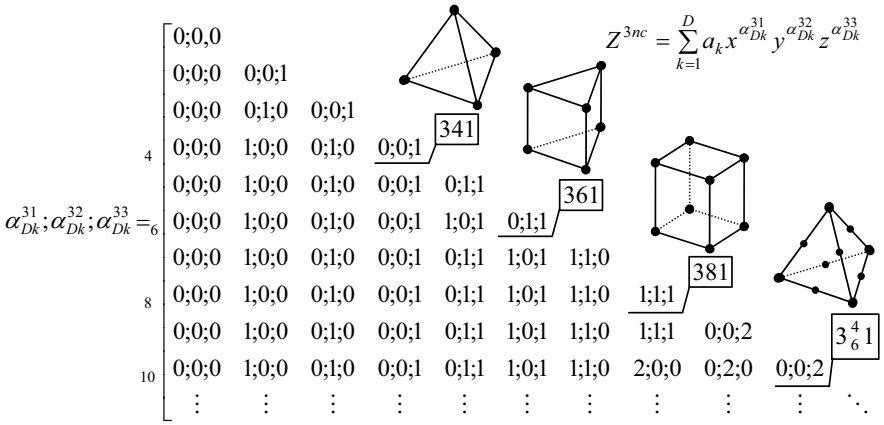

Figure 3. Matrix representation of Pascal pyramid of polynomial terms of solid elements 3*nc*

The interpolation polynomial for an arbitrary case can be represented as follows:

$$Z^{dnc}(x_1,\ldots,x_d) = \sum_{k=1}^{D} a_k x_1^{\alpha_{Dk}^{d1}} \ldots x_d^{\alpha_{Dk}^{dd}} = \sum_{k=1}^{D} a_k \prod_{q=1}^{d} x_q^{\alpha_{Dk}^{dq}}$$
$$= \underbrace{\{\Pi_{q=1}^{d} x_q^{\alpha_{D1}^{dq}} \quad \ldots \quad \Pi_{q=1}^{d} x_q^{\alpha_{DD}^{dq}}\}}_{\mathbf{x}(x_1,\ldots,x_d)} \cdot \underbrace{\{a_1 \quad \ldots \quad a_D\}^{\mathrm{T}}}_{\mathbf{a}} = \mathbf{x}(x_1,\ldots,x_d) \cdot \mathbf{a} \tag{1}$$

Symbols α_{Dk}^{dj} used as exponential coefficients are presented in figures 1 to 3. For example, $\alpha_{Dk}^{11} = k-1$.

The values of undefined constants a_k can be obtained from a linear system of equations when one evaluates Z^{dnc} and its proper derivatives at each node of the element:

$$\left.\frac{\partial^{\alpha_{Dj}^{d1}+\ldots+\alpha_{Dj}^{dd}} Z(x,y)}{\partial x_1^{\alpha_{Dj}^{d1}} \ldots \partial x_d^{\alpha_{Dj}^{dd}}}\right|_{\substack{\text{at node } i \\ x_q = x_{qi}}} \equiv \sum_{k=1}^{D} \underbrace{\prod_{q=1}^{d} (\alpha_{Dk}^{dq})_{-\alpha_{Dj}^{dq}} x_{qi}^{\alpha_{Dk}^{dq}-\alpha_{Dj}^{dq}}}_{W_{lk}} a_k = z_l \equiv Z_{i,j}, \quad \text{or} \quad \mathbf{W}\cdot\mathbf{a} = \mathbf{z}. \tag{2}$$

Components W_{lk} of the Wroński-type matrix $\mathbf{W}$ are defined in Eq. (2), where indices i, j and l are defined as follows for different groups of nodes: $i = 1,\ldots,n$; $j = 1,\ldots,c$; $l = (i-1)c + j$. Notation $(\alpha)_{-j}$ represents falling factorial: $(\alpha)_{-j} = \Pi_{i=0}^{j-1}(\alpha - i) = \frac{\alpha!}{(\alpha-j)!}$.

Finally, after solving Eq. (2) in terms of a, the polynomial Z takes the form

$$Z^{dnc}(x_1,\ldots,x_d) = \sum_{i=1}^{n}\sum_{j=0}^{c-1} \underbrace{\sum_{k=1}^{D}\prod_{q=1}^{d} x^{\alpha_{Dk}^{dq}} W_{kl}^{-1}}_{s_{i,j}^{2nc}(x_1,\ldots,x_d)} Z_{i,j} = \underbrace{\mathbf{x}(x_1,\ldots,x_d)\cdot\mathbf{W}^{-1}}_{\mathbf{s}^{2nc}(x_1,\ldots,x_d)}\cdot\mathbf{z} = \mathbf{s}^{2nc}(x_1,\ldots,x_d)\cdot\mathbf{z} \tag{3}$$

with the row matrix of shape functions $\mathbf{s}^{2nc}$ and the column matrix of nodal coordinates $\mathbf{z}$.

Modified code *dncm* for multiple fields, other extensions and conclusion

Simple three-digit nomenclature *dnc* for basic single-polynomial elements can be extended to multiple-field elements *dncm* using the fourth multiplier *m*, which represents the number of fields that are interpolated the same way. This allows enumerating a waste majority of existing finite elements by simple notation *dncm*, which is not descriptive only but is constructive, too: by changing digits *d*, *n*, *c*, and *m*, it is possible to find new elements not mentioned in literature before [1].

More complicated elements possess a set of nodal coordinates *X* that formally correspond to some code *dncm*; however, their kinematics require that an auxiliary element ($d\eta\varsigma\mu$) to be created using different topology η and kinematics ς, μ with a different set of nodal coordinates $\breve{X}$. Then, a transformation *T* towards coordinates *X* leads to an element systematically denoted by code $dncm(d\eta\varsigma\mu)\{\breve{X} = T(X)\}$, which is proposed in paper [2] and called the extended digital nomenclature code. Examples of such elements are planar triangles and rectangles with drilling degrees of freedom, quadrilaterals with extra shape functions, discrete Kirchhoff triangles and other elements, including rigid bodies.

References

[1] Oleg Dmitrochenko, Aki Mikkola, 'Digital Nomenclature Code for Topology and Kinematics of Finite Elements based on the Absolute Nodal Coordinate Formulation, *Proc. of Inst. of Mech. Engineers, Part K, J. of Multi-body Dyn.* 225(1), 2011, 34-51.

[2] Oleg Dmitrochenko, Aki Mikkola, 'Extended digital nomenclature code for description of complex finite elements and generation of new elements', *Mechanics Based Design of Structures and Machines* 39(2), 2011, 229-252.

Proceedings of the 24th Nordic Seminar on Computational Mechanics
J. Freund and R. Kouhia (Eds.)

Modal analysis used to estimate bone density in-vivo

Adam Kłodowski[1], Timo Rantalainen[2], and Aki Mikkola[3]

(1)Lappeenranta University of Technology, Skinnarilankatu 34, 53850 Lappeenranta, adam.klodowski@lut.fi
(2) Lappeenranta University of Technology, Skinnarilankatu 34, 53850 Lappeenranta, timo.rantalainen@lut.fi
(3) Lappeenranta University of Technology, Skinnarilankatu 34, 53850 Lappeenranta, aki.mikkola@lut.fi

Summary. This article presents a prospective method for in-vivo bone density estimation. Specially designed test bench allows measuring vibration response induced by impact impulse of force. Modal response of the bone is normalized with respect to total body mass to account for bone size. Finally output from the normalized modal response is correlated with bone mineral density measured by DXA. Resulting relationship can be used to classify subjects to two categories: high and low bone density with success rate at the level of 63%.

Key words: experiment, classification, mineral density, osteoporosis

Introduction

Bones fulfill important weight bearing function in human body. They create mechanical chains actuated by muscles which enable locomotion. External load applied to bones stimulates bone growth Ref. [1], and thus strengthening. Despite the fact, that human move each day, the amount of physical activity might be still insufficient to stimulate bone growth. At that stage the bone starts the resorption process, which in long run can lead to osteoporosis. The main problem with osteoporosis is that it is a silent disease, there are no visible symptoms and usually it is discovered when a bone fracture occurs. In many cases the disease is then at advanced stage and not many methods can be used to slow down its progress. For example, the number of hip fractures in Finnish people aged 50 or more increased more than three times from times between 1970 to and 1997 Ref. [2]. For that reasons prevention is of a key importance. Nowadays methods used to evaluate bone density are relatively expensive, and are based on ionizing radiation, what limits their usage. This inspired the authors to think of an inexpensive and radiation free method, which would allow determining bone condition. This preliminary study shows an idea of using vibration analysis in bone density estimation.

Methods

Modal frequencies Ref. [3] are associated directly with mass distribution, density and elasticity of the measured bone, and these parameters describe bone rigidity. Because of the fact that bones in living humans are covered with soft tissues that have damping properties the effect of soft tissue needs to be studied Ref. [4] as well. Previous research on the subject showed correlation between bone mineral density and natural frequencies Ref. [4]. According to the researchers, the bone natural frequency increases with the increase of the bone mineral density. Vibration analysis in the referred study was performed using modal hammer. That setup does not allow applying precise force impulse. In addition, the accelerometers were held by hand introducing additional noise to the measurement. In the new setup that was created during the current project, vibration generator with force sensor is used, which guarantees precise impulse force generation. Two force sensors are uses in order to allow for detecting any measurements errors. Both sensors are attached by elastic straps to provide good contact with the bone, remove any extra noise, and constrain the range of force used to press the sensors against bone. Moreover, boundary conditions are chosen to reduce the muscle damping effect, as leg is suspended in the air supported just under ankle and knee. The improvements in the proposed project yield much more accurate vibration measurements with high repeatability. The devise is depicted in figure 1.

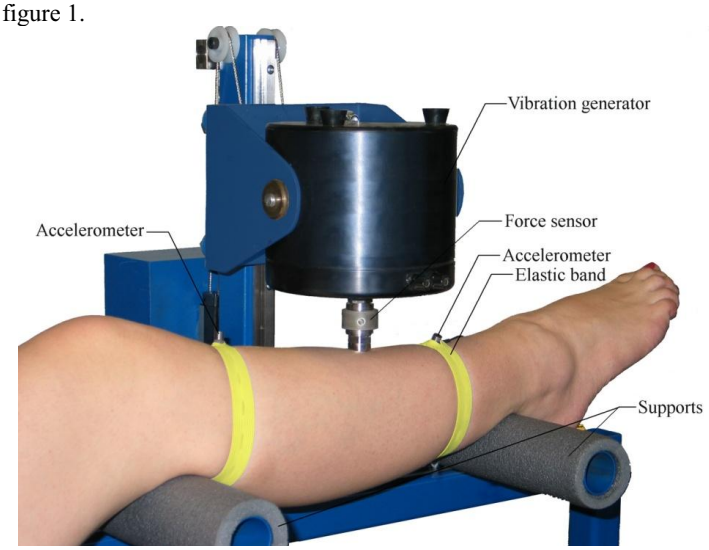

Figure 1 Equipment for measuring the natural frequencies of tibia.

The whole process of measurement of tibia vibrations takes approximately 5 minutes. The subject is equipped with accelerometers attached by elastic straps and sited with his leg placed on two adjustable supports. Then the vibration generator support is adjusted to place the tip over the tibia. The system allows regulating the initial pressure between the generator's tip and the leg. The localization of the impact place is chosen over the most visible surface of tibia in the middle of its length. In principle, only one accelerometer is needed to perform a measurement, the usage of two sensors allows for validation of the accelerometers contact with the bone.

The measurement requires four successive impulse hits with the force of 40N as excitation, to measure bone vibration response. Those four measurements are combined into one averaged response. A sample response is shown in figure 2. None of the subjects reported the experiment

as unpleasant. As it can be seen from figure 2, peak locations from sensors mounted on one leg compared with sensor responses from the other leg are in good correlation. The trial was performed on 20 postmenopausal women, who gave their informed consent to the experiment. Bone density of the subjects was first measured with standard DXA equipment for reference with the new method.

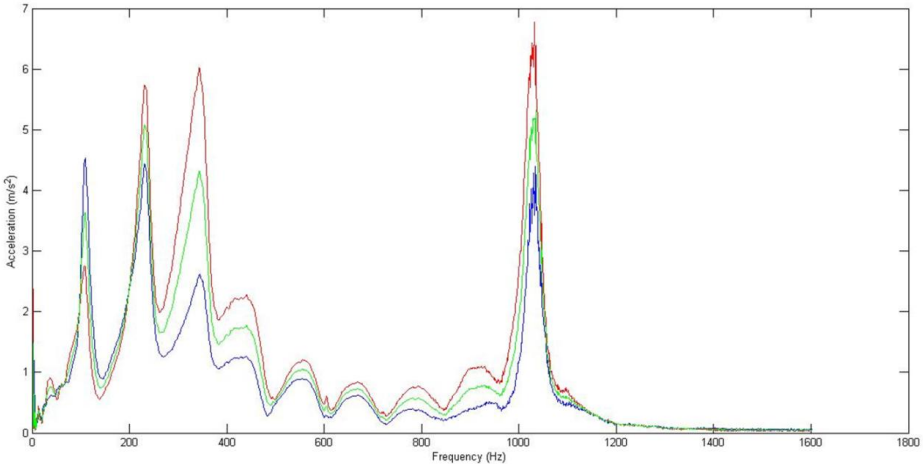

Figure 2 Bone response measured on both tibias of a single subject using two sensors on each of the legs.

Anthropometric parameters: weight, height and tibia length of each of the participants were collected. Natural frequencies of a body depend on total mass, dimensions and mass distribution. It was thus concluded that frequency response as such do not give absolute information about bone density, and two other parameters have to be normalized. For simplicity authors have assumed that mass distribution within a bone is uniform and that bone size is proportional to the body size. The most significant deformation mode is bending in the saggital plane, as indicated in Ref. [5]. It is also the first deformation mode, thus the first modal frequency is considered as the representative. Normalization with respect to mass, height, length of tibia and body mass index, which is defined as:

$$\mathrm{BMI} = \frac{\mathrm{m}}{\mathrm{h}^2} \tag{1}$$

Where m is the mass of the subject in kg, and h is the height of the subject in meters.

Results and conclusions

From the set of 21 measurements, one had to be rejected due to the difficulty in unambiguous determination of the first modal frequency. Remaining 19 measurements were correct and were used in analysis. Correlation between first modal frequency with respect to bone density measured by DXA was low (R^2=0,025). Normalizing the frequency with respect to body mass index, length of tibia, and height improved the result giving: R^2=0,115; R^2=0,071; R^2=0,029 respectively. The best result was however obtained after normalization with respect to the total body mass (R^2=0,121). Using the relationship between normalized first natural frequency with respect to total body mass and bone mineral density, classification into two categories was

performed. The classification succeeded in 12 out of 19 cases which gives success rate of about 63%.

At the current state the method allows only to classify the subjects to those of high and low bone mass. It is expected that in future better normalization method can be found allowing for regression rather than simple classification of the density-natural frequency response.

References

[1] Turner, C. H., Three rules for bone adaptation to mechanical stimuli., *Bone*, 23, 399-407, 1998

[2] Kannus, P, Niemi, S, Parkkari, J, Palvanen, M, Vuori, I, Järvinen, M, Hip fractures in Finland between 1970 and 1997 and predictions for the future, *Lancet*, 353, 802-805, 1999

[3] Christensen, A. B., Ammitzboll, F., Dyrbye, Assessment of tibial stiffness by vibration testing in situ. I. Identification of mode shapes in different supporting conditions, *Journal of Biomechanics*, 19(1), 53-60, 1986

[4] Bediz, Bekir, Nevzat Ozgüven, H.; Korkusuz, Feza Vibration measurements predict the mechanical properties of human tibia, *Clinical Biomechanics*, 25(4), 365-371, 2010

[5] Al Nazer, R., Klodowski, A., Rantalainen, T., Heinonen, A., Sievänen, H., Mikkola, A., Analysis of dynamic strains in tibia during human locomotion based on flexible multibody approach integrated with magnetic resonance imaging technique, *Journal of Multibody System Dynamics*, 20, 287-306, 2008

Proceedings of the 24th Nordic Seminar on Computational Mechanics
J. Freund and R. Kouhia (Eds.)

Human walking simulation by using optimization

Daniel Garcia-Vallejo

Department of Mechanical and Materials Engineering, University of Seville, Camino de los Descubrimientos s/n, 41092 Seville, Spain, e-mail: dgvallejo@us.es

Summary. Inverse dynamics simulation is a convenient approach often used in robotics and mechatronic systems for feed-forward control to reproduce a desired output trajectory of a nonlinear multibody system. Usually the engineering systems are completely actuated or underactuated, respectively, for economical reasons. In contrary, the musculoskeletal multibody systems found in biomechanics are highly overactuated due to the many muscles, and they show switching number of closed kinematical loops. The method of inverse dynamics is extended to overactuated systems by parameter optimization, and simulation results of human walking are presented.

Key words: Inverse dynamics, parameter optimization, human walking dynamics.

Introduction

Parameter optimization techniques have been frequently used for motion synthesis of biped robots [4]. These techniques have been proven to be powerful in two-dimensional human walking simulation as shown by Ackermann [1]. The basics of this approach are the parameterization of the muscle forces and generalized coordinates and the search for their optimal values by minimizing a cost function that includes an energy expenditure estimation and a measure of deviation from normal walking patterns. The method is very much based on inverse dynamics since at each iteration of the optimization algorithm an inverse dynamic problem is solved by using the motion reconstructed from the optimization parameters. The main advantage of this approach is the complete elimination of the forward integrations of the equations of motion, what significantly reduces the computational cost of simulation.

Multibody model

The human body model used is a three-dimensional rigid multibody system actuated by muscles. The equations of motion of the system are obtained by using the multibody software Neweul-M^2 [5], which generates the equations of motion in symbolic form for efficiently analyzing, simulating and optimizing multibody systems. The skeleton is first considered as an open kinematic chain built from rigid bodies that are connected by holonomic joints and

described by a set of n_c generalized coordinates. Thus, the equations of motion are written in terms of the generalized coordinates by virtue of the d'Alembert's principle [7] as

$$\mathbf{M}(\mathbf{q})\ddot{\mathbf{q}} + \mathbf{k}(\mathbf{q},\dot{\mathbf{q}}) = \mathbf{q}_r(\mathbf{q},\dot{\mathbf{q}}) + \mathbf{B}\mathbf{A}\mathbf{f}^m, \tag{1}$$

where $\mathbf{M}(\mathbf{q})$ is the mass matrix of the system, $\mathbf{q}$, $\dot{\mathbf{q}}$ and $\ddot{\mathbf{q}}$ are the position, velocity and acceleration vectors, respectively, $\mathbf{k}(\mathbf{q},\dot{\mathbf{q}})$ is a vector describing the generalized Coriolis forces, $\mathbf{q}_r(\mathbf{q},\dot{\mathbf{q}})$ is a vector including generalized gravitational forces, passive generalized moments at the joints due to tissues interacting with the joints according to the model of Riener and Edrich [6] and generalized viscous damping torques at the knees and hips according to the model of Stein et al. [8] and $\mathbf{B}\mathbf{A}\mathbf{f}^m$ is a vector that includes the generalized forces exerted by the muscles actuating the model.

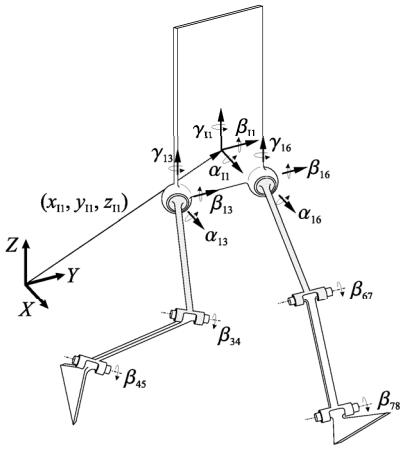

Figure 1. Simplified multibody model for human walking simulation.

The three-dimensional model of the human body used in this research is composed of 7 rigid bodies, two thighs, two shanks, two feet, and a body called HAT representing the pelvis, trunk, arms and head, which are connected by holonomic joints, see figure 1. The thighs are connected at the hips to the HAT by spherical joints, the shanks and thighs are connected by revolute joints representing the knees and the foot and shanks are connected by revolute joints representing the ankles. This is a simplification of other three-dimensional models that can be found in Anderson and Pandy [2, 3]. However, this simplification allows the derivation by software Neweul-M^2 [5] of the equations of motion of the 7 bodies tree without any constraint.

The kinematic chain in Figure 1 is described by the following vector of 16 generalized coordinates

$$\mathbf{q} = [x_{I1} \quad y_{I1} \quad z_{I1} \quad \alpha_{I1} \quad \beta_{I1} \quad \gamma_{I1} \quad \alpha_{13} \quad \beta_{13} \quad \gamma_{13} \quad \beta_{34} \quad \beta_{45} \quad \alpha_{16} \quad \beta_{16} \quad \gamma_{16} \quad \beta_{67} \quad \beta_{78}]^T, \tag{2}$$

where the subscript *I* refers to the inertial frame, subscript 1 refers to body HAT, subscripts 3 and 6 refer to right and left thighs, respectively, subscripts 4 and 7 refer to right and left shanks, respectively, and subscripts 5 and 8 refer to right and left feet, respectively. When a subscript is written as *ij* it means a relative motion of body *j* with respect to body *i*. It shall be noted here that Neweul-M^2 is programmed based on the most common sequence of rotation 123, while in Biomechanics the sequence 213 is usually considered anatomically meaningful, Zatsiorsky [9]. Once the kinematic chain representing the skeleton is described, the contact of this chain with the ground is added through unilateral constraints. Due to the use of an optimization framework it is possible to constrain the normal contact forces to be only positive. Then, the contact can be modelled using simple bilateral constraints. Therefore, the contact forces can be easily added to the model by using a vector of Lagrange multipliers as

$$\mathbf{M}(\mathbf{q})\,\ddot{\mathbf{q}} + \mathbf{k}(\mathbf{q},\dot{\mathbf{q}}) = \mathbf{q}_r(\mathbf{q},\dot{\mathbf{q}}) + \mathbf{B}\,\mathbf{A}\,\mathbf{f}^m + \mathbf{C}_{ph}^T\boldsymbol{\lambda}_{ph} \quad (ph = 1,2,\ldots 8), \tag{3}$$

where $\boldsymbol{\lambda}_{ph}$ is the vector of Lagrange multipliers at phase *ph* of the motion.

Optimization framework

The simulation of human walking motion is treated as a large parameter optimization problem. The design variables are used to reconstruct the muscle force histories and the generalized coordinate histories of a walking cycle as well. Such a set of parameters are found by minimizing a cost function which is evaluated based on energetic and aesthetic reasons. Finally, the motion and muscle forces time histories reconstructed from the optimization parameters are asked to fulfill many constraints. The constraints of the constrained optimization problem ensure the fulfillment of the equations of motion of the multibody system, the kinematic constraints as well as other physical and physiological relations.

The complete set of design variables are summarized in vector $\boldsymbol{\chi}$ which includes:

1. A vector $\mathbf{q}_i$, i = 1, 2, ...n_c, containing nodal values of the generalized coordinates.
2. A vector $\mathbf{f}_j^m$, j = 1, 2, ...N_m, containing nodal values of the different muscle forces.
3. A vector representing the durations of the eight phases of a walking cycle $\mathbf{t}_{ph}$.
4. A geometrical parameters vector describing the kinematic constraints of the feet on the ground $\mathbf{p}_g$.

According to the previous explanation, the vector of design variables can be written as:

$$\boldsymbol{\chi} = \left[\mathbf{q}_i^T \quad \mathbf{f}_j^{mT} \quad \mathbf{t}_{ph}^T \quad \mathbf{p}_g^T\right]^T, \tag{4}$$

where indices *i*, *j* and *ph* are running from 1 to n_c, N_m and 8, respectively, and *g* is just a subscript meaning that parameters in $\mathbf{p}_g$ are geometrical. In the three-dimensional model presented before the number of coordinates n_c is equal to 16 while the number of muscles N_m is equal to 28.

Numerical results

This section shows some numerical results of the simulations carried out using the optimization framework presented. A symmetrical motion occurring in the sagittal plane has been analyzed to

check the performance of the approach and the convergence of the model for different parameterizations. The symmetry of the model allows a big simplification in the number of optimization variables. In fact, it is assumed that the left leg experiences in the second half of the walking cycle the same motion as the right leg in the first half. In addition, the motion of the pelvis is assumed to be the same in both halves of the cycle.

Table 1 shows the results of several models that differ one to another in the number of nodes used to parameterize the generalized coordinates and muscle forces. The convergence of the different models to a unique solution is remarkable.

Table 1: Performance of the different models (*NN* stands for number of nodes, f is the cost function, E' is the metabolical cost of transportation, J_{dev} is the measure of deviation from normal walking patterns and CT stands for computation time). * Estimated CT values.

NN	f	E' [J/m]	J_{dev}	*CT* [hours]
19	13.33	626.00	7.07	0.55
21	7.54	415.73	3.38	1.85
23	6.52	351.01	3.01	2.87
25	5.50	310.62	2.39	3.25
27	4.99	283.28	2.16	5.65*
29	4.62	254.22	2.08	8.66
31	4.45	246.32	1.99	9.52
33	4.37	238.57	1.98	13.17
35	4.31	236.10	1.95	16.16*

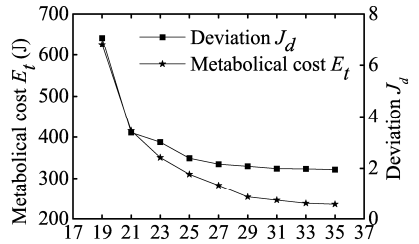

Acknowledgement

This research was supported in part by the Spanish Ministry of Science and Innovation through the project TRA2010-16715. This support is gratefully acknowledged.

References

[1] Ackermann, M. Dynamics and energetics of walking with prostheses. PhD thesis, Institut für Technische und Numerische Mechanik, Stuttgart, 2007.

[2] Anderson, F., and Pandy, M. A dynamic optimization solution for vertical jumping in three dimensions. Computer Methods in Biomechanics and Biomedical Engineering **2** (1999), 201–231.

[3] Anderson, F., and Pandy, M. Dynamic optimization of human walking. Journal of Biomechanical Engineering **123** (2001), 381–390.

[4] Bessonnet, G., Seguin, P., and Sardain, P. A parametric optimization approach to walking pattern synthesis. The International Journal of Robotics Research **24**, 7 (2005), 523–536.

[5] Kurz, T., Eberhard, P., Henninger, C., and Schiehlen, W. From Neweul to Neweul-M^2: Symbolical equations of motion for multibody system analysis and synthesis. Multibody System Dynamics **24**, 1 (2010).

[6] Riener, R., and Edrich, T. Identification of passive elastic joint moments in the lower extremities. Journal of Biomechanics **32** (1999), 539–544.

[7] Schiehlen, W. Multibody system dynamics: Roots and perspectives. Multibody System Dynamics **1** (1997), 149–188.

[8] Stein, R., Zehr, E., Lebiedowska, M., Popovic, D., Scheiner, A., and Chizeck, H. Estimating mechanical parameters of leg segments in individuals with and without physical disabilities. IEEE Transactions on Rehabilitation Engineering **4**, 3 (1996), 201–211.
[9] Zatsiorsky, V. Kinematics of Human Motion. Human Kinetics, 1998.

Proceedings of the 24th Nordic Seminar on Computational Mechanics
J. Freund and R. Kouhia (Eds.)

Collapse simulations of flexible multibody systems

Jari Mäkinen

Tampere University of Technology, Mechanics and Design,
P.O. Box 589, 33101 Tampere, jari.m.makinen@tut.fi

Summary. A procedure for modelling the dynamic collapse of flexible multibody systems using a non-linear finite element method is presented. The flexible multibody system is assembled by Reissner's geometrically exact beam elements. The primary interest is to model and simulate hydraulic-driven multibody systems under oversized load causing a failure.

Key words: stress resultant theory, geometrically exact beam, plasticity, return mapping

Introduction

In this paper, the flexible multibody system is assembled by Reissner's geometrically exact beam elements [1]. Our aim is to model and simulate hydraulic-driven multibody systems under oversized load causing a failure. These collapse simulations can be utilized in the accident analyses or the detection of the device in the extreme conditions that could advise in design. The hydraulic system, and especially hydraulic cylinder, is modelled by a length controlled bar element [2]. In order to model the failure, an elasto-plastic material model is required.

Since plastic material model should be robust to utilize the material model in simulations, a stress resultant formulation is introduced. In the spatial case, the Reissner's beam element has six stress resultants: normal and two shear force vectors and three bending moments. The stress resultant formulation avoids the through-thickness integration. However, the yield surface depends on the shape of the cross-section. In this paper, the study is restricted to rectangular hollow cross-sections and a stress resultant formulation for elasto-plastic material is introduced.

Return mapping algorithm

For yield condition in the stress resultant formulation we choose simply

$$f(\boldsymbol{\Sigma}) := \sum_{i=1}^{3}\left(\frac{N_i}{N_\mathrm{p}}\right)^2 + \sum_{i=1}^{3}\left(\frac{M_i}{M_\mathrm{p}}\right)^2 - 1 \tag{1}$$

where N_p is the fully plastic normal force and M_p is the fully plastic bending moment. The stress resultants and corresponding strains for Reissner's spatial beam are [1]

$$\boldsymbol{\Sigma} := \begin{pmatrix} \mathbf{N} \\ \mathbf{M}_{\mathbf{R}} \end{pmatrix}, \ \mathbf{E} := \begin{pmatrix} \boldsymbol{\Gamma} \\ \mathbf{K}_{\mathbf{R}} \end{pmatrix} \tag{2}$$

The return mapping algorithm reads in this case

$$\begin{aligned} &\mathbf{E}_{n+1} = \mathbf{E}_n + \Delta\mathbf{E} \\ &\mathbf{E}^{\mathrm{p}}_{n+1} = \mathbf{E}^{\mathrm{p}}_n + \Delta\mathbf{E}^{\mathrm{p}} = \mathbf{E}^{\mathrm{p}}_n + \lambda_{n+1}\mathbf{r}, \quad \mathbf{r} := \frac{\partial f}{\partial \boldsymbol{\Sigma}} \\ &\boldsymbol{\Sigma}_{n+1} = \mathbf{C}_{\mathrm{NM}}\left(\mathbf{E}_{n+1} - \mathbf{E}^{\mathrm{p}}_{n+1}\right) \\ &f_{n+1} := f(\boldsymbol{\Sigma}_{n+1}) \le 0 \end{aligned} \tag{3}$$

where $\mathbf{C}_{\mathrm{NM}}$ is the elasticity matrix of the cross-section, and λ is the plasticity parameter in the flow rule. The elastic trail in the return mapping algorithm reads

$$\begin{aligned} &\mathbf{E}^{\mathrm{p}}_{n+1} = \mathbf{E}^{\mathrm{p}}_n, \ \ \lambda = 0 \\ &\boldsymbol{\Sigma}^{\mathrm{trail}}_{n+1} = \mathbf{C}_{\mathrm{NM}}\left(\mathbf{E}_{n+1} - \mathbf{E}^{\mathrm{p}}_n\right) \end{aligned} \tag{4}$$

So, in order to solve the residual equations

$$\begin{aligned} &\mathbf{a} := -\mathbf{E}^{\mathrm{p}}_{n+1} + \mathbf{E}^{\mathrm{p}}_n + \lambda_{n+1}\mathbf{r}_{n+1} = \mathbf{0} \\ &f = f(\boldsymbol{\Sigma}_{n+1}) = 0 \end{aligned} \tag{5}$$

we have the following iterative formulas for increments

$$\begin{aligned} &\delta\lambda = \frac{f - \mathbf{r}^T\tilde{\mathbf{C}}\mathbf{a}}{\mathbf{r}^T\tilde{\mathbf{C}}\mathbf{r}}, \ \ \tilde{\mathbf{C}} := \left(\mathbf{C}^{-1}_{\mathrm{NM}} + \lambda\mathbf{r}_{\boldsymbol{\Sigma}}\right)^{-1} \\ &\Delta\boldsymbol{\Sigma} = \tilde{\mathbf{C}}(-\mathbf{a} - \delta\lambda\mathbf{r}) \end{aligned} \tag{5}$$

In addition, the algorithmic tangential modulus reads

$$\mathbf{C}^{\mathrm{alg}} = \left(\tilde{\mathbf{C}} - \frac{\tilde{\mathbf{C}}\mathbf{r} \otimes \tilde{\mathbf{C}}\mathbf{r}}{\mathbf{r}^T\tilde{\mathbf{C}}\mathbf{r}}\right) \tag{6}$$

The governing equations of motion in the dynamic case are solved by using the implicit Newmark time integration method. A numerical example considering the hydro-mechanical flexible multibody system is presented where a heavy load with sudden stop of hydraulic cylinder causes the collapse of the system. In this example, dynamic effects in the limit load are evident.

References

[1] Mäkinen J (2007) "Total Lagrangian Reissner's Geometrically Exact Beam Element without Singularities", I*nternational Journal for Numerical Methods in Engineering*, Volume 70, Issue 9, pp. 1009-1048.

[2] Marjamäki H & Mäkinen J (2006) "Modelling a Telescopic Boom - The 3D Case: Part II", *Computers & Structures*, 84(29-30), pp. 2001-2015.

Proceedings of the 24th Nordic Seminar on Computational Mechanics
J. Freund and R. Kouhia (Eds.)

Loop formation in NiTi suture materials

Antti-Jussi Vuotikka

Department of Mechanical Engineering, University of Oulu, FIN-90014 Oulu, Finland
antti-jussi.vuotikka@oulu.fi

Summary. Several works have investigated the use of NiTi wire for flexor tendon repair. The material has been shown to have several advantages compared with commonly used suture materials. However, it has also some drawbacks. This study investigates the torsional instabilities of thin martensitic and austenitic wire. Commonly used suture material braided polyester (4-0 Ethibond®) is used as a control material.

Key words: NiTi, suture, kink, snarling

Introduction

Nickel-titanium (NiTi) wire has been proposed as an alternative material for flexor tendon core suture. Several papers have studied its suitability in flexor tendon repair [1], [2]. The NiTi circumferential repairs showed superior stiffness, gap resistance and load to failure when compared to polypropylene repairs.

The NiTi wire has several properties that show potential if it is used as a suture material. The wire is easy to handle, strong and biocompatible, but it also has some drawbacks. In particular, martensitic NiTi wire shows kinking behaviour, which reduces repair speed and ultimately leads to fracture of suture during flexor tendon repair. The purpose of this study was to evaluate the material behaviour of 100 μm austenitic and martensitic NiTi wire, which is used in flexor tendon repair. Part of this study is reported in ref [6], which involves measurements of tensile, creep, bending and knotting properties. The main focus of this report is on measurements of torsional instabilities. The study attempted to find an evaluation method for kink formation in different suture materials. Commonly used suture material braided polyester (4-0 Ethibond®) was used as a control material.

Kink formation

The physical background of kink formation in wire relates to the phenomenon of torsional instability, which involves large displacements (see Figure 1). If the wire (rod) is compressed, it loses stability by buckling. The complete loop is gained when the one end of the wire reaches the other end. If the wire is twisted before giving slack, the loop forms earlier when a section of it flips into a loop. This depends on what value of tension is enough to keep the system in trivial

equilibrium. Snarling may occur after loop formation if more slack is given for the wire (see Figure 1c). Failure to properly remove the loop or snarl can result in permanent deformation, which is known as a kink. A more detailed description of the phenomenon can be found in the references [4] and [5].

Figures 1a, 1b and 1c. Formation of instability phenomenon in wire.

A different kind of criteria for loop forming is presented in [4]. If the wire is subjected under pure torsion, following equations (1)–(3) represents the criteria for loop forming. The first equation was derived by Ross, the second by Coyne and the final equation by Yabuta.

$$\frac{B}{L} = \frac{1}{2nN} \tag{1}$$

$$\frac{B}{L} = \frac{2}{\pi N\left(n - \frac{1}{2}\right)} \tag{2}$$

$$\frac{B}{L} = \frac{1}{n\sqrt{N}} \tag{3}$$

where L is the initial length of wires, n is the number of turns applied to the wire, and $N=GI_p/EI$ is the ratio between torsional GI_p and bending stiffness EI.

Measurements and results

The bending stiffness of the suture is measured and reported in the reference [6], and some of the results are shown in Table 1. The torsional stiffness of the suture was measured using a torsional pendulum [3]. Five different measurements were made for one sample material. The effect of the length of sample and the effect of the mass of weight was studied. Five periods were measured from the pendulum and the mean value and standard deviation was calculated. The equation for torsional stiffness of the suture is expressed in equation (4). Table 1 presents the results. The initiation of loop formation for each suture material can be estimated using criteria (1)–(3) (see Figure 2).

$$GI_p = \left(\frac{2\pi}{T}\right)^2 JL, \tag{4}$$

where T is periodic time, J is the moment of inertia and L is the length of the suture.

Table 1. Mean and standard deviation values for torsional and bending stiffness of sutures.

Suture material	GI_P [Nm^2]		EI [Nm^2]	
	Mean	Std	Mean	Std
Austenitic NiTi	7.93E-07	3.24E-08	3.29E-09	4.80E-10
Martensitic NiTi	1.39E-06	8.08E-08	1.13E-09	1.43E-09
4-0 Ethibond	1.79E-07	2.25E-08	2.27E-10	2.62E-10

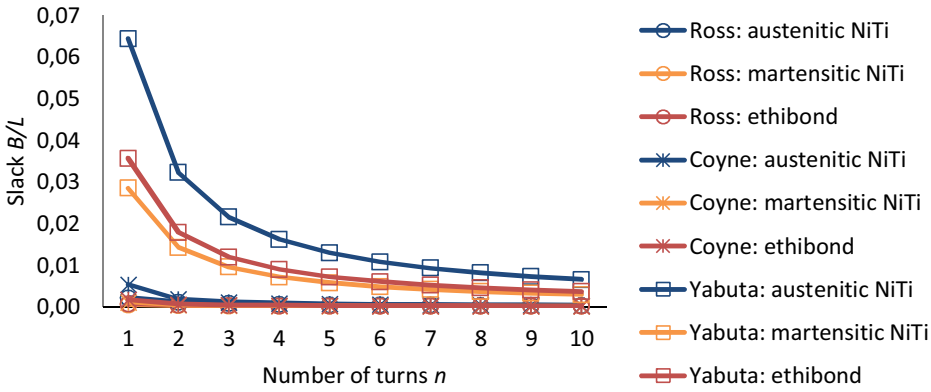

Figure 2. The loop formation of suture materials.

In the measurement of loop formation, the upper end of the suture was fastened to the tensile testing machine and the lower end of the suture was fastened to the drill chuck. The tensile test machine was used to ensure tensionless sample and to measure the slack of the sample. Twist was introduced to the suture by turning the chuck one revolution steps (n). In every turn, the slack needed to induce the loop was measured. If the equilibrium state of the sample snapped to another one, the slack (B/L) was measured. The measurements were made using three different lengths of the sample: 70, 100 and 155 mm. The austenitic and matensitic NiTi sutures were turned 1–5 revolutions clockwise and counter-clockwise. The Ethibond suture was turned 3–10 revolutions respectively. Figure 3 shows the results for different suture materials.

Discussion

According to Figure 3, austenitic NiTi suture resists loop formation at the beginning more than martensitic NiTi in a small number of turns. When the number of turns increased, the results of austenitic NiTi collapsed to the level of martensitic NiTi and it started to snarl. The formation of the loops in the martensitic NiTi required the smallest amount of slack and those loops easily caused kinks. The biggest difference between NiTi sutures and the control material was that clear loop formation started after one turn in NiTi sutures, but four turns were required with

Ethibond. When the length of sample was increased, more turns were needed before there was a clear formation of the loop.

The criteria did not predict the phenomenon accurately because all of the used criteria clearly over-estimated the loop formation. Yabuta's criterion yielded the best results, although the results of criterion differed by at least one decade compared to the measurements. So, the estimation method for the loop and kink formation of different suture materials has not yet been found.

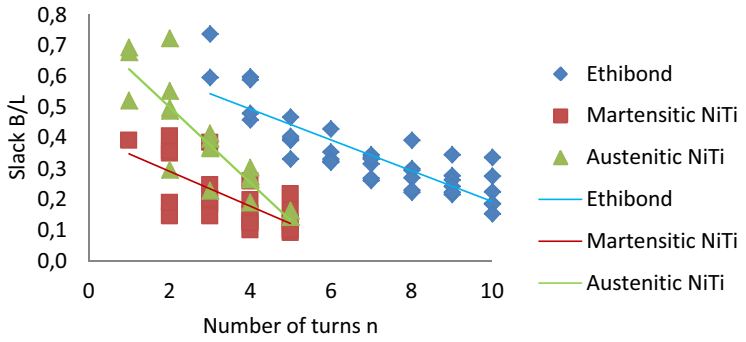

Figure 3. The loop formation of suture materials.

References

[1] T. Karjalainen, H. Göransson, A. Viinikainen, T. Jämsä, J. Ryhänen, Nickel-titanium wire as a flexor tendon suture material: An ex vivo study. *Journal of Hand Surgery: European Volume*, 35(6):469–474, 2010.

[2] T. Karjalainen, M. He, A.K.S. Chong, A.Y.T. Lim, J. Ryhanen, Nickel-Titanium Wire in Circumferential Suture of a Flexor Tendon Repair: A Comparison to Polypropylene. *Journal of Hand Surgery*, 35(7):1160–1164, 2010.

[3] S.J. Deteresa, S.R. Allen, R.J. Farris, R.S. Porter, Compressive and torsional behavior of Kevlar 49 fibre. *Journal of Materials Science,* 19:57–72, 1984.

[4] V.G.A Goss, G.H.M. van der Heijden, J.M.T. Thompson, S. Neukirch, Experiments on Snap Buckling, Hysteresis and Loop Formation in Twisted Rods, *Experimental Mechanics,* 45(2):101–111, 2005.

[5] N.S. Ermolaeva, J. Regelink, M.P.M. Krutzen, Hockling behavior of single- and multiple-rope systems, *Engineering Failure Analysis*, 15:142–153, 2008.

[6] T. Karjalainen, S. Kujala, A. Vuotikka, J. Näpänkangas, T. Jämsä, J. Ryhänen, The Material And Knotting Properties Of Martensite and Superelastic Nitinol Wires, *to be published.*

Proceedings of the 24th Nordic Seminar on Computational Mechanics
J. Freund and R. Kouhia (Eds.)

Crack propagation in rails under RCF loading conditions based on material forces

Jim Brouzoulis[1] and Magnus Ekh[1]

[(1)]Chalmers University of Technology, 412 96 Gothenburg Sweden, jim.brouzoulis@chalmers.se

Summary. In this paper, numerical simulations of crack growth in rails are presented. More specifically, this paper focus on short surface (head-check like) cracks that are often observed at the rail gauge corner. A fatigue propagation law expressed in terms of a crack driving force, derived from the concept of material forces, is presented. This model has been used for parametric studies of crack propagation, investigating key parameters such as loading and crack geometry. The results obtained together with additional investigations suggest that anisotropic effects should be included in order to simulate head-check growth in rails more accurately.

Key words: Material forces, RCF, crack propagation, head checks

Introduction

Rolling Contact Fatigue (RCF) of rails and wheels is a major problem in the railway industry worldwide. More specifically, RCF is currently one of the largest factors affecting the maintainability and operational safety of the track [1]. Furthermore, maintenance associated with rail deterioration (inspections, repairs, grinding) are very costly and time consuming for infrastructure holders [2]. Having accurate and efficient tools for life prediction of rails is, therefore, a pre-requisite for optimizing maintenance and (re)investments and also for modifying operational conditions to decrease deterioration and costs.

RCF damage observable in rails include several defects such as *tounge lipping*, *head checks*, *squats*, *pitting* and *spalling*, see for example [2] for an overview. Although there are many different kinds of rail defects, the studies in this paper are limited to head check-like cracks and in particular the numerical simulation of their growth.

In this paper a 2D crack propagation model is formulated in terms of a *crack driving force* based on the concept of material forces [3]. Based on the propagation law, the growth of a single head check-like crack in a piece of rail, under realistic RCF loading conditions, is simulated by using a 2D FE model. Results from parametric studies, varying parameters such as initial crack angle, initial crack length and surface friction, are presented and qualitatively compared to field observations.

Fatigue crack propagation

The choice of crack driving force $\boldsymbol{\mathcal{G}}$, adopted in this study, which holds for hyper-elasticity, can be expressed as, cf. [4]

$$\boldsymbol{\mathcal{G}} = \int_{\Omega_{\mathrm{X}}} -\boldsymbol{\Sigma} \cdot (W \, \boldsymbol{\nabla}_{\mathrm{X}}) \, \mathrm{d}\Omega_{\mathrm{X}} \tag{1}$$

with the so-called Eshelby stress tensor $\boldsymbol{\Sigma}$. Moreover, W is a suitably chosen weight function of unit value at the crack tip and $\boldsymbol{\nabla}_{\mathrm{X}}$ is the material gradient operator.

Based on the crack driving force introduced above, an example of a rate independent propagation law is formulated in the time domain as

$$\frac{\mathrm{d}\,\boldsymbol{a}}{\mathrm{d}t} = \dot{\boldsymbol{a}} = \gamma\langle\dot{\Phi}\rangle\boldsymbol{e}^* \tag{2}$$

where $\boldsymbol{a}$ is the crack tip position, γ is a material parameter, Φ is a crack-driving potential and $\langle\bullet\rangle = \frac{1}{2}(\bullet + |\bullet|)$ is the *MacCauley bracket*. Continuing, the potential Φ is assumed as follows

$$\Phi = \langle\boldsymbol{\mathcal{G}}\cdot\boldsymbol{e}^* - \mathcal{G}_{\mathrm{th}}\rangle \tag{3}$$

where $\boldsymbol{e}^*$ is the unit direction defined through

$$\boldsymbol{e}^* = \arg\max_{\boldsymbol{e}} \lim_{\epsilon\to 0} \boldsymbol{\mathcal{G}}(\boldsymbol{a}+\epsilon\boldsymbol{e})\cdot\boldsymbol{e} \tag{4}$$

In addition, $\mathcal{G}_{\mathrm{th}}$ is a fracture threshold similar to the threshold value K_{th} used in propagation laws of Paris' type.

Based on eq. (2), a fatigue crack propagation algorithm may be devised. Consider a load cycle defined over the time interval $I^N = [T^N, T^{N+1}]$; the average crack growth per cycle may be expressed as

$$\frac{\mathrm{d}\,\boldsymbol{a}}{\mathrm{d}N} = \frac{1}{|I^N|}\int_{I^N}\dot{\boldsymbol{a}}\mathrm{d}t \tag{5}$$

By (numerically) evaluating this propagation rate (in the cycle domain) the crack growth over a large number of cycles may then be determined by linear extrapolation.

Numerical examples

In order to study some characteristics of head check crack growth, in a piece of rail material subjected to a moving load, a simplified problem is investigated (see Figure 1). The normal load $p_{\mathrm{N}}(x,t)$ is assumed to be given by an elastic Hertzian contact pressure distribution with a contact width d, see for example [5] for details. Moreover, the traction stress $p_{\mathrm{T}}(x,t)$ is obtained from the normal pressure p_{N} and the coefficient of friction μ by assuming full slip between wheel and rail, i.e $p_{\mathrm{T}} = \mu p_{\mathrm{N}}$. The traction stress p_{T} is here chosen to act in the direction opposite to the velocity of the wheel indicating acceleration. Moreover, for the numerical investigations presented, the material is assumed to be linear elastic and in a state of plane strain.

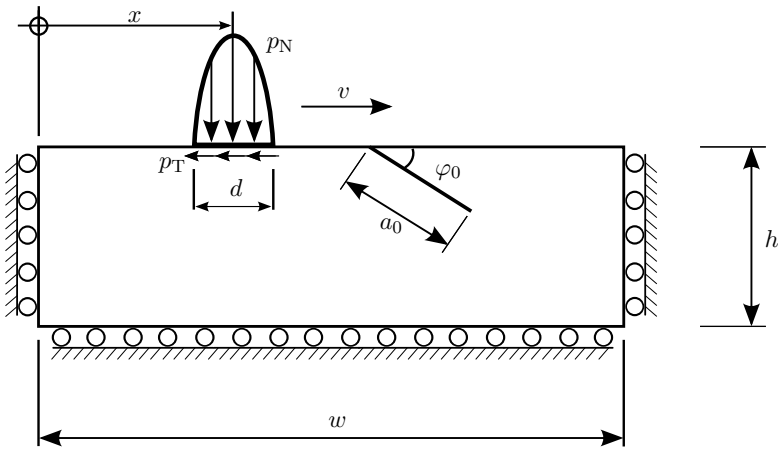

Figure 1: Problem geometry and boundary conditions.

Several parametric studies of crack growth have been carried out; however, only one set of results will be presented here. In Figure 2, simulated crack paths can be seen where the initial crack angle φ_0 have been altered. From the figure it is observed that all shallow cracks $(15° - 30°)$ propagate toward the surface while the deeper cracks curve downwards. Furthermore, a transition zone is observed somewhere between 30° and 40° indicating that crack growth in this region will be highly sensitive to perturbations.

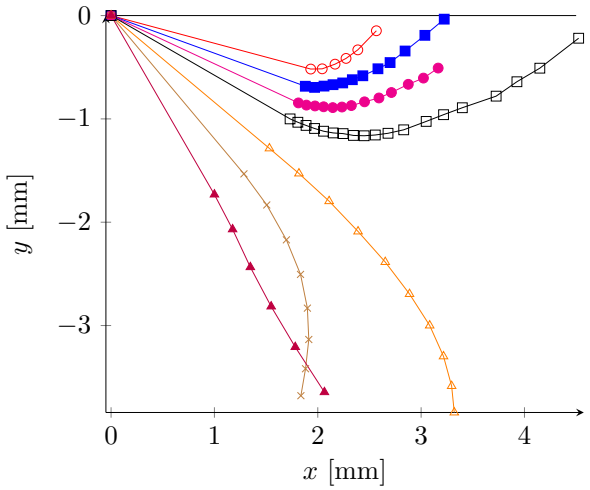

Figure 2: Crack paths for different initial angles $\varphi_0 = [15°, 20°, 25°, 30°, 40°, 50°, 60°])$ for $\mu = 0.45$ and $a_0 = 2\text{mm}$.

References

[1] G. N. Haidemenopoulos, A. D. Zervaki, P. Terezakis, J. Tzanis, A. E. Giannakopoulos, M. K. Kotouzas, Investigation of rolling contact fatigue cracks in a grade 900a rail steel of a metro track, Fatigue & Fracture of Engineering Materials & Structures 29 (11) (2006) 887–900.

[2] R. Lewis, U. Olsson (Eds.), Wheel-rail interface handbook, Woodhead Publishing Limited and CRC Press LLC, 2009.

[3] G. A. Maugin, Material forces: Concepts and applications, Appl. Mech. Rev. 48 (5) (1995) 213–245.

[4] R. Denzer, F. J. Barth, P. Steinmann, Studies in elastic fracture mechanics based on the material force method, International Journal for Numerical Methods in Engineering 58 (12) (2003) 1817–1835.

[5] K. Johnson, Contact Mechanics, Cambridge University Press, Cambridge, 2003.

Rakenteiden Mekaniikka (Journal of Structural Mechanics)
Vol. 44, No 3, 2011, pp. 243-259

Simulation of frictional effects in models for calculation of the equilibrium state of flexible pipe armouring wires in compression and bending

Niels Højen Østergaard, Anders Lyckegaard and Jens H. Andreasen

Summary. The motivation for the work presented in this paper is a specific failure mode known as lateral wire buckling occurring in the tensile armour layers of unbounded flexible pipes. Such structures are steel-polymer composites with a wide range of applications in the offshore industry. The tensile armour layers are usually constituted by two layers of oppositely wound steel wires. These may become laterally unstable when a flexible pipe is exposed to repeated bending cycles and longitudinal compression. In order to model the mechanical behavior of the armouring wires within the pipe wall, a formulation based on the equilibrium of a curved beam embedded in an initially cylindrical surface bent into a toriod is applied. In the present work, the response of a single armouring wire subjected to compression and cyclic bending will be studied, in order to detect lateral buckling of the wire. Frictional effects are included as distributed tangential and transverse loads based on a simple regularized Coulomb model.

Key words: curved beam equilibrium, wire mechanics, friction, flexible pipes, lateral buckling of armour wires

Niels Højen Østergaard, Anders Lyckegaard
NKT-Flexibles / Aalborg University, Department of Mechanical and Production Engineering
Priorparken 480, DK-2605 Broendby
Niels.HojenOstergaard@nktflexibles.com, Anders.Lyckegaard@nktflexibles.com

Jens H. Andreasen
Department of Mechanical and Production Engineering, Aalborg University
Pontoppidanstræde 103, DK-9000 Aalborg
jha@m-tech.aau.dk

Rakenteiden Mekaniikka (Journal of Structural Mechanics)
Vol. 44, No 3, 2011, pp. 206-217

Virtual testing of cold-formed structural members

Petr Hradil, Ludovic Fülöp and Asko Talja

Summary. This paper introduces new modelling and evaluation algorithms for automated virtual testing of cold-formed structural members. These algorithms are integrated in Abaqus CAE plugin and verified against real tests of stainless steel hollow sections. Our tool is capable of creating finite element models including complex material behaviour, residual stresses and strains, enhanced material properties and geometrical imperfections. Also, it automatically evaluates the load carrying capacity of such models and creates test reports. The algorithms presented here can successfully assist engineers and researchers during the numerical analysis.

Key words: virtual testing, Abaqus, cold-formed steel, thin-walled structures, stainless

Petr Hradil, Ludovic Fülöp and Asko Talja
VTT, Technical Research Centre of Finland
Kemistintie 3, PL 1000 02044 VTT, Finland
petr.hradil@vtt.fi

Proceedings of the 24th Nordic Seminar on Computational Mechanics
J. Freund and R. Kouhia (Eds.)

Models of multilayered shells in ophthalmology

S. M. Bauer and L. A. Karamshina

Department of theoretical and applied mechanics
St. Petersburg State University Russia, 198504, St. Petersburg, University avenue 28
s_bauer@mail.ru, l_karamshina@mail.ru

Summary.It is known that human eye has complex structure which includes many multilayered elements such as cornea, sclera and lamina cribrosa (LC). In this regard, three problems concerning the deformation of multilayered shells in ophthalmology are considered. In the first problem the stress-strain state of lamina cribsosa of the optic nerve is regarded. In the second problem the stress-strain state of a three-layered outer shell of the eye is considered. In the third problem the effect of cornea multilayer structure on measurements of intraocular pressure (IOP) by Goldman's and Maklakov'sapplanationtonometers is analyzed.

Key words: multilayered shells, FEM, intraocular pressure.

The stress-strain state of lami na cribsosa of the optic nerve

It is known that under glaucoma the visual field changes due to atrophy of the visual – nerve fibres, which are deformed just at the level of lamina cribrosa[1].

According to ophthalmologic data [2], LC consists of a few parallel layers of connective tissue containing elastic fibers. In [3,4] it was suggested that perhaps essential shear of the layers could cause the atrophy of the visual nerve fibres. In paper [5] it was revealed that when intraocular pressure increases "inflection point" appears. In order to detect the "point of inflexion" (Fig. 1) – the point, in which derivative of normal flexure with respect to radial coordinate attains its maximum value, the LC is modeled as multilayer shell of revolution with elastic ties between the layers.

The complete system of 5n+2 differential equations is obtained. The boundary problem is solved numerically for shells with two and three layers with different values of the elastic parameters taking into account that the "outer" layer is the thickest one.

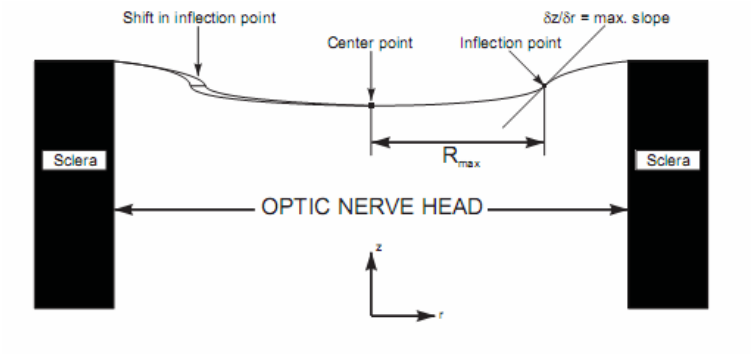

Figure 1.The scheme of LC from data [5].

The numerical solution of the problem for different values of elastic parameters revealed that the essential shear of the layers occurs at the periphery of the LC. And the largest shear occurs at the level of the last layer, as it was observed by ophthalmologists. This phenomenon may lead to the atrophy of the optic nerve fibres.

The results of calculation for the proposed moment model provided deflection mode that well agrees with clinical data [5].

The stress-strain state of a three-layered outer shell of the eye

It is known that outer shell of the eye has multilayered structure and consists of a thick fibrous shell - the sclera, the middle shell - choroid, and the very thin and soft inner shell - the retina [6].

There are experimental data that the elastic properties of these shells are very different. Moreover, choroid refers to the “active” structures of the eye [7]: its size and stiffness varies deeply depending on blood filling, therefore it can change its biomechanical properties during the day.

In order to estimate the influence of these factors on the possible development ofchoroidal and retinal detachments the problem of stress-strain state of a three-layered spherical shell under normal pressure in view of various thicknesses and elastic properties of its layers is considered.

According to experimental data [6] sclera and cornea can be considered as transversally-isotropic shells. In this regard, the antecedent problem for two-layered spherical shell consisting of two transversely-isotropic layers of different thickness and biomechanical properties under normal intraocular pressure is considered. Both problems are solved using the three-dimensional theory of elasticity. Analysis of the stress-strain state of the eye is carried out with the possibility of the choroid to change it biomechanical properties.

The comparison of the obtained results for the shell, consisting of three layers with different elastic properties, with the results obtained for one-layered shell with average elastic properties showed a significant change in the stress-strain state of the eye.

Results obtained for multi-layered shell with different elastic properties reveled appearance of kinks on the graphs for the displacement and normal stresses and discontinuities on the

graphs for tangential stresses at the points corresponding to the boundaries of conjugation of the shells.

With an increase of intraocular pressure an increase of kinks on the graphs for the displacements and normal stresses and discontinuities on the graphs for the tangential stresses is observed. Thus effects may lead to internal detachments of the softer layers of the eye shell - the sclera and choroid under increased intraocular pressure.

Variation of elastic coefficients of choroidal shell most affects on displacements of the layers. At lower values of Young's modulus of the choroid larger displacements and stronger thinning of the choroid and retina is observed. Strong thinning of tissues can also lead to their detachments and tears.

The effect of cornea multilayer structure on measurements of intraocular pressure (IOP) by Goldman's and Maclakov'sapplanationtonometers

In the cornea are five basic layers, which vary in thickness as well as in its structure and, consequently, have different biomechanical and elastic properties [6]. Therefore in ANSYS Mechanical software the corneoscleral eye shell is modeled as conjectured spherical transversally-isotropic shells with different diameters and elastic properties, therewith, the cornea splits into fourspherical layers with elastic properties. The modulus of elasticity in the thickness direction of both shells is assumed to be much smaller than the modulus of elasticity in the tangential direction.

Axisymmetricnonlinear calculations for various values of elastic modulus of cornea and sclera under constant real intraocular pressure were carried out. For each series of calculation was carried out comparison of results obtained for multilayered shell and one-layered shell with average elastic modulus.

It was shown that as the cornea on 90 % consists of stroma the elastic properties of cornea in the normal and tangential directions generally defines by elastic properties of stroma. The contribution of the stiff layers (Boumen's and Descemet's membrane) in the average value of the elastic properties of the whole cornea appears unessential. The calculations showed that the stiffnesses of these shells affect the distribution of the contact stresses and dimensions of the contact surfaces.

The comparison of the obtained results with the use of Maclakov method (weight 10 g) for multilayered cornea with the results obtained for one-layered shell with average elastic properties reveled that contact area in the first case is bigger than in the second case, hence the value of the tonometric pressure is lower. The Goldman's method revealed the similar results. In that case the contact area has the constant value 3.06 mm, but the value of the applied force in the case of multilayered shell is smaller than in the case of one-layered shell with average elastic properties, hence the value of the tonometric pressure is lower. Therefore, when we take into account heterogeneity of the elastic properties of the cornea layers we get more precise estimations for tonometric and real intraocular pressure.

The results, carried out with account of multilayered structure of cornea revealed that the smaller contact area the greater part of strain goes to bending deformation.

The modeling with the use of Maclakov method, especially for plummet weight 10 g, the essential increase of the contact area and influence of sclera on process of deformation was revealed. Sense the area contact in Goldman's method equals to 3.06 mm while the use of Maclakov's method gives the bigger areas under average intraocular pressures (from 10 to 30 mm Hg), hence data for intraocular pressure obtained during measurements carried out by Goldman's tonometers occurs more sensitive to changes of the cornea thickness, then data obtained by Maclakov's tonometer. Moreover, the influence of the cornea thickness on data of

IOP obtained by Maclakov's tonometer with plummet with the weight 5 g higher, then data obtained by plummet with the weight 10 g, which is in good agreement with the experimental data[8].

References

[1]. Volkov V.V., Suchinina L.B., Ustinova E.I. *Glaucoma, preglaucoma and ophthalmogipertenzija*, L., Medicine, 1985.

[2]. A.G. Nesterov, *Glaucomatous optic atrophy. Actual Problems of Ophthalmology,*Moscow, Medicine, 1981.

[3]. J.D. Emery, *The lamina cribrosa in normal and glaucomatous human eyes*, Trans. Ac. Amer. Ophtalmol. 78 (2), 1974.

[4]. A. Lindsey, *Aetiology of field loss in chronic glaucoma*, Canadian J. Ophtalmology, № 6, 1971.

[5].D.B Yan, *Study of regional deformation of the optic verve head using scanning lazer tomography*, Current Eye Research, Vol. 17, 1998.

[6]. E.N. Iomdina, *Mechanical propertiesof tissuesof the human eye*, Modern Problemsof Biomechanics, Moscow State University, 2006.

[7]. M.V. Polos, E.N. Iomdina, *Activedeformationof the human eye*,Biomechanics,XAll-Russian Conferenceabstracts,University of Saratov Press, 2010.

[8]. E.P. Tarutta, V.P. Erichev, T.Yu. Larina, *Controlling intraocular pressure after keratorefractive operations*, Moscow, Ocular biomechanics,2004.

Proceedings of the 24th Nordic Seminar on Computational Mechanics
J. Freund and R. Kouhia (Eds.)

Testing and analysis of adhesively bonded single lap joints at sub-zero temperatures - a master thesis

Marit Liaaen Haslerud[1], Rune H. Gaarder[2], Frode Grytten[2], and Harald Osnes[1]

(1)University of Oslo, Department of Mathematics, P.O.Box 1053, Blindern, NO-0316 Oslo, Norway, maritlha@student.matnat.uio.no, osnes@math.uio.no
(2)SINTEF, Pb. 124 Blindern, NO-0314 Oslo, Norway,
rune.h.gaarder@sintef.no, frode.grytten@sintef.no

Summary. A two component toughened epoxy adhesive was subjected to a series of mechanical tests in order to assess the tensile, shear and compressive properties at room-temperature as well as sub-zero temperatures. Extensive modeling of the Iosipescu shear test specimen was conducted with the LS DYNA finite element software to verify the material models on coupon level. Different measurement methods, e.g. strain gauges and digital image correlation, were used to obtain accurate strains in the initial linear elastic part of the stress-strain curve and in the yield range for all test temperatures. The established material model will be used to predict the failure load of single lap joints with both composite and aluminium adherends.

Key words: adhesive, mechanical testing, modeling

Introduction

The aim of this work is to test and analyse the behaviour of adhesively bonded single lap joints at low temperatures. The work is carried out within the project Arctic Materials of which the main goal is to establish *"criteria and solutions for safe and cost-effective application of materials for hydrocarbon exploration and production in arctic regions"* [1]. Composite materials have a high strength-to-weight ratio, excellent mechanical properties at sub-zero temperatures and a resistance to corrosion making them applicable for products and structures that are exposed to extreme environments [2, 3]. Adhesive bonding is an important joining method for composite materials, and because of complex stress states in combination with toughened epoxy adhesives, the joints are difficult to model. Therefore, extensive coupon testing is necessary to obtain mechanical properties of the neat adhesive. The adhesive chosen for this study was the general purpose, room temperature curing, two component epoxy adhesive DP410 from 3M.

Mechanical testing

Coupon

To obtain the mechanical properties necessary to develop a numerical model for the adhesive, tests in tension, shear and compression were performed according to the standards ASTM D638, ASTM D5379 (Iosipescu) and ASTM D695, respectively. All tests were performed at three different temperatures; $+23°C$, $-5°C$ and $-30°C$. The most extensive testing was performed on the Iosipescu shear specimens. First, tests were performed at $+23°C$ using a bi-axial strain gauge oriented at $\pm 45°$ to the loading axis to measure nomial shear strain. This provided excellent results up to a strain of approximately 10%, before the strain measurements became unreliable. Since the DP410 is a ductile material (at $+23°C$), with a large plastic range, an

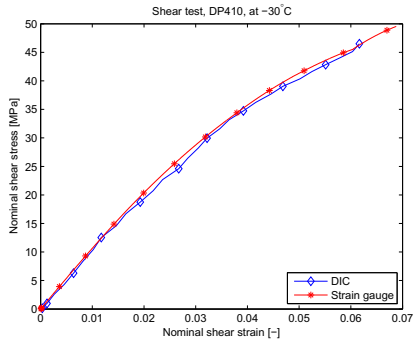

Figure 1. Nominal shear stress-strain for one specimen at $-30°C$, from DIC and strain gauge

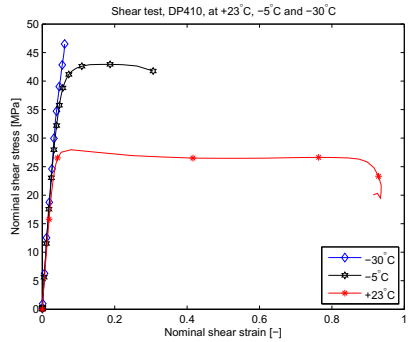

Figure 2. Shear stress-strain for $+23°C$,$-5°C$ and $-30°C$

optical non-contact measurement method, digital image correlation (DIC) was used to obtain strain measurements also for large deformations [4]. For the shear tests conducted at sub-zero temperatures DIC and strain gauge were used simultaneously on all the specimens, DIC at the specimen front side and strain gauge at the specimen back side. Results from the two measurement methods compared well at all temperatures, as with the stress-strain relation at $-30°C$ depicted in Figure 1. Figure 2 shows that the adhesive behaved markedly different for the three temperatures, changing from very ductile at room temperature to brittle at $-30°C$.

Single lap joints

Single lap joints were produced with quasi-isotropic glass fibre reinforced vinyl ester matrix composite adherends as well as aluminium adherends. The single lap specimens were produced from aluminium and composite sheets of dimensions 175 mm x 203 mm. Bondline thickness was 0.2 mm and spacers were used to control the thickness. To reduce eccentricity in the joints when testing, end tabs of the same thickness were adhered to the ends of the specimens. The overlap length used in this study was 12 mm. Specimens of 25 mm width was cut from the single lap sheets. Figure 3 shows the single lap joint, seen from the side. The joints will be tested according to ASTM D1002 - 10, and results compared to numerical simulations.

Figure 3. Single lap

Numerical analysis

Numerical simulations were performed using the finite element software LS-DYNA.

Coupon

First, a model of the Iosipescu shear test was developed using stress-strain results from the testing as input to the adhesive material model, *MAT_024 Piecewise-linear-plasticity. At this point, the simulation was only performed up to the level of applied displacement where fracture occured in the test, so no damage/failure criterion was necessary. The calculated strain distribution was in good agreement with the measurements from the DIC, see Figures 4 and 6

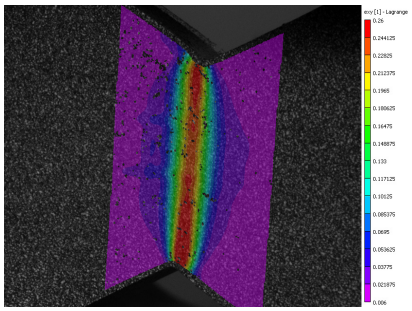

Figure 4. Shear strain distribution from DIC, when cracking initiates

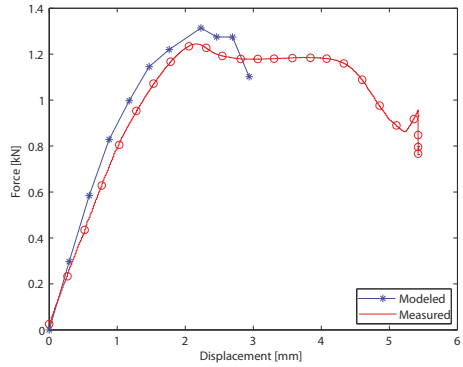

Figure 5. Force-displacement measured during testing and force-displacement output from LS-DYNA

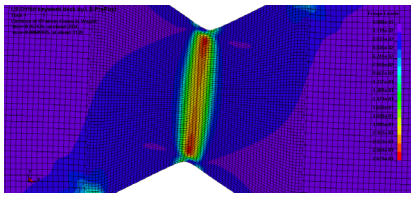

Figure 6. Shear strain distribution modeled in LS-DYNA

for shear strain distribution and Figure 5 for the force applied during testing and force output from LS-DYNA. Second, a failure/damage criterion had to be implemented in order to simulate the adhesive failure. A user-defined model was developed, using Voce hardening to describe the stress-strain relation, Eq. (1), and a Johnson-Cook damage model describing strain at fracture, Eq. (2):

$$\sigma = \sigma_0 + \sum_{i=1}^{2} \left(Q_i \left(1 - \exp^{-C_i \varepsilon^p} \right) \right) \tag{1}$$

$$\varepsilon_f = D_1 + D_2 \exp^{D_3 \sigma^*} \tag{2}$$

σ_0 is yield stress, ε^p is damage-equivalent plastic strain, Q_i, C_i, D_1, D_2 and D_3 are constants to be determined and σ^* is the stress triaxiality (hydrostatic pressure to von Mises stress ratio). Fracture strains from tension ($\sigma^* = \frac{1}{3}$), shear ($\sigma^* = 0$) and compression ($\sigma^* = -\frac{1}{3}$) tests were used to estimate the damage model constants.

This material model is still under development at the time of writing, but as can be seen when comparing the test results (Figure 7) with numerical simulations (Figure 8), the fracture process is initialized at the correct location.

Single lap joints

The material model developed for the adhesive will be used in simulations of single lap joints. Figure 3 shows the single lap joint as modeled in LS-DYNA. The modeling of the adhesive fillet (Figure 9) was based on microscopy investigation of the fillet geometry from the single lap joint specimens (Figure 10). Results from numerical prediction of the lap joint ultimate load as well as failure mode using the established material models will be compared to results from tensile tests of the single lap joints.

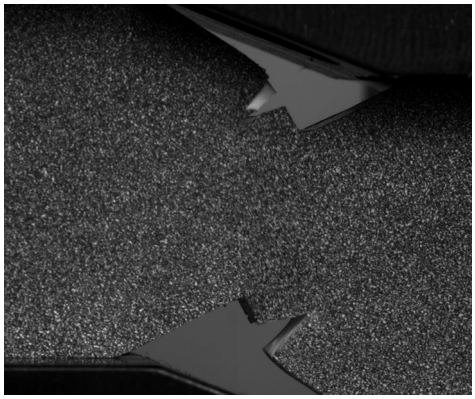

Figure 7. Iosipescu shear specimen after fracture has occured

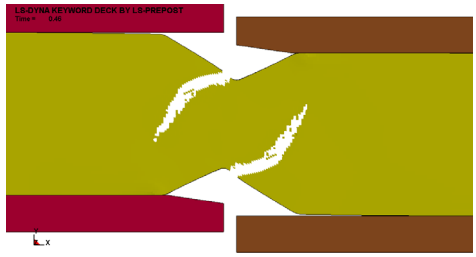

Figure 8. LS-DYNA simulation at crack initialization

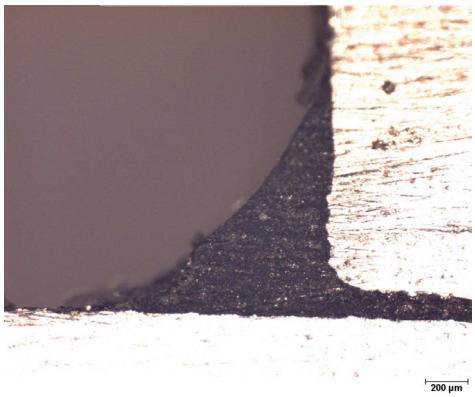

Figure 9. Microscope image of fillet from single lap joint with aluminium adherends

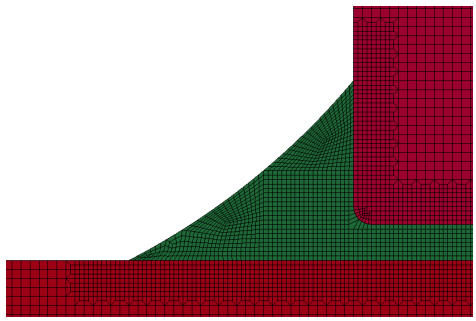

Figure 10. Fillet geometry in LS-DYNA

References

[1] http://www.sintef.se/upload/Materialer_kjemi/Anvendt%20mekanikk%20og%20korrosjon/bruddmekanikk/dokument/arctic_materials-web.pdf

[2] Bhagwan D. Agarwal, Lawrence J. Broutman and K. Chandrashekhara. *Analysis and Perfomance of Fiber Composites - 3rd edition.* John Wiley & Sons, Inc., Hoboken, New Jersey, 2006.

[3] J.B. Schultz. Properties of composite materials for cryogenic applications. *Cryogenics*, 38(1998) 3-12.

[4] M. Jerabek, Z. Major and R.W. Lang. Strain determination of polymeric materials using digital image correlation. *Polymer testing* 29(2010) 407-416.

Proceedings of the 24th Nordic Seminar on Computational Mechanics
J. Freund and R. Kouhia (Eds.)

Determination of the elastic fields of an elliptic nano-inhomogeneity in anti-plane couple stress elasticity using RKPM

Hossein M. Shodja[1], Saba T. Yaghoubi[2], and Bita Alemi[3]

(1)Department of Civil Engineering, Sharif University of Technology,
P. O. Box 11155-9313 Tehran, Iran, shodja@sharif.edu
(2)Department of Civil and Environmental Engineering, Aalto University,
P. O. Box 12100 00076 Aalto, Finland, saba.tahaei@aalto.fi
(3) Department of Civil Engineering, Sharif University of Technology,
International Campus, Kish Island, Iran, nina_al132@yahoo.com

Summary. Recently, Shodja et al. [1] presented reproducing kernel particle method (RKPM) with augmented corrected collocation method for treatment of material discontinuities in the context of traditional elasticity. The idea is extended to consider material discontinuities in the framework of couple stress elasticity in the present study. Subsequently, it is employed to calculate the elastic fields associated with a nano-sized elliptic inhomogeneity under a remote anti-plane applied stress field.

Key words: reproducing kernel particle method (RKPM), augmented corrected collocation method, couple stress theory, elliptic inhomogeneities.

Introduction

Consider an infinite isotropic body containing an isotropic elliptic cylindrical inhomogeneity subjected to far-field uniform anti-plane loading as shown in Fig. 1. The length of the cylinder is assumed to be infinitely extended parallel to the direction of the applied load, and the dimensions of its cross-section are in the order of a few nanometers. If the principle purpose of interest is the calculation of the elastic fields in the vicinity of a nano-size inhomogeneity the traditional theory of elasticity fails to provide an accurate solution. Moreover, it is incapable of making distinction between similar but different sizes of inhomogeneities. As a remedy it is proposed to formulate the problem in the framework of couple stress elasticity which makes the interpretation of the size effect possible. Although a few problems of couple stress elasticity are analytically solved by different authors ([2],[3],[4]), but most of the boundary value problems in the context of this theory are generally too complicated to be tackled analytically. Hence; numerical methods such as reproducing kernel particle method (RKPM) can be utilized in order to circumvent this difficulty.

Recently, Shodja et al. [1], developed RKPM with augmented corrected collocation method for treatment of material discontinuities in the context of traditional elasticity. Utilizing this simple and accurate technique, they analyzed a problem of crack-inhomogeneity interaction subjected to uniaxial tension. In this work, in the presence of couple stresses the above-mentioned method is employed in combination with the penalty method, in order to determine the elastic fields of elliptic and circular inhomogeneities subjected to remote anti-plane stress. Comparison of the numerical results to the analytical solution obtained by Haftbaradaran and Shodja [2], proves the accuracy and efficacy of the numerical method.

Numerical example

The elliptic inhomogeneity with semi-axes a_1 and a_2, shear modulus μ_1 and curvature modulus η_1 is considered. As illustrated in Fig.1, the inhomogeneity is surrounded by an infinite matrix with shear modulus μ_2 and curvature modulus η_2, and is subjected to far-field anti-plane loading, $\sigma_{13} = 1$ units. The numerical example is solved assuming $\mu_1/\mu_2 = 5$, $a_1 = 3$ nm, and $a_2 = 2$ nm. In Fig. 1 (ω, ξ) denotes the elliptic coordinates pair. Due to the symmetries, only one-quarter of the plate has been considered. For the interior of the inhomogeneity and its exterior matrix, 309 and 503 particles are used, respectively.

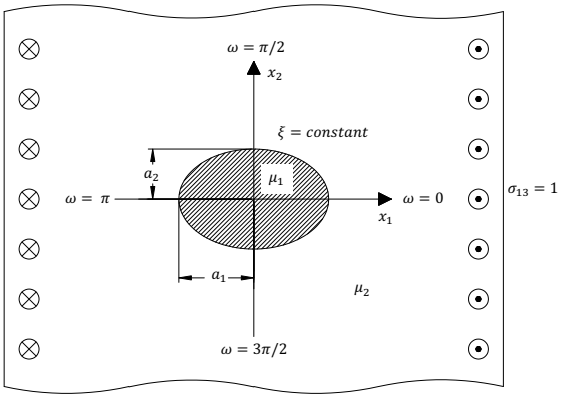

Figure 1. An elliptic inhomogeneity system subjected to far-field anti-plane loading.

The results obtained by utilization of augmented corrected collocation method are plotted and compared to the analytical solutions in Figs. 2 and 3. It can be seen that the results of the proposed numerical method are in reasonable agreement with the analytical solutions. In these figures, $\boldsymbol{\sigma}^{cl}$ represents the classical stress tensor, whereas $\boldsymbol{\sigma}^{s}$ denotes the symmetric part of the total stress tensor $\boldsymbol{\sigma}$ in the framework of couple stress elasticity.

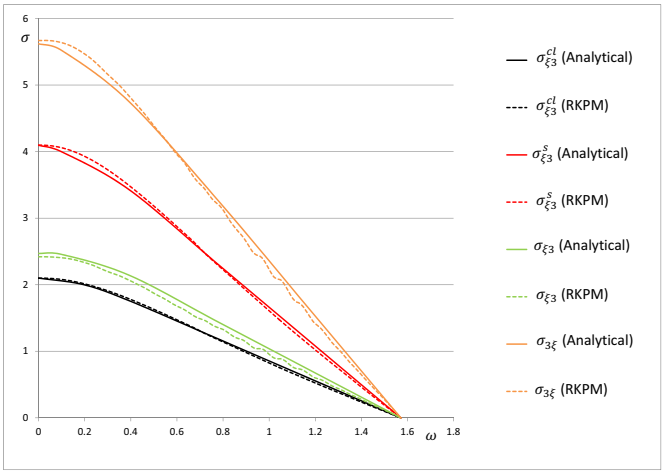

Figure 2. A comparison between RKPM and the analytical solutions; $\xi 3$ and 3ξ-components of stresses along the inhomogeneity-matrix interface, just inside the inhomogeneity.

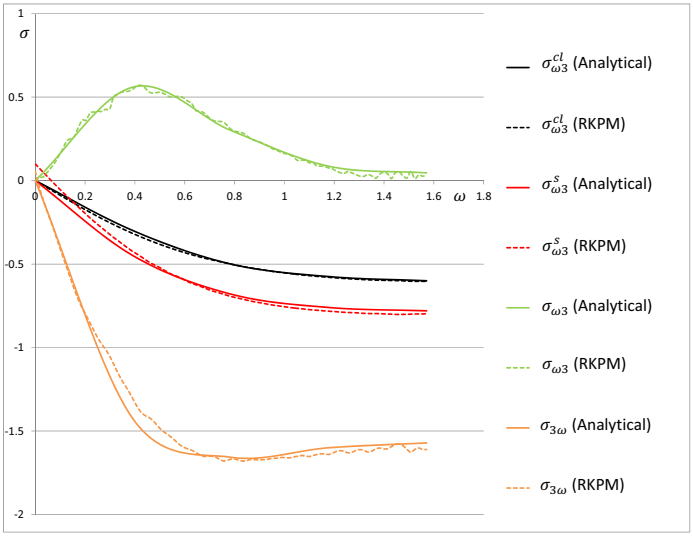

Figure 3. A comparison between RKPM and analytical solutions; $\omega 3$ and 3ω-components of stresses along the inhomogeneity-matrix interface, just outside the inhomogeneity.

References

[1] H.M. Shodja, M. Khezri, A. Hashemian, and A. Behzadan. RKPM with augmented corrected collocation method for treatment of material discontinuities. *CMES: Computer Modeling in Engineering and Sciences*, 62:171-204, 2010.

[2] H. Haftbaradaran, H.M. Shodja. Elliptic inhomogeneities and inclusions in anti-plane couple stress elasticity with application to nano-composites. *International Journal of Solids and Structures*, 46:2978-2987, 2009.

[3] V.A. Lubarda. Circular inclusions in anti-plane strain couple stress elasticity. *International Journal of Solids and Structures*, 40:3827-3851, 2003.

[4] R.D. Mindlin. Influence of couple-stresses on stress concentrations. *Experimental Mechanics*, 3:1-7, 1962.

Proceedings of the 24th Nordic Seminar on Computational Mechanics
J. Freund and R. Kouhia (Eds.)

Atomistic modeling of Phase transformation in ZnO nanorods

J. Y. He, S. Nagao, J. Y. Wu, Z. L. Zhang

NTNU Nanomechanical Lab, Department of Structural Engineering, Norwegian University of Science and Technology (NTNU), 7491, Trondheim, Norway.
jianying.he@ntnu.no, shijo.nagao@ntnu.no, jianyang.wu@ntnu.no, zhiliang.zhang@ntnu.no

Summary. Molecular dynamic simulations are performed to systematically investigate the structural□mechanical properties of ZnO nanorods (NRs) using the empirical Buckingham potential. The considered NRs have hexagonal cross-sections with lateral dimension ranging from 1-10nm and constant length 10.4nm. Different from its bulky counterpart, the results show that ZnO NRs undergo a size dependent four-stage deformation process: elastic stretching of initial Wurtzite structure, Wurtzite to body-centered tetragonal (BCT-4) phase transformation, stretching of the resulting BCT-4 structure and eventually brittle fracture. The critical stress for phase transformation decreases while the critical strain increases with increasing the NR size. The analyses indicate that the size dependency of phase transformation is dominated by the size effect on the Young's modulus.

Key words: ZnO Nanorods, molecular dynamic simulations, phase transformation, Young's modulus, fracture.

Introduction

Quasi-one-dimensional nanostructures made of semiconductors possess large potential applications in electromechanical devices because of the unique electrical and mechanical properties associated with their finite size [1]. In particular, ZnO nanostructures, such as nanorods (NRs), nanowires and nanobelts have received great attention due to their excellent performance in electronic, piezoelectric, ferroelectric and optical applications [2]. The mechanical, optical and electric as well as piezoelectric properties of ZnO have been experimentally investigated. However, experimental evaluation of mechanical properties at the nano-scale is full of challenges and uncertainties due to crystalline structure, sample manipulation, geometry condition, instrument calibration, and so on [3]. Instead, atomistic simulations provide an alternative way to predict the structural□mechanical properties of ZnO nanostructures [4]. While it is not observed in experimental study, a novel transformation from original Wurtzite to body-centered tetragonal (BCT-4) phase has been numerically discovered on ZnO NRs under tension along with <0001> axial orientation [4]. To clarify those

controversial results between experiments and simulations, molecular dynamics (MD) simulations using LAMMPS (Large-Scale Atomic/Molecular Massively Parallel Simulator) code are performed in this study to investigate the mechanical properties of ZnO NRs. In addition to the elastic property, the size-dependent phase transformation as well as the fracture behaviour of ZnO NRs under uniaxial tension is examined.

MD methods

Wurtzite ZnO NRs oriented in <0001> with hexagonal cross-sections were generated with the lattice constant a = 3.2501Å, c = 5.2071Å, and internal parameter u = 0.3817 [5]. The lateral dimension D of the NRs varied from 1.0, 1.8, 2.4, 3.0, and 5.0 to 10nm, while the length L was constant 10.4nm. Empirical Buckingham potential (equation (1)) with Binks parameters (Table 1) was adopted to describe the short-range atomic interactions [6]. As for the long-range Coulombic force, Ewald summation method was used.

$$E_{total}(r_{ij}) = \sum_{i=1}^{N} \sum_{j \neq i} A \exp(-\frac{r_{ij}}{\rho}) - \frac{C}{r_{ij}^6} + E_{long}(r_{ij}) \quad (1)$$

Periodicity required for Ewald summation were imposed on three directions for accurate Coulombic force calculation, therefore a sufficiently large gap along lateral directions was given to avoid interactions between neighbouring NRs. After geometric construction, an annealing process with an integration time step of 1 fs was performed to relax the NRs under the ambient pressure (*NPT*) in <0001> direction to stabilize the ZnO NRs. The uniaxial tensile strain with strain rate of 0.001/ps was applied to the NRs by extending the length along the tension direction to 30% strain, under *NVT* conditions at 5K.

Table 1. Short-range interaction parameters for ZnO.

Species		A, eV	ρ, Å	C, eV Å
O^{2-}	O^{2-}	9547.96	0.21916	32.00
Zn^{2+}	O^{2-}	529.70	0.3581	0.00
Zn^{2+}	Zn^{2+}	0.00	0.00	0.00

Results and discussions

The stress–strain relationships for different sizes of ZnO NRs are compared in figure 1. The results suggest that the deformation process of ZnO NRs consists of four stages: elastic stretching represented by the initial linear region, a phase transformation indicated by the stress relaxation, stretching of the new phase structure, and eventual fracture by the secondary stress relaxation. The mechanical response of ZnO NRs is significantly size dependent during the entire deformation process. In an effort to clarify the size effect, the Young's modulus and the critical stress/strain for phase transformation are summarized as a function of the NR size in figure 2. The Young's modulus was obtained from the slope of the initial elastic region on stress–strain curves. Critical stress and strain for phase transformation were directly read the corresponding values at the starting points of the first stress relaxation.

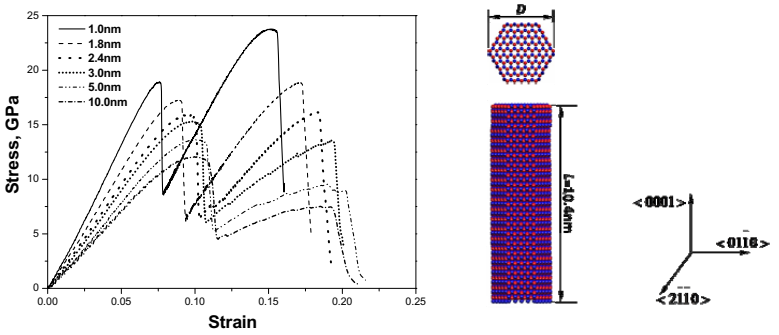

Figure 1. Stress□strain curves for sizes ranging from 1.0 to 10.0nm.

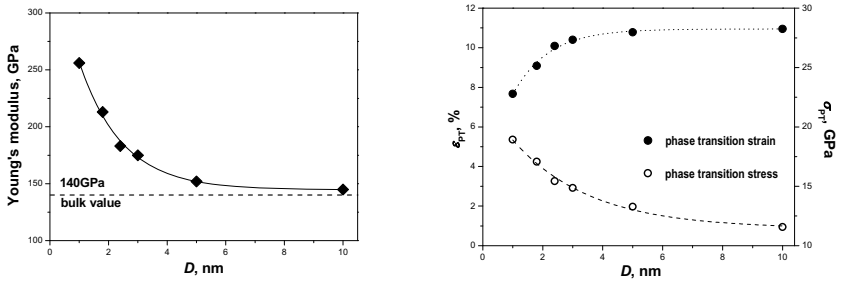

(a) (b)

Figure 2. Size-dependent mechanical properties of ZnO NRs: (a) Young's modulus and (b) critical strain and stress for phase transformation.

The Young's modulus of NRs within the sampling size is always higher than that of the bulk counterpart. With increasing the size from 1.0 to 10.0nm, the Young's modulus decreases from about 260GPa to 145GPa which approaches the bulk value. Within the size range from 1.0 to 10.0nm, the critical stress for phase transformation decreases about 40% while the strain increases 43%. Both critical stress and critical strain referred to different sizes of the NRs converge to a constant value when the size is sufficiently large.

During the uniaxial tension, the system temperature is kept constant 5K at which atomic vibrations are well suppressed so that the thermal effect on the ductility is minimized. All ZnO NRs display brittle fracture at a relatively high strain over 15%, as shown in figure 3. Comparing with the previous study, this cleavage fracture at high strain is unique for the hexagonal cross-sectional NRs, distinguished from the cylindrical NRs that exhibit super ductility [7], and also from the square cross-sectional NRs that display lower fracture strain around 6% [8]. The main reason is that the cylindrical and square cross-sectional NRs cannot keep close-packed hexagonal (HCP) lattice structure in wurtzite ZnO during equilibrium and are distorted to a twisted configuration and even an amorphous structure. Therefore the initial structure prior to deformation is not perfect Wurtzite.

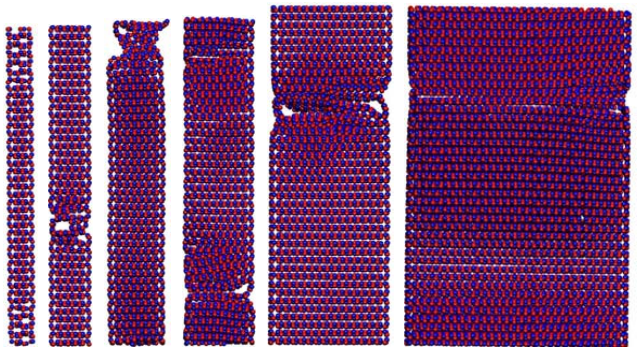

Figure 3. The fracture morphology of ZnO NWs with the size from 1.0 to 10.0nm.

Conclusions

Large-scale molecular dynamic simulation has been carried out to investigate the size-dependent mechanical properties of ZnO NRs. Under uniaxial tension, ZnO NRs possess a four-stage deformation process. In addition to the size-dependent Young's modulus reported by previous studies, the phase transformation is also influenced by the size of NRs. The critical stress for phase transformation drastically increases while the critical strain decreases as the NR size decreases. It suggests that larger NRs attempt to keep the original Wurtzite structure comparing with smaller ones.

References

[1] J. G. Lu, P. Chang, and Z. Fan, Quasi-one-dimensional metal oxide materials-Synthesis, properties and applications, *Materials Science and Engineering R*, 52(1-3):49-91, 2006.

[2] Z. L. Wang, ZnO nanowires and nanobelts platform for nanotechnology, *Materials Science and Engineering R*, 64(3-4):33-71, 2009.

[3] C. Q. Chen, Y. Shi, Y. S. Zhang, J. Zhu, and Y. J. Yan, Size dependence of Young's modulus in ZnO nanowires, *Physical Review Letters*, 96(7):075505, 2006.

[4] R. Agrawal, B. Peng, and H. D. Espinosa, Experimental-computational investigation of ZnO nanowires strength and fracture, *Nano Letters*, 9(12):4177-4183, 2009.

[5] E. H. Kisi, and M. M. Elcombe, *u* parameters for the Wurtzite structure of ZnS and ZnO using powder neutron diffraction, *Acta Crystallographica*, 45:1867-1870, 1989.

[6] D. J. Binks, *Computational modeling of zinc oxide and related oxide ceramics*, PhD thesis, University of Surrey, Harwell, 1994.

[7] A. J. Kulkarni, M. Zhou, and F. J. Ke, Orientation and size dependence of the elastic properties of zinc oxide nanobelts, *Nanotechnology*, 16(12):2749-2756, 2005.

[8] L. Dai, W. C. C. Cheong, C. H. Sow, C. T. Lim, and V. B. C. Tan, Molecular dynamics simulation of ZnO nanowires: size effect, defects and super ductility, *Langmuir*, 26(2):1165-1171, 2010.

Proceedings of the 24th Nordic Seminar on Computational Mechanics
J. Freund and R. Kouhia (Eds.)

All-atom molecular dynamics study on mechanical properties of polystyrene glass

Shijo Nagao, Jianyang Wu, Jianying He, and Zhiliang Zhang

NTNU Nanomechanical Lab. Structural Engineering, NTNU, Richard Birkelands vei 1A, NO-7491, shijo.nagao@ntnu.no

Summary. We examine all-atom molecular dynamics to obtain mechanical properties of glass polystyrene, based on COMPASS force-field. Linear polymer glass model is built by self-avoiding walk on a diamond lattice, including the exclusive volume effect of the bulky side group of polystyrene. This fast modeling method of full atom polystyrene enables us to obtain reliable mechanical properties of glass polystyrene.

Key words: molecular dynamics, all-atom polymer model, polystyrene

Introduction

Considerable effort has been made to achieve computational modelling of polymer materials [1-4]. However, it is in principle tough work to create reasonable atomistic models of glassy polymer solids [2-3]. A popular idea to obtain a glass model by quenching a molten molecular structure is disregarded for full atom modelling, due to the extremely low mobility of heavily polymerized molecules even in its molten states. Even if we could simulate a liquid polymer system, liquid-glass phase transitions – where the molecule's mobility is drastically reduced as called "slow-down" – is to be properly considered to obtain a good glassy solid polymer model. Hence the quality of glass model is limited by the cooling rate of MD simulations. The difficulty of low mobility increases with increasing the molecular weight, so that simulating realistic length of long polymer molecules is still a challenge to high-performance computing facilities to date.

Many of the preceding studies therefore concern the acceleration of molecular simulations. Among them, two major trends have been found to accelerate liquid polymer simulations; one is course-grained (CG) molecular dynamics [4], and the other Monte Carlo (MC) with so called "double-bridging". However, those methods have also drawbacks; CG potentials are usually meant for liquid, and give accurate results only at the tuned temperature. Hence quenching molten polymer to glass state using CG is no longer correct. On the other hand, MC methods like double-bridging are difficult to implement for all-atom simulations, so that most of MC polymer melting methods accept CG models. Remapping from fictitious CG super-atom to real all-atom model requires "push-out" process that may induce another uncertainty into the model. Concerning various available polymerization methods often without melting, amorphous glass polymer can be modelled without simulating molten structures.

In the present study, we rather go back to the old idea of the similarity between self-avoiding random-walk (SARW) and linear polymer molecules [2-3]. For glass polymer modelling, many studies based on the idea have been examined in the literature. We here have explicitly introduced an exclusive volume effect caused by the bulky side group, especially in the case of polystyrene (PS), and implemented a program code of full-atom polymer growth by SARW on diamond lattice. Our algorithm maintains reasonable local conformations suitable for starting structure of any molecular dynamics, and even provides a way to control global molecular arrangements represented by characteristic ratio. Furthermore, use of diamond template enables us to create nano-structured polymer models, like nano-spheres, nano-rods, or thin-films.

Modeling method

Random walk on diamond lattice is the most reasonable template for vinyl polymers because each carbon of polymer backbone has tetrahedral bonding structure similar to that in diamond. Actual bonding angles of the polymer backbone slightly deviate from the exact tetrahedral coordination due to the asymmetry. Such distortions in PS are mainly caused from the ionic interaction among the side groups, even though the electronic orbital still shows minimum energy for the symmetric tetrahedral bonding. Hence it is reasonable to use the diamond lattice as a template of PS molecules before introducing the side group effect.

When growing a PS molecule by SARW, the new monomer in the current growth step of walk should have no wrapping over any other atoms. We introduce a spherical exclusive volume (see Fig. 1***a***) to represent the phenyl ring of the side group, and make sure that there is no atom in the sphere in each possible configuration. When an overwrapping is detected, this configuration is removed from the candidates for the next monomer. If there is no possible place for a new monomer, then it is regarded as a case of collision, and a few steps of backtracking is executed before starting a next trial of polymer growth.

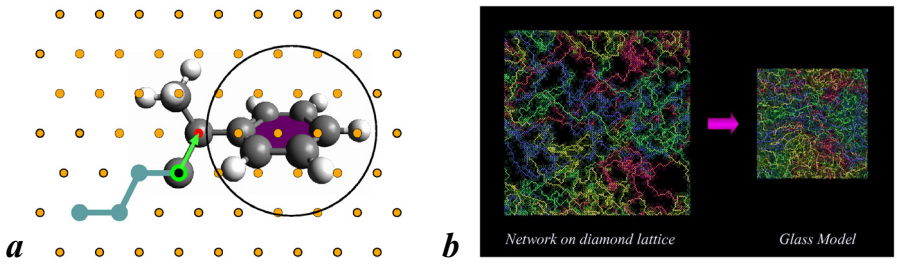

Figure 1. (***a***) Schematic of the random walk process with the explicit exclusive volume of the phenyl ring. (***b***) The glass formation after equilibration and quenching process.

Due to the bulky side group, the SARW process does not achieve a desired density of dense glassy polystyrene. Some compaction process is hence necessary to obtain a realistic model after the SAW (see Fig. 1***b***). This process, however, affects the resulting characteristic ratio that determines the polystyrene glass property. The annealing process in compression scales the characteristic ratio of linear PS molecules with n monomers as

$$C_n = \frac{\left\langle R_n^2 \right\rangle}{nl^2} = \alpha^2 \frac{\left\langle R_{n0}^2 \right\rangle}{nl^2}, \tag{1}$$

where R_n is the end to end distance of the equilibrated system, and R_{n0} of the initial structure generated by SARW. The scaling factor α can be obtained from the target and initial density as follows:

$$\alpha = \left(\frac{\rho_0}{\rho_{\text{target}}} \right)^{1/3}. \tag{2}$$

Thus achieving higher density is the key to obtain a reasonably large characteristic ratio. On this purpose, the size of exclusive volume is adjusted, in balance of maintaining both a reasonable local conformation and the small scaling factor.

The generated structure models are then confirmed to have no crossing phenyl rings. This is assured by calculating atomistic von Mises stress that shows an order of higher value for the atoms in the critically anomalous configuration than other normal ones.

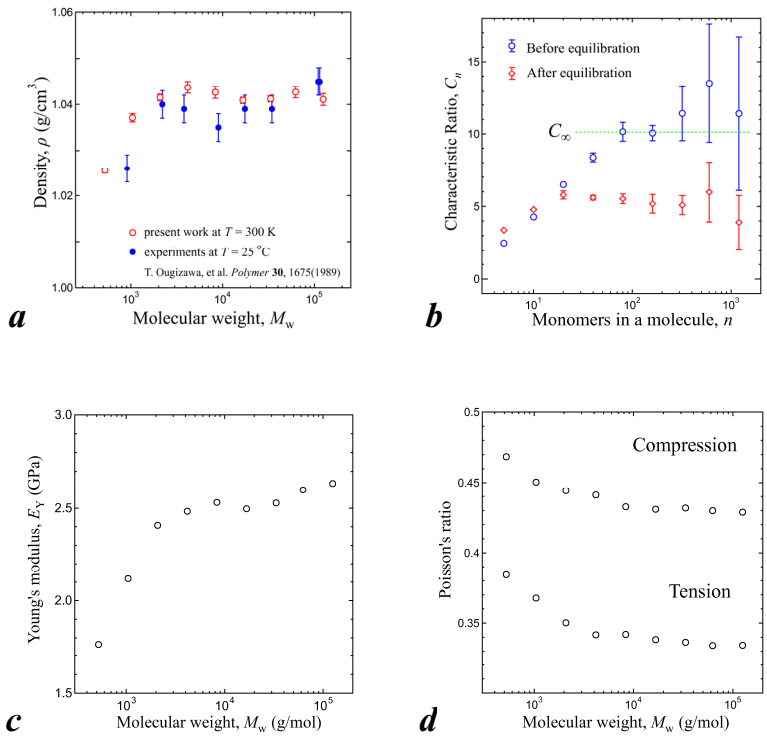

Figure 2. The properties of full-atom models of linear polystyrene, as a function of molecular weight: (***a***) density, (***b***) characteristic ratio, (***c***) Young's modulus, and (***d***) Poisson's ratio determined by uniaxial tension and compression tests.

Simulation Results

All-atom models of linear PS glass are generated by the method described above, and COMPASS force field is assigned of reach atom [5-6]. Each model consists of 4800 monomers in about 9×9×9 nm size of periodic cell, while the molecular length is varied from 5 monomers to 1200 monomers per molecule. After equilibration and compression process in the elevated temperature of 600 K, the generated models are quenched to RT. The final densities obtained at the ambient pressure are shown in Fig. 2***a***, showing excellent agreement with reported experimental values [7]. The obtained characteristic ratio (Fig. 2***b***) may be reasonable, though those of longer molecules are lower than the values reported for free molecules in θ-solvent. Bond length, bond angle, dihedral angle distributions are confirmed to be adequate, in addition to radial distribution functions. The equilibrated models are then subjected to tension/compression tests by molecular dynamics at RT, and Young's modulus and Poisson's ratio are determined for each molecular weight (Fig. 2***c*** and 2***a***).

Concluding Remarks

All-atom molecular dynamics of linear polystyrene glass with various molecular weights has been examined. The new modeling method developed by the authors enables fast generation of reasonable glass models, resulting in better statistics and accuracy in the determined mechanical parameters. The obtained properties show excellent agreement with experimental properties.

Acknowledgements

This work was supported by the Research Council of Norway under NANOMAT KMB (MS2MP) Project No. 187269 and the computational resources provided by NOTUR – The Norwegian Metacenter for Computational Science.

References

[1] B. Vorselaars, A. V. Lyulin, M. A. J. Michels, *J. Chem. Phys.* **130**, 074905 (2009)
[2] D. N. Theodorou, U. W. Suter, *Macromolecules* **18**, 1467 (1985)
[3] M. Kotelyanskii, N. J. Wagner, M. E. Paulaitis, *Macromolecules* **29**, 8497 (1996)
[4] V. A. Harmandaris, N. P. Adhikari, N. F. A. van der Vegt, K. Kremer, *Macromolecules* **39**, 6708 (2006)
[5] H. Sun, *J. Phys. Chem. B* **102**, 7338 (1998)
[6] C. Li, P. Choi, P. R. Sundararajan, *Polymer* **51**, 2803 (2010)
[7] T. Ougizawa, G. T. Dee, D. J. Walsh, *Polymer* **30**, 1675 (1989)

Proceedings of the 24th Nordic Seminar on Computational Mechanics
J. Freund and R. Kouhia (Eds.)

Equilibrium crystal shapes on a non-horizontal wall

Mika Reivinen and Eero-Matti Salonen

Aalto University, School of Engineering, P.O.Box 12100, FI-00076 Aalto, Finland
mika.reivinen@aalto.fi, emsalone@cc.hut.fi

Summary. A formulation on equilibrium crystal shape determination based on the principle of virtual work is presented. Previous shape determination studies are based on the assumption of a horizontal wall below the crystal, but in the present study this restrictive assumption is no more used. The treatment is restricted to two dimensions.

Key words: crystal shape, surface tension, contact, virtual work

Introduction

Classical methods to determine equilibrium shapes of crystals are the Wulff construction and the Landau-Andreev formulation [1]. The present article reviews a method based on the principle of virtual work [2], [3]. A generalization to cover cases where the shape of the wall below the crystal may be arbitrary is made. The presentation is limited to two dimensions but the formulation can be extended rather straightforwardly also to three dimensions. The problem statement is given, the discrete formulation is presented shortly, and some numerical results are presented.

Problem statement

Let us consider Figure 1. The basic setting consists of a crystal (C), surrounded by liquid (L) and resting in equilibrium on a solid surface wall (W). The task is to determine the position of the interface surface *S* between the crystal and the liquid. The shape of the wall surface $\hat{S}$ is considered as given.

The interface energy density γ depends on the orientation of the interface surface or here on the direction angle $\psi : \gamma = \gamma(\psi)$. The interface energy density between the wall and the crystal phase γ_{CW} and interface energy density between the wall and the liquid phase γ_{LW} depend in principle on a given way on the position on $\hat{S}$. The interface touches the wall at points *a* and *b*, with contact angles θ_a and θ_b which are all initially unknowns of the problem. The cross-sectional area A_{C} of the crystal is assumed to be given in the problem statement. Correspondingly, the pressure p_{C} in the crystal is an unknown constant. The known pressure in the liquid is taken according to the hydrostatic pressure distribution $p_{\mathrm{L}} = p_0 - \rho_{\mathrm{L}} g z$, where

ρ_{L} is the constant density of the liquid, g the acceleration of gravity, z the upwards measured coordinate and p_0 a given pressure associated with the level $z=0$. The position vector $\mathbf{r}$ on S is expressed in the form $\mathbf{r}=\mathbf{r}(s)$ where the s is arc length. The position vector $\hat{\mathbf{r}}$ on $\hat{S}$ is expressed (sometimes in a piecewise manner) in the form $\hat{\mathbf{r}}=\hat{\mathbf{r}}(u)$ where u is a suitable curve parameter. The unit normal vectors $\mathbf{n}$ and $\hat{\mathbf{n}}$ on S and $\hat{S}$ are directed into the liquid and into the crystal and the unit tangent vectors $\mathbf{t}$ and $\hat{\mathbf{t}}$ into the increasing directions of s and u, respectively

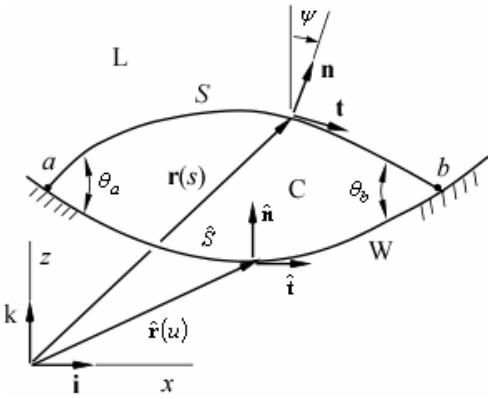

Figure 1. Some notations.

In the case of non-constant interface energy, the equilibrium requires the torque acting on the surface. The torque m is obtained from [3]

$$m=-\frac{\mathrm{d}\gamma}{\mathrm{d}\psi}. \tag{1}$$

Depending on the choice of interface energy density $\gamma(\psi)$, the crystal shape is necessarily no more a smooth curve, but it may consist of straight parts, and perhaps of angular points where the tangent of interface is not continuous.

Virtual work

The principle of virtual work is a well-known formulation with wide application areas in mechanics. The virtual work equation for the interface problem under study is

$$\bar{\delta}W\equiv\bar{\delta}W^{\mathrm{int}}+\bar{\delta}W^{\mathrm{ext}}+\bar{\delta}W^{\mathrm{bound}}=0\,, \tag{2}$$

where $\bar{\delta}W^{\mathrm{int}}$ is the virtual work of the internal, forces $\bar{\delta}W^{\mathrm{ext}}$ is the virtual work of the external forces and $\bar{\delta}W^{\mathrm{bound}}$ is the virtual work of from the boundary terms. The principle of virtual work states that (2) is valid for any virtual movement of the interface. The three virtual work terms are presented in detail in [2] and [3]. Further, it is shown that the relevant equations follow from (2).

Discrete formulation

The discrete formulation is based on a kind of finite element method. The interface is discretized by two-noded line elements or segments. Figure 2 shows the notations for a generic line segment.

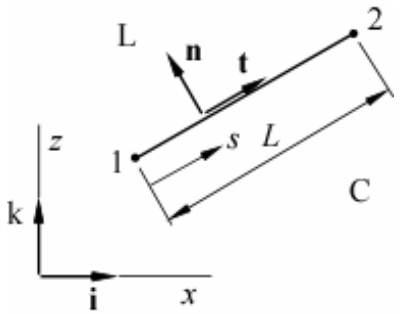

Figure 2. A generic line segment.

The geometry of the discrete interface model is fixed by a list consisting of the nodal Cartesian coordinates, say **X**, and of the global node numbers of the segments in the model. The task is to determine that **X** for which the main system equations (equilibrium equations) are satisfied. An additional unknown is the pressure p_{C} in the crystal. The corresponding additional system equation is the area constraint $A = A_{\mathrm{C}}$. It is to be noted that p_{C} appears in the equilibrium equations but not in the constraint equation. As the interface determination problem is strongly non-linear, the solution must be found iteratively.

The virtual work for the interface model (with respect to a current configuration) obtains the form

$$\bar{\delta} W = \sum_{i=1}^{N_{\mathrm{dof}}} Q_i \, \delta q_i \,, \tag{3}$$

where Q_i is the *i*:th generalized force corresponding to the *i*:th movement q_i (or generalized coordinate) and N_{dof} the total number of movements. The generalized forces must vanish and the area constraint must be satisfied. Thus, the system equations are

$$\begin{aligned} &Q_i = 0, \quad i = 1,2,\cdots N_{\mathrm{dof}} \,, \\ &A = A_{\mathrm{C}} \,. \end{aligned} \tag{4}$$

In the case of non-horizontal wall, the contribution from the wall to the cross-sectional area A has to be taken into account. The area can be determined straightforwardly using the discretized interface between crystal and liquid and the interface between crystal and wall. The contribution to the cross-sectional area from the line segment is

$$\Delta A = \frac{1}{2}\left(x_2 z_1 - x_1 z_2 \right), \tag{5}$$

where x_1, z_1, x_2 and z_2 area the Cartesian coordinates of nodal points.

Applications

In the case of constant interface energy density, $\gamma = \text{const}$, it is possible to compare the numerical solution with analytical solution, and in some cases of horizontal wall and non-constant interface energy density, $\gamma = \gamma(\psi)$, one may assess the numerical solution applying Wulff construction. In this study both cases are included, but here only two simple cases with constant surface tension are presented. In the first example the wall is a horizontal plane $z = 0$. In the second example the wall consists of an incline $z = -x$ when $x < 0$, and a horizontal plane $z = 0$ when $x \geq 0$. The energy density γ is constant so no torque appears. Gravity is neglected, and therefore the pressure difference between crystal and liquid is constant. The fixed area for both cases is given as two units. The solution is a "soap bubble" with a constant radius with $\gamma_{\text{LW}} - \gamma_{\text{CW}} = -1/\sqrt{2} \cdot \gamma$, and the well-known Young's formula gives the contact angle $\theta = 3\pi/4$. In the first example point *a* is fixed at the origin and point *b* is free, while in the second example both boundary points are free.

The solution of first case is presented in Figure 3(a), and of the second case in Figure 3(b). It can be seen that the accuracy of the discrete solutions are acceptable.

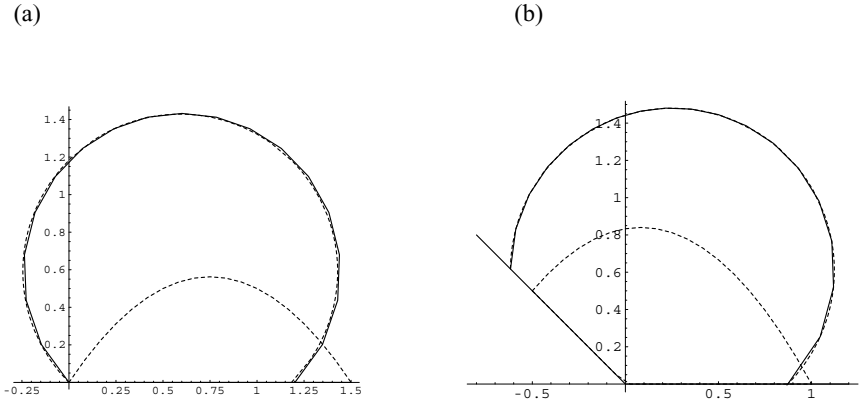

Figure 3. Initial, exact (dashed) and final shapes. (a) Crystal on a horizontal wall, (b) Crystal on a non-horizontal wall.

References

[1] P. Nozieres. Shape and growth of crystals, in *Solids far from equilibrium*, Cambridge University Press, edited by C. Godrèche, 1989.

[2] M. Reivinen, E.-M. Salonen, Surface tension problems, virtual work and free boundary, *Proceedings of the IX Finnish Mechanics Days*, 2006.

[3] M. Reivinen, E.-M. Salonen, V.P. Vaskelainen, Surface tension problems with distributed torque, *Proceedings of the X Finnish Mechanics Days*, 2009.

Author index

NSCM-24 sponsors

INSINÖÖRITOIMISTO PONTEK OY

VTT

FEMdata

INSINÖÖRITOIMISTO MAGNUS MALMBERG OY CONSULTING ENGINEERS

stx Finland

numerola

KONECRANES Lifting Businesses

TVO

PROCESS FLOW

Finnforest

ETI PRODUCTS

SITO

FMC GROUP

Finnmap Consulting FMC GROUP

KPM-Engineering FMC GROUP

Aaro Kohonen FMC GROUP

ril

RUUKKI

Magnus Ehrnrooth Foundation

Federation of Finnish Learned Societies

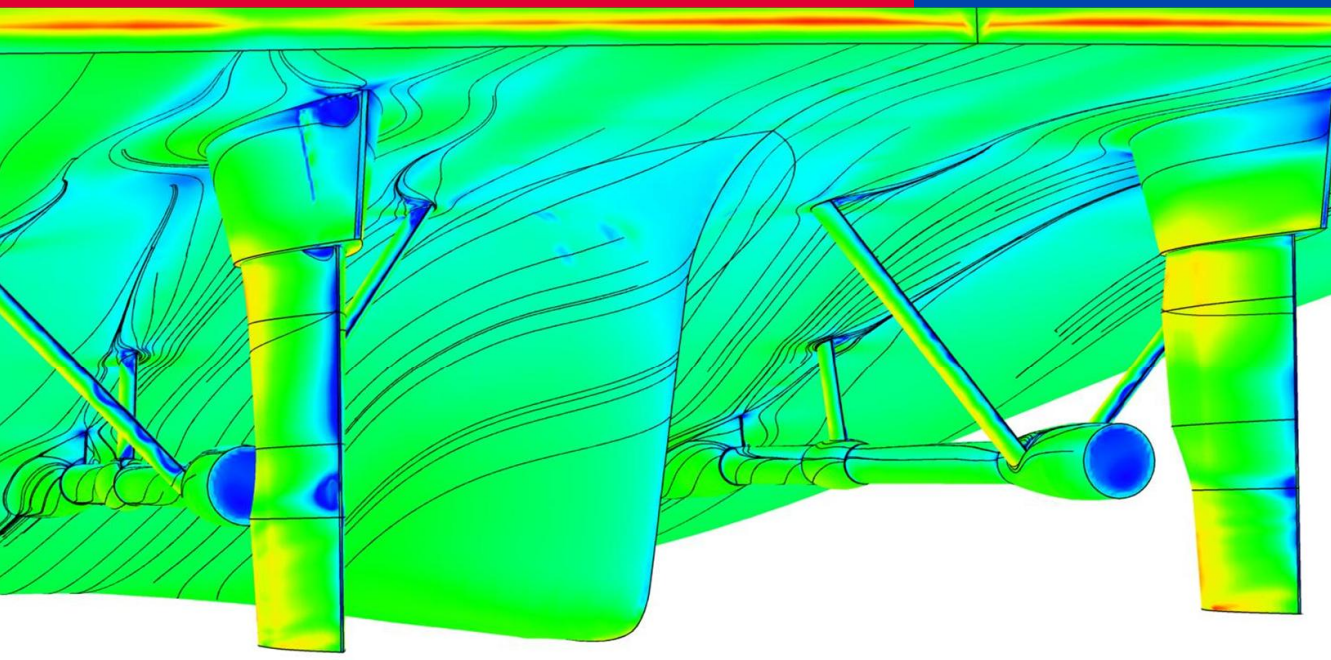

CFD & FEM

STX Finland utilizes advanced numerical simulation to design best ships in the world

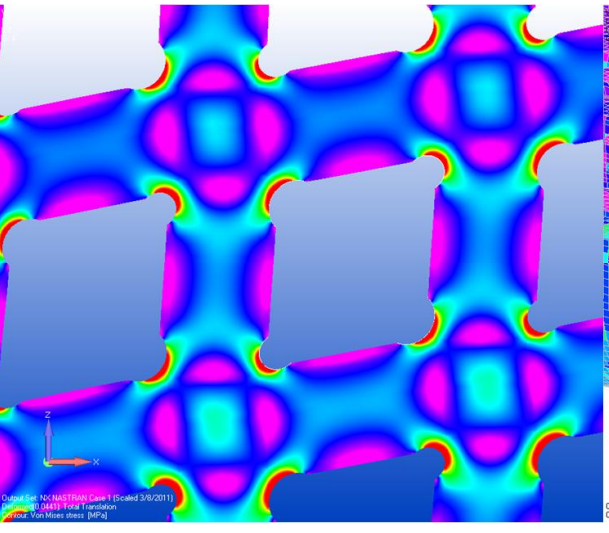

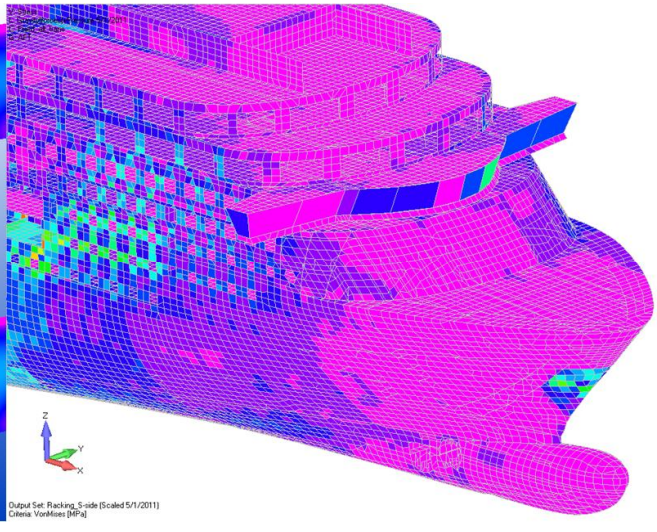

stx Finland

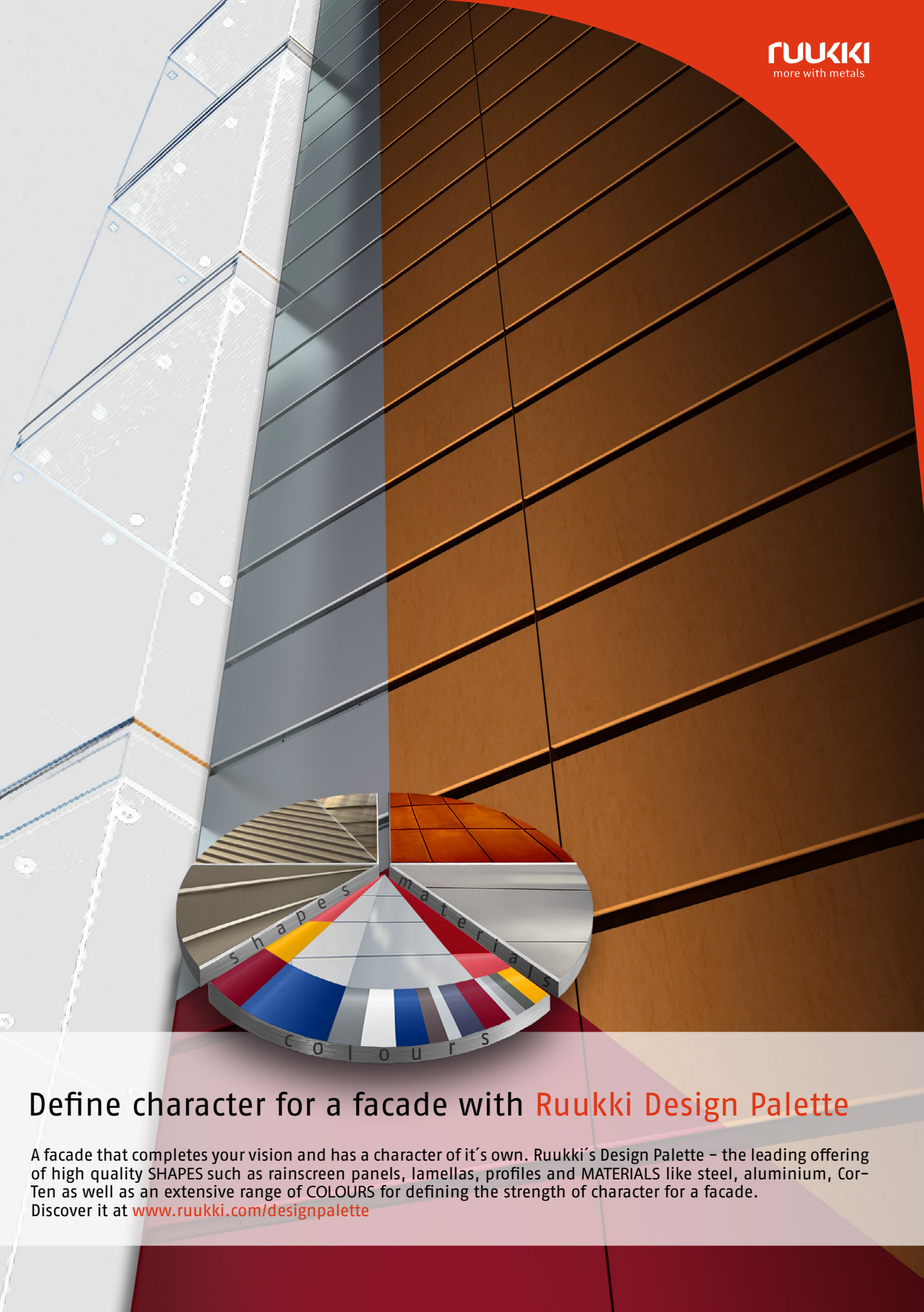

Define character for a facade with Ruukki Design Palette

A facade that completes your vision and has a character of it´s own. Ruukki´s Design Palette – the leading offering of high quality SHAPES such as rainscreen panels, lamellas, profiles and MATERIALS like steel, aluminium, Cor-Ten as well as an extensive range of COLOURS for defining the strength of character for a facade.
Discover it at www.ruukki.com/designpalette

FEMdata

FEM -programs for:
Piping (EN, ASME)
Steel structures (EC3)
General structures

Support and user training

Ukkohauentie11-13 B
02170 Espoo, Finland
358-9-420 8855

STRUCTURAL ENGINEERING IN FMC GROUP

FMC Group is a Finnish structural engineering design and consultancy firm in a market leadership position in Finland and we hold a significant presence in the international market. Our services include building, industrial, infrastructure and reconstruction project design as well as design inspection for all types of construction projects.

COMPETENCE AND COMPREHENSIVE EXPERTISE ARE KEY

In addition to our expertise in the entire life-cycle of buildings, the strength of our experience and knowledge of the needs of all stakeholders of the project combine in a comprehensive package to offer the very best for our customers and the environment. We can handle all types of building materials and building methods and are experts in detailed design. Most importantly, we maintain control over the entire project so the customer's quality, life-cycle, safety and operational requirements are realised.

CREATING A BETTER FUTURE

Comprehensive life-cycle strategy and sustainable development form a key part of our service. We keep ourselves and our customers at the forefront of the latest industry development by actively investing in our personnel and cutting edge research. We are continuously working in research and development activities with our partners, including builders, the construction industry, universities, research institutes and software vendors, with a view to improve built-up environment development and the construction industry as a whole. For example, we are pioneers in information modelling for the benefit of the entire construction industry and its productivity.

REFERENCES:

Shopping and leisure centres: Shopping Centre Kamppi, Leppävaara Business Centre. **Office and commercial buildings:** Varma-Salmisaari, Tapiola Financial Services' Head Office. **Residential buildings:** Plazanpuisto, Plazankuja and Allotrianpuisto, Estella of Eira. **Public and service buildings:** Main library building in Turku, Joensuu Arena. **Industrial buildings:** Extension of Avesta-polarit steel factory in Tornio, Atria Nurmo. **Infrastucture references:** The western by-pass road in Tampere, Kerava-Lahti shortcut railway. **Power Plants:** Olkiluoto OL3 nuclear power plant, Hanasaari heating plant. **Reconstruction projects:** Stockmann Kasvu, Helsinki zoological museum. **International projects:** Arena Magnitogorsk, Prystan Shopping Centre (Kiev). **Project inspection:** Blue1 airplane hangar, Panorama Tower. **Research and development:** Ruukki steel foundation system.

Industries

- House Building
- Reconstruction
- Industrial Buildings
- Power Plants
- Engineering Structures
- Infrastructures
- Life-cycle Design
- Inspection and Risk Management

Areas of expertise

- Steel Structures
- Concrete Structures
- Precast Concrete Elements
- Wood Constructions
- Glass Structures
- Composite Material Structures
- Research and Development
- Information Modelling
- Structural Physics
- Structural Analyses

FMC GROUP

→ www.fmcgroup.fi

AB ETIPRODUCTS OY, a subsidiary of Eti Mine Works, a Turkish State owned Company, previously known as Eti Holding AS or Etibank, was established in 1982 in Helsinki, Finland.

Our parent company, which is the Turkey's biggest and oldest mining company, is mainly involved in mining, and metallurgy and chemical industries that are directly connected to its own mining operations. Although it is the producer of many different kinds of minerals and metallurgical and chemical products, it is famous for being the world's leading boron minerals and chemicals producer.

Only a few of the many minerals that contain boron are commercially valuable. Substances containing boron oxide are commonly known as borates. The borate minerals (colemanite, tincal and ulexite) are produced in Turkey.

Boron compounds are used in a wide variety of products and manufacturing processes such as; textile glass fiber, insulation glass fiber, cellulosic insulation, borosilicate glasses, enamels and glazes, metallurgy, chemistry, abrasives, detergents and soaps, corrosion inhibitors, fertilizer as micronutrient and other usages. www.etiproducts.com.

Turkey possesses roughly two thirds of the world's boron minerals reserves and is the largest exporter of these minerals. Borate production is concentrated to the western part of the country (Eskishehir, Balikesir, Kutahya and Bursa).

Turkey's boron operations are under the control of Eti Mine Works G.M.**(**former Eti Holding and Etibank), a state-owned company. As the largest single mining company in the country, Eti Mine Works G.M. has been developing the country's natural resources since its establishment in 1935. Eti Mine Works produces a range of boron minerals and refined products such as ground colemanite, ground ulexite, calcined tincal, borax pentahydrate, borax decahydrate, boric acid, anhydrous borax, boron oxide, disodium octaborate tetrahydrate.

In 1982, **Etibank** and the Finnish mining and multimetal Outokumpu group established a joint-venture "**Ab Etiproducts Oy**" for marketing Etibank's products on the Scandinavian market. In 1993 Outokumpu's share was transferred to Etimine SA, a sister company of **Ab Etiproducts Oy**, responsible for the marketing of Turkish boron products in Western Europe.

Ab Etiproducts Oy is the exclusive sales agent and distributor of Eti Mine Works' Boron products for Scandinavia, Poland, Baltic States and CIS.

Ab Etiproducts Oy has several warehouses in the Baltic rim (Uddevalla/Sweden, Inkoo/Finland, Gdynia/Poland and Liepaja/Latvia).

With its head office in Helsinki, Ab Etiproducts Oy is managing the sales and distribution of Boron Products with a well-spread logistics network.

Since its establishment Ab Etiproducts Oy has gained a reputation as a reliable and competitive supplier of boron products. The company's marketing exclusivity for Turkish boron products presently covers Finland, Sweden, Norway, Denmark, Iceland, Poland, Estonia, Latvia, Lithuania, Russia, Ukraine, Belarus, Kazakhstan and the other C.I.S. countries.

In order to improve our services in the promising Russian market, Ab Etiproducts Oy established its own subsidiary company 'Etiproducts ltd.' in 2005 which is responsible for Russian market. Etiproducts ltd has a stock place in Black Sea region (Azov).

Address	Telephone	Telefax	E-mail & Web	ALV rek.
Ab Etiproducts Oy	INT. +358 9 819 444 0	INT. +358 9 819 444 4	sales@etiproducts.com	VAT reg no FI4873431
Piispanportti 9	NAT. (09) 819 444 0	NAT. (09) 819 444 4	www.etiproducts.com	Trade reg no. 308.853
02240 Espoo, FINLAND				

Bank: Nordea Bank Finland Plc	EUR 158330-109881	USD FI771583 5200 0411 03	NOK FI46 1583 5200 0410 79
Swift address: NDEAFIHH	EUR FI41 1583 3000 1098 81	SEK FI02 1583 5200 0410 95	DKK FI55 1583 5200 0411 11

PONTEK OY
Consulting Engineers Ltd

KUTOJANTIE 2 C
02630 ESPOO
Tel +358 (0)9 2530 4500
firstname.lastname@pontek.fi
www.pontek.fi

MAIN BUSINESS AREAS
- Structural engineering
- Bridge design

ADDITIONAL BUSINESS AREAS
- Construction services and real estate management
- Water construction and engineering

PROCESS FLOW

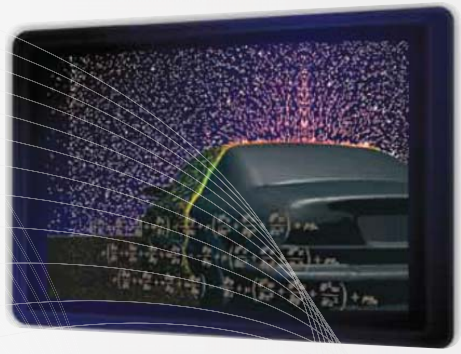

PROCESS FLOW

The cornerstones of our business operations are:

- Modelling and simulation services
- Modelling and simulation software tools

These cornerstones are built on a strong technological know-how and an in-depth understanding of mathematical modelling, computational fluid dynamics (CFD), finite element analysis (FEA) and industrial processes.

The simulation software used and represented by Process Flow are widely recognized as de facto standard tools for large-scale industrial simulation.

We use these cornerstones to provide consulting services for our industrial customers. In addition to this our experienced staff offers professional training and technical support for our software clients to facilitate seamless use of the represented software in their daily business. The members of our staff hold high academic degrees in quantitative fields; we are also capable of customizing the simulation tools for a successful solution, should your problem require it. We have over 10 years of experience working with large international CAE software companies.

HISTORY

Process Flow is a private held Finnish company whose three owners all work within the company. For many years, Process Flow has been on the leading edge of industrial CFD in Finland, while simultaneously expanding its know-how and business operations to FEM, acoustics, optimization and other areas of modeling and simulation. At present, Process Flow is the leading provider of computer-aided engineering software and services in Finland.

"PROCESS FLOW LIVES ON KNOW-HOW. KNOW-HOW CREATES UNDERSTANDING. UNDERSTANDING IS THE KEY TO REALISTIC SOLUTIONS."

RIL - Finnish Association of Civil Engineers

Organisation for civil engineers with Master of Science degree and university students of civil engineering. Founded in 1934, more than 6200 members.

RIL supports the development of building, urban planning and environmental technology and acts to preserve solid and durable building and maintenance traditions.

RIL also supervises the benefits of its members and promotes their professional skill and welfare. RIL unites the most highly educated professionals in civil engineering to form a versatile network.

Vision

- RIL is a network for versatile and prosperous professionals.
- RIL is an association with high influence on development of society.

Mission

- RIL promotes a continuous development of its members' professional skills and welfare.
- RIL promotes sustainable development of the built environment.

Professional Publications

The goal for RIL's publishing activity is to maintain and develop the professional skills its members and of the building industry personnel in general. This is achieved by producing high class, well adapted and up to date professional publications.

Professional Education

RIL arranges further education directed to the civil engineering professionals. Together with leading local and global scientific and professional partner institutions, RIL also arranges international symposiums and conferences in Finland.

Public Affairs

RIL cooperates with and offers its specialist services for a wide range of stakeholders. Engineering design competitions give clients a wide and cost-effective pool of ideas for real-life projects. State of the Nation of the Built Environment report joins almost 100 professionals to assess and create scenarios for the field every second year. With its position papers and statements RIL offers its ideas for public administration and other professional bodies.

www.ril.fi

Strong constructional know-how

We design concrete, steel and wood bridges, and provide bridge refurbishment programmes. Our core service involves also the design of other infrastructure-related structures, such as support walls, waterfront structures, noise barriers, etc.

SITO

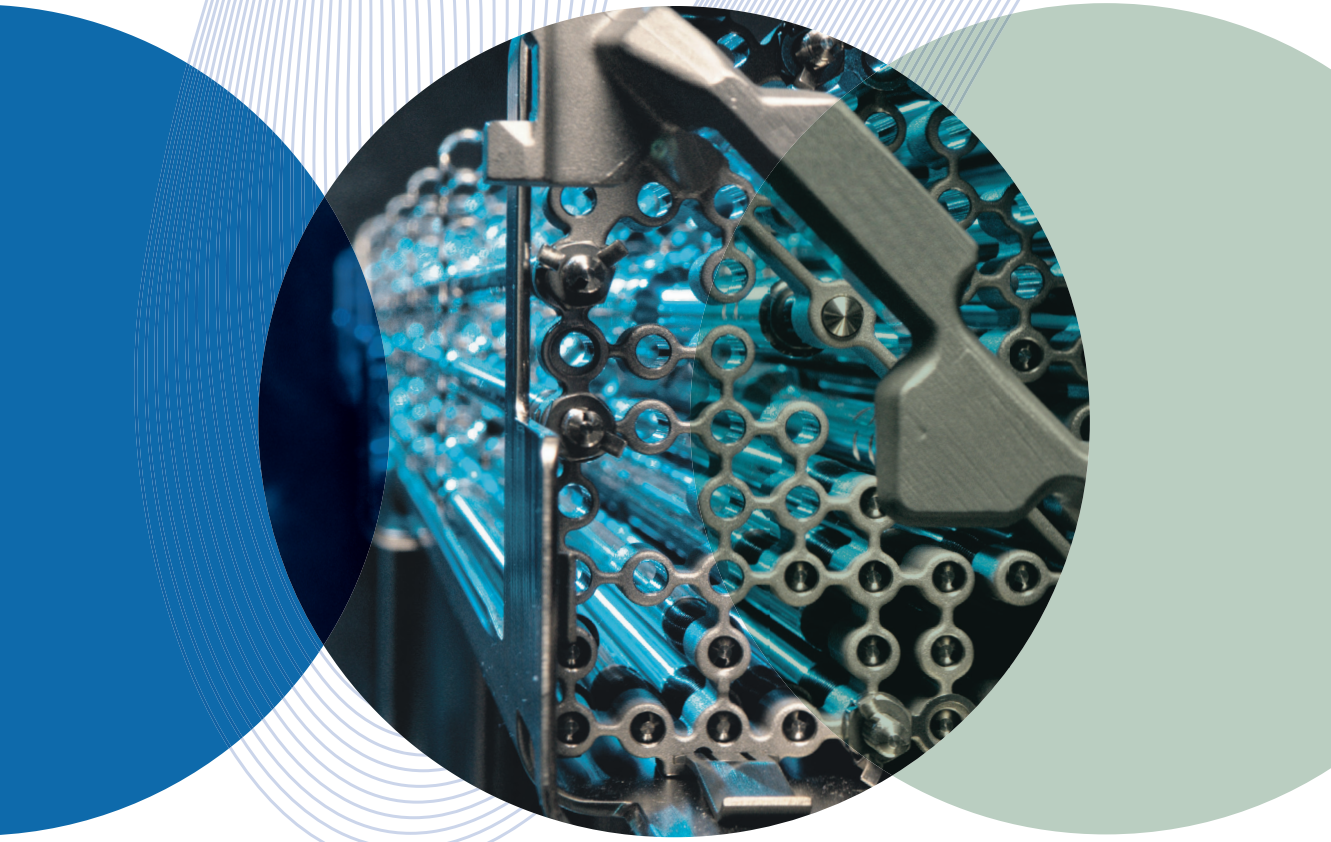

CLEARLY A PIONEER

The years of big projects at Olkiluoto are here now. We are modernising the existing plant units that are operating, building and planning two new nuclear power plant units and building excavating a final disposal facility a repository for spent nuclear fuel. These projects are a tour de force which will keep Finnish nuclear expertise at top level and strengthen our position as a forerunner pioneer in our the field.

www.tvo.fi

TVO

Business from technology

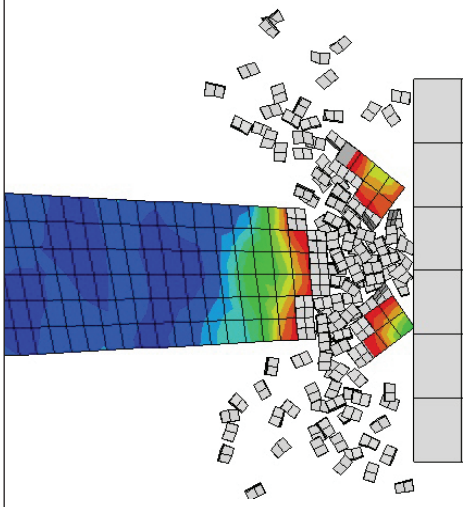

VTT Technical Research Centre of Finland is a leading European multitechnological applied research organisation. VTT creates new technology and science-based innovations in co-operation with domestic and foreign partners. VTT's turnover is EUR 290 million and personnel 3,100.

VTT - a research partner in **structural mechanics**

Approximately 30 specialists at VTT are using their knowledge and passion in structural integrity analyses for various sectors and applications.

Experimental results are used for verification and development of numerical methods and calculation models. The benefits of structural analysis are most commonly linked to the safety, prolonged life-time and efficiency of structures and components. These lead not only to better productivity but also to more environmentally friendly solutions.

VTT's key expertise and research cover the following research fields:

- Impact loaded reinforced concrete structures
- Computational fracture mechanics
- Fluid-structure interaction
- Modelling of materials and multi-material composites
- Smart structures and functional materials
- Ice-structure interaction, ice mechanics
- Risk-informed life management of structures
- Simulation of ships and other vehicle
- Non-linear simulation of welding and manufacturing processes

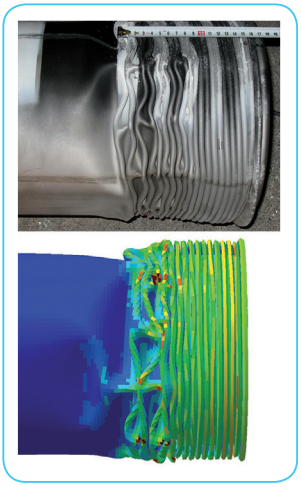

Additional information
Eila Lehmus, Technology Manager
Tel. +358 20 722 6946, eila.lehmus@vtt.fi

VTT TECHNICAL RESEARCH CENTRE OF FINLAND
www.vtt.fi

MAGNUS MALMBERG OY ON RAKENNESUUNNITTELUUN ERIKOISTUNUT INSINÖÖRITOIMISTO.

Päätoimialamme ovat liike- ja toimistorakennusten, julkisten rakennusten, teollisuusrakennusten sekä vaativien asuinrakennusten rakennesuunnittelu kaikkine osa-alueineen. Teemme sekä uudisrakentamisen että korjausrakentamisen projekteja.

Viimevuosien kohteitamme ovat olleet mm.:

- **Skanska Oy:n pääkonttori Ruskeasuolle**
- **Makkaratalon saneeraus**
- **Metla, puurakenteinen toimistotalo, vuoden puurakenne 2005**
- **Laajasalon kirkko, vuoden puurakenne 2004**
- **Merikeskus Vellamo Kotkassa, vuoden teräsrakenne 2008**

Panostamme yhteistyökykyyn, vastuullisuuteen ja innovatiiviseen suunnitteluun. Tarjoamme asiakkaillemme ratkaisuja ja sitoutumista saamiimme toimeksiantoihin. Tavoitteenamme on olla alan johtava asiantuntija.

Keväällä 2011 on aloittanut täydennyskoulutusohjelmamme MM Rakenneinstituutti (*, joka tarjoaa junioreille pätevöitymiskoulutusta ja senioreille mahdollisuuden pitää teoreettisen ammattitaidon ajan tasalla.

Haluamme kantaa vastuumme myös tulevaisuuden asiantuntijoiden kasvattamisesta. Kesäkaudeksi 2011 palkkasimme 12 harjoittelijaa, puolet aiemmin olleita, puolet uusia, puolet TUT:stä, loput Aalto yliopistosta ja AMK Metropoliasta.

TANGO, FEM-MALLI

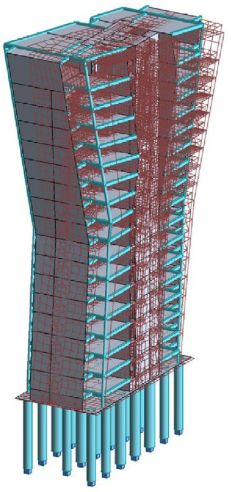

INSINÖÖRITOIMISTO MAGNUS MALMBERG OY
Lauttasaarenmäki 4 00200 Helsinki
Puhelin (09) 618 460
www.magnusmalmberg.fi

*) **MM Rakenneinstituutti**
Yhteistyössä:
Magnus Malmberg
Ylimäki | Tinkanen
Rakennusteollisuuden Koulutuskeskus RATEKO

Metsäliitto Cooperative, Finnforest

Metsäliitto Wood Products Industry, Finnforest delivers competitive solutions developed according to customer needs. Our main strengths include a service-oriented operating model, long expertise in advanced and ecological wooden structures and reliability of delivery.

Our solutions utilize high-quality Nordic wood as a raw material. Due to the slow growth of Nordic forests, our premium products have excellent durability and appearance properties, which make them ideal for demanding applications and end-uses. Also, by using wood as a building material our customers can contribute to mitigating climate change.

To ensure that our customers receive the best value on the market, we continuously invest in the development of our products, services and expertise. This way we can meet the ever-tightening technical, environmental and energy requirements.

We specialize in serving the needs of the construction industry, other industrial customers as well as the home and living area. In these segments, we are the leading wood products supplier in Europe, and offer our customers a comprehensive service network that is present in 20 countries. We serve home improvers and end-users through DIY chains and other distributors.

We are the leading wood product supplier in the following customer segments in particular:

- Commercial, public and residential building and construction
- Industrial customers, such as window, door and moulding manufacturers, other manufacturers serving building and construction, and the transport vehicle industry
- Interior decoration, renovation, garden and yard furnishing

Our four business lines, complementary to each other, include Solid Wood, Engineered Wood, Building Products and Home and Living. We are a European forerunner in engineered wood products and solutions, investing in research and in the continuous development of products and know-how to meet increased customer requirements.

Our annual sales total 902 million euros, and we employ 3,000 professionals. Finnforest is a part of the Metsäliitto Group, an international forest industry group present in some 30 countries.

Thursday 03.11

8:00	**Opening**	
8:15	**S1 Plenary**	
	A new concept for a very large twin hull cruise ship	**P.G. Bergan**, J.C. Jang
	Motion of a solid with large deformations	E. Bonetti, P. Colli, **M. Frémond**
	Standard gradient models and gradient plasticity	**Q.-S. Nguyen**
10:15	**Coffee break**	
10:45	**S2A Isogeometric analysis** Thematic session organised by T. Kvamsdal, K.M. Mathisen	
	Isogeometric analysis of finite deformation nearly incompressible solids	K.M. Mathisen, K.M. Okstad, T. Kvamsdal, S.B. Raknes
	Analysis-suitable modeling for isogeometric shell analysis	S. Støle-Hentschel, G. Skeie
	Isogeometric Kirchhoff-Love plate elements	K.M. Okstad, T. Kvamsdal, K.M. Mathisen, S.B. Raknes
	Adaptive mesh refinements using LR B-splines for elliptic problems	T. Kvamsdal, K.A. Johannessen
	On the spurious oscillations in B-spline finite element method	R. Kolman, J. Plešek, M. Okrouhlik, D. Gabriel
10:45	**S2B Constitutive modeling**	
	A classical lamination theory model of bi-stable woven composite tape-springs	Y. Prigent, P. Mallol, G. Tibert
	Experiments on Nomex® honeycomb compliance	A. Karakoç, J. Freund
	Hypo- and hyperinelasticity applied to modeling of compacted graphite iron machining simulations	G. Ljustina, M. Fagerström, R. Larsson
	Dispersion analysis of a continuum damage model	J. Hartikainen, K. Kolari, R. Kouhia
	Computational modeling of case II diffusion in polymeric materials	S. Bargmann, A. McBride, P. Steinmann
	A DAE approach for solving the elasto-plastic boundary value problem	M. Wallin, E. Borgqvist
10:45	**S2C Numerical techniques**	
	System modeling for delamination detection using support vector machines and neural networks	L. Feklistova, H. Hein
	Artificial neural networks for nonlinear dynamic response simulation in mechanical systems	N.H. Christiansen, J. Høgsberg, O. Winther
	Investigation of a finite element formulation of Lighthill's acoustic analogy	J. Nilsson, R.-Z. Szasz, P.-A. Wernberg, P.-E. Austrell
	Reducing the integration error of cohesive elements	B.L.V. Bak, E. Lund
	A residual based a posteriori error estimator for postprocessed MITC plate elements	L. Beirão da Veiga, J. Niiranen, R. Stenberg
	Acceleration of large self consistent iterations with the quasi-Newton method	K. Baarman, T. Eirola, V. Havu
12:45	**Lunch**	
13:45	**S3 Plenary**	
	Rail- and roadway dynamics – uncoupled and coupled analysis	**N.-E. Wiberg**
	Modeling and analysis of rotating solids and structures	**S. Krenk**
15:15	**S4A Multiscale modeling in solid mechanics** Thematic session organised by F. Larsson	
	A discontinuous Galerkin multiscale method for first order hyperbolic equations	M. Larson, A. Målqvist, R. Söderlund
	On the emergence of asymmetric waves in the Mindlin-Engelbrecht-Pastrone model	K. Tamm, A. Salupere
	Analysis of volume average relations in continuum mechanics	A. Ahadi, P. Lindström
	Chloride transport in concrete modeled by the FE ^{2}-method	F. Nilenius, F. Larsson, K. Lundgren, K. Runesson
	Multiscale modeling of porous media	C. Sandström, F. Larsson, H. Johansson, K. Runesson
15:15	**S4B Optimisation**	
	Minimizing structure-borne noise of rotating machinery in the room of a light-weight building	B. Niu, N. Olhoff, J. B. Larsen
	Design optimization of a light-weight robotic arm under structural constraints	S. Bai, L. Zhou
	Thickness optimization of fiber reinforced composite laminates with the discrete material optimization method	S.N. Sørensen, E. Lund
	Block aggregation for strength criteria in multi-material topology design of laminates	E. Lund
	Optimal design of stiffened plate using metamodeling techniques	O. Heinonen, S. Pajunen
15:15	**S4C Stability**	
	Buckling of plates with cut-outs made of non-isotropic materials	A.V. Lebedev, A.L. Smirnov
	Eigenfrequencies in moving material problems: practical challenges	J. Jeronen
	Simplified buckling analysis of imperfection sensitive reinforced concrete column	N. Challamel, J. Hellesland
	Unexpected behavior of linearized eigenvalue problem in the context of stability analysis	A. Fedoroff, R. Kouhia
	Static instability analysis of an elastic band travelling in the gravitational field	N. Banichuk, J. Jeronen, T. Saksa, T. Tuovinen
17:15	**Coffee break**	
17:30	**S5 Plenary**	
	Adaptive reduction of finite element models in computational solid mechanics	**M. Larson**, H. Jakobsson
	Variationally consistent computational homogenization -- Selected issues and applications	**K. Runesson**, F. Larsson

Friday 04.11

8:00	**S6 Plenary**	
	Atomistic simulation of metal-polymer adhesion	J.Y. Wu, S. Nagao, J.Y. He, **Z. Zhang**
8:40	**Coffee break**	
9:00	**S7A Multibody mechanics 1** Thematic session organised by J. Mäkinen and M. Matikainen	
	The equations of motion and the power theorem in multibody dynamics	P. Lidström
	Numerical simulation of dynamic Brazilian disc test on rock	T. Saksala, M. Hokka, V.-T. Kuokkala, J. Mäkinen
	Sensitivity analysis of Snelson-type tensegrity booms due to member loss	S. Dalil Safaei, A. Eriksson, G. Tibert
	Three-dimensional solid elements employing slopes in the absolute nodal coordinate formulation	A. Olshevskiy, O. Dmitrochenko, C.-W. Kim
	On the characteristic based split (CBS) method in an arbitrary Lagrangian Eulerian (ALE) framework	M. Mikkola
9:00	**S7B Dynamics**	
	Investigation of the steady state vibration of flexible supported rigid rotors attenuated by a new controlable damping element	J. Zapoměl, P. Ferfecki
	On non-dimensional groups for characterization of energy absorption of tubes at constant crushing velocity	J. Dahl
	Reduction of traffic-induced vibrations at high -tech facility using trenches	P. Persson, K. Persson, G. Sandberg
	Analysis of vibration reduction at high-tech facility by stabilising the soil	O. Flodén, K. Persson, G. Sandberg
	Interaction of vocal fold and vocal tract oscillations	A. Aalto, D. Aalto, J. Malinen, M. Vainio
	On the self-exited vibrations of a viscoelastically covered cylinder in rolling contact using FE method	A.T. Karttunen, R. von Hertzen
9:00	**S7C Solids and fluids**	
	Two phase flow in complicated geometries: Modeling the Frio data using improved computational meshes	M. Juntunen, M.F. Wheeler
	Simulation of a helicopter rotor flow	J. Ilkko, J. Hoffren, T. Siikonen
	Accuracy assessment of the Cartesian grid method for compressive inviscid flows using a simplified ghost point treatment	M. Asif Farooq, B. Müller
	CFD study of roll damping of a winget bullet	A. Laaksonen
	Electromechanics of polyurethane elastomers	A. Ask, M. Ristinmaa, A. Mentzel
	A unified solution attempt for the torsion problem	J. Aalto, R. Syrjä
11:00	**Lunch**	
12:00	**S8A Multibody mechanics 2** Thematic session organised by J. Mäkinen and M. Matikainen	
	Digital nomenclature code *dncm* for generation of finite-element kinematics	O. Dmitrochenko, A. Mikkola
	Modal analysis used to estimate bone density in-vivo	A. Kłodowski, T. Rantalainen, A. Mikkola
	Human walking simulation by using optimization	D. Garcia-Vallejo
	Collapse simulations of flexible multibody systems	J. Mäkinen
12:00	**S8B Applications**	
	Loop formation in NiTi suture materials	A.-J. Vuotikka
	Crack propagation in rails under RCF loading conditions based on material forces	J. Brouzoulis, M. Ekh
	Simulation of frictional effects in models for calculation of the equilibrium state of flexible pipe armouring wires in compression and bending	N.H. Ostergaard, A. Lyckegaard, J.H. Andreasen
	Virtual testing of cold-formed structural members	P. Hradil, L. Fülöp, A. Talja
	Models of multilayered shells in ophthalmology	S.M. Bauer, L.A. Karamshina
	Testing and analysis of adhesively bonded single lap joints at sub-zero temperatures - a master thesis	M.L. Haslerud, R.H. Gaarder, F. Grytten, H. Osnes
12:00	**S8C Micro- and nano-mechanics**	
	Determination of the elastic fields of an elliptic nano-inhomogeneity in anti-plane couple stress elasticity using RKPM	H. Shodja, S. Tahaei-Yaghoubi, B. Alemi
	Atomistic modeling of Phase transformation in ZnO nanorods	J. Y. He, S. Nagao, J. Y. Wu, Z. L. Zhang
	All-atom molecular dynamics study on mechanical properties of polystyrene glass	S. Nagao, J. Wu, J. He, Z. Zhang
	Equilibrium crystal shapes on a non-horizontal wall	M. Reivinen, E.-M. Salonen
14:00	**Break**	
14:15	**S9 Plenary**	
	Large eddy simulation studies on convective atmospheric boundary layer	**A. Hellsten**, S. Zilitinkevich
	Thermodynamic interpretation of finite volume algorithms	**A. Berezovski**
15:25	**Closing**	

Wednesday 02.11		Thursday 03.11				Friday 04.11			
Plenary lectures: Nordia Parallel sessions: A: Nordia B: Nautica C: Baltica		7:30	Registration Marina congress center						
		8:00	Opening			8:00	S6		
		8:15	S1			8:40	Coffee break		
		10:15	Coffee break			9:00	S7A	S7B	S7C
		10:45	S2A	S2B	S2C	11:00	Lunch		
		12:45	Lunch			12:00	S8A	S8B	S8C
		13:45	S3			14:00	Break		
		15:15	S4A	S4B	S4C	14:15	S9		
		17:15	Coffee break			15:25	Closing		
		17:30	S5						
18:00	Icebreaking reception and pre-registration Key West bar	18.40							
		19:45 20:15	Reception and dinner Hotel Kämp						

Edited by Jouni Freund and Reijo Kouhia

Proceedings of the 24th Nordic Seminar on Computational Mechanics

Aalto University

Aalto-ST 23/2011

BUSINESS + ECONOMY

ART + DESIGN + ARCHITECTURE

SCIENCE + TECHNOLOGY

CROSSOVER

DOCTORAL DISSERTATIONS

ISBN 978-952-60-4346-3 (pdf)
ISBN 978-952-60-4347-0
ISSN-L 1799-4896
ISSN 1799-490X (pdf)
ISSN 1799-4896

Aalto University
School of Engineering
Department of Civil and Structural Engineering
www.aalto.fi